iScience

CellPress
OPEN ACCESS

Review

# Recent progress and future prospects on halide perovskite nanocrystals for optoelectronics and beyond

Yuncheng Mu,[1] Ziyu He,[2] Kun Wang,[3] Xiaodong Pi,[3,4] and Shu Zhou[1,*]

## SUMMARY

**As an emerging new class of semiconductor nanomaterials, halide perovskite ($ABX_3$, X = Cl, Br, or I) nanocrystals (NCs) are attracting increasing attention owing to their great potential in optoelectronics and beyond. This field has experienced rapid breakthroughs over the past few years. In this comprehensive review, halide perovskite NCs that are either freestanding or embedded in a matrix (*e.g.*, perovskites, metal-organic frameworks, glass) will be discussed. We will summarize recent progress on the synthesis and post-synthesis methods of halide perovskite NCs. Characterizations of halide perovskite NCs by using a variety of techniques will be present. Tremendous efforts to tailor the optical and electronic properties of halide perovskite NCs in terms of manipulating their size, surface, and component will be highlighted. Physical insights gained on the unique optical and charge-carrier transport properties will be provided. Importantly, the growing potential of halide perovskite NCs for advancing optoelectronic applications and beyond including light-emitting devices (LEDs), solar cells, scintillators and X-ray imaging, lasers, thin-film transistors (TFTs), artificial synapses, and light communication will be extensively discussed, along with prospecting their development in the future.**

## INTRODUCTION

Halide perovskites are semiconductors described by the formula of $ABX_3$, where A, B, and X are organic/inorganic cation, metal cation, and halide anion, respectively. They have large optical absorption coefficients, high dual electron and hole mobility, tunable bandgap, and strong defect tolerance which are of critical importance for high-performance optoelectronic devices (Correa-Baena et al., 2017; Green et al., 2014; Jena et al., 2019; Tan et al., 2014; Wang et al., 2016b). As one of the most intensively studied variants of halide perovskites, halide perovskite nanocrystals (NCs) not only possess the size and surface-tunable electronic and optical properties like conventional semiconductor (*e.g.*, Si, CdSe, and PbS) NCs (Kuno et al., 1997; Law et al., 2008; Moreels et al., 2009; Ni et al., 2019), but also exhibit fascinating component-dependent behaviors (Huang et al., 2016; Kovalenko et al., 2017; Shamsi et al., 2019, 2021).

Impressive progress in the development of optoelectronics has recently been made by using versatile halide perovskite NCs. Solar cells based on mixed cesium and formamidinium lead iodide ($Cs_{0.5}FA_{0.5}PbI_3$) perovskite NCs achieved a certified record power conversion efficiency (PCE) of 16.6%, outperforming most conventional semiconductor-NC-based solar cells (Hao et al., 2020b; Lan et al., 2016; Sargent, 2012; Yuan et al., 2020). A high open-circuit voltage ($V_{oc}$) of ~1.65V was realized by using cesium lead bromide ($CsPbBr_3$) perovskite NCs, which was almost two times larger than that of solar cells based on PbS NCs (Biondi et al., 2021; Zhang et al., 2020b). Perovskite-NC-based green and red light-emitting devices (LEDs) have shown remarkable external quantum efficiency (EQE) exceeding 20% with high operation stability (Cao et al., 2018; Kim et al., 2021b; Li et al., 2021; Lin et al., 2018; Wang et al., 2021a). Efficient blue LEDs with a peak EQE of 13.8% have also been demonstrated by using strong-quantum-confined perovskite NCs embedded in a perovskite matrix, paving the way for the niche market application of perovskite LED technologies (Dong et al., 2020; Liu et al., 2019c, 2022). Multicolor perovskite-NC scintillators that are suitable for the mass production of ultrasensitive X-ray detectors and large-area flexible X-ray images have been created, holding substantial promise for advancing the X-ray sensing and imaging industry (Chen et al., 2018b; Gandini et al., 2020; Liu et al., 2019a). Solution-processed lasers with tunable wavelength

[1]School of Materials, Shenzhen Campus of Sun Yat-sen University, Shenzhen, Guangdong 518107, China

[2]Department of Material Science and Metallurgy, University of Cambridge, Cambridge CB3 0FS, UK

[3]State Key Laboratory of Silicon Materials and School of Materials Science and Engineering, Zhejiang University, Hangzhou, Zhejiang 310027, China

[4]Institute of Advanced Semiconductors and Zhejiang Provincial Key Laboratory of Power Semiconductor Materials and Devices, Hangzhou Innovation Center, Zhejiang University, Hangzhou, Zhejiang 311215, China

*Correspondence: zhoush67@mail.sysu.edu.cn

https://doi.org/10.1016/j.isci.2022.105371

and ultralow threshold were also demonstrated by using versatile perovskite NCs (Athanasiou et al., 2021; Xu et al., 2016; Yakunin et al., 2015). The success of halide perovskite NCs on optoelectronic devices has stimulated research on a variety of technological applications including thin-film transistors (TFTs), artificial synapses, photonic sources, light communication, gas sensors, and photocatalysts, making perovskite NCs a promising class of semiconductor nanomaterials for optoelectronics and beyond (Akkerman et al., 2018b; Dey et al., 2021; Sutherland and Sargent, 2016).

The great achievements largely stem from the continuous improvement of the optical and electronic properties of halide perovskite NCs. On one hand, many approaches such as hot-injection, ligand-assisted reprecipitation, laser writing, template-assisted method, emulsion method, ultrasonic or microwave-based method, solvothermal method, microfluidic method, ball milling, electrospinning or electrospray method have been developed for the synthesis of versatile perovskite NCs with well-defined size, surface and morphology (Imran et al., 2018; Protesescu et al., 2016; Zhong et al., 2018, 2019). On the other hand, effective methods to promote the properties of halide perovskite NCs have been established in terms of manipulating components (A-site, B-site, and X-site) of the perovskite NCs (Akkerman et al., 2017a; Liu et al., 2017a; Zhu et al., 2020). Moreover, post-synthesis methods such as ligand exchange and ion exchange have been extensively explored, providing an important complementary route to further design the properties of perovskite NCs (Imran et al., 2019; Jang et al., 2015). Consequently, high-quality perovskite NCs with near-unity light emission properties (*e.g.*, photoluminescence quantum yields (PLQYs) ≈ 100% and full width at half maximum (FWHM) < 20 nm) and a wide optical response spanning from UV to near-infrared (NIR) spectrum have been achieved (Pan et al., 2017a, 2018b; Rastogi et al., 2020; Yong et al., 2018). Multiphoton absorption (MPA), multiple exciton generation (MEG) as well as tunable Stocks shift which are of great importance to optoelectronics have also been demonstrated (Chen et al., 2017b; Manzi et al., 2018). Self-assembly of these high-quality perovskite NCs into highly ordered structures, *i.e.*, superlattices, gives rise to distinct superfluorescence (SF) that has been rarely observed in conventional semiconductor NCs (Raino et al., 2018).

In this review, we will first introduce the important structural properties and the unique defect physics of halide perovskite NCs. Advances in both synthesis and post-synthesis methods of various kinds of perovskite NCs will be present. In addition to adjusting the optical and electronic properties in terms of size-reduction-induced quantum confinement, recent progress in surface and component engineering to promote the properties of perovskite NCs will be highlighted. The distinct optical properties including near-unity light emission, large optical absorption coefficients, and size-dependent Stocks shift will be discussed together with the unique mixed ionic-electronic ambipolar transport properties. Tremendous investigations on the use of perovskite NCs to make diverse optoelectronic devices by taking advantage of the distinct optical and electronic properties of perovskite NCs will then be summarized. We will mainly focus on recent efforts for the rapid development of conventional optoelectronic devices including LEDs, solar cells, scintillators and X-ray imaging, lasers, and the exciting progress for exploring novel applications such as TFTs, synaptic devices, and light communication. The schematic illustration of the scope of this review is shown in Figure 1.

## STRUCTURE

### Dimensionality

Perovskites, named in honor of the Russian mineralogist Count Lev Alekseyevich von Perovski, have attracted great attention in optoelectronics in the recent decade because of their unique properties. The origin of perovskites can date back to 1839 (Lu et al., 2019; Zhou et al., 2019a). The mineralogist Gustav Rose from German firstly discovered the mineral $CaTiO_3$ in the Ural Mountains (Akkerman and Manna, 2020). Since then, compounds denoted by the general chemical formula of $ABX_3$ with a similar crystal structure as that of $CaTiO_3$ can be described as perovskite (Saidaminov et al., 2017; Shamsi et al., 2019). For metal halide perovskites (MHP), A could be a monovalent organic cation (*e.g.*, methylammonium [$MA^+$, $CH_3NH_3^+$], formamidinium [$FA^+$, $CH(NH_2)^{2+}$]) or inorganic metal cation (*e.g.*, $Cs^+$, $Rb^+$), B is a bivalent metal cation (*e.g.*, $Pb^{2+}$, $Sn^{2+}$, $Ge^{2+}$, $Cu^{2+}$, $Eu^{2+}$, and $Ni^{2+}$), X is one or more halides ($Cl^-$, $Br^-$, $I^-$ or pseud-halogen ions like $SCN^-$) (Cao et al., 2020; Jeong et al., 2021; Lu et al., 2020b; Saruyama et al., 2021; Zhou et al., 2017a).

A typical perovskite with an ideal cubic structure is schematically shown in Figure 2A. The A cations occupy the vertexes, the B cations are positioned at the center of the cube, and the X anions occupy the vertexes

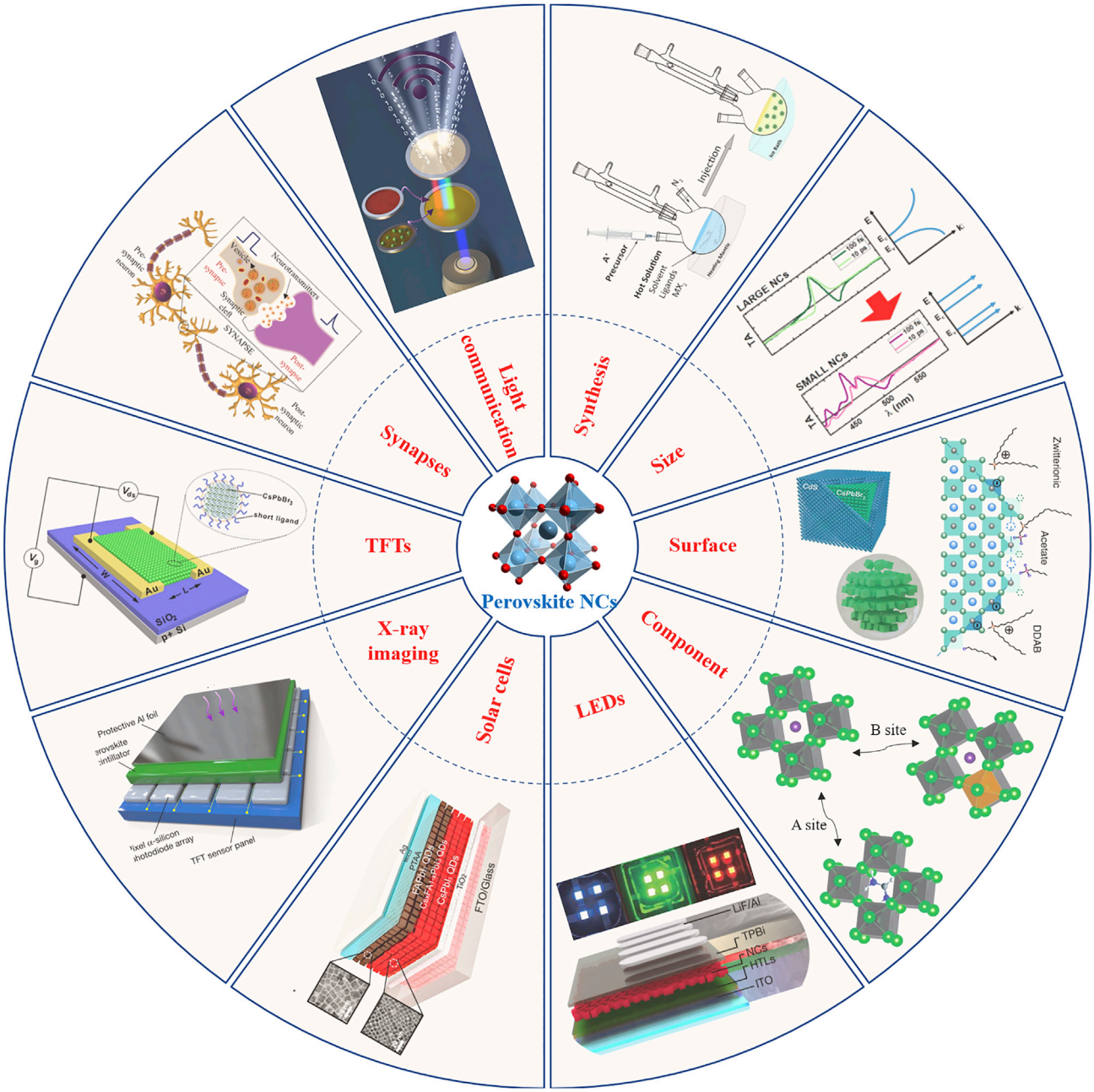


**Figure 1. Schematic illustration of the scope of this review**

The continuous improvement of the optical and electronic properties of halide perovskite NCs has been enabled by manipulating their size, surface, and component. The use of halide perovskite NCs for versatile optoelectronic devices and beyond such as light-emitting diodes, solar cells, X-ray imaging, thin-film transistors, and synaptic devices has been intensely explored in the past few years.

and face-centers, respectively. The central B cation octahedrally coordinates with six X anions in a $[BX_6]^{4-}$ configuration. Meanwhile, the A cations occupy the interval of octahedra, coordinated with 12 X anions (Wei et al., 2019). Through a continuous array of corner-sharing $[BX_6]^{4-}$ octahedra, one can attain an ideal three-dimensional (3D) cubic phase perovskite structure (space group Pm3m) (Saidaminov et al., 2017). Given that the cubic $ABX_3$ lattice can be easily converted into other phases, there is an immense investigation into perovskites with different structures and compositions, defined as "perovskite-related structures", such as a zero-dimensional (0D) $A_4BX_6$ (Akkerman et al., 2018a) and a two-dimensional (2D) $AB_2X_5$ (Iyikanat

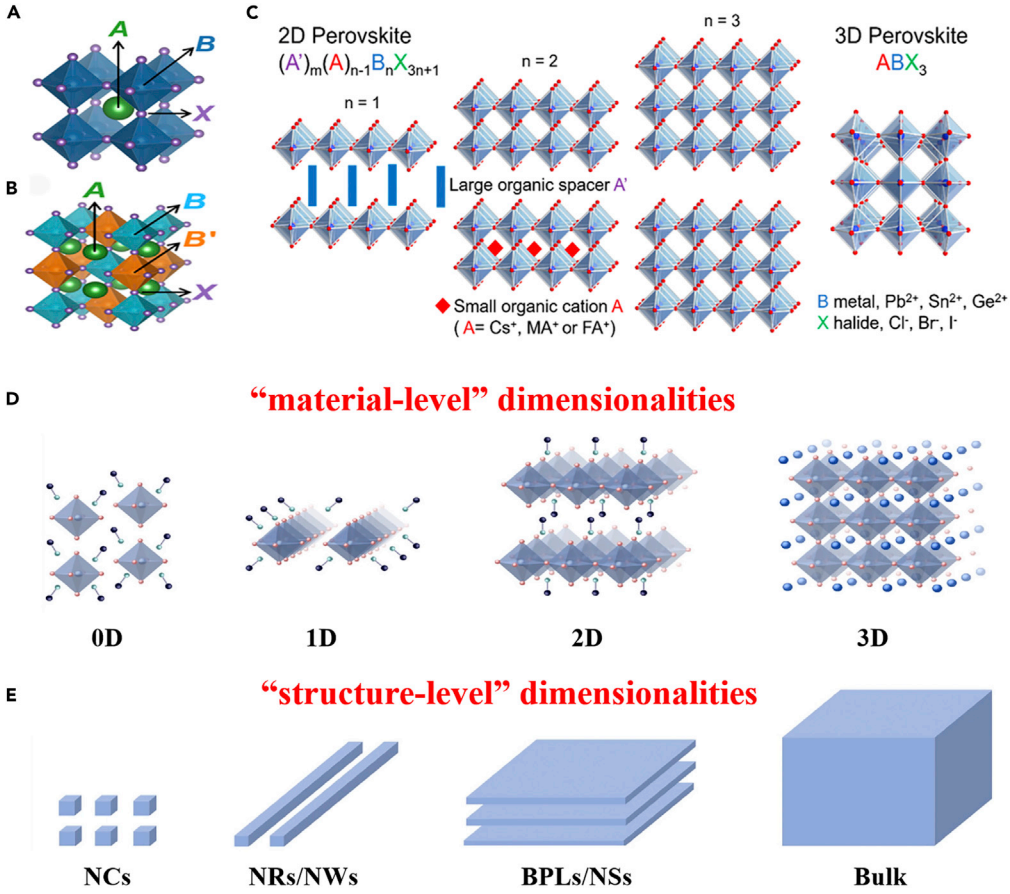


**Figure 2. Perovskites with reduced dimensionalities**

(A) $ABX_3$, the cubic single perovskite structure (Pm3m).

(B) $A_2MM'X_6$, the double perovskite structure (Fm $\bar{3}$ m). Figures A and B reprinted from (Bartel et al., 2019). Copyright © 2019, American Association for the Advancement of Science.

(C) Schematic showing the structural evolution from 2D perovskite to 3D perovskite with key components. Reprinted from (Mao et al., 2019). Copyright © 2019, American Chemical Society. (D and E) Schematic illustrations of low-dimensional perovskites and bulk perovskites from the view of "material-level" and "structure-level", respectively. Reprinted from (Zhu and Zhu, 2020). Copyright © 2020, Wiley.

et al., 2017). In a 3D perovskite, the $[BX_6]^{4-}$ octahedra is corner-shared along all three 4-fold octahedral axes. However, in a 2D perovskite with a layered structure, corner-shared $[BX_6]^{4-}$ octahedra has two octahedral axes, derived from 3D by slicing along specific crystallographic planes (Figure 2C) (Saidaminov et al., 2017). Sahin et al. reported the single-layer structures of perovskite-like $CsPb_2Br_5$ crystal which is formed by alternating A and $[B_2X_5]$- layers from theoretical respect by using first-principles density functional theory (DFT) calculations (Iyikanat et al., 2017). Similarly, 1D perovskites can also be obtained by slicing the sheets perpendicularly, with octahedra remaining connected only along one axis. 0D perovskites such as the $A_4BX_6$ structure is an extreme case, wherein the X is no longer shared by the $[BX_6]^{4-}$ octahedra completely decoupled in all dimensions (Akkerman et al., 2018a).

By introducing long chain amines or A-site cations with larger size, one can readily attain 2D perovskites, *i.e.*, Ruddlesden-Popper (RP) type layered perovskites. These 2D perovskites have the general formula $R_2A_{n-1}B_nX_{3n+1}$, where R is a long-chain alkyl or aromatic ammonium cation as a spacer between the inorganic sheets and n is an integer, defining the number of inorganic layers held together (Figure 2C) (Dou et al., 2015; Tsai et al., 2016; Wang et al., 2019d). In general, n = 1 corresponds to a pure 2D layered structure, n = ∞ constitutes a 3D structure. If n is any other integer, it corresponds to a quasi-2D layered RP structure (Wang et al., 2019a). Quasi-2D perovskites combine the enhanced stability of pure 2D perovskites with the good optoelectronic properties, *e.g.*, long-range carrier diffusion, of bulk perovskites.

Research in 2D perovskites started much earlier. For instance, Meresse et al. reported the Raman scattering and X-ray diffraction (XRD) study of the structural transformation of $(C_3H_7NH_3)CdCl_4$ last century (Mokhlisse et al., 1985). It was found that the 2D structure exhibited intrinsic quantum and dielectric confinement effects as a result of the few-unit-cell thickness of the high-dielectric inorganic layers (Fu et al., 2019; Mao et al., 2019). Hence, the structure might boost the performance of solar cells, LEDs, and many other new applications (Fang et al., 2021a). In 2016, Quan et al. reported the preparation of a series of quasi-2D perovskite films with the formula of $PEA_2(CH_3NH_3)_{n-1}Pb_nI_{3n+1}$ using phenylethylammonium iodide (PEAI) as the spacer (Quan et al., 2016). The quasi-2D perovskite films exhibited improved stability while retaining the high performance of conventional 3D perovskites. Importantly, solar cells based on the quasi-2D perovskite films demonstrated a 15.3% certified PCE with negligible hysteresis and greatly improved longevity. Stoumpos et al. reported the scalable synthesis, crystal structure, and optical properties of the homologous 2D series of $(CH_3(CH_2)_3NH_3)_2(MA)_{n-1}Pb_nI_{3n+1}$ and found that the n = 2–4 compounds displayed optoelectronic properties that are different from either the n = 1 or n = ∞ end-members with a strong PL emission at room temperature (Stoumpos et al., 2016). Zhang et al. demonstrated a lead-free 2D RP type $(C_{18}H_{35}NH_3)_2SnBr_4$ perovskite with strong emission from the self-trapped states with PLQYs in colloidal suspension and in a film up to 88 and 68% respectively, which could be an emitting layer in inverted LED structures (Qiu et al., 2018). Recently, Najman and coworkers performed a series of DFT calculations to investigate the surface properties of the 2D Ruddlesden-Popper perovskite crystals (n = 1, 2, 3) with low-index facets. It was shown that the surface energies of 2D perovskite facets critically depended on the amount of truncated $[PbI_6]^{4-}$ octahedral, cleavage of van der Waals bonds, as well as the reorganization of hydrogen bonding networks following surface cleavage (Najman et al., 2021). Considering that the atomistic information about the structural stability and growth kinetics of 2D perovskite materials by current state-of-the-art characterization tools is no picnic, it is foreseeable that this work will make a difference in fabricating high-quality single crystal 2D perovskite materials for potential applications.

Double perovskite ($A_2MM'X_6$), in which two divalent $B^{2+}$ cations are replaced by a monovalent and a trivalent cation (Figure 2B), is another type of well-studied perovskites (Igbari et al., 2019). Lead halide perovskites usually demonstrate poor ambient stability and lead-related toxicity immensely hindering their applications, which could be resolved by double perovskites (Bekenstein et al., 2018; Wolf et al., 2021). Volonakis et al. firstly synthesized $Cs_2AgBiCl_6$ with a double perovskite structure. They found that the $[Bi\text{-}Cl_6]^{3-}$ and $[AgCl_6]^{5-}$ octahedra in a rock-salt face-centered cubic structure were alternated, leading to an indirect bandgap of ~2.2 eV not ideal for optoelectronic applications (Volonakis et al., 2016). Shortly afterward, the same group fabricated and characterized a new In-based double perovskite compound $Cs_2AgInCl_6$ with a direct bandgap of ~3.3 eV, although the PLQY was very low (Volonakis et al., 2017). The breakthrough of the optical performance was subsequently achieved by Luo et al.. They synthesized alloyed $Cs_2(Ag_{0.60}Na_{0.40})InCl_6$ NCs by incorporating $Na^+$ into $Cs_2AgInCl_6$ to break the dark transition and the optimally alloyed product emitted warm-white light with PLQY up to 86% and worked for over 1,000 h (Luo et al., 2018).

Recently, Wu et al. reported the synthesis of a large family of 2D Ruddlesden-Popper type lead-free halide double perovskites $Cs_{n+1}In_{n/2}Sb_{n/2}I_{3n+1}$ ($M^+$: $In^+$, $Cu^+$, $Ag^+$, $Au^+$; $M^{3+}$: $Bi^{3+}$, $Sb^{3+}$; n = 3) and related heterostructures (Wu et al., 2018a). It was demonstrated that the energy gap could be effectively reduced by increasing the layer thickness. Vacancy-ordered double perovskites such as $Cs_3Sb_2Br_9$ are another kind of perovskite derivative, which can be considered by removing part of the Sb atoms at each center of the $[SbBr_6]^{3-}$ octahedron at regular intervals (Zhang et al., 2017c). However, such a structure implies lower-dimensional connectivity of metal halide octahedral, leading to lower electronic mobility compared to the standard $ABX_3$ perovskites (Liu et al., 2021d). As a result, there are not very suitable for optoelectronic applications.

We would like to point out that it is pivotal to distinguish the difference between "material-level" and "structure-level" low dimensionalities (Zhu and Zhu, 2020). The "material-level" low dimensionalities mean that the individual metal halide species are partially isolated from each other by organic cations with the different corner-sharing of the $[BX6]^{4-}$ octahedral (Figure 2D). By contrast, the "structure-level" low dimensionalities describe the geometric morphologies of perovskites (Figure 2E) and usually refer to versatile nanostructures like NCs, nanoplatelets (NPLs), nanosheets (NSs), nanowires (NWs), nanorods (NRs), and nanocubes (NCus). Note that different categories are established to elaborate on different aspects of these materials and are not on opposite sides although there are overlaps between them. In the

following, we will mainly concentrate on perovskite NCs that have already shown great promise in versatile optoelectronics and beyond.

## Quantum confinement effect

Perovskite NCs offer unique size-dependent tunability on the optical and electronic properties because of the quantum confinement effect. The quantum confinement effect describes changes in the electronic band structure of a semiconductor as a result of the reduction in the dimensionality below a certain threshold, *i.e.*, exciton Bohr diameter. The quantum confinement, on one hand, gives rise to a blue shift of the PL energy. On the other hand, it causes perovskite NCs to emit light much more efficiently than their bulk counterparts. Compared to conventional NCs such as PbSe, InSb, and CdSe, the exciton Bohr radius of perovskite NCs is rather small (*e.g.*, ~4.6 nm for $MAPbX_3$) (Baranowski and Plochocka, 2020; Ni et al., 2016; Pi et al., 2008; Qu and Peng, 2002; Raino et al., 2018; Sikorski and Merkt, 1989). Thus, quantum confinement will be observed for perovskite NCs with a radius smaller than 5 nm.

In 2016, Yamauchi et al. reported the observation of quantum confinement in monodisperse $MAPbX_3$ NCs (Malgras et al., 2016). They prepared monodisperse $MAPbX_3$ NCs inside the mesoporous silica templates. In this case, the size of NCs is governed by the pore size of the templates. The gradual shift of the light emission peak and absorption onset toward higher energy together with the dependence of PL lifetime on the NC size provide direct evidence that fine-tuning of the optical properties can be obtained from simply controlling the size of perovskite NCs in terms of the quantum confinement effect. Son et al. reported precise tuning of quantum confinement in monodisperse $CsPbBr_3$ NCs utilizing the thermodynamic equilibrium instead of the kinetic control (Dong et al., 2018). They measured both single-particle and assembly PL spectra of $CsPbBr_3$ NCs with different sizes, demonstrating near-perfect spectroscopic homogeneity.

Hodgkiss et al. investigated the evolution of quantum confinement in $CsPbBr_3$ NCs by using ultrafast transient absorption spectroscopy (Butkus et al., 2017). For $CsPbBr_3$ NCs above ~7 nm edge length, the spectral signatures were similar to bulk perovskites. Only a small perturbation in the free carrier photophysics was observed because the NCs were actually within the weak confinement regime. While for smaller $CsPbBr_3$ NCs with ~4 nm edge length strong quantum confinement was manifested in the transient absorption spectral dynamics, featuring discrete energy states and enhanced bandgap renormalization energy. These results are well consistent with the increase of optical bandgap observed in the steady-state absorption and emission spectra.

Recently, Zhou et al. measured the electronic band structure of versatile perovskite NCs (Zhou, 2021). The lowest unoccupied molecular orbital (LUMO), the highest occupied molecular orbital (HOMO), and Fermi level were plotted as a function of the NC size. It is revealed that the quantum confinement more significantly impacts the LUMO than the HOMO for all perovskite NCs. Specifically, the LUMO readily moves toward the vacuum level while the HOMO only changes slightly. This is in close agreement with what has been observed in the tuning of band structures of quasi-2D perovskites and colloidal semiconductor NCs via the quantum size effect (Jasieniak et al., 2011; Yuan et al., 2016).

## Structural stability

Structural stability is the foremost challenge that must be addressed before practical perovskite-NC-based devices can be realized (Ahmed et al., 2021). It has been recognized that as easy as it is to make perovskite NCs, it is just as easy to destroy them (Kovalenko et al., 2017). In order to evaluate and predict the stability and distortion of perovskite structures, enormous efforts have been made. Goldschmidt firstly proposed a semiempirical tolerance factor (***t***) last century (Huang et al., 2017b). The tolerance factor is defined as

$$t = \frac{R_A + R_X}{\sqrt{2}(R_{B+} R_X)} \qquad \text{(Equation 1)}$$

where $R_A$, $R_B$, and $R_X$ refer to ionic radii of A, B, and X ions, respectively. Notably, ***t*** should be 1 for an ideal cubic perovskite structure because the A cation must be accommodated into the framework of $[BX_6]^{4-}$ octahedron, and the ion spheres should be tangent to each other. In general, stable perovskite structures such as cubic, orthorhombic, tetragonal, and hexagonal structures, will be formed if ***t*** is between 0.813 and 1.107, whereas other perovskite-related structures are more stable outside this range (Wei et al., 2019). Therefore, the tolerance factor can be utilized to determine whether the A-site cations can fit in the cavities within the $[BX_6]^{4-}$ octahedron. If the A cation is relatively smaller, it will lead to octahedral tilting,

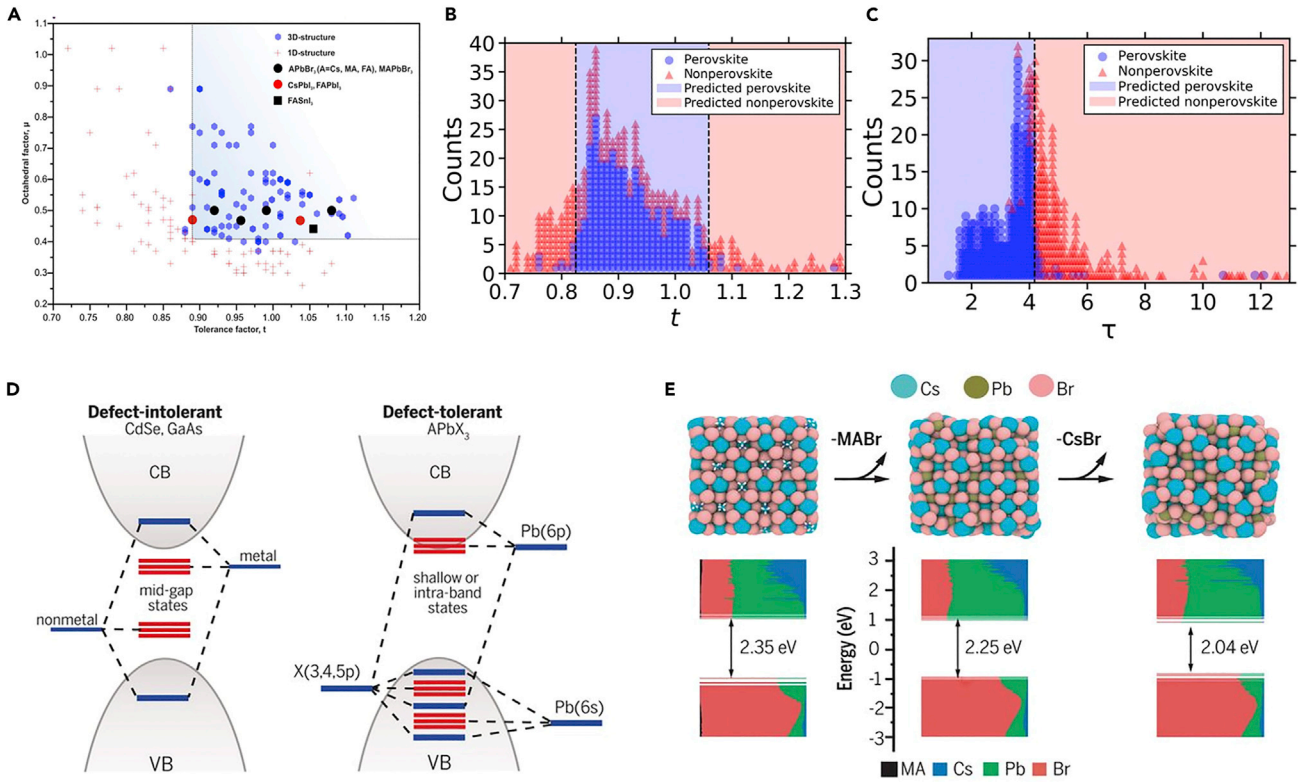


**Figure 3. Structural stability and defect tolerance**

(A) **μ-t** structural map of different $ABX_3$ perovskite compounds. The light blue squared area represents the region in which stable compounds are located. Reprinted from (Protesescu et al., 2017). Copyright © 2017, American Chemical Society.

(B) A decision tree classifier determines the optimal bounds for perovskite formability using $0.825 < t < 1.059$, which yields a classification accuracy of 74% for 576 experimentally characterized $ABX_3$ solids.

(C) t achieves a classification accuracy of 92% on the set of 576 $ABX_3$ solids based on perovskite classification for $t < 4.18$, with this decision boundary identified using a one-node decision tree. Figures B and C reprinted from (Bartel et al., 2019). Copyright © 2019, American Association for the Advancement of Science.

(D) Electronic structure of typical III–V, II–VI, or group IV semiconductors (*e.g.*, CdSe, GaAs, and InP) compared to lead halide perovskites.

(E) Electronic structure of $CsPbBr_3$ NCs obtained before and after removing ligands from the surface. All structures have been computed at the DFT/PBE level of theory, where PBE is Perdew-Burke-Ernzerh of exchange-correlation functional. Figures D and E reprinted from (Kovalenko et al., 2017). Copyright © 2017, American Association for the Advancement of Science.

distortion, or even a phase transition. However, if the A-site cation is too large for the $[BX_6]^{4-}$ octahedral framework, other perovskite-related structures tend to form like the Ruddlesden-Popper type layered perovskite structures (Lu et al., 2020a).

In addition to the tolerance factor, octahedral factor ($\boldsymbol{\mu}$) is another semiempirical geometric parameter for assessing the structural stability of the $[BX_6]^{4-}$ octahedra (Li et al., 2008), which is defined as

$$\boldsymbol{\mu} = \frac{R_B}{R_X} \qquad \text{(Equation 2)}$$

Typically, the $[BX_6]^{4-}$ octahedra are stable when $\mu$ is between 0.442 and 0.895 (Protesescu et al., 2017; Travis et al., 2016). Clearly, the ionic radii play a crucial role in the crystal structural stability (Figure 3A). Note that a reasonable $\boldsymbol{t}$ and $\boldsymbol{\mu}$ are necessary but not sufficient for the formation of a stable 3D $ABX_3$ perovskite. In particular, when the organic cations are non-spherical, the assumption that the ions are unpolarizable hard spheres, especially for the iodide anion may not be valid (Fedorovskiy et al., 2021). In 2016, Travis et al. carefully assessed the validity of the tolerance factor for halide perovskites and proposed an alternative method by introducing a revised set of ionic radii for cations that are anion dependent, which could help a more accurate prediction of the possible perovskite combinations (Travis et al., 2016).

It is striking that theoretical calculation together with data-driven computation are acting an increasingly important role in predicting the stability of perovskites (Han et al., 2020; Ranke et al., 2021). In 2018, Giustino et al. demonstrated that the Goldschmidt tolerance factor enabled predict perovskites with a fidelity of 80% by combining inferential statistics with large-scale web data extraction. They enumerated 90,000 hitherto-unknown compounds awaiting discovery, offering untapped opportunities in structure prediction and materials design (Filip and Giustino, 2018). Afterward, Bartel and coworkers developed a new tolerance factor ($\tau$) by using the SISSO (sure independence screening and sparsifying operator) approach which can predict 92% of the compounds, while this figure is limited to 74% for its counterpart $t$ (Figure 3B) (Bartel et al., 2019). The factor $\tau$ is defined as follows:

$$\tau = \frac{R_X}{R_B} - n_A\left(n_A - \frac{R_A/R_B}{\ln(R_A/R_B)}\right), \quad \text{(Equation 3)}$$

where $n_A$ is the oxidation state of the cation A. Using the new descriptor, $\tau$ was shown to generalize outside the training set for 1034 experimentally realized single and double perovskites (91% accuracy), as shown in Figure 3C. Specifically, the values of $\tau$ for typical halide single perovskites such as $CsPbBr_3$, $CsPbCl_3$, $CsPbF_3$, $MAPbBr_3$, and $FAPbBr_3$ are calculated to be 4.10, 3.98, 3.57, 3.68 and 3.47, respectively, all within the regime of $\tau < 4.18$ for the formation of stable perovskites. However, the value (4.30) of $\tau$ for $CsPbI_3$ is >4.18, suggesting $CsPbI_3$ is less stable than the other perovskites. Furthermore, the probability of double perovskite formation for thousands of unexplored compounds was predicted, resulting in a library of stable perovskites ordered by their likelihood of forming perovskites, which would guide experimentalists and theorists toward finding the most stable perovskites. Recently, Sun et al. developed a closed-loop optimization framework that seamlessly marries data from first principle calculations and high throughput experimentation into a single machine learning algorithm and achieved more than 17-fold higher stability within a combinatorial space of $Cs_xMA_yFA_{1-x-y}PbI_3$ rapidly (Sun et al., 2021).

## Defect tolerance

It is widely accepted that weakly bonding orbitals or localized non-bonding, *i.e.*, dangling bonds, in semiconducting NCs generate trap states in the bandgap, which facilitate nonradiative recombination like auger recombination, thereby reducing the overall PLQY. However, things may be different in halide perovskite NCs. Numerous experimental studies on the optical properties suggest perovskite NCs are defect-tolerant and do not suffer similar quenched emission from surface defect states even without additional surface passivation. Subsequent theoretical simulations indicate that the defect tolerance is basically related to the unique electronic band structure configurations of perovskite NCs (Figure 3D) (Kovalenko et al., 2017; ten Brinck and Infante, 2016). In a conventional defect-intolerant band structure, the VB is mainly composed of bonding orbitals while the conduction band (CB) is predominantly composed of antibonding orbitals. In perovskite NCs, the energetic position of most trap states lies in the conduction or valence bands rather than within the bandgap, leading to negligible effects on the PLQYs. DFT calculations on the energy levels of various defects confirm the absence of trap states in the bandgap (Dirin et al., 2016; Tablero Crespo, 2019). Furthermore, it has been proved that the perovskite NC maintains both structural and electronic integrity with trap-free bandgaps despite these substantial displacements of ligands from the NC surface (Figure 3E), although there is a slight change of bandgap (ten Brinck and Infante, 2016).

As research steps forward, it has been recently found that the energy of defect formation in halide perovskite NCs may also account for the strong defect tolerance (Huang et al., 2017b). Compared to the bulk perovskite crystals, the energetics of defect formation in perovskite NCs should change dramatically (ten Brinck et al., 2019). Firstly, a complex chemical equilibrium usually exists at the NC-ligands-solvent interface which can expose defects to a different environment than in the bulk crystals. Secondly, the defect is more likely to be formed at the NC surface instead of the core because of the large number of surface atoms. A study on the cubic-phase stability of $CsPbI_3$ NCs suggest the lattice strain due to low dimensionality makes perovskite NCs more stable than bulk perovskites (Swarnkar et al., 2016). Consequently, perovskite NCs are expected to be more defect tolerant than bulk perovskite crystals. The relatively low formation energy of vacancies in perovskite NCs results in a large number of Schottky-type defects, *i.e.*, equal number of anion and cation vacancies or halide and A-site vacancies. These defects can compensate for each other and maintain the overall charge neutrality of the lattice. Meanwhile, the interstitial and the antisite defects are absent due to the large bonding energy in the ionic lattice. In this context, perovskite NCs could yield high PLQYs without the same high purity, high temperature, or equipment-intensive vacuum synthesis as conventional semiconductor NCs, which make them more easily scalable for mass production.

Despite the high defect tolerance, the deep-level defects occur to perovskite NCs still degrade their optical properties. Owing to their ionic structure, perovskite NCs still are not stable upon exposure to air, polar solvent, heat, moisture, and light, which would cause substantial problems with synthesis, modification, storage, and application (Shangguan et al., 2020). Methods to avoid defects and confront their instability will be discussed in the following section of the synthesis of perovskite NCs.

## SYNTHESIS OF PEROVSKITE NANOCRYSTALS

To meet the diverse requirements of versatile applications, a great deal of effort has been devoted to reliable and straightforward synthetic strategies of perovskite NCs with tunable properties. Many synthetic methods have been developed including hot-injection (HI), ligand-assisted reprecipitation (LARP), laser writing, emulsion method, ultrasonic or microwave-based method, solvothermal method, microfluidic method, template-assisted method, ball milling, electrospinning or electrospray method, and chemical vapor deposition (CVD) (Haydous et al., 2021). These methods can be classified into two strategies, *i.e.*, "top-down" and "bottom-up" (Kostopoulou et al., 2019; Shamsi et al., 2019; Zhang et al., 2019b). The "top-down" approach involves the breaking down of the bulk materials into nanostructures and particles such as ball-milling and chemical exfoliation, which are inherently an extension of those that have been used for producing micron-sized products. In contrast, the "bottom-up" approach is a more effective build-up of a material from the very bottom via atom by atom, molecule by molecule, or cluster by cluster (Zhang et al., 2021b). Besides, post-synthesis methods such as ligand and ion-exchange reaction will also be discussed.

### Synthesis methods

#### *Hot injection*

Hot injection is a well-established and popular method for the synthesis of high-quality metal chalcogenide and other semiconductor NCs. This method involves the rapid injection of a precursor into a hot mixed solution (usually over 100°C) of the remaining precursors, organic ligands, and a high boiling solvent under an inert atmosphere like $N_2$ or argon, as shown in Figure 4A. Specifically, the organic ligands are usually alkyl chain acid and amine. Upon quick injection of the precursor, a rapid nucleation burst occurs with a simultaneous formation of small nuclei. The nucleation stage stops as a result of the rapid depletion of monomers. Within several seconds, plenty of NCs with a narrow size distribution was formed. Due to the rapid reaction rate, the nucleation and growth stages cannot be well separated in time, exposing added difficulties in controlling the NC size and morphology (Campbell et al., 2020).

In 2015 Kovalenko's group extended the HI method for the synthesis of all-inorganic cesium lead halide perovskite NCs ($CsPbX_3$, X = Cl, Br, and I or mixed halide systems Cl/Br and Br/I) (Protesescu et al., 2015). The composition and size of perovskite NCs can be readily adjusted, yielding tunable absorption bandgap energies across the entire visible spectral region of 410-700 nm (Figures 4B and 4C). PL spectra of $CsPbX_3$ NCs further confirmed their prominent optical properties, including narrow emission line widths of 12-42 nm, high QYs of 50-90%, and short radiative lifetimes of 1-29 ns.

Later, the synthesis of versatile perovskite-related nanomaterials and structures was demonstrated (Wang et al., 2016a). Using a modified HI method, Akkerman et al. prepared $Cs_4PbX_6$ (X = Cl, Br, I) NCs, which were nearly monodisperse with larger bandgaps (Akkerman et al., 2017b). The optical absorption spectra of $Cs_4PbX_6$ NCs featured strong and narrow transition bands independent of the NC size. Alivisatos and coworkers synthesized $Cs_2AgBiBr_6$ NCs by injecting cesium oleate solution into the mixture of $BiBr_3$, $AgNO_3$, 1-octadecene (ODE), oleic acid, and HBr at 200°C under a $N_2$ atmosphere (Bekenstein et al., 2018). The resulting $Cs_2AgBiBr_6$ NCs have a uniform cubic morphology and high crystallinity.

Recently, Huang et al. employed an improved HI method for the synthesis of lead-free $CsEuCl_3$ NCs (Huang et al., 2020). $Eu^{2+}$ can be easily oxidized into $Eu^{3+}$ when exposed to air and has a strong tendency to bind to solvent molecules. In this regard, $EuCl_3$ opted as an initial precursor. $Eu^{3+}$ was first reduced to $Eu^{2+}$ by using oleylamine (OAm) as a reagent. After that cesium oleate was injected into a noncoordinating solvent along with the obtained $Eu^{2+}$ precursor in the presence of oleic acid (OA) at 250°C for 45 min (Figure 4D). The reaction was then quenched in an ice–water bath. By using high-resolution transmission electron microscopy (HRTEM) and associated fast Fourier transform (FFT) simulation (Figure 4E), they found that the obtained NCs are ~15 nm in diameter. Moreover, The $CsEuCl_3$ NCs had PL emission centered at 435 nm, with a small FWHM of 19 nm comparable to lead halide perovskite NCs.

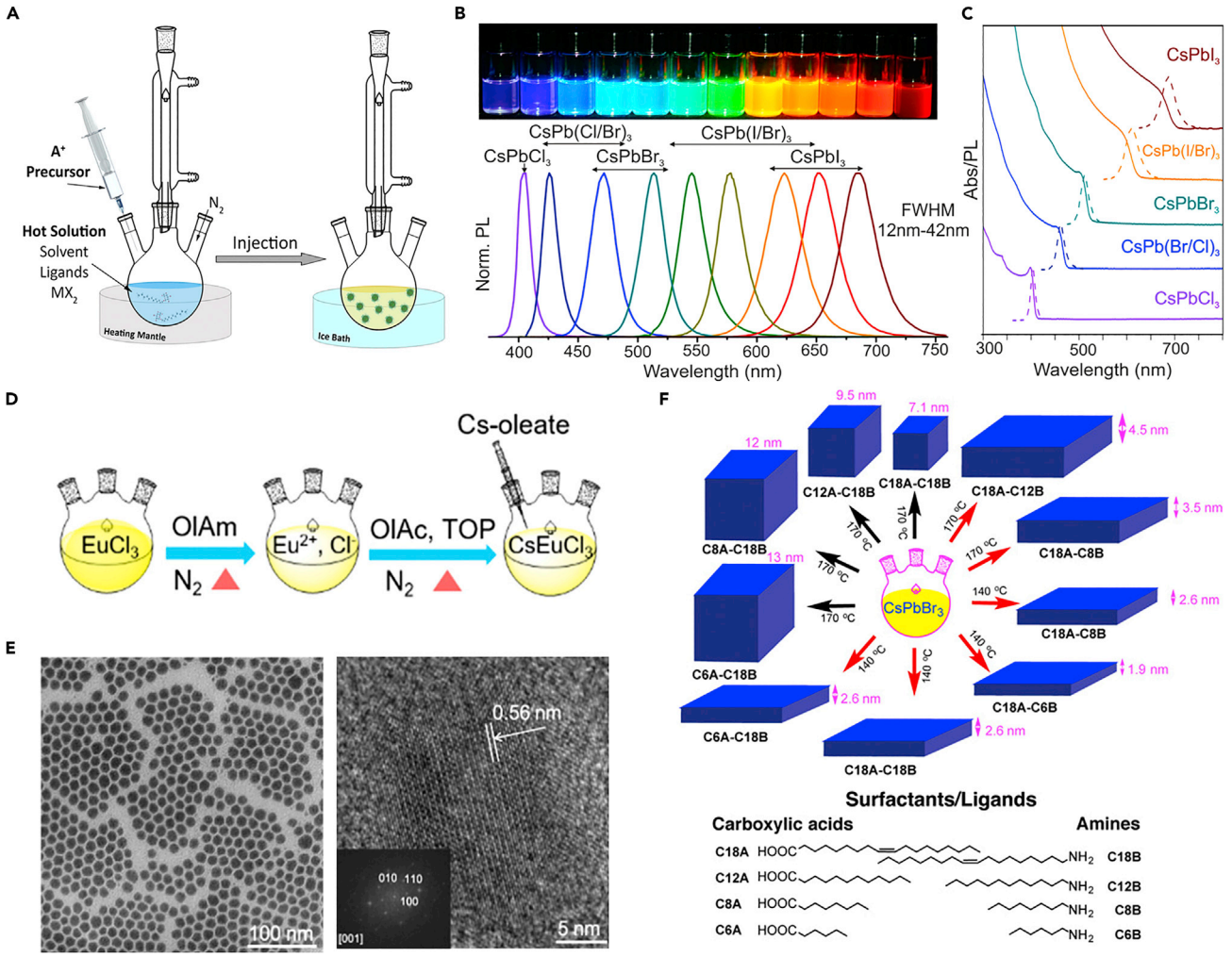


**Figure 4. Synthesis of perovskite NCs by hot-injection**

(A) Schematic of the hot-injection method used for the synthesis of perovskite NCs. Reprinted from (Shamsi et al., 2019). Copyright © 2019, American Chemical Society.

(B) Up: colloidal solutions of all-inorganic $CsPbX_3$ NCs in toluene under UV lamp (λ = 365 nm); Down: representative PL spectra ($\lambda_{exc}$ = 400 nm for all but 350 nm for $CsPbCl_3$ samples).

(C) Typical optical absorption and PL spectra. Figures B and C reprinted from (Protesescu et al., 2015). Copyright © 2015, American Chemical Society.

(D) Schematic of the hot-injection method used for the synthesis of lead-free $CsEuCl_3$ NCs.

(E) Left: representative TEM image of $CsEuCl_3$ NCs; Right: HR-TEM and corresponding FFT (inset). Figures D and E reprinted from (Huang et al., 2020). Copyright © 2020, American Chemical Society.

(F) Schematic of $CsPbBr_3$ NCs with different sizes and shapes synthesized under a temperature of 140 or 170°C using different length of ligands. Reprinted from (Pan et al., 2016a). Copyright © 2016, American Chemical Society.

By tuning the reaction temperature, reaction time, ligand, and precursor engineering, one may readily achieve precise control over the size, surface, and component of perovskite NCs. It has been shown that control over the reaction temperature on the HI synthesis of perovskite NCs could lead to different nanostructures. For instance, lower reaction temperatures of 90-130°C strongly favored asymmetric growth through oriented attachment, resulting in 2D NPLs or NSs (Bekenstein et al., 2015). As for the effect of ligands, Pan et al. varied the hydrocarbon chain composition of carboxylic acids and amines to systematically investigate the surface chemistry, *e.g.*, the independent impact of acid and amine, on the size and shape of perovskite NCus (Figure 4F) (Pan et al., 2016a). They confirmed that the average edge length of $CsPbBr_3$ NCus would increase from 9.5 to 13 nm when the chain length of the carboxylic acids is shortened. Using oleic acid and amine with shorter carbon chain lengths, NPLs were obtained except in the case

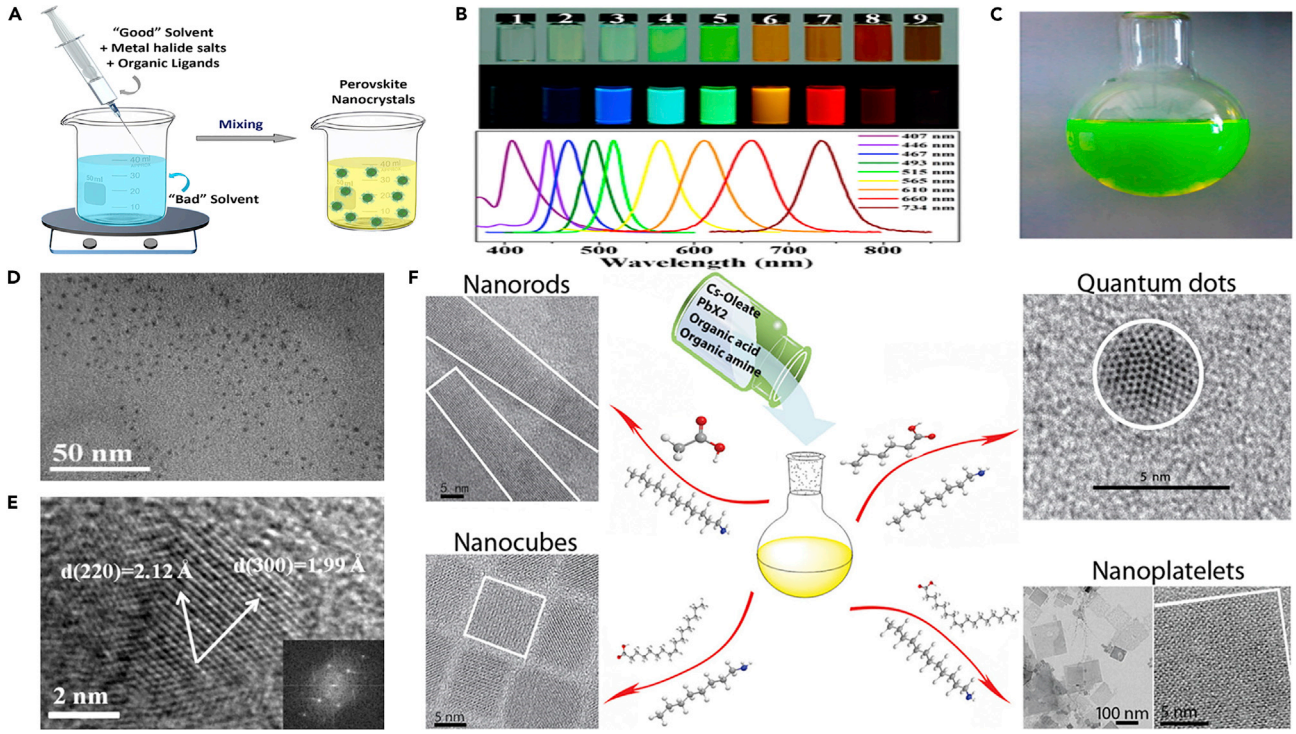


**Figure 5. Synthesis of perovskite NCs by ligand-assisted reprecipitation**

(A) Schematic illustration of the reaction system for the LARP method. Reprinted from (Shamsi et al., 2019). Copyright © 2019, American Chemical Society.

(B) PL spectra and optical images of color-tunable $MAPbX_3$ NCs produced by LARP.

(C) Typical optical image of colloidal $MAPbX_3$ solution.

(D) TEM image of colloidal $MAPbX_3$ NCs.

(E) HRTEM image of a typical $MAPbX_3$ NC. The inset is the corresponding FFT image. Figures B–E reprinted from (Zhang et al., 2015). Copyright © 2015, American Chemical Society.

(F) Tuning the dimensionality of inorganic $CsPbX_3$ NCs by varying the organic ligands. Specifically, hexanoic acid and octylamine were used for spherical NCs, oleic acid and dodecylamine were used for nanocubes, acetate acid and dodecylamine were used for NRs, and oleic acid and octylamine were used for few-unit-cell-thick NPLs. Reprinted from (Sun et al., 2016). Copyright © 2016, American Chemical Society.

of oleylamine and the thickness of NPLs was dependent on the chain length, with the thinnest reaching only three perovskite unit cells.

Hence, the HI method represents an effective and fast method to synthesize perovskite NCs with outstanding structural properties and high PLQYs. However, high temperatures and an inert atmosphere are required, which inevitably increases the costs and has an output limitation in mass production (Akkerman et al., 2018b). In this light, alternative novel approaches need to be developed to address these drawbacks.

### *Ligand-assisted reprecipitation*

Ligand-assisted reprecipitation (LARP) method is a simple process by dropping a good solvent with designed precursor salts, *e.g.*, $MX_2$ (M = Pb, Sn, and so forth), CsX, MAX, and FAX, into a bad solvent in the presence of organic ligands based on the principle of supersaturation (Figure 5A) (Sun et al., 2016). A good solvent with high polarity could be N,N-dimethylformamide (DMF), dimethyl sulfoxide (DMSO), γ-butyrolactone (GBL), N-Methyl-2-pyrrolidone (NMP), or acetonitrile (ACN), while the bad solvent is usually nonpolar such as hexane or toluene. An instantaneous supersaturation will occur after the mixture of the two solvents, resulting in the nucleation and continuous growth of perovskite NCs (Sun et al., 2016). Similar to the HI method, it is rather challenging to separate the nucleation and growth stages in the LARP method. However, the LARP method was still extensively studied due to its simplicity, fast operation, and capability for large-scale fabrication in air (Chen et al., 2016b).

Schmidt et al. reported the successful synthesis of $MAPbBr_3$ perovskite NCs by using the LARP method for the first time in 2014 (Schmidt et al., 2014). They prepared 6 nm-sized $MAPbBr_3$ NCs by using an ammonium bromide with a medium-sized carbon chain. This enables the NCs dispersed in a wide range of organic solvents. Both the NC powders and concentrated solutions can be maintained stable for several months and a mesoporous material for encapsulation is not required.

Zhang et al. adopted the LARP strategy to fabricate brightly luminescent and color-tunable colloidal $MAPbX_3$ NCs with absolute QYs up to 70% at room temperature and low excitation fluencies (Figures 5B and 5C) (Zhang et al., 2015). Firstly, a mixture of $PbBr_2$, MABr, n-octylamine, and oleic acid was dissolved into DMF to form a clear precursor solution. Subsequently, a fixed amount of precursor solution was added to toluene under vigorous stirring. After that, a yellow-green colloidal solution contains $MAPbX_3$ NCs was obtained. The formation of $MAPbX_3$ NCs could be achieved even without the use of amines. But control of the NC size and morphology is rather poor (Figures 5D and 5E). They concluded that the role of amines was to regulate the kinetics of the crystallization and the acids were thought to suppress the aggregation of NCs. In another work, they further investigated the interactions between perovskite precursors and various polar solvents as well as their influence on the crystallization of $MAPbI_3$. This helped produce $MAPbI_3$ NCs with better air stability (Zhang et al., 2017b).

Several groups reported improvement in the LARP method by optimizing the organic ligands (Figure 5F). Deng et al. demonstrated that hexanoic acid and octylamine could tailor the NCs into spherical NCs (Zhang et al., 2018). Oleic acid and dodecylamine would shape the NCs into nanocubes. Acetate acid and dodecylamine would shape the NCs into NCs, while the oleic acid and octylamine would transform the NCs into NPLs. Zero-dimensional $Cs_4PbI_6$ and $Cs_4PbBr_6$ NCs have also been synthesized, exhibiting unexpected luminescent properties (Chen et al., 2016a; Liu et al., 2020). Leng et al. reported the synthesis of lead-free $MA_3Bi_2Br_9$ NCs with low toxicity by using a modified LARP approach without the use of organic ligands (Leng et al., 2016). The $MA_3Bi_2Br_9$ NCs with a mean size of ~3 nm show a PLQY up to 12%, much higher than that of Sn-based perovskite NCs. In addition, the PL peaks of $MA_3Bi_2Br_9$ NCs can be widely tuned from 360 to 540 nm by controlling the anion composition. Xie et al. reported the synthesis of $Rb^+$-containing zero-dimensional $Rb_7Bi_3Cl_{16}$ NCs by using the same method (Xie et al., 2019). The synthesized NCs presented a blue light emission at 437 nm with a PLQY of 28% with good moisture stability for one month and thermal stability up to 400°C, signifying the great potential of lead-free perovskite NCs.

Although it is advantageous in terms of the reaction temperature, conditions, and large-scale production, some considerable problems remain to be resolved (Ali et al., 2019; Wang et al., 2017a). Firstly, a polar solvent is utilized during the synthesis, which is generally toxic like DMSO and DMF. On one hand, one needs to explore green solvents instead of toxic ones to avoid or reduce pollution to the environment. On another hand, it is likely that the synthesized NCs experience degradation or phase change in polar solvents, which is detrimental to their applications. (Zhang et al., 2017b) Furthermore, control over the size and morphology of perovskite NCs is still not good and should be improved in future work (Jin et al., 2018).

### *Template method*

Over the past few decades, template methods have been widely used to synthesize various inorganic nanoparticles such as metals, oxides, carbons, or semiconductors with simple compositions. The templates can be categorized into four groups, *i.e.*, mesoporous silicon dioxide (Dirin et al., 2016; Malgras et al., 2016), mesoporous metal oxides (Ashley et al., 2016; Kojima et al., 2012), mesoporous silicon nanowires (Ghosh et al., 2018), and metal-organic frameworks (MOFs) (Ren et al., 2019; Zhang et al., 2017a). These highly ordered mesoporous materials have also been used as templates to guide the confined growth of versatile perovskite nanostructures.

In analogous to other methods, the precursor solution is prepared by dissolving metal halide salts into a good solvent such as DMF. Subsequently, the precursor solution is spin-coated onto the template, where the perovskite products can be obtained after being dried (Han et al., 2021b; Rubino et al., 2020). In 2012, Kojima et al. first synthesized $MAPbBr_3$ NCs by rapid self-organization on a mesoporous aluminum oxide ($Al_2O_3$) film (Kojima et al., 2012). The insulate $Al_2O_3$ template hardly affects the luminescence properties of perovskite NCs. In 2016, Dirin et al. reported that the infiltration of perovskite precursor solutions into the pores of mesoporous silica, followed by drying, led to the template-assisted formation of perovskite NCs, which could be applied to a large variety of perovskite compounds, hybrid and fully inorganic (Figures 6A

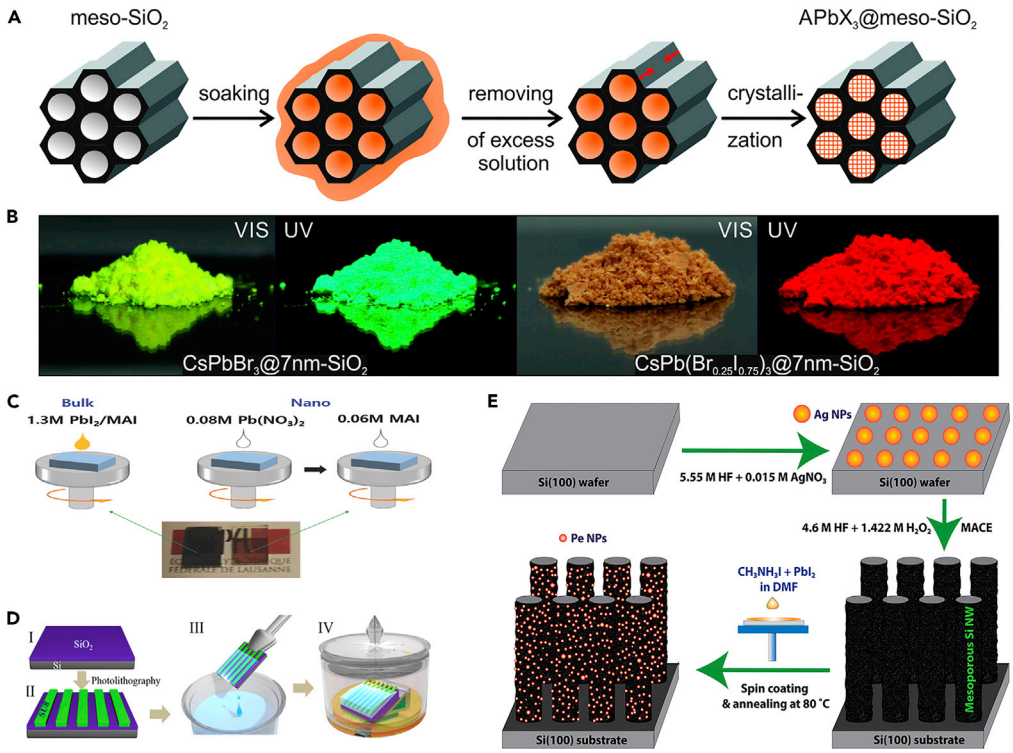


**Figure 6. Template synthesis of perovskite NCs**

(A) Schematic of the template-assisted synthesis of perovskite NCs in the pores of mesoporous silica. The mesoporous template (pore width of 2.5, 4.0, or 7 nm) is impregnated with precursor solution, followed by the removal of excess solution and finally the drying-induced crystallization of the $APbX_3$ NCs.

(B) Photographs of mesoporous silica impregnated with $CsPbBr_3$ (left) and $CsPb(Br_{0.25}I_{0.75})_3$ NCs (right) under daylight and UV illumination. Figures A and B reprinted from (Dirin et al., 2016). Copyright © 2016, American Chemical Society.

(C) Schematic diagram of the one-step spin-coating process for preparing a bulk-$MAPbI_3$ film from high-concentrated precursors, while two-step deposition for a nano-$MAPbI_3$ perovskite sensitized $TiO_2$ film from low-concentrated precursors. Reprinted from (Lee et al., 2018). Copyright © 2018, Wiley.

(D) Schematic illustration of template method for the fabrication of $MAPbI_3$-NW array. Reprinted from (Deng et al., 2017). Copyright © 2017, American Chemical Society.

(E) Illustration of growth of mesoporous Si NWs by a two-step metal-assisted chemically etching process followed by the spin-coating of the perovskite layer to fabricate the perovskite nanoparticles on the Si NW template. Reprinted from (Ghosh et al., 2018). Copyright © 2018, American Chemical Society.

and 6B) (Dirin et al., 2016). Because of the intrinsic defect tolerance, the templated NCs exhibit a high PLQY exceeding 50%. Malgras et al. also demonstrated a simple and versatile method to grow monodisperse $MAPbBr_xI_{x-3}$ NCs inside mesoporous silica templates (Malgras et al., 2016). Because of the relatively low interfacial surface tension between DMF and silica, the dissolved perovskite precursors can be carried inside the channels with minimal resistance. In this situation, the NC size is mainly governed by the pore size of the templates (3.3, 3.7, 4.2, 6.2, and 7.1 nm). In-depth structural analysis shows that the NCs maintain the perovskite crystal structure with slight distortion. The authors pointed out that the chemistry underlying the formation of perovskite crystals did not involve the formation of any side products that might require subsequent extraction.

Owing to the precise control of the growth position and orientation, the template method appears more suitable to grow anisotropic low-dimensional perovskite nanostructures, especially for NW arrays that are rather difficult to be obtained in conventional solution methods such as hot injection (Qiu et al., 2018). Ashley et al. synthesized uniform $MAPbI_3$, $FAPbBr_3$, and $Cs_2SnI_6$ NW arrays by employing anodized aluminum oxide templates with oriented, cylindrical nanopores (Ashley et al., 2016). They showed that this technique did not require the use of unique ligands or surface reagents for each new perovskite composition. Mesoporous $TiO_2$ or $ZrO_2$ film can also be the template to synthesize a well-defined nanoscale $MAPbI_3$ by a

two-step sequential adsorption and reaction of $Pb^{2+}$, as shown in Figure 6C (Lee et al., 2018). By using this technique, Lee et al. obtained a $MAPbI_3$ photosensitizer and a $MAPbBr_3$ light emitter with well-defined nanoscale morphology. A promising initial PCE of 6.23% was obtained when the nano-$MAPbI_3$ was tested as a photosensitizer in a solid-state dye-sensitized solar cell configuration with a very thin (~650 nm) $TiO_2$ mesoporous film, opening up possibilities for perovskite-NC-based optoelectronic devices. Deng et al. reported the large-scale fabrication of high-quality $MAPb(I_{1-x}Br_x)_3$ (x = 0, 0.1, 0.2, 0.3, 0.4) NW arrays with a smooth surface as a result of the slow crystallization process and moisture-isolated growth environment (Figure 6D) (Deng et al., 2017). Periodically aligned SU-8 photoresist stripes on the $SiO_2$/Si substrate were used as the template. The perovskite NW arrays had continuously tunable absorption edges from 680 to 780 nm.

Ghosh et al. reported an easy and cost-effective fabrication of $MAPbI_3$ NCs (5-70 nm) on a mesoporous silicon-NW template with high PLQY up to 10%, and unraveled the mechanism behind the superior photophysical properties of the perovskite NCs decorated on mesoporous Si NWs (Figure 6E) (Ghosh et al., 2018). Zhang et al. used a Pb-based MOF as a starting precursor to realize confidential information protection and storage (Zhang et al., 2017a). Ren et al. embedded $CsPbX_3$ NCs into the mesostructure zinc-based MOF (MOF-5) crystals to obtain a $CsPbX_3$/MOF-5 composite with high stability (Ren et al., 2019). They firstly expanded the pore structure of MOF-5 crystals to mesopores by using templating agents. The following mixing of $CsPbX_3$ NCs with the mesoporous MOF-5 crystals in solution leads to composites with high thermal stability, photostability and long-term stability against anion exchange.

### *Laser writing*

The use of femtosecond laser irradiation as a material processing tool and fast patterning technique has attracted increasing interests in recent years due to its precision, fast speed, and highly localized control of heat (Zhong and Wang, 2020). By simply combining a focused femtosecond laser beam with a computer-controlled 3D XYZ translation stage, different structures can be controllably created (Figure 7A). In 2020 Dong et al. demonstrated the *in situ* synthesis and patterning of luminescent halide perovskite NCs for the first time inside a transparent glass by using femtosecond laser pulses (Figures 7B and 7C) (Huang et al., 2019). The $CsPbBr_3$ perovskite NCs in glass were fabricated by laser irradiation followed by heat treatment (Figure 7F). The TEM images (Figures 7D and 7E) provide direct evidence of the formation of perovskite NCs in the glass. The $CsPbBr_3$ NCs has a mean size <5 nm with a narrow size distribution, demonstrating the excellent control of the NC size by laser writing. Compared with *ex situ* solution-processed perovskite NCs, the *in situ* fabricated NCs inside the transparent glass present uncompromised PL, easy integration, and much improved long-term stability that has long been considered the main obstacle toward practical applications of such materials. It is interesting that the green emission from $CsPbBr_3$ NCs could also be immediately eliminated by further femtosecond laser irradiation, and completely recovered after low-temperature annealing. Importantly, the cycle of erasing and recovery could be reproduced many times (>10 times) without a significant drop in the PL (Figure 7I). The reversible PL property of perovskite NCs in transparent glass makes them suitable for applications such as data storage. It was demonstrated that information could be encrypted using the 3D patterns of perovskite NCs (Figures 7G and 7H). The code was invisible in daylight but could be decrypted under UV (365 nm) excitation to induce green PL from the laser-written $CsPbBr_3$ NCs. Finally, a mechanism of reversible formation and decomposition of $CsPbBr_3$ NCs was proposed which was responsible for the reversible PL property (Figure 7J). By using the femtosecond laser-induced *in situ* crystallization technique in glass with Cs, Pb, and Br elements, a bulk structure containing bright luminescent $CsPbBr_3$ NCs could be obtained and decomposed because of the inherent low formation energy of $CsPbBr_3$ NCs ($\Delta E_{form}$ = −6.45 eV). The minimum laser power density required for the complete decomposition of NCs is around 1 kW/cm$^2$, which is below the threshold for causing structural damage inside the glass.

Recently, Zhong et al. reported an efficient and simple scheme for patterning $CsPbI_3$ NCs during the formation process using *in situ* direct laser writing (Figure 7K) (Zhan et al., 2021). A composite film with perovskite precursor was firstly prepared by spin coating a precursor solution of DMF with fixed amounts of CsI, $PbI_2$, and PMMA. A 405 nm ns laser was used to write patterns on the preformed composite films with perovskite precursors. The residual solvent of DMF could be removed with the accumulation of heat by laser irradiation, resulting in the nucleation and crystallization of $CsPbI_3$ NCs. The fabricated γ-phase $CsPbI_3$-NC patterns show bright PL with a QY up to 92%. By changing the power and scanning speed of the direct laser writing, a minimum line width of 900 nm could be achieved. This enables the patterning

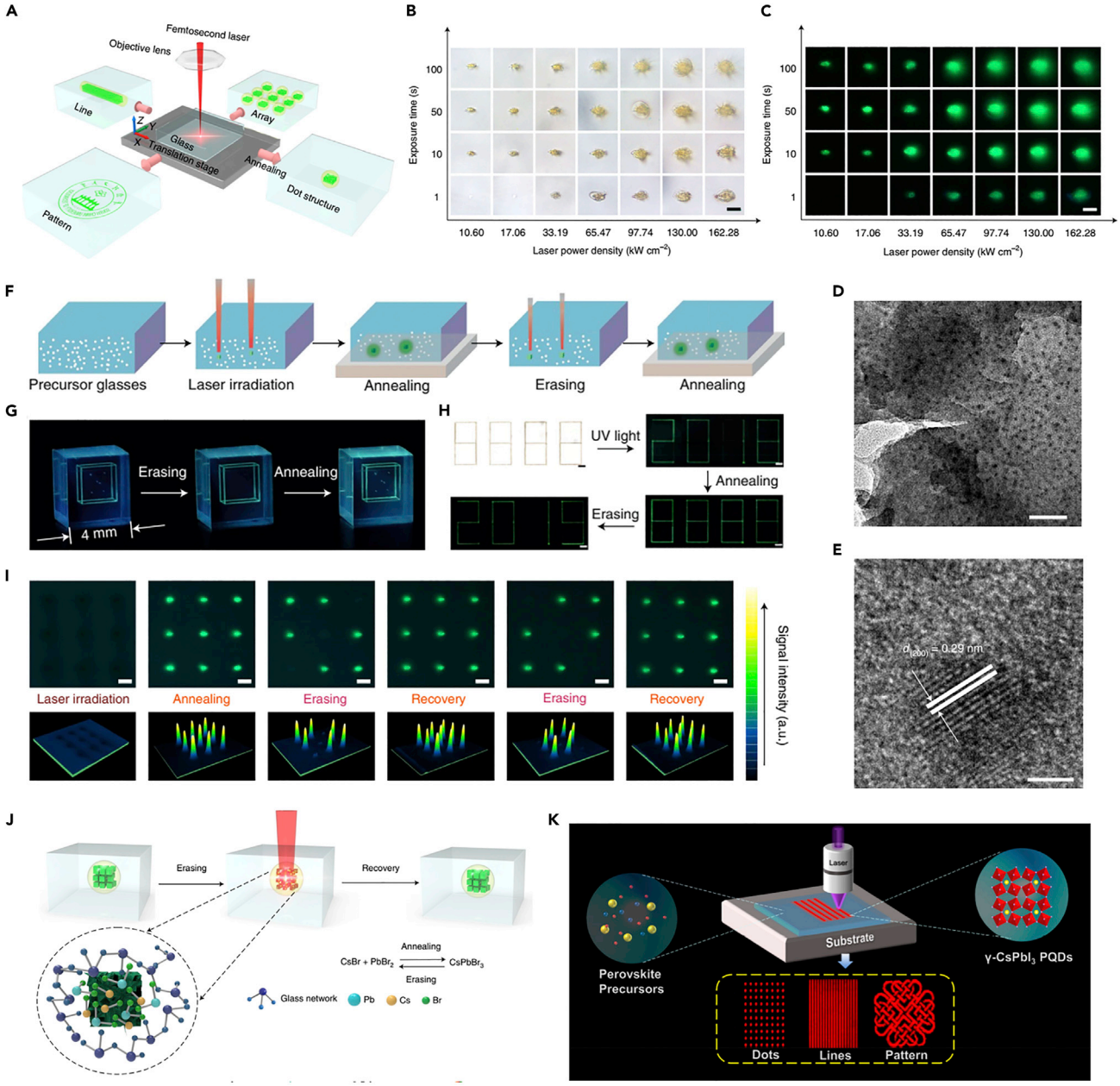


**Figure 7. Synthesis of perovskite NCs by laser writing**

(A) Schematic of a femtosecond laser writing system. Optical images (B) under daylight and (C) 365 nm UV light of the femtosecond laser-induced dots (after annealing) formed at different laser power densities and exposure times. Scale bars, 50 μm.

(D) TEM and (E) HRTEM image of synthesized $CsPbBr_3$ NCs. The scale bar in d and e are 40 and 2 nm, respectively.

(F) Schematic diagram of the laser writing, annealing heat treatment, erasing, and recovery of $CsPbBr_3$ NCs in glasses.

(G) Photographs of cubic samples of glass featuring reversible 3D patterns of $CsPbBr_3$ NCs.

(H) Example of reconfigurable data encryption with a date that is laser written into glass by a pattern of luminescent $CsPbBr_3$ NCs. Figures F–H reprinted from (Zhong and Wang, 2020). Copyright © 2020, Springer Nature (I) Optical images (upper) and readout signal intensity mapping images (lower) of a $CsPbBr_3$ NC array during the erasing-recovery processes under UV light. Scale bars, 100 μm.

(J) Proposed mechanism of reversible formation and decomposition of $CsPbBr_3$ NCs. Figures A–E, I, and J reprinted from (Huang et al., 2019). Copyright © 2019, Springer Nature.

(K) *in situ* patterning of perovskite NCs on a substrate by direct laser writing fabrication. Reprinted from (Zhan et al., 2021). Copyright © 2021, American Chemical Society.

of perovskite NCs with more complex structures. The patterned structures demonstrated optical grating with extrinsic structural colors and intrinsic PL emission. Note that the method is fast, cost-effective, and convenient for large-scale fabrication. These pioneer studies highlight the potential of laser direct writing as a promising methodology with precise control over the size and morphology of halide perovskite NCs for optoelectronics and beyond.

### *Heat-up method*

Heat-up is a single-step cost-effective non-injection method utilizing controlled heating to induce the nucleation and growth of NCs with high reproducibility (van Embden et al., 2015). Chen et al. first demonstrated the capacity of this approach for synthesizing high-quality all-inorganic $CsPbX_3$ NCs by direct heating of precursors in octadecene in the air (Chen et al., 2016b). It was found that the size and composition of perovskite NCs can be easily tuned by varying the reaction temperature. In particular, the heat-up method can produce a gram-scale product of perovskite NCs with a high PLQY of up to 87%. Li et al. demonstrated that high-quality hybrid perovskite NCs such as $MAPbBr_3$ and $FAPbBr_3$ NCs could also be synthesized by directly heating all precursors (Li et al., 2018c). No transfer and purification steps were required. An impressive mass production of 1.8 g within a short reaction time was achieved. The obtained NCs possess ultranarrow size distribution, high QYs, and could be directly employed for red, green, and blue LEDs. A wide color gamut of 140% of the National Television System Committee standard (NTSC) was realized due to its excellent optical properties. In another work reported by Li et al., a novel strategy based on bromobenzene and alkane amine aliphatic nucleophilic substitution was proposed for the synthesis of high-quality $CsPbBr_3$ NCs (Li et al., 2019a). Under continuous heating, the precursors were released in a controllable manner by regulating the reactivity of bromobenzene and alkane amine. This enables precise control over the nucleation and growth kinetics of $CsPbBr_3$ NCs. When 1,3,5-tris(bromomethyl)benzene and oleylamine were used, $CsPbBr_3$ NCs with a high PLQY of 88% and a narrow FWHM of 22 nm could be obtained. The whole process could be completed within 10 min with high reproducibility.

Heat-up method has also been employed for the synthesis of lead-free perovskite NCs. Lee et al. presented the heating-up synthesis of cesium bismuth bromide perovskite NCs (Lee et al., 2020a). CsBr and $BiBr_3$ were used as the precursors and a solvent mixture of ODE, OA, and OAm was used to render nucleation and growth of NCs. Unlike the HI method discussed previously, an intermediate product, *i.e.*, BiOBr NCs, was formed at the early reaction stage. At higher reaction temperature, the BiOBr NCs were then transformed into $Cs_3Bi\text{-}Br_6$ NCs. Particularly, both the size and composition of perovskite NCs could be readily controlled by changing the reaction time, reaction temperature, and amount of OA and OAm added to the reaction mixture. These studies demonstrate that the heating-up method is a reliable means for scalable synthesis of perovskite NCs with controlled size, shape, and composition.

### *Milling*

Milling or mechanochemistry (chemistry driven by mechanical force) is a green alternative to traditional solution synthesis methods (Prochowicz et al., 2019), making mass-production of nanomaterials possible. This method was firstly proposed by Prochowicz et al. for the synthesis of $MAPbI_3$ particles with a size of several hundred nanometers (Prochowicz et al., 2015). Protesescu et al. reported a wet ball-milling method of bulk $APbBr_3$ (A = Cs, FA) mixed with solvents and capping ligands, yielding green luminescent colloidal NCs with a high overall reaction yield and optoelectronic quality on par with that of NCs of the same composition obtained by HI method (Figure 8A) (Protesescu et al., 2018). It is expected that the fast downsizing achieved by this synthesis could be used as a general method for testing whether certain bulk materials, such as soft metal halides, can become bright emitters in the form of NCs. Recently, Masuhara et al. proposed a novel and simple ultrasound-assisted bead milling process based on the characteristics of facile crystallization, wherein milling is combined with capping ligands and milling beads in a reaction vessel and irradiated ultrasounds dispersed milling beads. This approach facilitated an intense collision between the beads and the perovskite precursors (Figure 8B), which helped to form highly luminescent colloidal $MAPbBr_3$ NCs (Umemoto et al., 2020). They found that the increase in mass of the bead maximized the PLQY value and the milling time played a crucial role in realizing the narrow line width of the PL spectra.

In addition to the reduction of the size, milling also enables active tuning of the component of perovskite NCs. Meng et al. demonstrated that the A-site cation of lead-free $Cs_4SnBr_6$ NCs could be partially substituted via a balling process at room temperature while the pristine $Cs_4SnBr_6$ NCs were fabricated using an HI method (Meng et al., 2021). By mixing the $Cs_4SnBr_6$ NCs with pure metal bromide salts (KBr and

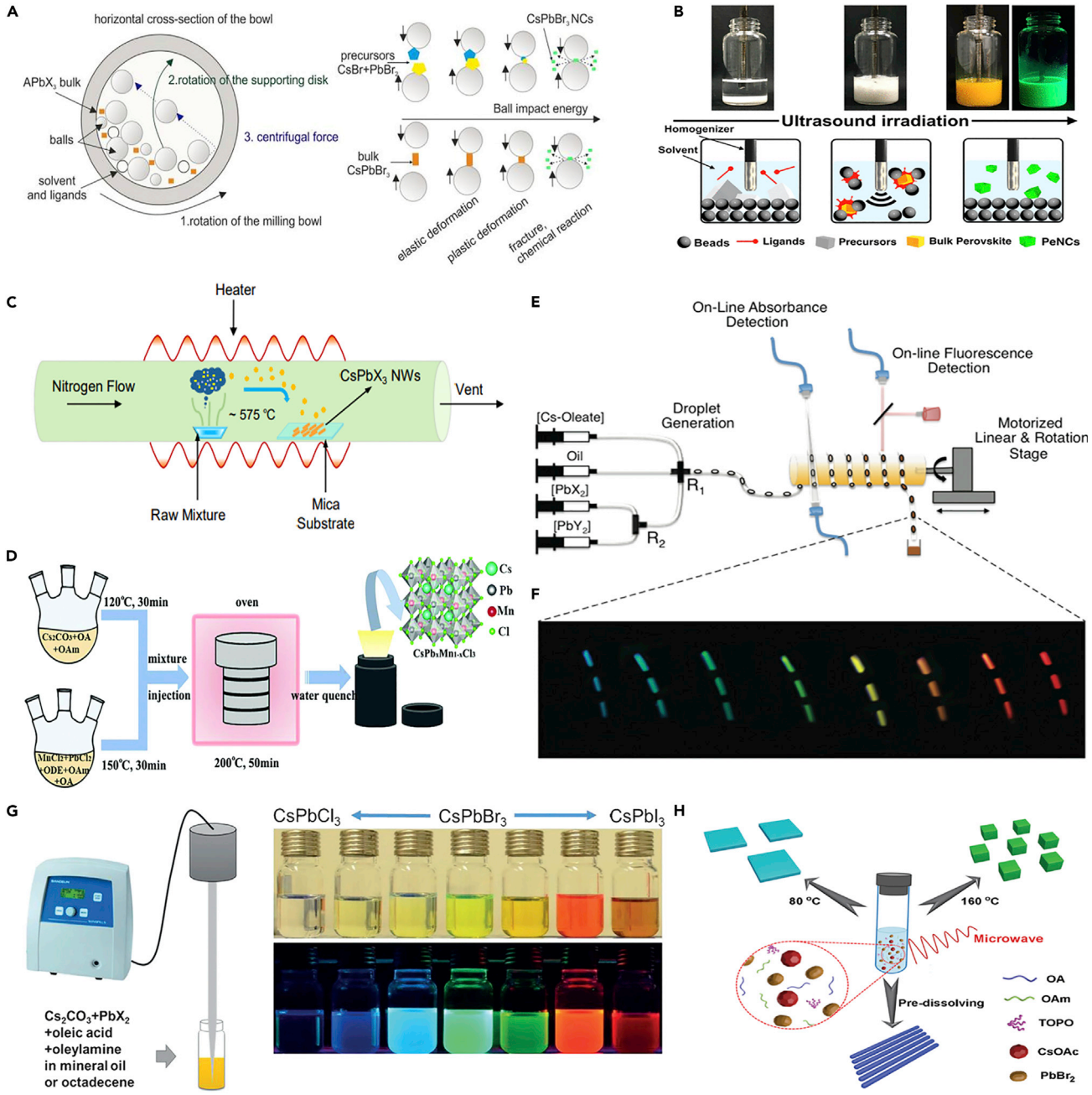


**Figure 8. Synthesis of perovskite NCs by novel methods**

(A) Mechanochemical synthesis of perovskite NCs. Left: schematic of the working principle of the planetary ball mill showing the horizontal cross-section of the bowl during the wet ball-milling experiments. Right: schematic of the processes. Photographs show the obtained colloids of $CsPbBr_3$ NCs. Reprinted from (Protesescu et al., 2018). Copyright © 2018, American Chemical Society.

(B) Schematic illustration of the ultrasound-assisted bead milling. Left: reaction vessel containing milling beads, capping ligands, the perovskite precursors, and dispersant before processing. Middle: zirconia beads strikingly collide in the vessel during ultrasound irradiation. Right: uncentrifuged $MAPbBr_3$ colloids after processing under room light (left) and brightly green luminescent can be clearly observed under UV light (right). Reprinted from (Umemoto et al., 2020). Copyright © 2020, American Chemical Society.

(C) Schematic showing $CsPbX_3$ nanoarrays growth by CVD. The raw mixtures are placed at the heating center of furnace while mica at the downstream. The growth temperatures for $CsPbBr_3$, $CsPbCl_3$ NWs are 575 and 620°C, respectively. Reprinted from (Gao et al., 2018). Copyright © 2018, Wiley.

(D) Schematic showing the solvothermal synthesis of Mn-doped $CsPbCl_3$ NCs. Reprinted from (Chen et al., 2018a). Copyright © 2018, Royal Society of Chemistry.

**Figure 8. *Continued***

(E) Schematic illustration of the droplet-based microfluidic platform integrated with online absorbance and fluorescence detection for the synthesis and real-time characterization of $CsPbX_3$ NCs.

(F) Image of the generated droplets after exiting the heating zone under UV excitation, showing bright PL of $CsPbX_3$ NCs. Figures E and F reprinted from (Lignos et al., 2016). Copyright © 2016, American Chemical Society.

(G) Synthesis of $CsPbX_3$ NCs through a single-step tip sonication. Reprinted from (Tong et al., 2016). Copyright © 2016, Wiley.

(H) Schematic for growth of $CsPbBr_3$ NCs through the microwave-assisted synthesis approach. Without pre-dissolution of precursors, $CsPbBr_3$ NPLs are obtained at low temperature (80°C), and monodisperse nanocubes can be prepared at elevated temperature (160°C). When the precursors are pre-dissolved, $CsPbBr_3$ NRs are obtained. Reprinted from (Pan et al., 2017b). Copyright © 2017, Royal Society of Chemistry.

RbBr), the transformation of Cs to mixed Cs/Rb and mixed Cs/K could be readily achieved. After the A-site doping, the bright fluorescence of $Cs_{4-x}M_xSnBr_6$ could be tuned from dim green to greenish-cyan with a relatively high PLQY of ~39%. Compared to the pristine $Cs_4SnBr_6$ NCs, the doped $Cs_{4-x}M_xSnBr_6$ NCs demonstrated superior air stability and much improved photocatalytic activity for $CO_2$ reduction reaction with high selectivity of $CH_4$ gas with a higher yield rate, signifying the potential of perovskite NCs for versatile photochemical conversion applications.

### *Other methods*

*Chemical vapor deposition.* Gas-phase methods such as nonthermal plasma have been well-established for the synthesis of a variety of freestanding semiconductor NCs in the past decades (Zhou et al., 2014, 2015a, 2015b, 2016, 2018). Nevertheless, the synthesis of freestanding perovskite NCs remains unexplored to date. However, the gas-phase synthesis of perovskite NCs embedded in a matrix has been studied. As shown in Figure 8C, chemical vapor deposition (CVD) is one of the vapor-phase epitaxial growth methods for versatile perovskite nanostructures with higher crystallization quality, lower defect density, and better reproducibility compared with solution-phase growth technique (Ha et al., 2017; Zhou et al., 2017b).

Xiong et al. prepared $MAPbI_3$ NPLs by a CVD system with lateral dimension in the range of 5-30 μm and thickness ranging from several atomic layers to several hundred nanometers for the first time (Ha et al., 2014). The NPLs possess a high electron diffusion length of over 200 nm and good optical properties. Zhou and coworkers reported the growth of high-quality $CsPbX_3$ triangular micro/nanorods on $SiO_2$/Si substrates with complete composition tuning via an improved vapor deposition method (Zhou et al., 2017b). The perovskite nanostructures showed strong multicolor PL in the range of 415-673 nm by varying the halide ion, which could act as high-quality Fabry-Perot (FP) cavities due to low lasing thresholds (~14.1 μJ $cm^{-2}$) and high Q factors (~3500). Gao et al. successfully synthesized well-defined $CsPbBr_3$ and $CsPbCl_3$ NW arrays with average thickness below 15 and 7 nm on muscovite mica substrates by a facile CVD approach (Gao et al., 2018). When the NW thickness increases, the emission polarization ratio of NW undergoes a nearly invariant decrease, and small oscillation regions, which was attributed to a combination of factors originating from the electrostatic mismatch, the rising of light wave characteristics, and multi-waveguide modes competition, respectively (Gao et al., 2018).

*Emulsion method.* Huang et al. developed a facile nonaqueous emulsion method for the synthesis of colloidal perovskite NCs by the controlled addition of demulsifier into an emulsion of perovskite precursors. The NC size could be tuned from 2 to 8 nm by varying the amount of demulsifier (Huang et al., 2015). The PLQY of perovskite NCs was generally in the range of 80-92% and can be well-preserved after purification (~80%). Zhang et al. reported a reverse microemulsion method to synthesize rhombohedral-phase $Cs_4PbB_{r6}$ NCs with a mean size of 26 nm (Zhang et al., 2017d). Control over the stoichiometric ratio of the reactants resulted in a high reaction yield (~85%) of phase-pure products. The PLQY of NC colloid was measured to be 65% and can be largely maintained in thin films by drop casting.

*Solvothermal method.* Solvothermal approach was proposed by Chen's group (Figure 8D) (Chen et al., 2017a). They prepared high-quality $CsPbX_3$ NCs with controlled size, morphology, and composition. Full-visible-spectrum luminescent properties with a high PLQY over 80% and a narrow FWHM (~12 nm) were achieved for both $CsPbX_3$ NCs and ultrathin NWs because of the strong quantum confinement effect (Chen et al., 2017a). Lately, they intentionally doped $Mn^{2+}$ into $CsPbCl_3$ NCs using the same method. The doped NCs were found to be more stable than those prepared by using hot-injection (Yong et al., 2018). Furthermore, they employed a Cl-to-Br anion exchange method to produce $Mn^{2+}$-doped $CsPbX_3$ NCs with a mixed ratio of Br and Cl for tunable luminescence. These multicolor perovskite NCs could be

potentially used as color converters for constructing white LEDs and optical thermometric medium for accurate temperature sensing.

*Microfluidic reactor method.* Microfluidic reactor method is adapted from the conventional hot-injection method providing enhanced process control for applications in chemistry and reaction engineering. This method possesses unique attributes including controlled and reproducible transport (heat and mass) characteristics, well-defined interfacial areas, and ease of scalability (Campbell et al., 2020). Kovalenko's group reported the synthesis of $CsPbX_3$ NCs using a droplet-based microfluidic platform and explored the formation mechanism of these perovskite NCs by *in situ* optical absorption/PL measurements (Figures 8E and 8F) (Lignos et al., 2016). Unique insights have been gained into the formation mechanism of perovskite NCs, in particular the early stages of nucleation and growth within the initial 0.1-5 s. Subsequently, Maceiczyk et al. used the same technique to successfully synthesize monohalide perovskite NCs of $FAPbBr_3$ and $FAPbI_3$ NCs and mixed-halide perovskite NCs of $FAPb(Br/I)_3$. and identify optimal conditions for the monohalide NC compositions and reveal different growth mechanisms for iodide and bromide perovskite NCs (Maceiczyk et al., 2017).

*Ultrasonication.* Ultrasonication represents an efficient, scalable, single-step, low-cost, and environmentally friendly method for the synthesis of perovskite NCs without the use of polar solvents (Huang et al., 2017c). Tong and coworkers obtained high-quality colloidal $CsPbX_3$ NCs with tunable halide composition and thickness by a direct ultrasound-assisted reaction of the corresponding precursor solutions in the presence of organic capping molecules (Tong et al., 2016). They showed that this synthesis method could be applied to versatile perovskite NCs by simply replacing the components in turn (Figure 8G). In 2018, Rao et al. synthesized $CsPbBr_3$ NCs with desired shape and size in a one-pot reaction by introducing ultrasonication and nontoxic and polar-free-solvent liquid paraffin (Rao et al., 2018). By tuning the ratios and types of capping ligands as well as ultrasound power and radiation time, the optimized NCs showed a high PLQY of up to 83% with versatile morphology. Gates et al. demonstrated a facile sonication-assisted approach for the preparation of perovskite-related $Cs_3Bi_2I_9$ NCs using propylene carbonate as a green, alternative solvent (Ali et al., 2019).

*Microwave method.* Zhang et al. reported the use of the microwave as a heat source for synthesizing high-quality $CsPbX_3$ NCs with controllable morphologies and outstanding luminescent properties (Figure 8H) (Pan et al., 2017b). A plausible kinetics-controlled growth mechanism was proposed in which the reaction temperature, capping ligands, and ion concentration played the key role in controlling the shape of perovskite NCs. The microwave method was also adopted by Rogach et al. for the controlled synthesis of $CsPbBr_3$ NCs (Li et al., 2018d). Compared to the commonly used HI approach, the microwave-assisted technique slows down the reaction time from a few seconds to 25 min, allowing better control over the growth of NCs. This facilitates examination of the intermediate stages during the growth process and helps to gain insights into the formation mechanism of perovskite NCs.

Apart from the direct synthesis methods mentioned above, post-synthesis treatments, especially ligand exchange and ion exchange are also frequently employed as powerful means to tailor the optoelectronic properties (*e.g.*, absorption bandgap, PL energy, and PLQY) and stabilities of perovskite NCs due to the high mobility of halide ions and the rigid nature of cationic sublattice of perovskites (Creutz et al., 2018; Lu et al., 2020a; Luo et al., 2019).

## SIZE ENGINEERING

### Structural properties

Compared to conventional semiconductor NCs, there have been few attempts to understand the size-dependent structural properties of halide perovskite NCs largely due to the difficulty in producing high-quality monodisperse NCs over a wide range of sizes. For instance, the typical size dispersion of CdSe or PbS NCs has been reduced to nearly 3% after decades of research. However, the size dispersion (*e.g.*, hot injection) is typically larger than 10% for perovskite NCs.

To confront this challenge nanoseperation has been proposed as a complementary method to achieve NC monodispersity in a controlled manner to attain size-dependent properties (Zhou, 2021). A size-selective precipitation method was employed to obtain monodisperse $CsPbI_3$ NCs for the study of their structural properties (Zhao et al., 2019b). Based on the TEM results, the size ($L$) of $CsPbI_3$ NCs using this size-selective method

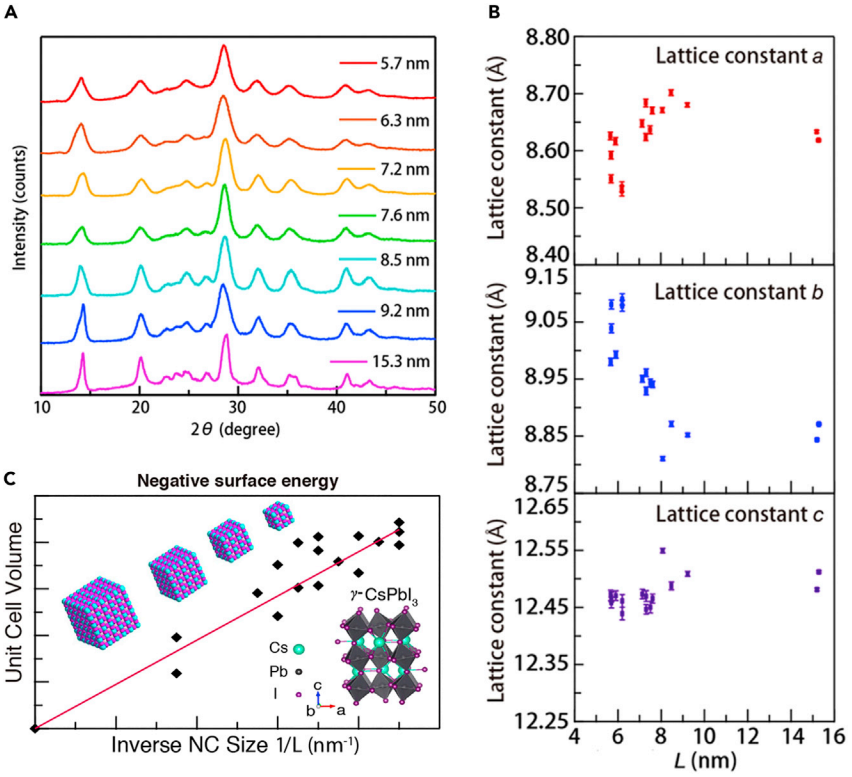


**Figure 9. Size-dependent structural properties**

(A) XRD patterns of $CsPbI_3$ NCs with sizes of 5.7, 6.3, 7.2, 7.6, 8.5, 9.2, and 15.3 nm.

(B) Lattice parameters with corresponding error bars of $CsPbI_3$ NCs for various crystal sizes (L) calculated from the refinement.

(C) Unit cell volume plotted versus 1/L. The values calculated for each sample (solid squares) are fitted to a linear function (solid line). Figures A–C reprinted from (Zhao et al., 2019b). Copyright © 2019, American Chemical Society.

can be tuned from 5.2 ± 0.6 to 15.3 ± 1.7 nm. The size dispersion (~11%) in this wide regime is reported to be the smallest for $CsPbI_3$ NCs, but still larger than $CsPbBr_3$ NCs. XRD data for the $CsPbI_3$ NCs with different sizes were then recorded (Figure 9A). It was found that all $CsPbI_3$ NCs were better described by a lower-symmetry orthorhombic phase rather than a cubic phase, as suggested by the subtle peaks between 20 and 28°. This finding was further confirmed by the Rietveld refinement of the XRD patterns. The average grain sizes obtained by Scherrer analysis coincide well with the TEM results. In this respect, the lattice parameters (*a*, *b*, *c*) for all $CsPbI_3$-NC samples could be extracted from the XRD patterns by refining to the orthorhombic phase (Figure 9B). A clear trend toward larger value is observed for the lattice parameter *a* as the *L* increased. However, an opposite trend is seen for the lattice parameter *b*. The lattice parameter *c* remains almost unchanged. These results imply an increased average tilting between adjacent octahedra as the *L* increases. Such octahedral tilting indicates that a significant size-dependent strain presents in the NCs. The plot of the unit cell volume ($V = abc$) versus $1/L$ clearly shows a lattice expansion that scales linearly with $1/L$ (Figure 9C). By analyzing the size-dependent volume dilatation the surface energy could be calculated. For the ligand-stabilized $CsPbI_3$ NCs it is estimated to be between −3.0 and −5.1 eV $nm^{-2}$ (~-1.2 to −2.0 eV per surface unit cell), well consistent with the lattice expansion induced by negative surface tension. Giving that the $Cs^+$ ion is generally too small to retain a corner-sharing octahedral geometry required for the perovskite phases, such negative surface tension can produce enough tensile strain for $CsPbI_3$ NCs which enables retention of the perovskite structure at room temperature (Swarnkar et al., 2016).

## Optical properties

### *Optical emission*

When the dimension of a semiconductor material is reduced below the Bohr exciton radius of the bulk semiconductor, the quantum confinement becomes prominent which makes the optical properties of

materials size-dependent. As the size of perovskite NCs decreases in the quantum confinement regime, the peak of light emission readily shifts toward higher energy as a result of the broadening of the bandgap (Figure 10A) (Malgras et al., 2016). Besides, the efficiency of light emission is also in close relation to the NC size because the excitons that are confined in a small volume of perovskite NCs could lead to very efficient radiative recombination. For ligand-free perovskite NCs that are grown in a mesosilica template, it was observed that the overall PL lifetime consistently decreased with the crystal size although the QYs were not reported in that work (Figure 10B) (Malgras et al., 2016). When the surface of NCs was capped by OA/OAM, a clear trend of QYs is observed dependent on the NC size (Figure 10C) (Liu et al., 2017b). Specifically, the NCs with the smallest size demonstrate the highest QY. These results demonstrate that fine-tuning the optical emission can be obtained by simply controlling the size of perovskite NCs in terms of the quantum confinement effect. It is worth noting that the trioctylphosphine (TOP) capped NCs exhibited near-unity light emission (~100% PLQY) in all sizes.

Near-unity light emission is one of the most important criteria which sets perovskite NCs apart from other semiconductor NCs. A combined spectroscopy study on the origin of the light emission suggests that the near-unity PL upon crystal size reduction to a few nanometers in the presence of ligands is mainly due to favored exciton recombination together with a reduced surface trapping by taking advantage of both the quantum confinement effect and defect passivation (Droseros et al., 2018). With the advance in the synthesis of high-quality perovskite NCs, near-unity light emissions spanning the whole visible spectrum have been achieved. Koscher et al. reported a thiocyanate salt treatment method to obtain essentially trap-free $CsPbBr_3$ colloidal NCs, leading to green light emission (~510 nm) with near-unity PLQYs (Koscher et al., 2017). But this method is not applied to mixed halide perovskite NCs such as $CsPbBr_xCl_{3-x}$ and $CsPbBr_xI_{3-x}$. Pan et al. described bidentate ligand passivation of $CsPbI_3$ NCs that effectively increases their PLQY, leading to near-unity values of red light emission (~680 nm) with good stability (Pan et al., 2018b). They achieved similar results for other halide perovskite NCs, signifying the positive role of the bidentate ligand. Compared with the red and green light emission, efficient blue light emission from perovskite NCs is more challenging. Sun et al. found that the use of dopant like $Ni^{2+}$ during the hot-injection method can greatly improve the PLQY of $CsPbCl_3$ NCs (~410 nm) to near-unity (Yong et al., 2018). The benefit of Ni doping mainly lies in the increased defect formation energy, resulting in greatly improved short-range order of the perovskite lattice and thus near-unity PLQY. This strategy can also be applied to boost the PL of $CsPbCl_2Br$ NCs with near-unity QYs (~430 nm). In a similar work, Samanta et al. reported a room temperature post-synthesis treatment of weakly blue-violet-emitting $CsPbCl_3$ NCs by using $CdCl_2$ (Mondal et al., 2018). Adding $Cd^{2+}$ into $CsPbCl_3$ NCs leads to an instantaneous enhancement of the PLQY to near-unity without affecting the PL peak position (406 nm) and spectral width.

It has been recognized that the high PLQY of semiconductor NCs in solution is typically not retained in the resulted films because the NCs in films are not as well passivated as in solutions. On one hand, the NCs are more easily to be exposed to oxygen, moisture, or other ambient contaminants. On another hand, close packing in NC films increased energy transfer to trap-states and self-absorption, a process where photons emitted by an NC are absorbed and re-emitted, one or multiple times by neighboring NCs. Konstantatos et al. demonstrated near-unity PLQY (>95%) for films assembled from $CsPbBr_3$ NCs (Di Stasio et al., 2017). The PL enhancement stems from a combination of the synthetic method employed and post-treatment with $PbBr_2$. The close to unity PLQY obtained in both solutions and films makes perovskite NCs attractive for a variety of optoelectronics.

### *Optical absorption*

The optical absorption coefficient ($\alpha$) of lead halide perovskite NCs is very important for understanding their photophysical properties, especially those in close relation to the density of photoexcited charge carriers. In comparison to conventional CdSe NCs, the $\alpha$ of perovskite NCs is about 2 orders of magnitude larger, indicating strong light−matter interaction in the perovskite NCs. Roo et al. determined the absorption coefficient of ~8 nm $CsPbBr_3$ NCs by combining inductively coupled plasma mass spectrometry (ICP-MS) and absorption spectrophotometry (De Roo et al., 2016). They found large discrepancies existed among the reported values of $\alpha$ determined by using different methods.

To accurately determine the $\alpha$ of different perovskite NCs Hens et al. reported a post-synthesis size-selective precipitation method to separate the polydisperse crude product of $CsPbBr_3$ perovskite NCs into distinct, monodisperse fractions (Maes et al., 2018). The size selection of perovskite NCs is accomplished

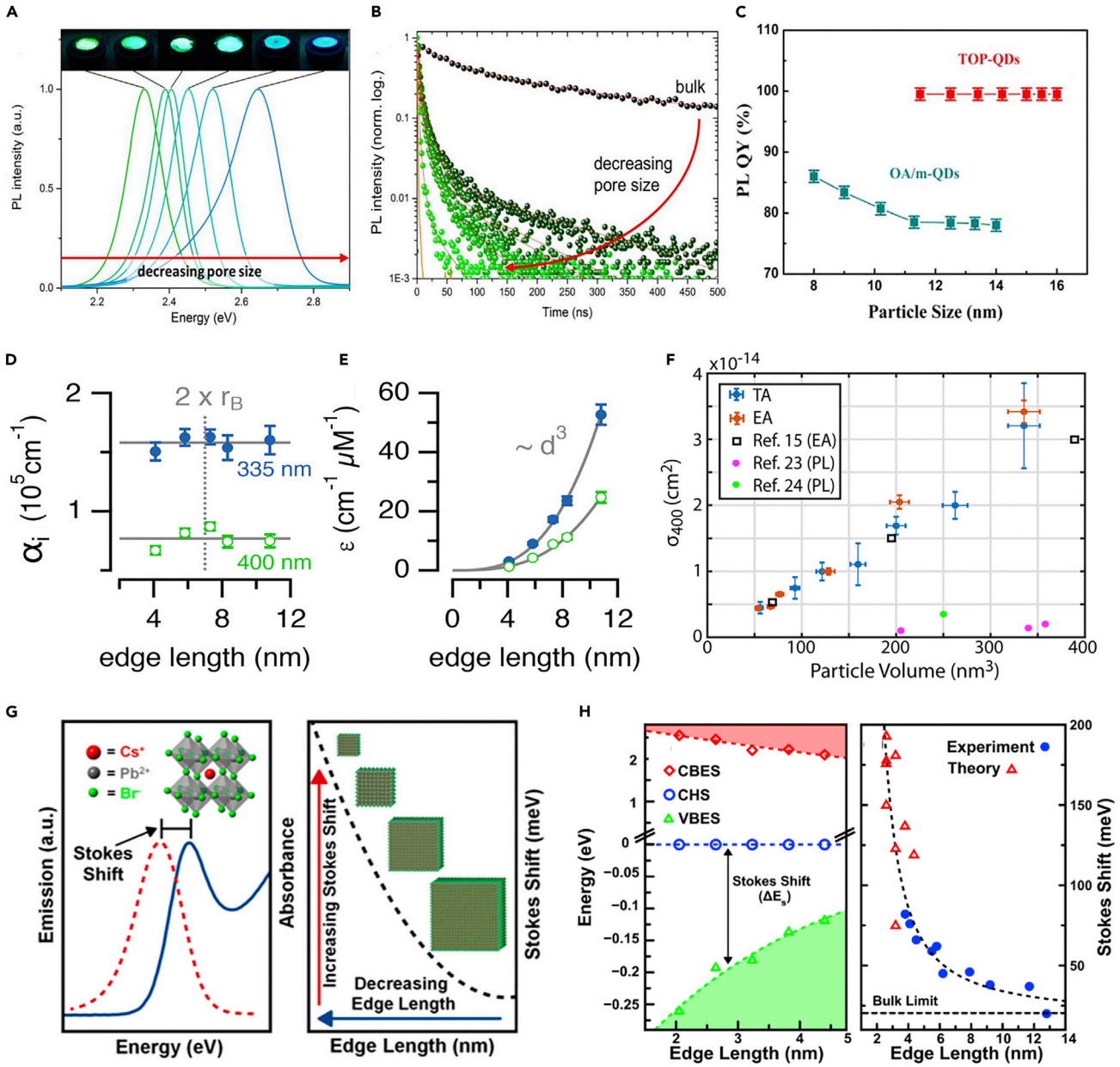


**Figure 10. Size-dependent optical properties**

(A) Photographs and PL spectra of $MAPbBr_3$ NCs impregnated in the various silica template (from bulk on the left to $d_{pore} \approx 3.3$ nm on the right) under black light ($\lambda = 364$ nm).

(B) PL decays measured for $MAPbBr_3$ NCs impregnated in the various silica template (green) along with their respective triple exponential fitting (red dotted curves). Figures A and B reprinted from (Malgras et al., 2016). Copyright © 2016, American Chemical Society.

(C) Dependence of the PLQYs of the OA/m−QDs and TOP−QDs on their particle size. Reprinted from (Liu et al., 2017b). Copyright © 2017, American Chemical Society.

(D) Size-independent intrinsic absorption coefficient $\alpha_i$ for $CsPbBr_3$ NCs dispersed in *n*-hexane, where $r_B$ denotes the Bohr radius.

(E) The related size-dependent molar attenuation coefficient $\varepsilon$. Figures D and E reprinted from (Maes et al., 2018). Copyright © 2018, American Chemical Society.

(F) The absorption cross-section of $CsPbBr_3$ NCs of different sizes at 400 nm ($\sigma_{400}$) determined from elemental analysis (EA) and transient absorption (TA). Reprinted from (Puthenpurayil et al., 2019). Copyright © 2019, AIP Publishing.

(G) Representative room temperature absorption (solid black lines) and emission spectra (dashed red lines) of $CsPbBr_3$ NC ensembles (left), and size-dependent Stokes shifts (right). (Brennan et al., 2017b).

(H) Size-dependent NC CBES and VBES energies plotted relative to CHS energies (left), and experimental band edge excitation-derived $\Delta E_s$ values (closed blue circles) plotted against theoretical Stokes shifts (right). CHS: confined hole state; CBES (VBES): conduction (valance) band edge state. Reprinted from (Brennan et al., 2017a). Copyright © 2017, American Chemical Society.

by repeatedly centrifuging a colloidal suspension from low speed to high speed in order to achieve separation. Firstly, the addition of a small amount of acetone to the NC dispersion in n-hexane, resulted in the precipitation of the biggest particles. By centrifugation, a first fraction could be separated and redispersed in n-hexane. This procedure was then repeated on the supernatant and every precipitation step yielded particles with a smaller average diameter than the one before. The resulted monodisperse NCs possessed a much lower size distribution. By combining elemental analysis and absorption spectroscopy the intrinsic absorption coefficient ($\boldsymbol{\alpha_i}$) of $CsPbBr_3$ NCs is calculated and plotted as a function of the NC size. By using the law of Bouguer–Lambert–Beer $\boldsymbol{\alpha_i}$ is calculated as

$$\alpha_i = \frac{ln10A}{fL}, \qquad \text{(Equation 4)}$$

where A is the absorbance of an NC dispersion, f is the volume fraction of the NC defined as the ratio between the NC volume and the dispersion volume, and L is the optical path length (Hens and Moreels, 2012). It is found that $\boldsymbol{\alpha_i}$ of $CsPbBr_3$ NCs is size-independent within the 4-11 nm size regime though the composition of the NCs depends on their size (Figures 10D and 10E). In addition, for both $CsPbBr_3$ and $CsPbCl_3$ NCs the NC shape (cubic versus spherical) minimally impacts the $\boldsymbol{\alpha_i}$. But large error was observed for $CsPbI_3$ NCs. Importantly, they observed that the $\boldsymbol{\alpha_i}$ shows a pronounced dependence on the refractive index of the solvent, which necessitates a proper recalculation when measurements involve solvents other than n-hexane or toluene. Because $\boldsymbol{\alpha_i}$ can be readily converted into the molar absorption coefficient ($\boldsymbol{\alpha_m}$) or the $\boldsymbol{\alpha}$ of $CsPbBr_3$ NCs, $\boldsymbol{\alpha_i}$ is one of the most convenient quantities to quantify the light absorption of $CsPbBr_3$ NCs.

Absorption cross-section ($\boldsymbol{\sigma}$) is another important parameter that has been frequently used to characterize the ability to absorb a photon of a particular wavelength (λ). Unlike the $\boldsymbol{\alpha_i}$ intrinsic to the material, the optical absorption efficiency of a semiconductor NC could be quantified by using the $\boldsymbol{\sigma}$. The $\boldsymbol{\sigma}$ of a perovskite NC is related to the $\boldsymbol{\alpha_m}$ as

$$\sigma = \alpha_m \frac{2303}{N_A}, \qquad \text{(Equation 5)}$$

where $N_A$ is Avogadro's number. Son et al. measured the $\boldsymbol{\alpha}$ at 400 nm of $CsPbBr_3$ NCs with varying sizes by using a combination of elemental analysis and transient absorption saturation methods (Puthenpurayil et al., 2019). The $\sigma_{400}$ depends directly on the number of atoms within the NC counted for each element, which varies with the size of the NC (Figure 10F). The results were also compared with the reported values determined from elemental analysis and transient PL saturation methods. It is suggested that reliable $\boldsymbol{\sigma}$ of perovskite NCs could be obtained from the elemental analysis and TA saturation methods, while many previously reported values determined from the PL saturation method underestimate the $\boldsymbol{\sigma}$.

Multi-photon absorption (MPA) process involving the simultaneous absorption of multiple monochromatic infrared photons that excites an electron to a higher energy state, has recently been observed in perovskite NCs. Chen et al. revealed that $CsPbBr_3$, $MAPbBr_3$, and core-shell $MAPbBr_3/(OA)_2PbBr_4$ NCs possess ultra large MPA properties, with five-photon action cross-sections ($\eta\sigma_5 \sim 10^{-136} cm^{10} s^4 photon^{-4}$) much higher than those of conventional inorganic semiconductor NCs and organic chromophores, highlighting their potential for nonlinear optics and bio-imaging applications (Chen et al., 2017b).

In contrast to MPA, multiple exciton generation (MEG) describes the generation of multiple excitons from one absorbed photon with energy typically exceeding the bandgap (usually several times of $E_g$), holding considerable promise to overcome the Shockley-Queisser Limit. Li et al. reported enhanced MEG (up to 75%) and low-MEG threshold energies (down to 2.25 $E_g$) in quantum-confined $FAPbI_3$ NCs, providing a distinct advantage for the enhancement of the solar cell efficiency (Li et al., 2018a). Manzi et al. found that multiple excitons could also be generated in $CsPbBr_3$ NCs under the excitation of multiple photons with specific energies lower than the bandgap (0.5-0.8 $E_g$). In particular, the MEG could be enhanced through below-band-gap MPA, opening up possibilities for various energy conversion systems exploiting high light intensities (Manzi et al., 2018). Very recently, Chen et al. achieve efficient MEG in narrower-bandgap perovskite NCs ($FAPb_{1-x}Sn_xI_3$ NCs; $x \leq 0.11$) (Chen et al., 2022). They observed the substantial impact of MEG on the photocurrent quantum efficiency exceeding 100% with a low threshold in the NC-based photoconductors. These intriguing studies pave the way toward practical applications of MPA and MEG effects in perovskite-based optoelectronics in the future.

*Stokes shift*

Stokes shift describes the difference in wavelengths between the emission and the band-edge absorbing state, which is a unique property of colloidal semiconductor NCs (Efros et al., 1996). The presence of a Stokes shift is intriguing because it indicates that the absorbing and emitting states are not necessarily the same for a given semiconductor.

Kuno et al. unveiled the existence of a size-dependent Stokes shift in $CsPbBr_3$ NCs for the first time (Figure 10G) (Brennan et al., 2017b). Stokes shifts range from ~30 to 100 meV for $CsPbBr_3$ NCs with edge lengths between ~4 and 12 nm. Lately, they confirmed that the size-dependent Stokes shift is not a result of extrinsic factors (Brennan et al., 2017a). Using theoretical calculations of the size-dependent density of states (DOS) and electronic band structure of $CsPbBr_3$ NCs, the existence of an inherent, size-dependent, confined hole state locating at ~260 to 70 meV above the valence band edge state for NCs (2-5 nm) is revealed responsible for the observed Stokes shifts. The distinction between the absorbing and emitting states in $CsPbBr_3$ is likely a general feature of other perovskite NCs and can be tuned via NC size to enable applications involving these materials (Figure 10H). Zhou et al. observed a change in the Stokes shifts in doped $CsPbBr_3$ NCs because of the doping-induced perturbation to the band edge states or variation of the size distribution (Di et al., 2015). Recently, Jia et al. demonstrated that photon recycling remarkably increases the external Stokes shift of small $CsPbBr_3$ NCs in the strong quantum confinement regime, which is experimentally supported by the concentration-dependent PL redshift and ultrafast TA results (Gan et al., 2019). It is suggested that the size-dependent Stokes shift may be caused by the photon reabsorption instead of the confined hole state discussed previously.

In fact, the origin of Stokes shifts in semiconductor NCs remains highly debated to date because contradictory signatures of both surface and bulk characters were reported for the associated electronic states. For CdSe NCs, size-dependent Stokes shifts ranging from ~100 to 10 meV were observed when the size changes between ~1 and 5 nm (Kuno et al., 1997). Detailed theoretical modeling suggests the size-dependent Stokes shift in CdSe NCs largely originates from the existence of band edge excitonic fine structure. Voznyy et al. observed an excess Stokes shift in PbS NCs in a polydispersed ensemble in the solution, which originates from the energy transfer among the NCs (Voznyy et al., 2017). Such energy transfer, however, is largely due to the NC aggregation and can be substantially eliminated by extreme dilution, higher-viscosity solvent, or better-dispersed colloids.

## SURFACE ENGINEERING

### Organic ligands

Semiconductor NCs are originally surface terminated with organic ligands derived from a colloidal synthesis method. On one hand, these organic ligands modify the NC surface to be either hydrophilic or hydrophobic, making them suitable for wet-chemical processing. On the other hand, the formation of strong covalent bonds between the surface atoms and the ligands passivates the trap states in the bandgap, leading to improved optoelectronic properties.

For halide perovskite NCs, surface modification can be accomplished during the synthesis process by using versatile organic ligands (*e.g.*, alkyls, amides, thiolates, sulfonates phosphonic acids). A general classification of these ligands is based on the number of electrons involved in the metal-ligand interaction and the identity of the electron donor and acceptor groups (De Roo et al., 2016). L-type ligands are neutral two-electron donors with a lone electron pair that enable coordination with the metal ions, while X-type ligands could offer one electron to form a two-electron covalent bond with the metal ions. Z-type ligands are Lewis acids, offering an empty orcbital. L-type ligands such as OA and OAm were initially used for capping the perovskite-NC surface (Protesescu et al., 2015). Highly dynamic binding was observed between the L-type ligands, *i.e.*, a pair consisting of an anion ($Br^-$ or oleate, $OA^-$) and a cation (oleylammonium, $OLAH^+$), and the oppositely charged NC surface ions. In the meantime, a mutual equilibrium exists between the ionized and molecular forms of these ligands ($OA^- + OLAH^+ \leftrightharpoons OLA + OAH$ or $OLAH^+ + Br^- \leftrightharpoons OLA + HBr$) (De Roo et al., 2016). These dynamics, however, could cause rapid desorption of the capping ligands upon the isolation and purification of the NC colloids, resulting in a significant loss of colloidal stability and a rapid decrease in PLQY. To gain insights into the complex reaction dynamics, $^1H$ solution nuclear magnetic resonance (NMR) spectroscopy was performed to understand the surface chemistry evolution of perovskite NCs (De Roo et al., 2016). Interestingly, it was found that the NC surface is actually dynamically stabilized by X-type ligands, either oleylammonium bromide or oleylammonium carboxylate, forming an

$NC(X)_2$ binding. These ligands on the surface act as an ionic pair, *i.e.*, ammonium groups displace a surface A-site cation, whereas carboxylates (bromides) act as surface anions.

Effective strategies toward a stable surface of perovskite NCs are highly desired for their practical implementation in various optoelectronic applications. The introduction of a different L-type ligand, *i.e.*, TOP, into the synthesis of perovskite NCs combined with OA/OAm has been shown to significantly enhance the phase stability (Wang et al., 2018a). In particular, it is found that the functional group together with the length of carbon chains attached to phosphine can critically impact the stability of perovskite NCs. Due to the lone electron pair of the P atom of TOP, lead halide reagent can be readily dissolved and formed an active TOP-$PbX_2$ precursor. This facilitates the nucleation and growth process and improved the optical properties of perovskite NCs.

In 2018 Kovalenko et al. proposed a new X-type ligand capping strategy utilizing long-chain zwitterionic molecules (Krieg et al., 2018). The use of X-type zwitterionic ligands such as sulfobetaines, phosphocholines, γ-amino acids and so forth, resulted in much improved chemical durability and stability. In particular, this class of ligands allows for the isolation of clean perovskite NCs with high PLQYs of above 90% after four rounds of precipitation/redispersion along with much higher overall reaction yields of uniform and colloidal dispersible NCs.

Lately, Zeng et al. developed a "Br-equivalent" ligand strategy in which the proposed X-type ligands, for example, strong ionic sulfonate heads, could firmly bind to the exposed Pb ions to form a steady binding state, and effectively eliminate the exciton trapping probability caused by bromide vacancies (Yang et al., 2019). In this case, the sulfonate heads acted a similar role as natural Br ions in a perfect perovskite lattice. Using this approach, high PLQYs >90% could be facilely achieved without the need for amine-related ligands. For $CsPbBr_3$ NCs that were prepared only with dodecylbenzene sulfonic acid (DBSA), the high PLQYs were well maintained after eight purification cycles, more than five months of storage, and high-flux photo-irradiation.

In addition to the organic ligands discussed above, inorganic ligands such as $K^+$ have also been well studied as Z-type electron-acceptor ligands (Wang et al., 2021a, 2022). These inorganic ligands could be regarded as Lewis acids which coordinate with the halide anions. The termination of inorganic ligands is usually accomplished by including metal salts in the synthesis or purification process to exchange long organic ligands at the surface of perovskite NCs. Next, we will discuss the methods for post-synthetic ligand exchange treatments that have been well-established for manipulating the surface of perovskite NCs.

## Ligand exchange

Many efforts have been devoted to improve the properties of $CsPbX_3$ NCs by ligand exchange (Almeida et al., 2019). The option of the right ligands for both the synthesis and post-synthesis process is crucial to achieve high stability, excellent photophysical properties, and optoelectronic efficiency (Kazes et al., 2021). For instance, OA and oleylamine OAm were firstly employed to heal the defects originating from undercoordinated ions on the NC surface. However, these strongly adsorbed bulky organic ligands that are standard for high-quality NC synthesis may not be ideal for use in optoelectronic and electronic devices due to the incorporation of the insulating ligands or ligand components into the NC films. A common route is to exchange the surface bulky ligands with short organic or inorganic ligands that are suitable for charge transport. The methods for ligand exchange could be classified into two categories, *i.e.*, solution-phase exchange and solid-state exchange.

### *Solution-phase exchange*

There are multiple recipes to exchange the initial OA and OAm surfactants with shorter-chain ligands within the solution phase after the synthesis of the NCs. Pan et al. utilized a ligand-exchange strategy to replace the L-type long-chain OA/OAM ligands with relatively short X-type di-dodecyl dimethyl ammonium bromide (DDAB) ligand in $CsPbX_3$ NC solutions (Figure 11A) (Pan et al., 2016b). DDAB is particularly appealing to replace OA/OAm surface ligands and can provide better colloidal stability and balanced charge mobility. As a result, the LEDs based on short ligand-capped $CsPbX_3$ NCs demonstrated much higher EQE and luminescence than those of OA/OAm ones. Chen et al. also obtained $CsPbBr_3$ NCs with the $DDA^+$ capped on the NC surface and found that they could be well dispersed in octane and maintained for at least 5 days without any precipitation, compared with the original NCs that were precipitated

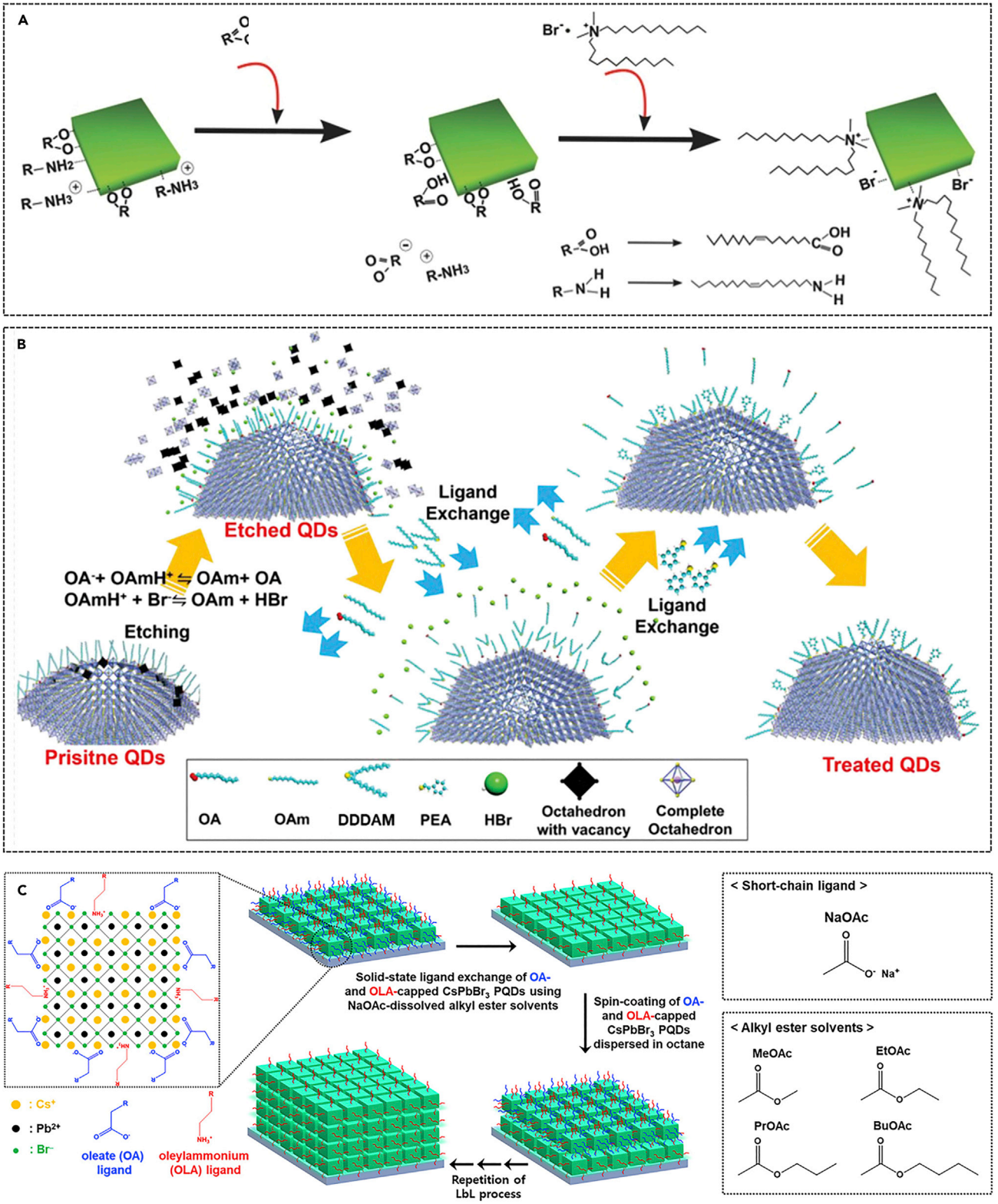
A
B
Etched QDs
Ligand Exchange
OA⁻+ OAmH⁺ ⇋ OAm+ OA
OAmH⁺ + Br⁻ ⇋ OAm + HBr
Etching
Prisitne QDs
Ligand Exchange
Treated QDs
OA
OAm
DDDAM
PEA
HBr
Octahedron with vacancy
Complete Octahedron
C
: Cs⁺
: Pb²⁺
: Br⁻
oleate (OA) ligand
oleylammonium (OLA) ligand
Solid-state ligand exchange of OA- and OLA-capped CsPbBr3 PQDs using NaOAc-dissolved alkyl ester solvents
Spin-coating of OA- and OLA-capped CsPbBr3 PQDs dispersed in octane
Repetition of LbL process
< Short-chain ligand >
NaOAc
< Alkyl ester solvents >
MeOAc
EtOAc
PrOAc
BuOAc

**Figure 11. Surface engineering by post-synthetic ligand-exchange**

(A) Illustration of the ligand-exchange mechanism on $CsPbBr_3$-NC surface. Reprinted from (Pan et al., 2016b). Copyright © 2016, Wiley.

(B) Schematic illustration of ligand exchange process on perovskite NC surface driven by acid etching. Reprinted from (Bi et al., 2021). Copyright © 2021, Wiley.

(C) Schematic representation of the solid-state ligand-exchange process of $CsPbBr_3$ NCs using NaOAc-dissolved carboxylate ester solutions such as MeOAc, EtOAc, PrOAc, and BuOAc. Reprinted from (Cho et al., 2020a). Copyright © 2020, American Chemical Society.

to the bottom of the glass bottle after 1 day (Chen et al., 2018c). Besides, the as-prepared LED device using the well-passivated NCs exhibited a maximum current density of 0.62 cd $A^{-1}$ and an EQE of 0.58%, which was nearly nine times higher than that of the device based on unmodified NCs. Furthermore, Zheng et al. realized complete surface passivation of $CsPbBr_3$ NCs by treatment with DDAB and sodium thiocyanate, resulting in dispersions with photostable PLQY (~100%) and NC films with high carrier mobility (Zheng et al., 2019a).

Compared with organic ligands, inorganic ligands have a stronger binding with NCs and can passivate surfaces better. Chan' group demonstrated that the colloidal $CsPbBr_3$ NCs surfaced-treated by $PbBr_2$ dissolved in a mixture of OA acid and OAm not only raised their PLQY to nearly unity but also observably increased their trion PL lifetime from ~0.9 to ~1.6 ns (Wang et al., 2018c). In particular, the PL stability in the air was prolonged from days to months. Further study revealed the ligands effectively passivated exposed Cs or Pb ions at the NC surface by solid-state NMR spectroscopy which was responsible for the improved optical performance (Chen et al., 2020). Wang et al. reported an inorganic ligand exchange for $CsPbI_3$ perovskite NCs. The $CsPbI_3$ NCs were firstly washed with methyl acetate to remove organic ligands. Inorganic ligands were then attached to the NC surface by adding a KI/DMF solution diluted in toluene into the NC solution (Wang et al., 2021a). It is found that the $K^+$ passive NC films were oriented and mechanically coupled, enabling strain increase across the film. XRD characterization showed that films' structure was the α-phase—with no observable-phase XRD signature. Furthermore, Time-resolved PL decay and transient absorption spectroscopy revealed that the treated films have a lower trap density than the untreated QD films, indicating that the NC surfaces were passivated well. An *in situ* inorganic ligand exchange strategy has been proposed by directly introducing KI or NaI into the antisolvents for the purification of $CsPbI_3$ NCs (Wang et al., 2022). This method avoids the loss of PLQY and colloidal stability. The small inorganic cations provide a rich surface coverage superior to that offered by long-chain organic ligands, resulting in perovskite solids with storage stability of 1 year in ambient conditions (25°C and 40% humidity). In LEDs, the materials enable an EQE of 24.4% with high operating stability.

Recently, Tian's group devised a novel acid etching-driven ligand exchange strategy to achieve pure-blue emitting small-sized (~4 nm) $CsPbBr_3$ NCs with ultralow trap density and excellent stability (Bi et al., 2021). As shown in Figure 11B, HBr was firstly employed to heal imperfect $[PbBr_6]^{4-}$ octahedrons, thereby removing surface defects and excessive carboxylate ligands. Subsequently, didodecylamine and phenethylamine were successively introduced to bond the residual uncoordinated sites of the NCs via *in situ* exchange with the original long-chain ligands. It is marvelous that the NCs possessed a near-unity PLQY of 97% and remarkable stability even in UV lighting and ambient conditions. Additionally, the fabricated LEDs based on the treated NCs exhibited pure-blue emission at 470 nm, an EQE of 4.7%, a maximum luminance of 3850 cd $m^{-2}$ (record performance value for pure-blue perovskite LEDs), and long-term half-lifetime (above 12 h) under operational condition at the initial luminance of 102 cd $m^{-2}$, which is over one order of magnitude higher than the state-of-the-art blue perovskite LEDs. All these demonstrated that replacing the common ligand (OA or OAm) with other ligands is an effective method to enhance the stability and performance of perovskite NCs.

### *Solid-state exchange*

The recipes for solution-phase exchange produce conductive NCs that are suitable for LED applications, however, they may not be ideal for solar cell applications. (Hu et al., 2021; Sanehira et al., 2017; Swarnkar et al., 2016; Zhao et al., 2019a). For the latter, post-synthesis dipping is the mostly used solid-state exchange strategy. Perovskite NCs are firstly assembled into films followed by dipping in an antisolvent which results in ligand removal and electronically coupled NCs. Swarnkar et al. for the first time reported $CsPbI_3$-NC solar cells with a PCE over 10% (Swarnkar et al., 2016). A dipping method in a saturated Methyl acetate (MeOAc) solution of either $Pb(OAc)_2$ or $Pb(NO_3)_2$ was proposed to effectively remove the organic ligands such as oleylammonium, oleate, or octadecene. The solar cells' efficiency was subsequently improved by

precise manipulation of the surface chemistry based on the A-site cation halide salt (AX) treatments (Sanehira et al., 2017). Cho et al. realized green light-emitting solar cells with a high open circuit voltage of 1.6 V, via solvent miscibility-induced ligand exchange (Cho et al., 2020a). After investigating carboxylate ester-based short-chain ligand solutions including MeOAc, ethyl acetate (EtOAc), propyl acetate (PrOAc), butyl acetate (BuOAc), and their mixtures (Figure 11C), they found that longer carboxylate ester-based solutions resulted in more efficient removal of native long-chain ligands but at the same time showed an undesired less film thickness because of the stripping-out phenomena of the as-cast $CsPbBr_3$ NCs resulting from high miscibility with hydrophobic substances. Based on these results, they devise a suitably optimized solvent mixture of carboxylate esters to enable efficient ligand exchange with suppressed stripping-out phenomena.

## Molecular doping

Analogous to conventional semiconductors such as silicon and germanium, halide perovskites may also be remotely doped by attaching a molecule or an electrochemical cell to the surface (Kubicki et al., 2020). Huang et al. reported remote doping of $MAPbI_3$ bulk films by using a strong electron-withdrawing molecule, *i.e.*, 2,3,5,6-tetrafluoro-7,7,8,8-tetracyanoquinodimethane (F4TCNQ). Both film conductivity and the electronic contact with the conductive substrate were improved, resulting in a reduced series resistance (Wu et al., 2018b). This facilitated the extraction of photoexcited holes from perovskite directly to the conductive substrate, thereby improving the solar cell efficiency.

Given the large specific surface area of perovskite NCs, remote doping is also expected to be a versatile strategy to tailor the electronic properties of perovskite NCs by tuning the net doping without the burden of redesigning the processing and chemistry of the NC film fabrication, thus not interfering with NC surface chemistry, interdot spacing, and film order at the nanoscale (Kirmani et al., 2016). Jeffrey et al. demonstrated the tuning of the electronic properties of $CsPbI_3$ NC films using physically adsorbed molecular dopants (Gaulding et al., 2019). They found that pristine $CsPbI_3$ NC films were slightly *p*-type doped with increasing conductivity achieved by incorporating the electron acceptor and decreasing conductivity for the electron donor. The enhanced conductivity for *p*-type NC arrays enabled significant improvements for field-effect transistors and phototransistors. On another side, the PL of perovskite NCs quenches because the excess charge carriers induce Auger-mediated nonradiative recombination. It is thus concluded that molecular doping provides a route toward controlling carrier type and density for perovskite NCs which is pivotal in enabling widespread next-generation optoelectronic devices.

## Core-shell structure

To confront the instability of halide perovskite NCs, versatile inorganic materials have also been proposed as shell matrix to protect the perovskite core. Such core/shell architecture represents a promising avenue to alleviate the stability issue and likely push the devices' operational stability and performance forward (Table 1) (Ahmed et al., 2021).

Oxide materials such as silica ($SiO_2$), titanium oxide ($TiO_2$), alumina oxide ($Al_2O_3$), and zirconium oxide ($ZrO_2$) have been successfully used as the shell materials for the core-shell structured perovskite NCs to improve their mechanical rigidity and chemical stability (Zhang et al., 2021a). For instance, Shan et al. reported shelling of $CsPbBr_3$ NCs with L-α-phosphatidylcholine (LP) surfactant and a silica precursor—tetramethoxysilane (TMOS), to form a core/shell structure of $CsPbBr_3$/LP/$SiO_2$ ink for anti-counter-feiting applications (Zhang et al., 2019a). The LP surfactant and TMOS were respectively added to the pre-synthesized $CsPbBr_3$ NCs solution to enable the formation of the $CsPbBr_3$/LP/$SiO_2$ core/shell NC structure. Significantly, the high stability of the perovskite core against heat, UV light, water, and ambient oxygen was accomplished. Xia et al. reported the preparation of monodisperse $CsPbBr_3$/$TiO_2$ core-shell NCs by coating titanium precursor on the surface of colloidal $CsPbBr_3$ NCs at room temperature (Chen et al., 2021). The $CsPbBr_3$/$TiO_2$ nanocomposites exhibit excellent stability, remaining identical particle size, crystal structures, and optical properties. Zheng et al. developed a facial method for the coating of a $TiO_2$ shell on $CsPbBr_3$ NCs, which can serve as an efficient protective layer for $CsPbBr_3$ NCs (Li et al., 2017b). As a result, the $CsPbBr_3$/$TiO_2$ core/shell NCs were ultrastable with excellent water stability for more than 12 weeks with size, morphology, and crystallinity unchanged. Yin et al. proposed a simple method to prepare $CsPbBr_3$/CdS core-shell NCs (Liu et al., 2019b). In order to improve their photostability, a dense layer of $Al_2O_3$ was then formed on the NC surface. Such multishell structures effectively prevent the PL of $CsPbBr_3$ NCs from photodegradation.

**Table 1. Optical property, photo-stability, and related device performance of core-shell perovskite NCs**

| Core-shell structure | PLQY (%) | PL lifetime (ns) | photo stability (%) | EQE (%) | Ref. |
|---|---|---|---|---|---|
| $CsPbBr_3/LP/SiO_2$ | 44→90.5 | 9→15 | 70→90 | NA | (Zhang et al., 2019a) |
| $CsPbBr_3/TiO_2$ | NA | 2.52→4.04 | NA | NA | (Chen et al., 2021) |
| CsPbBr3/TiO2 | NA | 2.1→14.8 | 37→75 | NA | (Li et al., 2017b) |
| $CsPbBr_3/nCdS/Al_2O_3$ | NA | 51.19→15.80 | 45→80 | NA | (Liu et al., 2019b) |
| $CsPbBr_3$/PS-b-P2VP | NA→51 | NA | stable | NA | (Hou et al., 2017) |
| $MAPbX_3$/PS-b-P2VP | 55→NA | 0.59→0.41 | NA | NA | (Hintermayr et al., 2019) |
| $MAPbBr_3/(OA)_2PbBr_4$/PMMA | NA→88 | NA | stable | NA | (Mary Vijila et al., 2019) |
| $CsPbX_3/Cs_4PbX_6$ | 84.4→96.2 | 16.2→9.1 | 40→95 | NA | (Jia et al., 2018) |
| $CsPbBr_3$/A-$CsPbBr_X$ | 54→84 | 6.68→7.25 | stable | NA | (Wang et al., 2017b) |
| $FAPbBr_3/CsPbBr_3$ | 82→93 | 30.2→40.1 | 20→80 | 1.03→8.1 | (Zhang et al., 2020a) |
| $FAPbBr_3/CsPbBr_3$ | NA | NA | 60→90 | NA | (Zhang et al., 2021c) |
| $CsPbBr_3$/PCN-333(Fe) | NA | NA | stable | NA | (Qiao et al., 2021) |
| $MAPbBr_3$/MOF | 1.73→70.48 | NA | stable | NA→15.4 | (Tsai et al., 2021) |
| $CsPbBr_3$/MOF | NA | NA | stable | NA→5.6 | (Tsai et al., 2021) |
| $CsPbI_3$/KI | 75→96 | 7→10 | stable | 16→21.3 | (Wang et al., 2021a) |
| CsPbI3-in-matrix | 0.5→70 | NA | stable | 3→18 | (Liu et al., 2021c) |
| $CsPbBr_3$:Sr/PbBr(OH)/MS | NA→75 | NA→7.46 | stable | 15→36.5 | (Xuan et al., 2022) |
| $CsPbBr_3$-in-matrix | NA | NA | stable | 0.5→13.8 | (Liu et al., 2022) |

Photo stability: X→Y, represents that the PL intensity maintained X% of its initial value under a UV light or blue LED for the same time, X is for no protecting structure, and Y is for protecting structure.

*in situ* encapsulation of perovskite NCs in a polymer shell provides another route to obtain highly stable halide perovskite NCs. In 2017, Hou et al. successfully synthesized the first perovskite/multidentate polymer core/shell nanostructure by using a unique solution-based template method (Hou et al., 2017). $CsPbBr_3$ perovskite NCs were coated by a multidentate copolymer polystyrene-block-poly-2-vinylpyridine (PS-b-P2VP), forming a core/shell heterostructure. Later, Urban et al. applied the same diblock copolymer approach to shell $MAPbX_3$ NCs with PS-b-P2VP (Hintermayr et al., 2019). Again, the polymer micelles acted as nanoreactor growth templates to guide the core/shell structure formation. The PL intensity of the NC films exhibited more than 15 times enhancement in the lifetime as compared to unprotected NCs and survived in the water for more than 75 days. Jayaraj et al. reported the synthesis of a $MAPbBr_3/(OA)_2PbBr_4$ core/shell nanoparticles using the LARP method (Mary Vijila et al., 2019). The contrast in the TEM images confirmed the core/shell structure formation, as the core is usually darker than the shell due to a small variation in the electron density between the core and shell. High-resolution TEM images showed a single core/shell NC with a core size of 1.5 nm coated with a shell of $(OA)_2PbBr_4$ of thickness 4 nm. These core-shell nanoparticles could be incorporated into a PMMA matrix to form stable transparent nanocomposites, showing reduced wettability and improved PLQY of 88%.

Perovskite or perovskite derivatives can also be formed on the surface of perovskite NCs. Jia et al. firstly used a seeded growth approach to synthesize core/shell $CsPbBr_3/Cs_4PbBr_6$ perovskite NCs (Jia et al., 2018). The obtained core/shell NCs consisted of a light-emitting $CsPbX_3$ core with a narrow bandgap and a $Cs_4PbX_6$ passivating shell with a large bandgap (>3.2 eV). Such type II structure led to the observed improved PLQY. Tian et al. obtained core-shell structured cubic $CsPbBr_3$@amorphous $CsPbBr_x$ (A-$CsPbBr_x$) perovskite NCs via a facile hot injection method and centrifugation process (Wang et al., 2017b). The core-shell structure NCs showed a record blue emission PLQY of 84%, much higher than blue-emitting cubic $CsPbBr_3$ NCs and $CsPbBr_xCl_{3-x}$ NCs. It was found that the amorphous $CsPbBr_x$ shell protected the $CsPbBr_3$ core against radiative corrosion and enhanced the core's absorption ability, thereby improving the PLQY. In 2020 Yang et al. developed a novel method to grow mono-dispersed core-shell $FAPbBr_3/CsPbBr_3$ NCs (Zhang et al., 2020a). The formed $FAPbBr_3/CsPbBr_3$ NCs emitted light in the visible range 460-560 nm with narrow linewidth (~20 nm) and high PLQY up to 93%. In particular, the core/shell perovskite NCs exhibited enhanced optical stability under ambient conditions and UV radiation. The enhanced

properties could be attributed to the overgrowth of $FAPbBr_3$ with an inorganic $CsPbBr_3$ shell, which acted as a protective layer and enabled effective passivation of the surface defects. Very recently, using the same core-shell NCs of $FAPbBr_3/CsPbBr_3$, an amplified spontaneous emission (ASE) was observed by Chen et al. with a stable threshold of 447 $nJ/cm^2$ under pulsed nanosecond pumping (Zhang et al., 2021c).

MOFs have been previously applied to address the issues related to the toxicity of lead because they could capture the $Pb^{2+}$ leaked from the degraded perovskite solar cells by forming water-insoluble solids (Wu et al., 2020). Recently, integration and encapsulation of perovskite NCs with multifunctional MOFs to form perovskite NC@MOF composites, prove to be a promising strategy for enhancing stability. Yu et al. encapsulated $CsPbBr_3$ NCs into a stable iron-based MOF with mesoporous cages (~5.5 and 4.2 nm) via a sequential deposition route to obtain a perovskite-MOF composite material, $CsPbBr_3$@PCN-333(Fe), in which $CsPbBr_3$ NCs were stabilized from aggregation or leaching by the confinement effect of MOF cages (Qiao et al., 2021). A significant interfacial charge transfer from $CsPbBr_3$ NCs to PCN-333(Fe) was observed, which is ideal for photocatalysis. Perovskite NCs stabilized in MOF thin films could also make bright and stable LEDs. Nie et al. employed a two-step method for the fabrication of perovskite NCs stabilized in MOF thin film (Tsai et al., 2021). Firstly, a Pb/MOF thin film was deposited. It was then converted into the perovskite/MOF NCs by spin coating with the halide salt-containing precursor. Bright LEDs made from perovskite-MOF NCs were demonstrated with a maximum EQE of over 15% and high brightness of over 105 cd $m^{-2}$ after the device reached stabilization. The stabilization of perovskite NCs by a surrounding MOF proved to be a simple yet effective way to make extraordinarily bright perovskite-NC-based LEDs, with stable continuous operation of up to tens of hours.

## COMPONENT ENGINEERING

Component engineering, *i.e.*, doping or alloying, represents the most efficient way to tune the bandgap, crystal structure, and optical and electronic properties of semiconductor materials (Lu et al., 2020a; Luo et al., 2019). Beneficial from the ionic nature of perovskites, it is facile to achieve tunable properties by varying the composition of these compounds (Li et al., 2020a; Tablero Crespo, 2019). In terms of the location of substitution ions, we simply divided these strategies into three categories, *i.e.*, A-site, B-site, and X-site.

### A site

Dopants of A-site were always monovalent metal cations or organic cations. It has been demonstrated that A-site cations hardly change the electronic band structures of perovskites because the DOS is mainly contributed by the $[BX_6]^{4-}$ octahedra. However, A-site doping can adjust the tolerance factor ***t*** of the obtained perovskite structure to a more stable region and hence significantly improve the resulting optical properties as well as the device stability. For example, Amgar et al. reported on a mixed-cation system of $Rb_xCs_{1-x}PbX_3$ (where X = Cl or Br) perovskite NCs. (Amgar et al., 2018). The size and the average side lengths of the NCs showed a declining trend with an increase of the $Rb^+$ content for both Cl and Br, and the tolerance factors were also reduced slightly with the addition of more rubidium, which meant a more stable perovskite phase.

Li's group demonstrated the monovalent $K^+$ ion doping of $CsPbBr_3$ perovskite NCs by a post-modification method (Huang et al., 2018). Because $K^+$ and $Cs^+$ have the same valence and comparable ionic radii (1.67 Å for $Cs^+$ and 1.38 Å for $K^+$), it is concluded that $K^+$ ions can replace part of surface $Cs^+$ ions. The incorporation of $K^+$ not only increased the PLQY from 65% to 83% but also considerably improved the stability of $CsPbBr_3$ NCs. This implies that the doping of $K^+$ could effectively reduce the defects at the NC surface and facilitate the charge-carrier dynamics, thereby decreasing trap-dominated nonradiative recombination.

In addition to changing the perovskite structure stability by modifying the tolerance factor, the size of the A-site organic cation also changes the bandgap of perovskite NCs. Sapra et al. reported for the first time colloidal synthesis of $(EA)_x(MA)_{1-x}PbBr_3$ NCs. The bandgap was observed to be tuned from 2.38 to 2.94 eV by varying the ratio of ethylammonium (EA) and methylammonium (MA) cations (Mittal et al., 2016). The wide tuning of bandgap was further confirmed by electronic structure calculations using DFT, which explained the increase in the bandgap upon going toward larger "A" site cations in $APbBr_3$ NCs. The blue shift of optical emission was a result of the insertion of larger EA cations as compared to MA cations in the voids between corner sharing $[PbBr_6]^{4-}$ octahedra.

In fact, the impact of A-site cation on the properties of halide perovskites is rather complex. Very recently, Seok, Yang and Park et al. pointed out that the conventional roles of the A cation in bulk perovskites should

be reevaluated (Lee et al., 2022a). In particular, expanded roles of the A cations including phase stabilization, suppression of ion migration, and surface functionalization should be emphasized. Considering the difference between bulk perovskites and perovskite NCs, systematic studies are still required to gain deeper understanding of the doping mechanisms and their impact on the properties of perovskite NCs.

### B site

Compared with the A-site substitution, the B-site doping (or alloying) is more concerned, providing added freedom to design the properties of perovskite NCs. The B-site doping not only enables precise tuning of their properties and novel functionalities but also improves the stability, as well as reduces the use of toxic lead. Up to now, a variety of metal ions have been employed for B-site doping of perovskite NCs. These metal ions can be divided into two categories, *i.e.*, isovalent doping and heterovalent doping, according to the valence electrons of the extrinsic ions and the $Pb^{2+}$ host.

#### *Isovalent doping*

Isovalent metal ions with the same valence electron as the $Pb^{2+}$ host have been used to dope perovskite NCs for combined properties of perovskite NCs and the metal ions. For instance, manganese ion ($Mn^{2+}$)-doped perovskite NCs possess the combination of paramagnetic and optical properties that do not exist in undoped perovskite NCs. An early attempt to dope $Mn^{2+}$ into $CsPbCl_3$ and $CsPb(Cl/Br)_3$ perovskite NCs was reported by Son et al. using a one-pot hot injection method (Parobek et al., 2016). Intense orange luminescence sensitized by the d−d transition of $Mn^{2+}$ ions was observed, indicative of sufficiently strong exchange coupling between the charge carriers of the NC host and dopant d electrons mediating the energy transfer (Figure 12B). Subsequently, Klimov et al. discovered that the dual-color emission including the intrinsic band-edge emission and dopant-sensitized emission of $Mn^{2+}$ doped perovskite NCs could be controlled by the halide content (Figure 12A) (Liu et al., 2016). The mechanism of halide identity on relative intensities of the dual emission bands could be ascribed to the influence of the energy difference between the corresponding transitions on the characteristics of energy transfer between the dopant and the perovskite-NC host (Figure 12C). Further, Ricciarelli et al. simulated the electronic structure of $Mn^{2+}$-doped perovskite NCs in various charge and spin states. They found that both energy- and charge-transfer mechanisms contributed to the long-lived dopant-related luminescence and the enhanced PLQYs of perovskite host (Ricciarelli et al., 2021). Recently, Locardi et al. synthesized $Mn^{2+}$-doped $Cs_2AgInCl_6$ double perovskite NCs (Locardi et al., 2018). A bright PL emission with a much higher PLQY of ~16 $\pm$ 4% was obtained, compared to the weak white PL emission (PLQY ~ 1.6 $\pm$ 1%) of undoped NCs.

For $Ni^{2+}$ doping, a different mechanism is revealed for engineering the optical properties of perovskite NCs. Kim et al. reported improvement in both the PLQY and stability of $CsPbBr_3$ NCs by varying the concentration of $Ni^{2+}$ (Kim et al., 2021a). The $Ni^{2+}$ ion introduced impurity states in the perovskite structure, reducing the recombination rate of electrons and holes, thereby enhancing the optical performance. Under continuous UV light irradiation, the PL intensity of $Ni^{2+}$-doped $CsPbBr_3$ NCs drops by 18%. As a comparison, the PL intensity of undoped NCs decreases by 70%. Sun et al. reported controlled $Ni^{2+}$ doping of $CsPbCl_3$ NCs using the hot injection method (Yong et al., 2018). The $Ni^{2+}$ ions have a strong tendency to form octahedral coordination with halide ions, enhancing the short-range order of the lattice and thereby the violet PL of $CsPbCl_3$ NCs.

It is intriguing that the doping of metal ions into perovskite NCs can also be realized by post-synthesis cation-exchange methods although it was more difficult compared with the anion exchange. Donega et al. reported partial cation exchange of $Pb^{2+}$ in colloidal $CsPbBr_3$ NCs with several isovalent cations by using bromide salts, resulting in doped $CsPb_{1-x}M_xBr_3$ NCs (M = $Sn^{2+}$, $Cd^{2+}$, and $Zn^{2+}$; $0 < x \leq 0.1$) (van der Stam et al., 2017). Both the shape and size of the parent NCs were preserved, apart from a small contraction of the unit cells upon the incorporation of the guest cations (Figures 12D and 12E). A blue shift in the optical spectra was observed scale linearly with the lattice contraction that accompanies the $Pb^{2+}$ for $M^{2+}$ cation exchange. The high PLQYs, sharp absorption features, and narrow emission of the parent $CsPbBr_3$ NCs were all maintained.

When the metal precursors and $CsPbX_3$ NCs have a different halide species, both anion exchange and cation exchange can take place. Yang et al. investigated the interplay between anion exchange and cation exchange for efficient doping of $Sn^{2+}$ into $CsPbX_3$ NCs (Li et al., 2018b). It was found that the anion exchange reaction could provide a driving force, accelerating the cation exchange rate between the host $Pb^{2+}$ and guest $Sn^{2+}$.

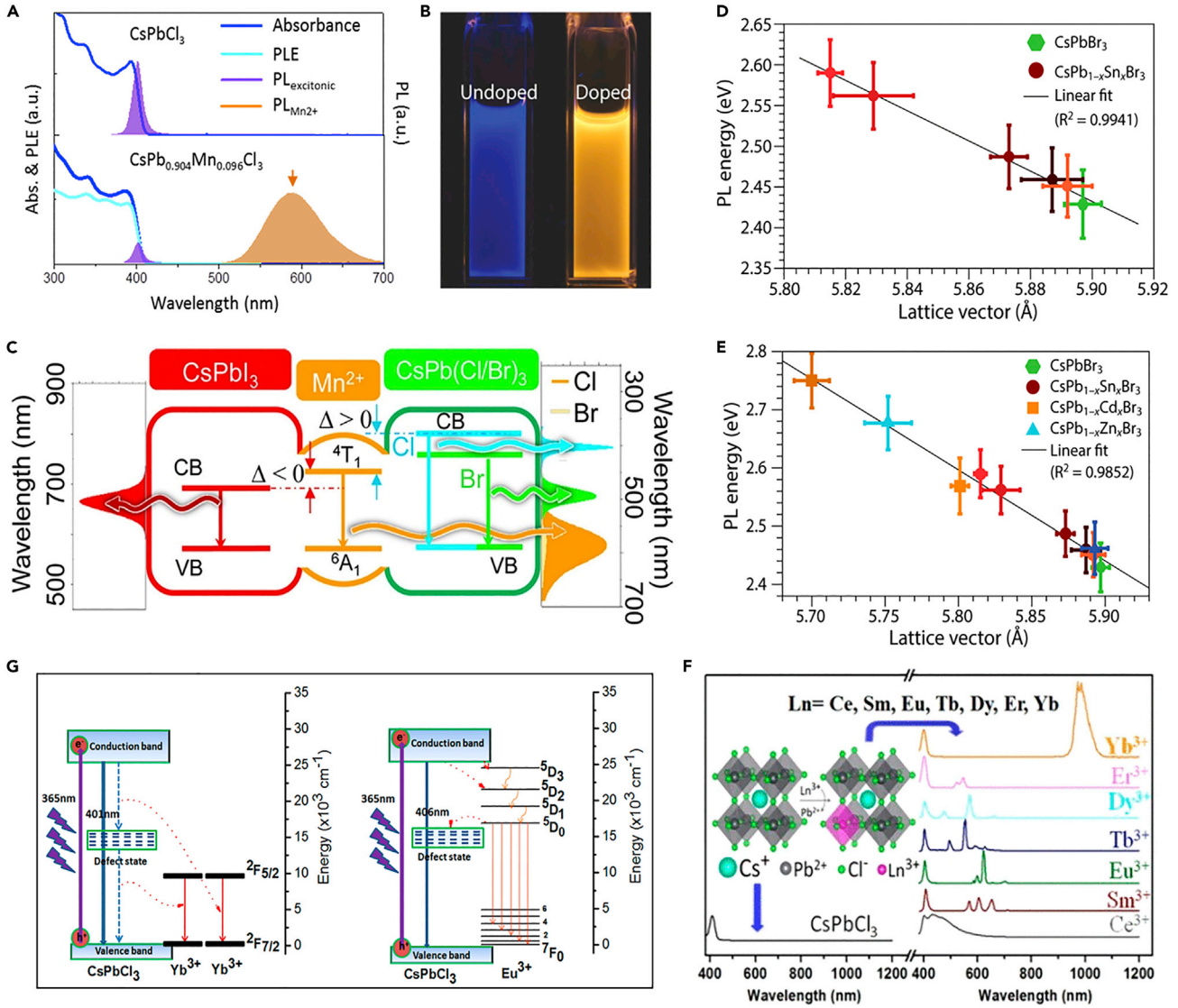


**Figure 12. Component engineering by metal ion doping**

(A) Absorption and PL spectra of undoped and $Mn^{2+}$-doped $CsPbCl_3$ NCs.

(B) Images of undoped and $Mn^{2+}$-doped $CsPbCl_3$ NC colloids under UV excitation. Reprinted from (Parobek et al., 2016). Copyright © 2016, American Chemical Society.

(C) Schematic showing the mechanism for dual-color emission in $Mn^{2+}$-doped perovskite NCs controlled by halide content. Figures A and C reprinted from (Liu et al., 2016). Copyright © 2016, American Chemical Society.

(D) PL energy as a function of the lattice vector in doped $CsPb_{1-x}Sn_xBr_3$ NCs obtained by post-synthetic $Pb^{2+}$ for $Sn^{2+}$ cation exchange in parent $CsPbBr_3$ NCs.

(E) PL energy as a function of the lattice vector in doped $CsPb_{1-x}M_xBr_3$ (M = Sn, Cd, and Zn) NCs obtained by post-synthetic $Pb^{2+}$ for $M^{2+}$ cation exchange in parent $CsPbBr_3$ NCs. Figures D and E reprinted from (van der Stam et al., 2017). Copyright © 2017, American Chemical Society.

(F) Emission spectra of $CsPbCl_3$ NCs doped with different lanthanide ions.

(G) Left: Energy level diagram of $Yb^{3+}$ ions doped $CsPbCl_3$ perovskite NCs and the possible quantum cutting mechanisms. Right: Energy level diagram of $Eu^{3+}$ ions doped $CsPbCl_3$ perovskite NCs and the possible PL mechanisms. Figures F and G reprinted from (Pan et al., 2017a). Copyright © 2017, American Chemical Society.

### *Heterovalent doping*

Perovskite NCs that are doped with heterovalent metal ions are also attracting great attention. Because a substitutional heterovalent impurity has one more or less valence electron than the host ion it replaces, the ionization of the heterovalent impurity by thermal energy could, in principle, generate an extra electron or

hole in the perovskite NC host. This leads to the shift of the Fermi level ($E_F$) and *n*- or *p*-type doping of perovskite NCs, which is particularly demanded creating various functional devices.

Motivated by the active role of heterovalent dopants in modulating the electronic properties Zhou et al. reported controlled doping of monovalent $Ag^+$ into $CsPbBr_3$ NCs via a facile room temperature synthesis method (Di et al., 2015). The $Ag^+$ ions act as substitutional dopants to replace $Pb^{2+}$ ions in $CsPbBr_3$ NCs, shifting the $E_F$ down toward the valence band and in turn inducing a heavy p-type character. Using the same method, they successfully doped $Bi^{3+}$ into $CsPbBr_3$ NCs (Lee et al., 2020b). A $Bi^{3+}$ ion has one more valence electron than the host $Pb^{2+}$. The substitution of a $Pb^{2+}$ with a $Bi^{3+}$ leads to the shift of the $E_F$ toward the conduction band and dedoping of $CsPbBr_3$ NCs. A theoretical study within the DFT regime performed by Lyons et al. confirmed that the $Bi^{3+}$ incorporates favorably at the Pb site and acts as a deep donor in $CsPbBr_3$ perovskites (Lyons, 2021).

By contrast, Begum et al. reported doping of trivalent $Bi^{3+}$ into $CsPbBr_3$ NCs by a hot-injection method (Begum et al., 2017). They found that $Bi^{3+}$ was successfully doped into the core of $CsPbBr_3$ NCs and quenched the PL because of the doping-induced trap states. The $Bi^{3+}$ doping modified the band structure of $CsPbBr_3$ NCs and shifted the $E_F$ toward the conduction band. This could improve the interfacial energy alignment between $CsPbBr_3$ NCs and molecular acceptors, which in turn facilitated the charge transfer at the interface. Meng et al. doped trivalent $Al^{3+}$ into $CsPbBr_3$ NCs using $AlBr_3$ as the dopant precursor (Liu et al., 2017c). During the growth, the incorporation of $Al^{3+}$ was favored due to the small disparity in bond strengths within the precursor and the host lattice, and the pre-existing Al-Br (bridging) bond that facilitated the binding to the host lattice. Further theoretical calculation suggested the $Al^{3+}$ doping introduced a new energy level in the bandgap due to the hybridization of the Al s-orbitals, the Br p-orbitals, and the Pb p-orbitals. This resulted in the extended bandgap compared with the undoped NCs. Therefore, the $Al^{3+}$ doped $CsPbBr_3$ NCs exhibited stable blue PL, being a possible down-convertor material for backlit displays.

Compared with $Bi^{3+}$ and $Al^{3+}$, trivalent rare earth (RE) ions possess abundant and unique energy levels. Multicolor emissions could be achieved by doping RE ions into perovskite NCs via energy transfer from the perovskite-NC host to RE impurities (Arfin et al., 2020; Marin and Jaque, 2021). Song et al. presented doping of various lanthanide ions ($Ce^{3+}$, $Sm^{3+}$, $Eu^{3+}$, $Tb^{3+}$, $Dy^{3+}$, $Er^{3+}$, and $Yb^{3+}$) into the lattices of $CsPbCl_3$ perovskite NCs through a modified hot-injection method, which endows tunable light emissions spanning from visible to NIR spectra (Figures 12F and 12G) (Pan et al., 2017a). The XRD patterns confirmed the incorporation of lanthanide ions into the lattice of perovskite NCs. The efficient energy transfer from $CsPbCl_3$-NC host to the lanthanide ions gave rise to intense emission bands from the intrinsic electronic transitions of lanthanide ions, *i.e.*, 4f−5days transition for $Ce^{3+}$, $^4H_{5/2}$-$^6H_J$ (J = 2/5, 2/7, 2/9, 2/11) for $Sm^{3+}$, $^5D_0$-$^7F_J$ for $Eu^{3+}$, $^5D_4$-$^7F_J$ (J = 3-6) for $Tb^{3+}$, $^4G_{5/2}$-$^6H_J$ (J = 15/2, 13/2, 11/2) for $Dy^{3+}$, $^2H_{11/2}$-$^4I_{15/2}$/$^4S_{3/2}$-$^4I_{15/2}$ for $Er^{3+}$, and $^2F_{5/2}$-$^2F_{7/2}$ for $Yb^{3+}$ ions. Using the same method, they prepared $Ce^{3+}$ and $Yb^{3+}$ codoped $CsPbCl_{1.5}Br_{1.5}$ NCs (Zhou et al., 2017a). The codoped NCs possessed larger absorption cross-sections, weaker electron-phonon coupling, and higher inner luminescent QY (146%) in terms of an efficient quantum cutting emission mechanism. Films assembled from these NCs were finally explored as a downconverter to enhance the performance of commercial silicon solar cells.

In another similar work, Milstein et al. synthesized $Yb^{3+}$:$CsPbCl_3$ NCs which reproducibly yielded sensitized $Yb^{3+}$ $^2F_{5/2}\rightarrow{}^2F_{7/2}$ luminescence with near-infrared PLQYs over 100%, while almost no excitonic luminescence was observed (Milstein et al., 2018). With the assistance of spectroscopy study, they proved that the extremely high PLQYs could be attributed to the energy captured by $Yb^{3+}$-induced defect and the subsequent transfer to two neighboring $Yb^{3+}$ ions in a single concerted step on the picosecond timescale.

Unlike $Yb^{3+}$, $Ce^{3+}$ has a similar ion radius as the $Pb^{2+}$ cation and forms higher energy level of conduction band with bromine. Therefore, the substitution of a $Pb^{2+}$ with a $Ce^{3+}$ would maintain the integrity of the perovskite structure without introducing additional trap states, thereby enhancing the interband excitonic luminescence. Yu et al. demonstrated the doping of $Ce^{3+}$ ions into $CsPbBr_3$ NCs via a facile hot-injection method (Yao et al., 2018). As expected, the excitonic luminescence of the $CsPbBr_3$ NC host was greatly enhanced when a proper amount of $Ce^{3+}$ was included. However, no PL from the electronic transitions of $Ce^{3+}$ was observed even at the highest concentration, in direct contrast to $Ce^{3+}$ doped $CsPbCl_3$ NCs. The underlying mechanism responsible for the PL evolution was elucidated by means of ultrafast transient

absorption and time-resolved PL spectroscopy, signifying the importance of halide identity on the characteristics of energy transfer between the dopant and the perovskite-NC host.

Recently, Yin et al. reported a binary RE-doped lead-free $Cs_2AgIn_{1-\gamma-x}Bi_xLa_\gamma Cl_6$ double perovskite NCs (Yin et al., 2021). The binary $La^{3+}$-$Bi^{3+}$ codoping can break the parity-forbidden transition and modify the associated optical functionalities. The doped NCs achieved a broadband bright warm-white emission in the visible regime with an excellent PL quantum yield of 60%. In a similar work reported by Zheng et al., a binary $Na^{+}$-$Bi^{3+}$ codoping strategy raised the PLQY up to 56% because the lattice symmetry breaking induced by doping relaxed parity-forbidden transition ($1S_0 \rightarrow 3P_2$) of Bi-$6s^2$ orbitals (Zheng et al., 2021). These findings can be used to optimize the optical properties of emerging lead-free halide perovskite NCs.

## X-site

In the framework of $ABX_3$ perovskites, ion exchanges at A-site and B-site are more difficult because of the octahedra structure. By contrast, it is much easier to achieve X-site anion exchange. Via a controlled anion exchange reaction using different halide precursors, one can finely tune the chemical composition and thereby the optical response of perovskite NCs across the entire visible spectrum at a fast rate in the presence of a high concentration of mobile halide vacancies ($V_X^+$) and singly charged $X^-$.

As shown in Figure 13A, Akkerman et al. demonstrated that the anion exchange approach was accessible to a wide variety of $CsPbX_3$ perovskite NCs without deteriorating the structure and the overall stability of the initial NCs. By simply mixing solutions of perovskite NCs having different halide compositions, the anion exchange could readily take place (Akkerman et al., 2015). Figure 13B shows that the PL of the pristine $CsPbBr_3$ NCs could be tuned within an energy interval comprised between 1.88 and 3.03 eV following the titration curves. Additionally, it is notable that the PLQY of the NCs generally dropped from the starting value of 78% when replacing $Br^-$ ions with either $Cl^-$ or $I^-$ ions, which may be relevant to the intrinsic properties of halide perovskites. Wang et al. further demonstrated that the fast anion exchange could extend the PL based on the as-synthesized $CsPb_2Br_5$ NPLs, signifying its potential for application in versatile optoelectronic devices (Wang et al., 2016a).

Moreover, Parobek et al. found that controllable anion exchange can be achieved in a dihalomethane solution of $CsPbX_3$ NC in the absence of any spontaneously reacting anion source using the photoexcitation of $CsPbX_3$ NCs as the triggering mechanism for the halide ion exchange (Parobek et al., 2017). The reaction starts only in the presence of excitation light and the rate and extent of the reaction could be controlled by varying the light intensity. Recently, a two-phase anion exchange (TAE) synthesis method (Figure 13C) was reported by Chen's group. They firstly prepared $CsPbBr_3$ NCs with a well-maintained cubic morphology and high PLQY of about 95% (Lv et al., 2020). Then they made the $Cl^-$ ions from water into hexane to complete a Br-to-Cl exchange. By controlling the concentration of Cl sources and reaction time, the ratio of Cl to Br could be adjusted. They also found that ultra-high PLQYs could be achieved only by employing $CdCl_2$ rather than $NH_4Cl$, $ZnCl_2$, $BaCl_2$, $SrCl_2$, and so forth as the halide source.

Lead-free double perovskites with less toxicity and higher stability have also gained plenty of attention. Via a novel anion-exchange protocol using trimethylsilyl iodide, Creutz et al. converted the as-synthesized colloidal $Cs_2AgBiX_6$ (X = Cl, Br) elpasolites NCs to new materials including $Cs_2AgBiI_6$. The resulting $Cs_2AgBiI_6$ NCs showed strong absorption throughout the visible region, suggesting that this material could be a promising photovoltaic absorber (Creutz et al., 2018). Liu et al. recently researched the stability and the bandgaps of $Cs_2TiX_6$ (X = Cl, Br, I) NCs using DFT. They confirmed that the bandgap increased slightly when the A-site cation changed from K to Rb and Cs, while the bandgap increased apparently with the increase of Cl concentration, especially for $Cs_2TiI_2Cl_4$ (Liu et al., 2021a). Other groups also investigated the pseudo-halide ion exchange process. For example, doping of $CsPbBr_3$ NCs with rod-like $SCN^-$ anion would introduce disorder in the crystal lattice, leading to lattice expansion. This impacted the electronic band structure of perovskite NCs and caused bandgap broadening (Lou et al., 2018). Interestingly, Yang's group combined the anion-exchange chemistry with nanofabrication to create high-quality spatially resolved multicolor $CsPbX_3$ (X = Cl, Br, I, or alloy of two halides) NW heterojunctions and patterns at the nanometer scale with a pixel size down to 500 nm, which could find practical applications in large-scale electronic circuit, information storage, full color displays, and photovoltaic cells (Dou et al., 2017).

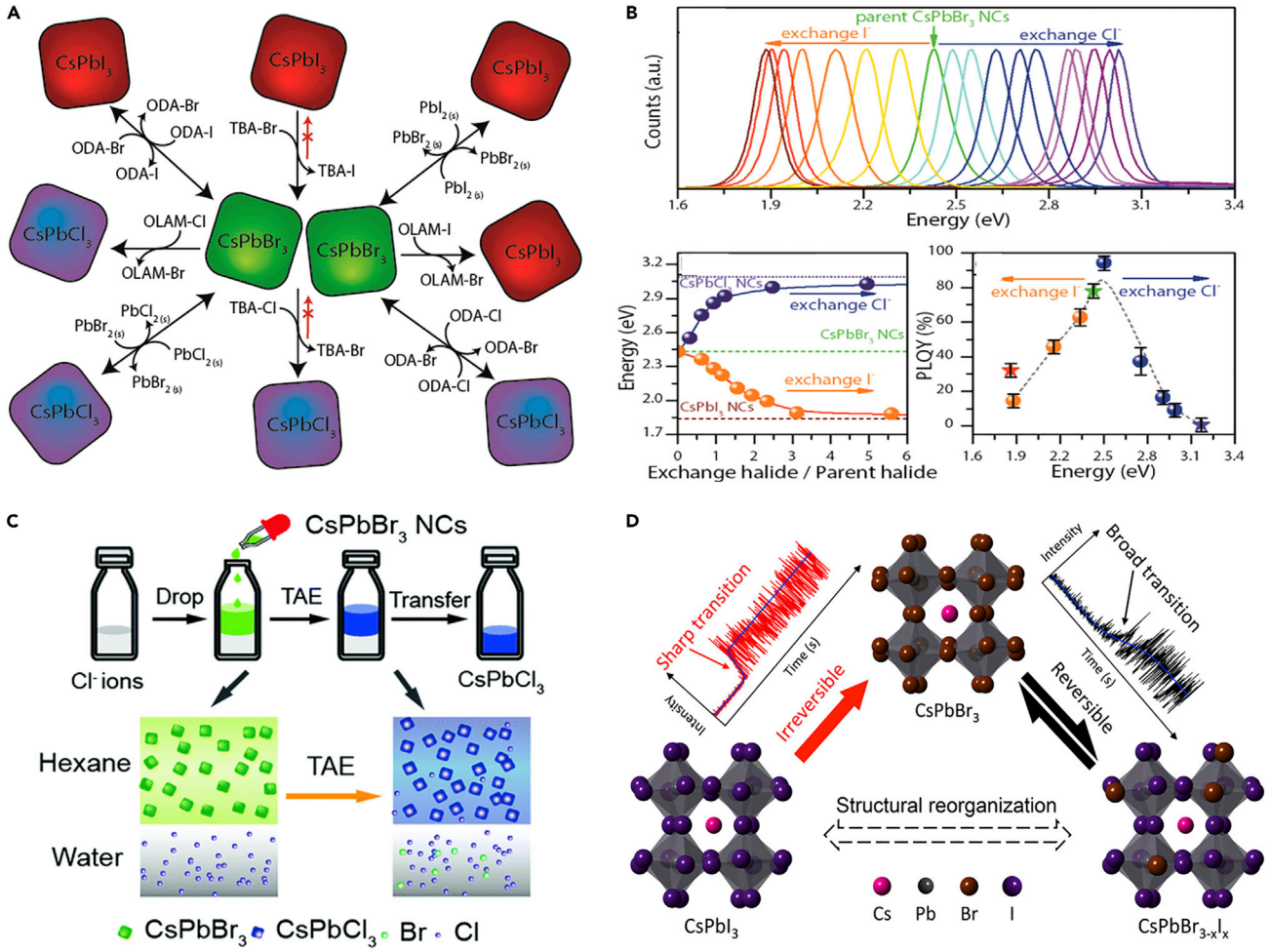


**Figure 13. Component engineering by post-synthetic anion-exchange**

(A) Illustration of the different routes and precursors for the anion exchange reactions on $CsPbX_3$ (X = Cl, Br, I) NCs.

(B) Top: PL spectra of the $CsPb(Br:X)_3$ (X = Cl, I) NCs prepared by anion exchange from $CsPbBr_3$ NCs. Bottom Left: PL calibration curves, a targeted emission energy could be obtained by adding a precise amount of halide precursor to a crude solution of $CsPbBr_3$ NCs. Bottom Right: PLQY recorded from the exchanged NCs and the directly synthesized NCs. Figures A and B reprinted from (Akkerman et al., 2015). Copyright © 2015, American Chemical Society.

(C) Illustration of the post-synthesis process and essential methodology using $CdCl_2$ as a $Cl^-$ ion source in the two-phase anion exchange method. Reprinted from (Lv et al., 2020). Copyright © 2020, Royal Society of Chemistry.

(D) Illustration of structural differences in when as-synthesized $CsPbI_3$ NCs undergo anion exchange to $CsPbBr_3$. Reprinted from (Wang et al., 2020a). Copyright © 2020, American Chemical Society.

So far, it is not clear whether the morphology of perovskite NCs is preserved during the anion exchange process. Two typical models have been proposed to explain the anion exchange between perovskite NCs. One is the lattice reconstruction model including disintegration, anion exchange, and lattice reconstruction, while the other is the general anion exchange model. By means of time-resolved *in situ* PL measurement Tian et al. found that the formation of mixed-halide perovskite NCs was dominated by both lattice reconstruction and anion-exchange processes rather than the general anion exchange model (Bi et al., 2018). Later, fluorescence microscopy was used to monitor the reaction trajectories of anion exchange between $CsPbBr_3$ and $CsPbI_3$ NCs (Wang et al., 2020a). It was found that $CsPbI_3$ NCs underwent more abrupt shifts in their emission characteristics when they transformed to $CsPbBr_3$ NCs, while $CsPbBr_3$ NCs exhibited a smoother transition during their transformation to $CsPbI_3$ NCs (Figure 13D), highlighting the structural differences between $CsPbX_3$ NCs directly synthesized by the HI method and those prepared by anion exchange. Later, to investigate time-dependent *in situ* PL spectra after mixing $CsPbBr_3$ and $CsPb(Br_{0.09}/I_{0.91})_3$ NCs, Gan et al. proposed a three-stage model involving photon reabsorption, initial anion exchange, and

adequate anion exchange (Sheng et al., 2020). The model is generally applicable when the two parent perovskite NCs were mixed in different orders and at different ratios.

## APPLICATIONS

### Light-emitting devices

Halide perovskite NCs are exceptional candidates for LEDs. Research on LEDs based on halide perovskite NCs started in 2015 (Song et al., 2015). The EQEs of the first LEDs based on all-inorganic $CsPbX_3$ NCs were 0.07%, 0.12%, and 0.09% for the blue, green, and orange emission, respectively. After a few years of intense efforts, the performance of perovskite-NC-based LEDs has been rapidly improved (Table 2), paving the way toward the niche market application of perovskite LED technologies.

#### *Red light-emitting devices*

Many strategies such as surface ligand management and metal ion doping have been proposed to improve the performance of red LEDs based on perovskite NCs. In order to confront the instability of cubic-phase $CsPbI_3$ NCs, Shen et al. reported a B-site doping strategy for stable and efficient red perovskite LEDs (Shen et al., 2021). $Ca^{2+}$ (1.00 Å) as a new B-site doping ion can successfully boost $CsPbI_3$ NC performance with both improved phase stability and optoelectronic properties. Red LEDs exhibited about triple enhancement for maximum EQE up to 7.8% and 2.2 times enhancement for half-lifetime $T_{50}$ of LED up to 85 min. By a sequential ligand post-treatment strategy, Lan et al. demonstrated spectrally stable and efficient pure red LEDs based on $CsPbI_3$ NCs with a mean size of ~5 nm (Lan et al., 2021). The sequential post-treatments using the ligands of 1-hydroxy-3-phenylpropan-2-aminium iodide (HPAI) and tributylsulfonium iodide (TBSI) led to a pure red LED with a peak EQE of 6.4% and a stable EL emission centered at the wavelength of 630 nm (Figure 14A). Similarly, the EQE of red LEDs (emission wavelength ~750 nm) based on $MAPbI_3$ perovskite NCs was boosted to greater than 15% by engineering the surface stoichiometry and chemical structure of bulky organoammonium ligands (Figure 14B) (Xiao et al., 2019). The NC surface was well passivated when the size was decreased to smaller than 5 nm. This strategy ensures minimal undercoordinated Pb and halide atoms on the surface, avoids the formation of 2D phases, and provides nanosized perovskite grains, leading to smooth and pinhole-free films, and thereby an excellent EQE (Figures 14C and 14D).

Inspired by the active role of $K^+$ in stabilizing perovskite solar cells, Wang et al. developed an inorganic ligand (KI) exchange strategy that could increase both phase stability and thermal transport of the $CsPbI_3$-NC films (Wang et al., 2021a). The atomic-ligand-exchanged NC films were mechanically coupled, resulting in distributed strain across the film. This makes cubic $CsPbI_3$ NCs more stable. Operando measurements of the temperature of the LEDs indicate that KI-exchanged NC films exhibit increased thermal transport compared to control films that rely on organic ligands. More importantly, the LEDs exhibit a maximum EQE of 23% with an EL emission centered at 640 nm (FWHM ~31 nm). These red LEDs provide an operating half-lifetime $T_{50}$ of 10 h (luminance of 200 cd $m^{-2}$) and operating stability that is 6-fold higher than that of control devices.

By contrast, Li et al. reported highly efficient and stable red LEDs based on stable tetragonal phase $CsPbI_3$ (β-$CsPbI_3$) NCs (Li et al., 2021). By incorporating poly(maleic anhydride-alt-1-octadecene) (PMA) into the NCs, the PLQY for β-$CsPbI_3$ NCs films remarkably increased from 34% to 89%. Moreover, the EQE of red LEDs based on β-$CsPbI_3$ NCs was up to 17.8%, and the time to half the initial EL intensity $T_{50}$ was over 300 h at a constant current density of 30 mA $cm^{-2}$, superior to most of the reported red perovskite LEDs to date.

Efficient red LEDs have also been demonstrated by using mixed-halide perovskite NCs. Hassan et al. fabricated efficient red LEDs centered at 620 nm with a high EQE of 20.3% by using $MAPb(I_{1-x}Br_x)_3$ NCs (Figure 14E) (Hassan et al., 2021). The key to stable EL operation is the treatment of the $MAPb(I_{1-x}Br_x)_3$ NCs with a lead-complexing multidentate ligand to 'clean' the NC surface through the removal of Pb atoms, and to suppress the segregation of halide ions (Figures 14F–14H). Both ligand-ligand and ligand-surface interactions are important to achieve a stable ligand shell on the NC surface. The work highlighted the role of perovskite-NC surface in stable LEDs and provided a route to control the formation and migration of surface defects which are detrimental to stable mixed-halide perovskite NCs.

Different from the strategies discussed above, Liu et al. explored bright and stable red LEDs by using $CsPbI_3$ NCs embedded in a mixed-halide perovskite matrix (Figure 14I) (Liu et al., 2021c). The $CsPbI_3$

**Table 2. Performance of red, green and blue LEDs based on perovskite NCs**

| Emitter layer (EL) | Device configuration | fabrication method | EL peak (nm) | $V_{on}$ (V) | $EQE_{max}$ (%) | CE (cd $A^{-1}$) | $L_{max}$ (cd $m^{-2}$) | CIE (x, y) | Operation stability | Ref. |
|---|---|---|---|---|---|---|---|---|---|---|
| $CsPbCl_3$ NCs | ITO/PEDOT:PSS/PVK/EL/TPBi/LiF/Al | spin coating | 455 | 5.1 | 0.07 | 0.14 | 742 | 0.19,0.04 | NA | (Song et al., 2015) |
| $CsPbBr_3$ NCs | ITO/PEDOT:PSS/PVK/EL/TPBi/LiF/Al | spin coating | 516 | 4.2 | 0.12 | 0.43 | 946 | 0.08,0.78 | NA | (Song et al., 2015) |
| $CsPbI_3$ NCs | ITO/PEDOT:PSS/PVK/EL/TPBi/LiF/Al | spin coating | 586 | 4.6 | 0.09 | 0.08 | 528 | 0.52,0.44 | NA | (Song et al., 2015) |
| $CsPbI_3$ NCs | ITO/PEDOT:PSS/EL/TPBi/LiF/Al | spin coating | 683 | 2.8 | 7.8 | NA | 790 | 0.72,0.27 | $T_{50}$ = 85 min | (Shen et al., 2021) |
| $CsPbI_3$ NCs | ITO/PEDOT:PSS/PTAA/EL/PO-T2T/LiF/Al | spin coating | 630 | 3.2 | 6.4 | NA | 1212 | 0.67, 0.32 | $T_{50}$ = 78 min | (Lan et al., 2021) |
| $MAPbI_3$ NCs | ITO/Poly-TPD/EL/TPBi/LiF/Al | spin coating | 774 | NA | 15.2 | NA | NA | NA | NA | (Xiao et al., 2019) |
| $CsPbI_3$ NCs | ITO/PEDOT:PSS/Poly-TPD/EL/TPBi/LiF/Al | spin coating | 640 | 2.0 | 23 | NA | 200 | 0.70,0.29 | $T_{50}$ = 10 h | (Wang et al., 2021a) |
| $CsPbI_3$ NCs | ITO/PEDOT:PSS/Poly-TPD/EL/TPBi/LiF/Al | spin coating | 689 | ~3.9 | 17.8 | NA | 618 | 0.721, 0.275 | $T_{50}$ = 317 h | (Li et al., 2021) |
| $MAPb(I_{1-x}Br_x)_3$ NCs | ITO/PEDOT:PSS/Poly-TPD/TFB/EL/TPBi/LiF/Al | spin coating | 620 | 2.8 | 20.28 | 31.28 | 627 | NA | NA | (Hassan et al., 2021) |
| $CsPbI_3$ NC-in-matrix | ITO/PEDOT:PSS:PFI/LiF/EL/TPBi/LiF/Al | spin coating | 650 | NA | 18 | NA | 4700 | NA | $T_{50}$ = 2400 h | (Liu et al., 2021c) |
| $CsPbBr_3$ NCs | ITO/PEDOT:PSS/Poly-TPD/EL/TPBi/LiF/Al | spin coating | 512 | 3.4 | 6.27 | 13.3 | 15,185 | 0.05,0.71 | NA | (Li et al., 2017a) |
| $CsPbBr_3$ NCs | ITO/PEDOT:PSS/PTAA/EL/TPBi/LiF/Al | spin coating | 515 | 2.75 | 11.6 | 45.5 | 55,800 | 0.09,0.71 | NA | (Song et al., 2018) |
| $CsPbBr_3$ NCs | ITO/PEDOT:PSS/PTAA/EL/TPBi/LiF/Al | spin coating | 516 | NA | 18.7 | 75 | 2.1 | NA | $T_{50}$ = 15.8 h | (Xu et al., 2020) |
| $CsPbBr_3$ NCs | ITO/PVK:F4–TCNQ/EL/TPBi/LiF/Al. | spin coating | 516 | NA | 16.8 | 62 | 7348 | NA | $T_{50}$ = 208 h | (Han et al., 2021a) |
| $CsPbBr_3$ NCs | ITO/PEDOT:PSS/PTAA/EL/TPBi/PO-T2T/LiF/Al | spin coating | 520 | 2.0 | 21.63 | 81.4 | 41,900 | 0.17, 0.74 | $T_{50}$ = 180.1 h | (Fang et al., 2021b) |
| $FA_{1-x}GA_xPbBr_3$ NCs | ITO/Buf-HIL/EL/TPBI/LiF/Al | spin coating | 531 | 2.7 | 23.4 | 108 | 25,000 | NA | $T_{50}$ = 132 h | (Kim et al., 2021b) |
| $MAPbBr_3$ NC-in-MOF | ITO/PEDOT:PSS/PFI/EL/TPBi/LiF/Al | spin coating | ~521 | 4.2 | 15.4 | NA | 120,000 | NA | $T_{50}$ = 2400 min | (Tsai et al., 2021) |
| $CsPbBr_3$ NCs/ PbBr(OH)/MS | EL + InGaN Mini-LED | inkjet printing | 525 | NA | 36.50% | NA | $3.3 \times 10^8$ | 0.318,0.341 | $T_{50}$ = 600 min | (Xuan et al., 2022) |
| $CsPbBr_3$ NCs | ITO/PEDOT:PSS/PTAA/LiF/EL/B3PymPm/LiF/Al | spin coating | 521 | 2.4 | 17.85 | 61.1 | 98 | 0.115,0.803 | $T_{50}$ = 175 min | (Yang et al., 2021) |
| $CsPbBr_3$ NCs | ITO/PEDOT:PSS/PTAA/EL/TPBi/LiF/Al | inkjet printing | 517 | 3.4 | 8.54 | 31.45 | 43,833.39 | 0.09,0.74 | $T_{50}$ = 63.84 min | (Wei et al., 2022) |
| $CsPbI_3$ NCs | ITO/PEDOT:PSS/PTAA/EL/TPBi/LiF/Al | inkjet printing | 688 | 4.2 | 5.54 | 0.46 | 455.20 | 0.73,0.27 | $T_{50}$ = 33.89 min | (Wei et al., 2022) |
| $CsPb(Br_xCl_{1-x})_3$ NCs | ITO/PEDOT:PSS/PTAA/EL/TPBi/LiF/Al | inkjet printing | 488 | 3.6 | 0.81 | 1.05 | 151.32 | 0.07,0.28 | $T_{50}$ = 1.97 min | (Wei et al., 2022) |
| $CsPb(Br_xCl_{1-x})_3$ NCs | ITO/NiOx/PVK:PVP/EL/TPBi/LiF/Al | spin coating | 477 | 2.6 | 11.0 | NA | 2180 | 0.107, 0.115 | $T_{50}$ = 1–2 min | (Karlsson et al., 2021) |
| $CsPb(Br_xCl_{1-x})_3$ NCs | ITO/NiOx/PVK:PVP/EL/TPBi/LiF/Al | spin coating | 467 | 2.9 | 5.5 | NA | 330 | 0.130, 0.059 | $T_{50}$ = 1–2 min | (Karlsson et al., 2021) |
| $CsPb(Br_xCl_{1-x})_3$ NCs | ITO/TFB/PFI/EL/3TPYMB/Liq/Al | spin coating | 471 | 4.5 | 6.3 | NA | 0.0465 | NA | $T_{50}$ = 99 s | (Zheng et al., 2020) |
| $Cs_xFA_{1-x}PbBr_3$ NCs | ITO/NiO/TFB/EL/TPBi/LiF/Al | spin coating | 483 | 3.3 | 9.5 | 12 | 700 | 0.094,0.184 | $T_{50}$ = 250 s | (Liu et al., 2019c) |

(*Continued on next page*)

**Table 2. *Continued***

| Emitter layer (EL) | Device configuration | fabrication method | EL peak (nm) | $V_{on}$ (V) | $EQE_{max}$ (%) | CE (cd $A^{-1}$) | $L_{max}$ (cd $m^{-2}$) | CIE (x, y) | Operation stability | Ref. |
|---|---|---|---|---|---|---|---|---|---|---|
| $CsPbBr_3$ NCs | ITO/PEDOT:PSS/PVK/EL/ZnO/Ag | spin coating | 470 | 3.7 | 4.7 | NA | 3850 | 0.13,0.11 | $T_{50}$ = 12 h | (Bi et al., 2021) |
| $CsPbBr_3$ NCs | ITO/PEDOT:PSS/PTAA/EL/TPBi/Al | spin coating | 479 | 2.8 | 12.3 | NA | 500 | NA | $T_{50}$ = 20 min | (Dong et al., 2020) |
| $CsPbBr_3$ NC-in-matrix solid | ITO/PEDOT:PSS:PFI (PEPFI)/EL/TPBi/LiF/Al | spin coating | 495 | NA | 13.8 | NA | 6113 | 0.11,0.37 | $T_{50}$ = 140 min | (Liu et al., 2022) |
| $CsPb(I_xBr_{1-x})_3$ NCs | ITO/PEDOT:PSS/Poly-TPD/EL/ETL/LiF/Al | spin coating | 642 | 2.6 | 24.4 | NA | 290 | NA | $T_{50}$ = 20 h | (Wang et al., 2022) |

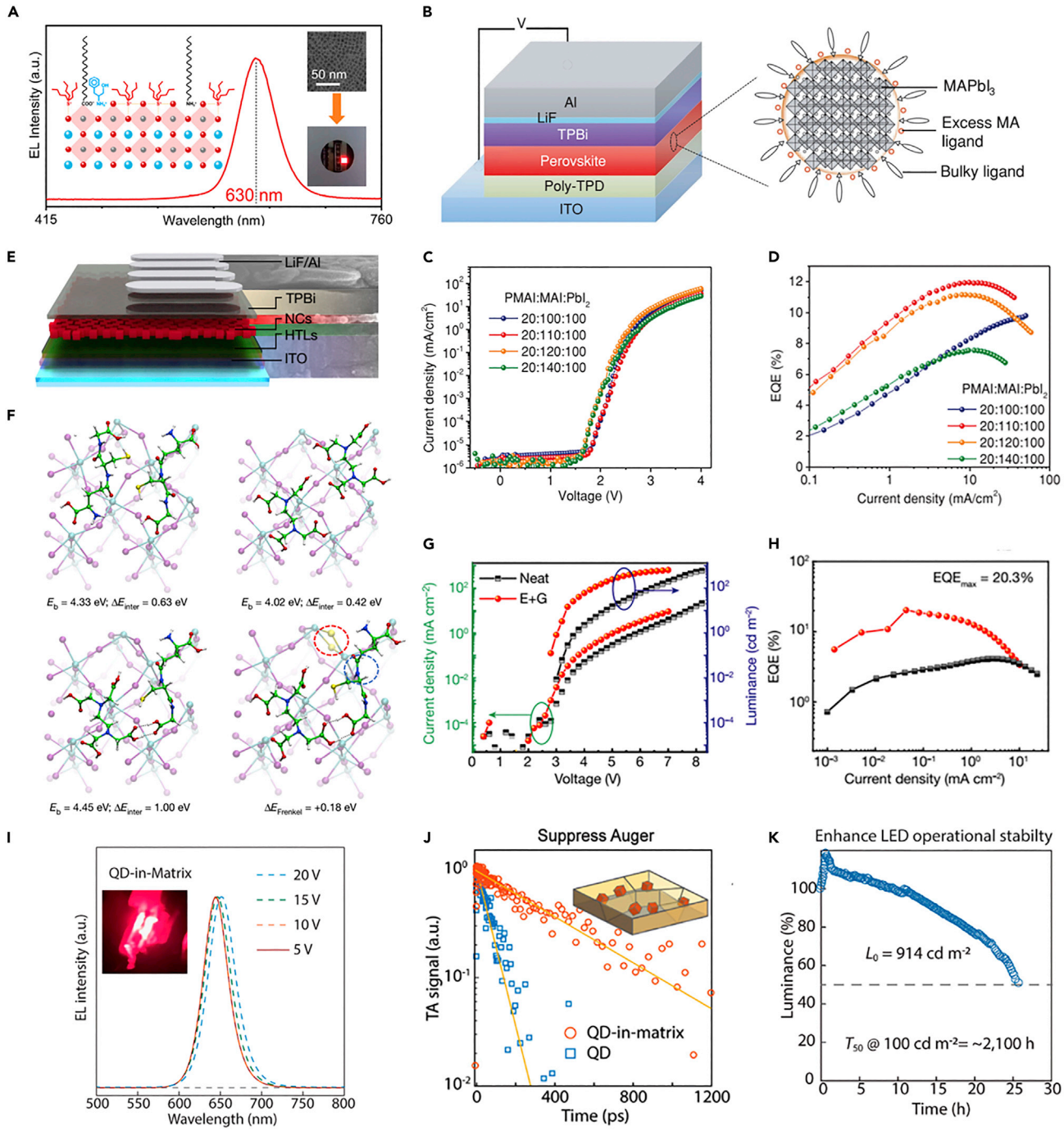


**Figure 14. Red LEDs based on perovskite NCs**

(A) Normalized EL spectra of LEDs based on H + T-treated $CsPbI_3$ NCs. Reprinted from (Lan et al., 2021). Copyright © 2021, American Chemical Society.

(B) Schematic of LEDs based on $MAPbI_3$ NCs terminated with bulky ligands.

(C) Current density versus voltage (J-V) and (D) EQE versus current density of LEDs with different MAI:$PbI_2$ molar ratios and constant PMAI loading. Figures B–D reprinted from (Xiao et al., 2019). Copyright © 2019, Wiley.

(E) Schematic of the LED architecture based on $MAPb(I_{1-x}Br_x)_3$ NCs and an SEM image showing the cross-section of a device.

(F) Optimized structures of interacting surface-adsorbed ligands. Reprinted from.

(G) J-V and luminance-voltage (L-V) curves, and (H) EQE-current density curves for LEDs incorporating neat and E + G-treated NC layers. Figures E–H reprinted from (Hassan et al., 2021). Copyright © 2021, Springer Nature.

**Figure 14. *Continued***

(I) EL spectrum of a representative $CsPbI_3$-NC-in-perovskite matrix LED at different driving voltages.

(J) Transient absorption kinetics of NC-only sample and NC-in-matrix sample.

(K) Relative luminance versus operation time at ambient condition, measured with a constant drive current and an initial luminance of 914 cd $m^{-2}$ (NC-in-matrix LED). Figures I–K reprinted from (Liu et al., 2021c). Copyright © 2021, American Chemical Society.

NCs (~4 nm, ~1.9 eV bandgap) remained stable in a thin layer of perovskite precursor solution and acted as nucleation centers to drive the homogeneous crystallization of the mixed-halide perovskite matrix (~40% Br, 5-8 nm thickness, ~2.2 eV bandgap). The NCs-in-perovskite solid demonstrated suppressed Auger biexcition recombination and bright luminescence at high excitation (600 W $cm^{-2}$) (Figure 14J). A high EQE of 18% was obtained from the LEDs which retained high performance to brightness exceeding 4700 cd $m^{-2}$. Moreover, the LEDs show an operating half-lifetime $T_{50}$ of 2400 h at an initial luminance of 100 cd $m^{-2}$ (Figure 14K), representing a 100-fold enhancement relative to the best primary red perovskite LEDs.

### *Green light-emitting devices*

Green-emitting $CsPbBr_3$ perovskite NCs are more phase stable at ambient conditions than $CsPbI_3$ NCs. Li et al. reported the progress of green LEDs by tuning the surface ligand density of $CsPbBr_3$ NCs that were originally capped by OA and OAm (Figures 15A and 15C) (Li et al., 2017a). Surface passivation and carrier injection that was in close relation to the ligand density could be balanced via controlling the number of purification cycles. A 50-fold EQE improvement (up to 6.27%) was finally achieved for green LEDs based on $CsPbBr_3$ NCs by modifying the solution process and device structure (Figures 15B and 15D). The EQE was further improved to 11.6% by surface engineering using a combination of short ligands of tetraoctylammonium bromide (TOAB), didodecyldimethylammonium bromide (DDAB), and octanoic acid (OTAc) (Song et al., 2018). Such triple-ligand strategy synergistically boosted ink stability, recombination dynamics, charge injection, and thereby the device performance. In the following, they proposed the bilateral passivation of both top and bottom interfaces of perovskite-NC film with organic molecules (Xu et al., 2020). The passivated device with TSPO1 achieves a maximum EQE of 18.7% and current efficiency of 75 cd $A^{-1}$. Particularly, the operational lifetime of $CsPbBr_3$-NC LEDs is enhanced 20-fold, achieving a half-lifetime $T_{50}$ of 15.8 h. Subsequently, the operational stability was further enhanced by a methylene-bis-acrylamide cross-linking strategy, demonstrating a $T_{50}$ lifetime over 200 h under continuous operation with an initial luminance of 100 cd $m^{-2}$ (Han et al., 2021a).

By modifying the device structure Song et al. demonstrated green perovskite-NC LEDs with simultaneously improved efficiency and operational lifetime (Fang et al., 2021b). The key to boost the device performance is using a bilayered electron transport structure to balance the charge injection. The champion device exhibited a color-saturated green emission with an FWHM of 18 nm and a peak at 520 nm, a low turn-on voltage of 2.0 V, a remarkable EQE of 21.63%, and operational lifetime of 1.15 h at an initial luminance of 4064 cd/$m^2$. The findings in this work highlight the importance of charge balance for constructing high-performance perovskite-NC-based LEDs.

Kim et al. reported doping of guanidinium ($Ga^+$) into $FAPbBr_3$ NCs to suppress defects for high-efficiency LEDs (Kim et al., 2021b). The $Ga^+$ drives a tendency to increase the surface-to-bulk ratio, leading to an increased charge carrier confinement without inducing added defects on the NC surfaces (Figure 15E). At low concentration (<0.6) the $Ga^+$ segregates to the NC surface and stabilizes the undercoordinated sites, resulting in a high PLQY (~90%) (Figure 15F). At high concentration (>0.6), the perovskite phase was destabilized with reduced crystallinity. Therefore, the PLQY quickly drops. To further reduce nonradiative recombination a surface-stabilizing 1,3,5-tris(bromomethyl)-2,4,6-triethylbenzene (TBDB) was applied as a bromide vacancy healing agent. LEDs based on $FA_{0.9}GA_{0.1}PbBr_3$ NCs and TBTB interlayers have a current efficiency of 108 cd $A^{-1}$ and an EQE of 23.4% (Figures 15G and 15H), which rises to 205 cd $A^{-1}$ and 45.5% when a light outcoupling hemispherical lens was applied onto the emitting glass substrate.

Perovskite NCs passivated by an inorganic shell could also be used to boost the device performance. Nie et al. demonstrated that perovskite NCs embedded in MOF thin films can make bright and stable LEDs (Tsai et al., 2021). Green LEDs constructed from the perovskite-MOF NCs demonstrated a maximum EQE of over 15% and a high brightness of over $10^5$ cd $m^{-2}$. Protected by the MOF matrix, both PL and EL could be maintained under continuous UV irradiation, heat, and electrical stress. The LED devices

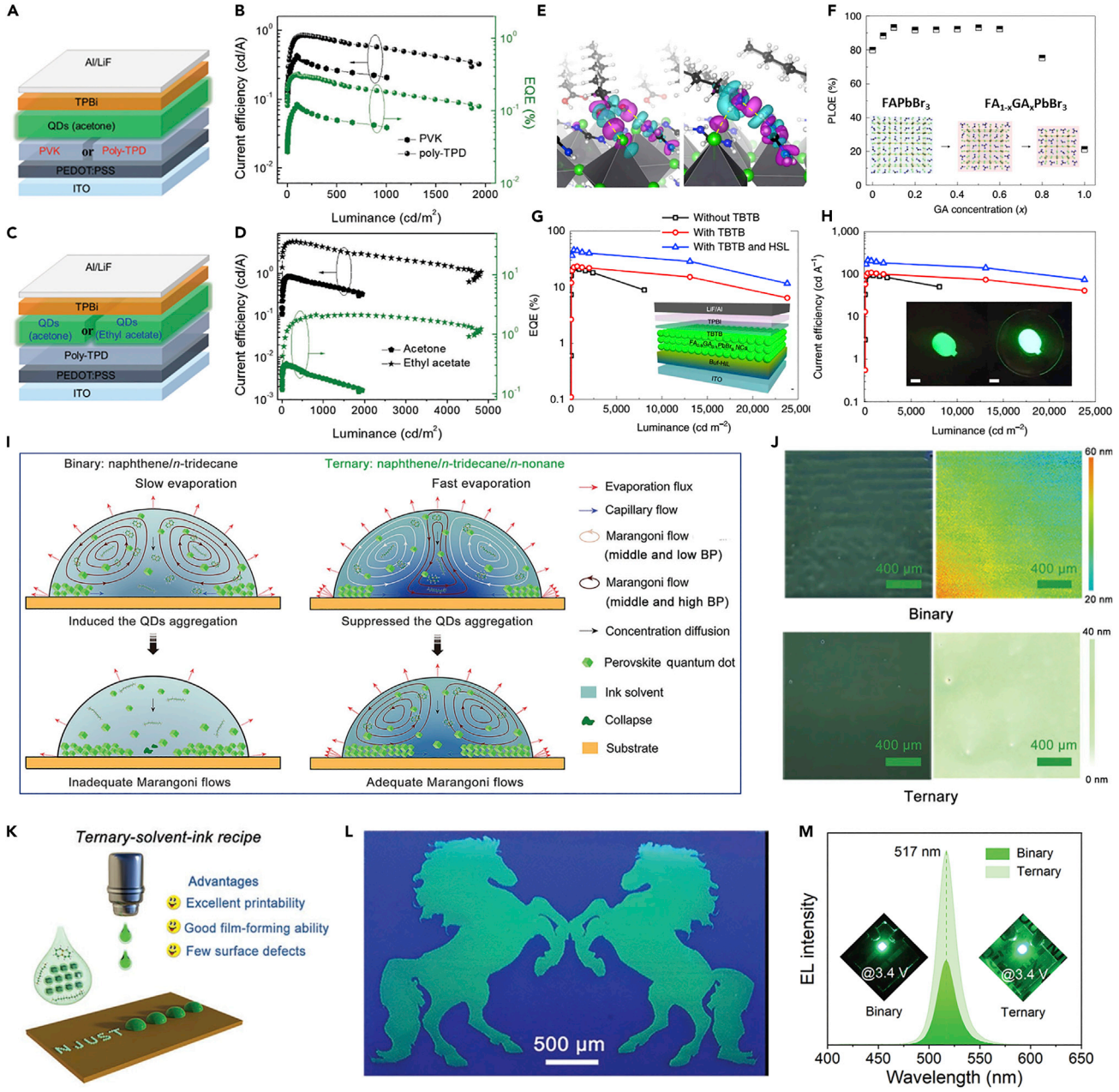


**Figure 15. Green LEDs based on perovskite NCs**

(A) Schematic illustration of the device for structure optimization and (B) corresponding comparison of current efficiency and EQE.

(C) Schematic illustration of device for purifying solvent optimization and (D) corresponding comparison of current efficiency and EQE. The NCs were all rinsed for one cycle with acetone or ethyl acetate. Figures A–D reprinted from (Li et al., 2017a). Copyright © 2017, Wiley.

(E) Three-dimensional charge density difference plots, showing the point chemical interactions between the perovskite surface and acid (left) or amine (right) ligands.

(F) PLQY and schematic crystal structures (inset) of $FA_{1-x}GA_xPbBr_3$ NCs.

(G) EQE and (H) current efficiency of LEDs with or without a TBTB interlayer and a hemispherical lens. Figures E–H reprinted from (Kim et al., 2021b). Copyright © 2021, Springer Nature.

(I) Schematic illustrations of solvent flow, solvent evaporation processes, and self-assembled NC thin film formation with binary and ternary perovskite NC ink system.

(J) Images of optical microscopy and 3D confocal microscopy of the inkjet-printed NC thin films.

(K) Schematic description of the advantages in ternary-solvent-ink recipe.

(L) The fluorescence optical microscopy image of double horses (lighting area, 44 × 28 $mm^2$).

(M) EL spectra of inkjet-printed LEDs recorded under an operating voltage of 3.4 V. Figures I–M reprinted from (Wei et al., 2022). Copyright © 2022, Wiley.

can work stably for over 50 h. Xuan et al. reported the use of green luminescent perovskite-NC composites with the structure of $CsPbBr_3$:Sr/PbBr(OH)/molecular sieve for stable mini-LED displays (Xuan et al., 2022). The excellent encapsulation by PbBr(OH) and molecular sieves together with the Sr doping leads to highly efficient and reliable Mini-LED backlights with a high luminous efficacy of 86 lm/W and a color area of ~93% of the Rec. 2020 standards by combining with a blue Mini-LED chip.

In order to improve the color purity of green LEDs, Yang et al. chose $CsPbBr_3$ NCs with a size far exceeding the Bohr exciton diameter. A hybrid ligand passivation strategy using calcium tributylphosphine oxide was proposed to produce highly dispersed large-size (18 nm) colloidal $CsPbBr_3$ NCs with a very weak size confinement effect and high PLQY (~85%) (Yang et al., 2021). The LEDs based on large-size $CsPbBr_3$ NCs demonstrated efficient green EL (EQE of 17.9%) with the highest color purity (FWHM of 16.4 nm) and rapid brightness rise around the turn-on voltage. The device operation half-life time was also improved to be 5-fold that based on small-size (9 nm) $CsPbBr_3$ NCs, providing a new avenue for improving the performance of LEDs based on unconventional large-size effects.

In order to meet the demand for low-cost and large-scale manufacturing, the development of high-quality and stable perovskite-NC inks for inkjet printing is a key step to push perovskite LED technology toward practical applications. For this purpose, Wei et al. proposed a novel ternary-solvent-ink strategy (naphthene, n-tridecane, and n-nonane) for strongly emissive and stable inks of perovskite NCs (Figures 15I–15K) (Wei et al., 2022). Compared with the binary-solvent (naphthene and n-tridecane) inks, the ternary-solvent system produces excellent printability and film-forming ability (Figure 15J). The inkjet-printed green $CsPbBr_3$-NC LEDs exhibited a peak EQE of 8.54% and maximum luminance of 43883.39 cd $m^{-2}$ (Figures 15L and 15M). This strategy can also be applied to inkjet-printed red and blue LEDs based on perovskite NCs with high efficiency.

### *Blue light-emitting devices*

Bright and efficient blue emission plays a key role in the development of halide perovskite LEDs. Blue emission could be achieved via component engineering for bandgap tuning, *i.e.*, using mixed halide perovskites. Gao et al. reported blue perovskite LEDs over a wide range of EL wavelengths from 490 to 451 nm, tuned by modifying the halide composition (Karlsson et al., 2021). However, the blue-emitting perovskites using mixed halide ions usually suffer from severe ion migration and phase segregation under external excitation of light or bias voltage. This problem is more serious in mix-halide perovskite NCs although they provide high EL efficiency in the red region by careful design of the NC surface (Vashishtha and Halpert, 2017; Zheng et al., 2020). By contrast, quantum-confined perovskite NCs with a single halide composition could provide efficient blue LEDs with spectrally stable light emission.

For a long time, the EQE of blue perovskite-NC LEDs lies below 2%. Until 2019 Jin et al. demonstrated blue perovskite-NC LEDs emitting at 483 nm with color coordinates of (0.094, 0.184) and operating with a peak EQE of up to 9.5% at a luminance of 54 cd $m^{-2}$ (Figures 16A–16E) (Liu et al., 2019c). The efficient blue EL originated from a unique core/shell structure of strong quantum-confined $CsPbBr_3$ NCs embedded within a quasi-two-dimensional perovskite shell with a relatively larger bandgap, which was prepared by an anti-solvent process. To improve the brightness, Tian et al. devised a novel acid etching-driven ligand-exchange strategy to synthesize pure-blue emitting small-sized (~4 nm) $CsPbBr_3$ perovskite NCs (Bi et al., 2021). The $CsPbBr_3$-NC-based LEDs exhibited pure-blue EL at 470 nm with an EQE of 4.7%, a remarkable luminance of 3850 cd $m^{-2}$, and a half-lifetime $T_{50}$ exceeding 12 h under continuous operation, which is superior than reported pure-blue perovskite LEDs.

The advance in blue LEDs technology has been speeding up in the recent two years. Dong et al. developed a bipolar-shell-passivation strategy to provide increased NC coupling and improved charge transport (Dong et al., 2020). The bipolar shell consisted of an inner anion shell, and an outer shell comprised of cations and polar solvent molecules. The outer shell was electrostatically adsorbed to the negatively charged inner shell. This strategy produced strongly confined $CsPbBr_3$-NC solids featuring improved carrier mobility ($\geq$0.01 $cm^2$ $V^{-1}$ $s^{-1}$) and reduced trap density. Films casting from the optimally exchanged NCs maintained a high PLQY (>70% for 4 nm NCs) under low excitation density (<1 mW $cm^{-2}$) even after purification (Figure 16F). Both efficient blue and green LEDs could be obtained by using the NCs. In particular, green devices with reduced trap density have an EQE of 22% and the blue devices achieve an EQE of 12.3%. Very recently, they developed $CsPbBr_3$-NC-in-perovskite matrix solids that exhibit high luminescent

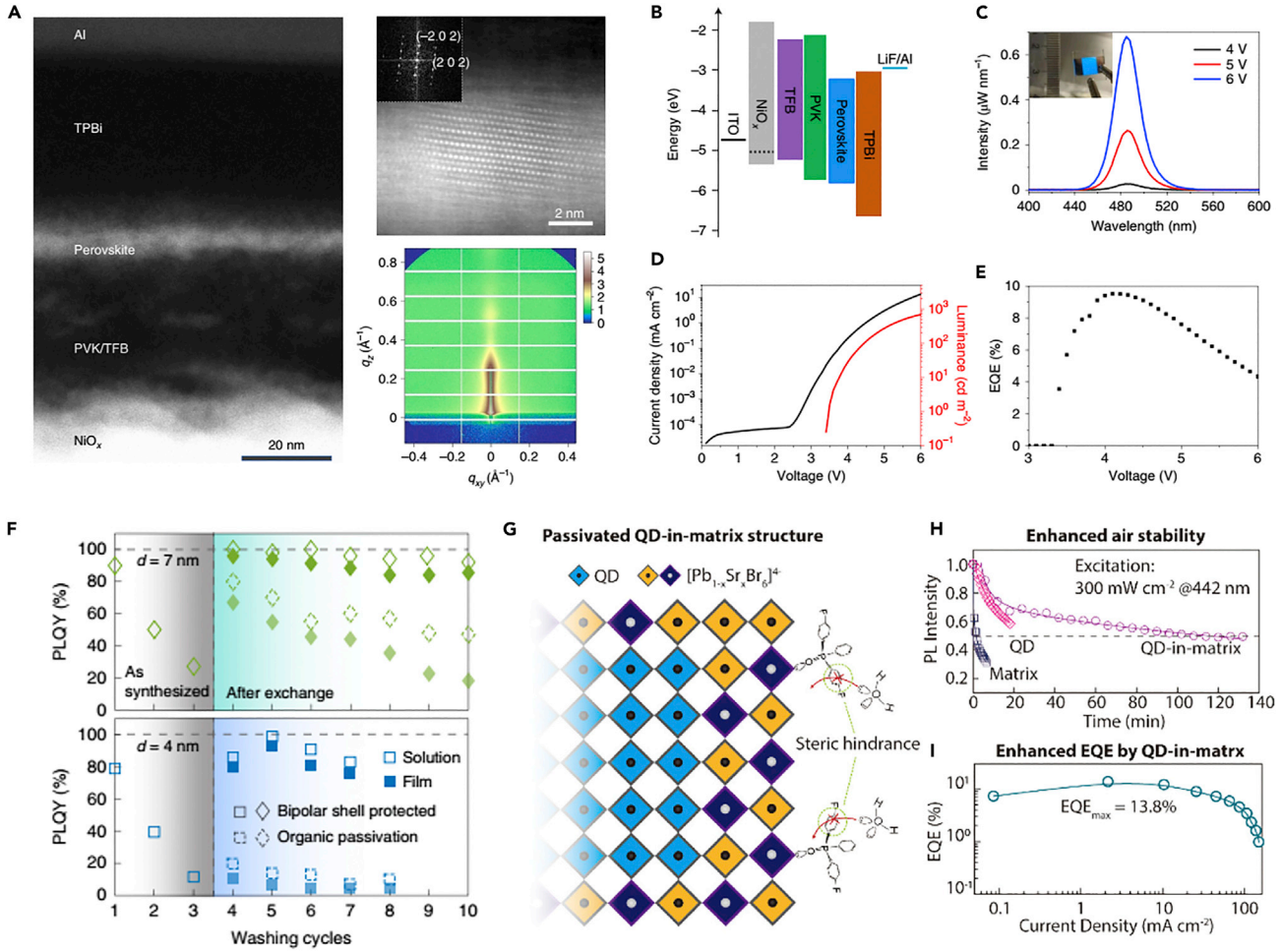


**Figure 16. Blue LEDs based on perovskite NCs**

(A) A cross-sectional STEM-HAADF image of LED devices based on quantum-confined bromide perovskite nanostructures. The zoomed-in STEM-HAADF image and GISAXS image show the crystal structure of a perovskite nanoparticle.

(B) Flat-band energy level diagram of the device.

(C) EL spectra under forward biases of 4, 5, and 6 V. Inset: a photograph of a blue LED (56 $mm^2$).

(D) Current density-luminance-voltage characteristics and (E) the corresponding EQE-voltage relationship of a device with a peak EQE of 9.5%. Figures A–E reprinted from (Liu et al., 2019c). Copyright © 2019, Springer Nature.

(F) PLQYs of NCs and NC films made from DDAB-treated perovskite NCs and bipolar-shell-stabilized NCs of two different diameters. The gray area represents washing iterations without the ligand exchange process and the green and blue areas represent iterations using bipolar exchanges or DDAB ligand exchanges, respectively. Reprinted from (Dong et al., 2020). Copyright © 2020, Springer Nature.

(G) Schematic of $Sr^{2+}$ cations passivated by DFPPO, which offers strong binding and steric hindrance to block $H_2O$.

(H) Time-resolved PL tracking under intense excitation and ambient condition for samples of matrix-only, $CsPbBr_3$ NC-only, and $CsPbBr_3$ NCs in a mixed Sr/Pb matrix.

(I) EQE as a function of current density for devices made from $CsPbBr_3$ NCs in a mixed Sr/Pb matrix. Reprinted from (Liu et al., 2022). Copyright © 2022, American Chemical Society.

efficiency and spectral stability with an optical bandgap of over 2.6 eV (Figure 16G) (Liu et al., 2022). Specifically, a $CsPb_{1-x}Sr_xBr_3$ perovskite matrix was employed in which alloying with $Sr^{2+}$ increased the bandgap of $CsPbBr_3$ and minimized lattice mismatch. Furthermore, the mixed Sr/Pb perovskite matrix was passivated by using bis(4-fluorophenyl)phenylphosphine oxide (DFPPO) molecules to overcome the hygroscopic nature of $Sr^{2+}$ cations. The resulting NC-in-matrix solids exhibit enhanced air- and photo-stability with efficient charge transport from the matrix to the NCs (Figure 16H). As a result, the fabricated blue LEDs exhibited an impressive EQE of 13.8% and a brightness exceeding 6000 cd $m^{-2}$, representing the highest efficiency and brightness for blue perovskite LEDs to date (Figure 16I).

Despite recent significant progress made on perovskite-NC LEDs, serious concerns should be addressed before their commercial applications. In particular, attention should be turned to the lifetime and stability issues of devices to meet the commercial demands when the EQEs are already high (Lee et al., 2022b; Liu et al., 2021b). Besides, more efforts should be spared to address lead toxicity, as what has been suggested for perovskite solar cells. The development of stable and high-performance optoelectronics based on lead-free perovskite NCs and their derivatives should also be encouraged.

Compared with red, green, and blue light emissions, white light emission from perovskite NCs appears to be more challenging due to the anion-exchange reaction when different NCs are mixed. Current progress for white LEDs based on perovskite NCs largely benefits from the codoping strategy, the use of a composite structure comprising of perovskite NCs and organic materials, or the anchoring of perovskite NCs on a YAG-based phosphor (Pan et al., 2018a; Shen et al., 2018; Wu et al., 2019). Although white perovskite-NC LEDs still require substantial improvements in terms of both efficiency and stability, investigations on novel structures and methodologies to construct efficient white LEDs are worth exploring given the vast market demand for advanced lighting and display technologies.

## Solar cells

### *Perovskite-nanocrystal solar cells*

In principle, the efficiency of solar cells based on halide perovskite NCs can hardly exceed that of their bulk counterparts. However, perovskite NCs offer tremendous potential to achieve excellent tuning of both structure and optical properties by means of quantum confinement, which is absent in bulk crystalline solar cells. In this light, perovskite NCs can offer new possibilities to resolve the challenges that impede the further development of thin-film perovskite solar cells.

Several groups contributed to boosting the efficiency of perovskite-NC solar cells (Table 3). In 2016 Swarnkar et al. for the first time reported perovskite-NC solar cells with a PCE over 10% by using cubic-phase $CsPbI_3$ NCs without volatile organic ligands (Figures 17A and 17B) (Swarnkar et al., 2016). These cubic-phase $CsPbI_3$ NCs are much more stable than the cubic phase of bulk $CsPbI_3$ in ambient air. Subsequently, they developed A-site cation halide salt (AX) treatments for surface chemistry tuning to improve the electronic coupling between $CsPbI_3$ NCs (Sanehira et al., 2017). The AX treatments doubled the film mobility, leading to increased photocurrent and a certified PCE of 13.43%. By using a variety of spectroscopic techniques they established a molecular-level understanding of the NC surface chemistry for the deposition of high-quality electronic coupled perovskite-NC films toward high photovoltaic performance (Wheeler et al., 2018). Combining the surface chemistry control with a predesigned charge separating heterostructure, *i.e.*, $CsPbI_3$ NCs/$Cs_xFA_{1-x}PbI_3$ NCs, a remarkable PCE of 15.52% was finally achieved (Zhao et al., 2019a). Further, Jia et al. introduced a "surface matrix curing" strategy to restore the surface matrix of $CsPbI_3$ NCs (Jia et al., 2021). With this strategy, the optoelectronic properties and stability of the NCs were significantly improved and the related solar cell yielded an improved PCE of 16.21% (stabilized power output efficiency of 15.45%). The charge carrier dynamics revealed that trap-assisted charge carrier recombination was significantly reduced after restoring the NC surface matrix, resulting in improved photovoltaic performance. Recently, the same group adopted 2-pentanol to mediate the ligand exchange of NCs due to its appropriate dielectric constant and acidity (Jia et al., 2022). The solvent of short ligands is tailored for the post-treatment of removing pristine insulating OAm ligands from the NC surface without introducing halogen vacancy defects. Consequently, the NCs solar cells delivered an efficiency of up to 16.53%.

Hao et al. developed a new OA ligand-assisted cation-exchange strategy that enabled the controllable synthesis of mixed cation $Cs_{1-x}FA_xPbI_3$ NCs with reduced defect density (Figure 17C) (Hao et al., 2020b). The champion device delivered a certified record PCE of 16.6% with negligible hysteresis (Figures 17D–17F). The nanoscale phase stabilization of $Cs_{1-x}FA_xPbI_3$ NCs resulted in enhanced photostability compared with their bulk counterparts. The device retains 94% of the original PCE under continuous 1-sun illumination for 600 h.

In addition, Li et al. constructed perovskite-NC solar cells by using a combinational absorbing layer based on stacked cubic $CsPbI_3$ and $FAPbI_3$ NCs (Figure 17G) (Li et al., 2019b). The bilayer structure produced a graded heterojunction for more efficient charge extraction, and an impressive PCE of 15.6% with improved ambient stability has been achieved. The device stability could be further improved by using a *p*-mercaptopyridine ligand post-treatment, showing decent efficiency after storage under ambient conditions for

**Table 3. Performance of solar cells based on perovskite NCs**

| Absorbing Layer (AL) | Device configuration | fabrication method | $J_{sc}$ (mA $cm^{-2}$) | $V_{oc}$ (V) | FF (%) | PCE (%) | area ($cm^2$) | Operation stability | Ref. |
|---|---|---|---|---|---|---|---|---|---|
| $CsPbI_3$ NCs | FTO/c-$TiO_2$/AL/spiro-OMeTAD/$MoO_x$/Al | spin casting | 13.47 | 1.23 | 65 | 10.77 | 0.10 | NA | (Swarnkar et al., 2016) |
| AX-coated $CsPbI_3$ NCs | FTO/c-$TiO_2$/AL/spiro-OMeTAD//$MoO_x$/Al | spin casting | 15.246 | 1.1626 | 76.63 | 13.43 | 0.058 | NA | (Sanehira et al., 2017) |
| $Cs_{0.25}FA_{0.75}PbI_3$ NCs | ITO/c-$TiO_2$/AL/spiro-OMeTAD/$MoO_x$/Al | spin coating | 18.91 | 1.2 | 76 | 17.39 | 0.059 | NA | (Zhao et al., 2019a) |
| $CsPbI_3$ NCs | ITO/$SnO_2$/AL/Spiro-OMeTAD/Ag | spin coating | 17.71 | 1.27 | 72 | 16.21 | 0.06 | ~83% of the initial PCE after 30 days | (Jia et al., 2021) |
| $CsPbI_3$ NCs | ITO/$SnO_2$/AL/Spiro-OMeTAD/Ag | spin coating | 17.80 | 1.27 | 73 | 16.53 | 0.04 | ~93% of the initial PCE after 960 h | (Jia et al., 2022) |
| $Cs_{0.5}FA_{0.5}PbI_3$ NCs | ITO//$SnO_2$/AL/spiro-OMeTAD/Au | spin coating | 18.3 | 1.17 | 78.3 | 16.6 | 0.058 | 94% of the initial PCE after 600 h | (Hao et al., 2020b) |
| CsPbI3/$FAPbI_3$ NCs | FTO/c-$TiO_2$/AL/$FAPbI_3$/PTAA/$MoO_3$/Ag | spin casting | 17.26 | 1.22 | 74 | 15.6 | 0.0725 | 84% of the initial PCE after 350 h | (Li et al., 2019b) |
| $CsPbI_3$ NCs | FTO/TiO2/AL/PTAA/MoO3/Ag | spin coating | 14.32 | 1.25 | 79 | 14.25 | NA | 75% of the initial PCE after 67 days | (Khan et al., 2020) |
| n-type $CsPbI_3$ NCs/ p-type$CsPbI_3$ NCs | FTO/c-$TiO_2$/AL/PTAA/$MoO_3$/Ag. | spin coating | 17.12 | 1.251 | 71.4 | 15.29 | 0.0725 | about 80% of the initial PCE after 90 h | (Zhang et al., 2022a) |
| $CsPbI_3$ NCs | Glass/ITO//$SnO_2$/PCBM/AL/PTB7/ $MoO_3$/Ag | spin coating | 15.2 | 1.26 | 78 | 15.1 | 0.072 | 70% of the initial PCE after 14 days | (Hu et al., 2021) |
| $CsPbI_3$ NCs | PET/ITO//$SnO_2$/PCBM/AL/PTB7/ $MoO_3$/Ag | spin coating | 13.6 | 1.24 | 73 | 12.3 | 0.072 | NA | (Hu et al., 2021) |
| $CsPbBr_3$ NCs | FTO/c-$TiO_2$/AL/spiro-OMeTAD/Au | spin coating | 5.512 | 1.505 | 62.8 | 5.20 | 0.0935 | NA | (Akkerman et al., 2016) |
| $CsPbBr_3$ NCs | FTO/c-$TiO_2$/AL/spiro-OMeTAD/Au | spin coating | 4.68 | 1.59 | 56.9 | 4.23 | 0.096 | over 90% of the initial PCE after 14 days | (Cho et al., 2020a) |
| $CsPbBr_3$ NCs | FTO/c-$TiO_2$/AL/PTAA/$MoO_3$/Ag | spin coating | 4.49 | 1.54 | 72.45 | 5.01 | 0.0725 | over 90% of the initial PCE after 100 days | (Zhang et al., 2020b) |
| $CsPbI_3$ NCs | FTO/c-$TiO_2$/AL/spiro-OMeTAD/Au | spray coating | 13 | 1.035 | 68.5 | 9.19 | 0.12 | 80% of the initial PCE after 30 days | (Yuan et al., 2019) |
| DPP:PC61BM:$FAPbI_3$ NCs | ITO/ZnO/$Ba(OH)_2$/AL/$MoO_x$/Ag | blade coating | 15.22 | 0.56 | 65.41 | 5.51 | 0.0104 | NA | (Soltani et al., 2018) |
| PTB7-Th:PC71BM:$CsPbI_3$ NCs | ITO/ZnO/AL/$MoO_3$/Ag | spin coating | 19.06 | 0.806 | 65.9 | 10.84 | 0.0016 | NA | (Guijarro et al., 2019) |
| PTB7-Th:FOIC:$CsPbI_3$ NCs | ITO/ZnO/AL/$MoO_3$/Ag | spin coating | 25 | 0.74 | 71.4 | 13.2 | 0.04 | 85.1% of the initial PCE after 3 h | (Wang et al., 2020b) |
| PM6:Y6:$CsPbI_3$ NCs | ITO/ZnO/AL/$MoO_3$/Ag | spin coating | 27.2 | 0.839 | 72.5 | 16.6 | 0.04 | NA | (Wang et al., 2020b) |
| PBDB-T:IT-M:$CsPbI_3$ NCs | ITO/PEDOT:PSS/AL/BFN-Br/Al | spin coating | 17.55 | 0.963 | 68.9 | 11.64 | NA | NA | (Li et al., 2020b) |
| PM6:Y6-BO:$CsPbBr_3$ NCs | ITO/ZnO/AL/$MoO_3$/Ag | spin coating | 27 | 0.83 | 74.7 | 16.9 | NA | 88% of the initial PCE after 35 days | (Miao et al., 2021) |

(*Continued on next page*)

**Table 3. *Continued***

| Absorbing Layer (AL) | Device configuration | fabrication method | $J_{sc}$ (mA $cm^{-2}$) | $V_{oc}$ (V) | FF (%) | PCE (%) | area ($cm^2$) | Operation stability | Ref. |
|---|---|---|---|---|---|---|---|---|---|
| PM6:Y6-BO:$CsPbI_3$ NCs | ITO/ZnO/AL/$MoO_3$/Ag | spin coating | 26.9 | 0.83 | 74 | 16.6 | NA | 79% of the initial PCE after 35 days | (Miao et al., 2021) |
| $MAPbBr_{3-x}I_x$ NCs | FTO/c-$TiO_2$/AL/spiro-OMeTAD/Au | spin coating | 18.62 | 0.913 | 70 | 12.03 | 0.122 | 83% of the initial PCE after 25 days | (Cha et al., 2016) |
| $CsPbBr_3$ NCs: $FA_{0.85}MA_{0.15}Pb(I_{0.85}Br_{0.15})_3$ | ITO/$SnO_2$/perovskite/$CsPbBr_3$/ spiro-OMeTAD/Au | spin coating | 23.19 | 1.11 | 76.93 | 19.45 | 0.102 | 87.60% of the initial PCE after 60 days | (Zai et al., 2017) |
| $CsPb(I_xBr_{1-x})_3$ NCs:$MAPbI_3$ | FTO/c-$TiO_2$/m-$TiO_2$/AL/P3HT/Au | blade coating/ spin coating | 2.79 | 8.842 | 71.4 | 17.6 | 18 | stable after 10,000 h | (Cheng et al., 2021) |
| $CsPb(I_xBr_{1-x})_3$ NCs:$MAPbI_3$ | FTO/c-$TiO_2$/m-$TiO_2$/AL/P3HT/Au | spin coating | 23.49 | 1.15 | 78.3 | 21.1 | 0.12 | stable after 500 h | (Cheng et al., 2021) |
| $MAPbI_3$:$CsPbBrCl_2$ NCs | ITO/PTAA/AL/C60/BCP/Cu | spin coating | 23.4 | 1.15 | 80 | 21.5 | NA | about 80% of the initial PCE after 500 h | (Zheng et al., 2019b) |
| $Cs_{0.05}(MA_{0.17}FA_{0.83})_{0.95}PbBr_3$ NCs:FAI/MABr/MACl/$PbI_2$ | FTO/$SnO_2$/AL/spiro-OMeTAD/Ag | spin coating | 23.82 | 1.10 | 80.8 | 21.10 | 0.09 | over 90% of the initial PCE after 550 h | (Xie et al., 2020) |
| $Cs_2AgBi_{0.1}In_{0.9}Cl_6$ NCs/$MAPbI_3$ | ITO/$SnO_2$/AL/spiro-OMeTAD/Ag | spin coating | 22.8 | 1.14 | 77 | 19.9 | 0.09 | 85% of the initial PCE after 30 days | (Zhang et al., 2022b) |

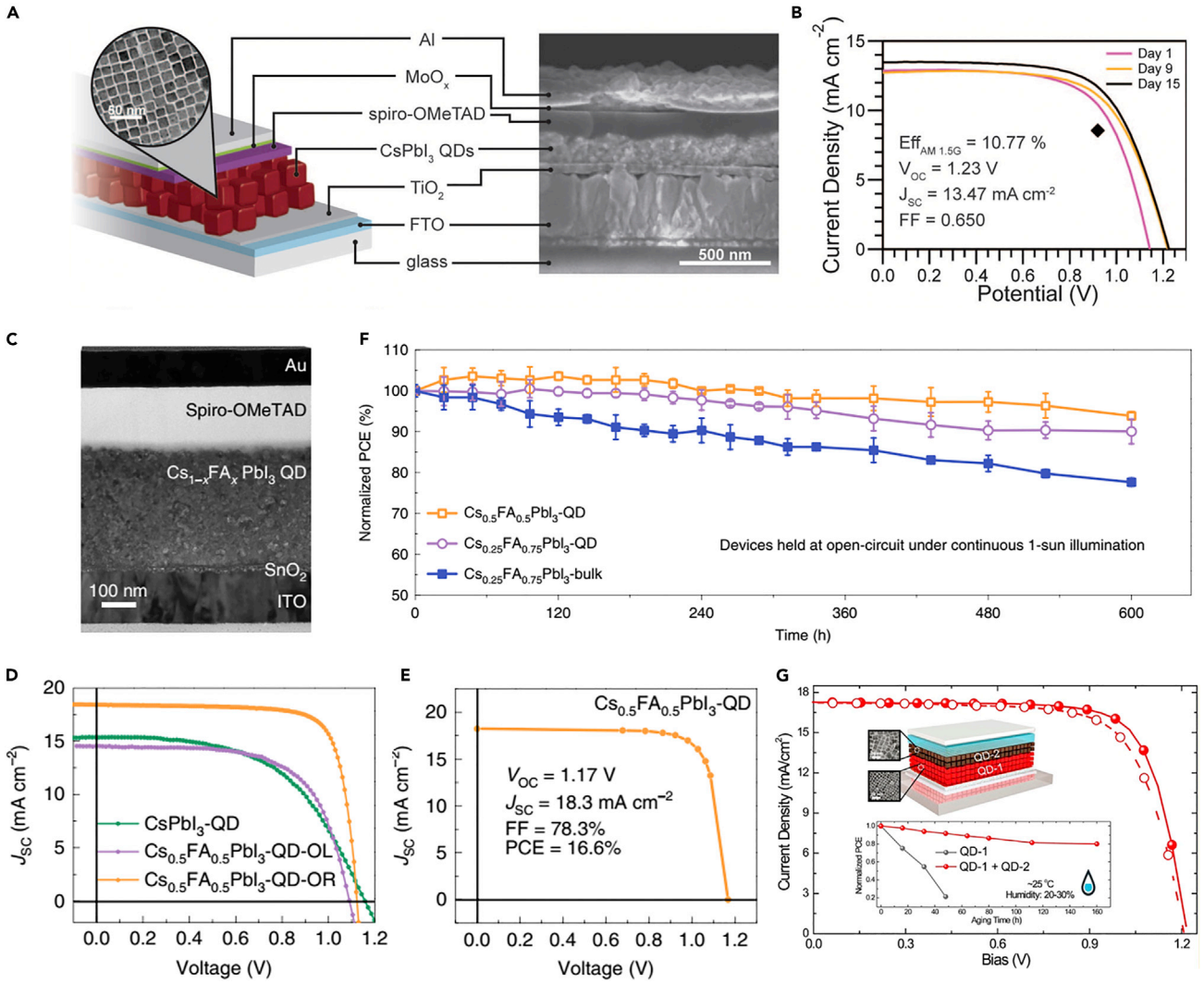


**Figure 17. High-efficiency solar cells based on perovskite NCs**

(A) Schematic (with TEM image of NCs) and SEM cross-section of the $CsPbI_3$-NC solar cell.

(B) Current density-voltage (J-V) curves of a device measured in air over the course of 15 days. The black diamond represents the stabilized power output of the device at 0.92 V. Figures A and B reprinted from (Swarnkar et al., 2016). Copyright © 2016, American Association for the Advancement of Science.

(C) Cross-section TEM image of the $Cs_{1-x}FA_xPbI_3$-NC solar cell.

(D) Typical current density-voltage curves of solar cells using different perovskite NCs.

(E) A certificated J-V curve.

(F) Long-term stability of unencapsulated solar cells fabricated with $Cs_{0.25}FA_{0.75}PbI_3$-bulk film, $Cs_{0.25}FA_{0.75}PbI_3$-NC film, and $Cs_{0.5}FA_{0.5}PbI_3$-NC film monitored at open circuit under 1-sun illumination in $N_2$ atmosphere (the device temperature was measured to be ~50-65°C). Figures C–F reprinted from (Hao et al., 2020b). Copyright © 2020, Springer Nature.

(G) J-V curves from reverse and forward scans of the perovskite-NC solar cells based on an α-$CsPbI_3$/$FAPbI_3$ bilayer structure (inset image), measured under AM 1.5G solar illumination. Inset figure shows the stability of corresponding perovskite NC solar cells under dark conditions in a $N_2$ atmosphere. Reprinted from (Li et al., 2019b). Copyright © 2019, American Chemical Society.

~70 days (Khan et al., 2020). In the previous section of remote doping, it has been shown that $CsPbI_3$ NCs that are originally *n*-type doped could be transformed to weak *p*-type by surface doping with F6TCNNQ. Using the *n*-type and weak *p*-type $CsPbI_3$ NCs, Zhang and his group succeeded in creating a *p*-*n* homojunction perovskite-NC solar cell (Zhang et al., 2022a). The *p*-*n* homojunction accelerated the separation, transport, and extraction of photoexcited carriers with minimum recombination loss. In particular, the $CsPbI_3$-NC solar cells with such *p*-*n* homojunction were highly thickness tolerant, maintaining a high efficiency of 12.3% for a 1.2 μm-thick NC layer.

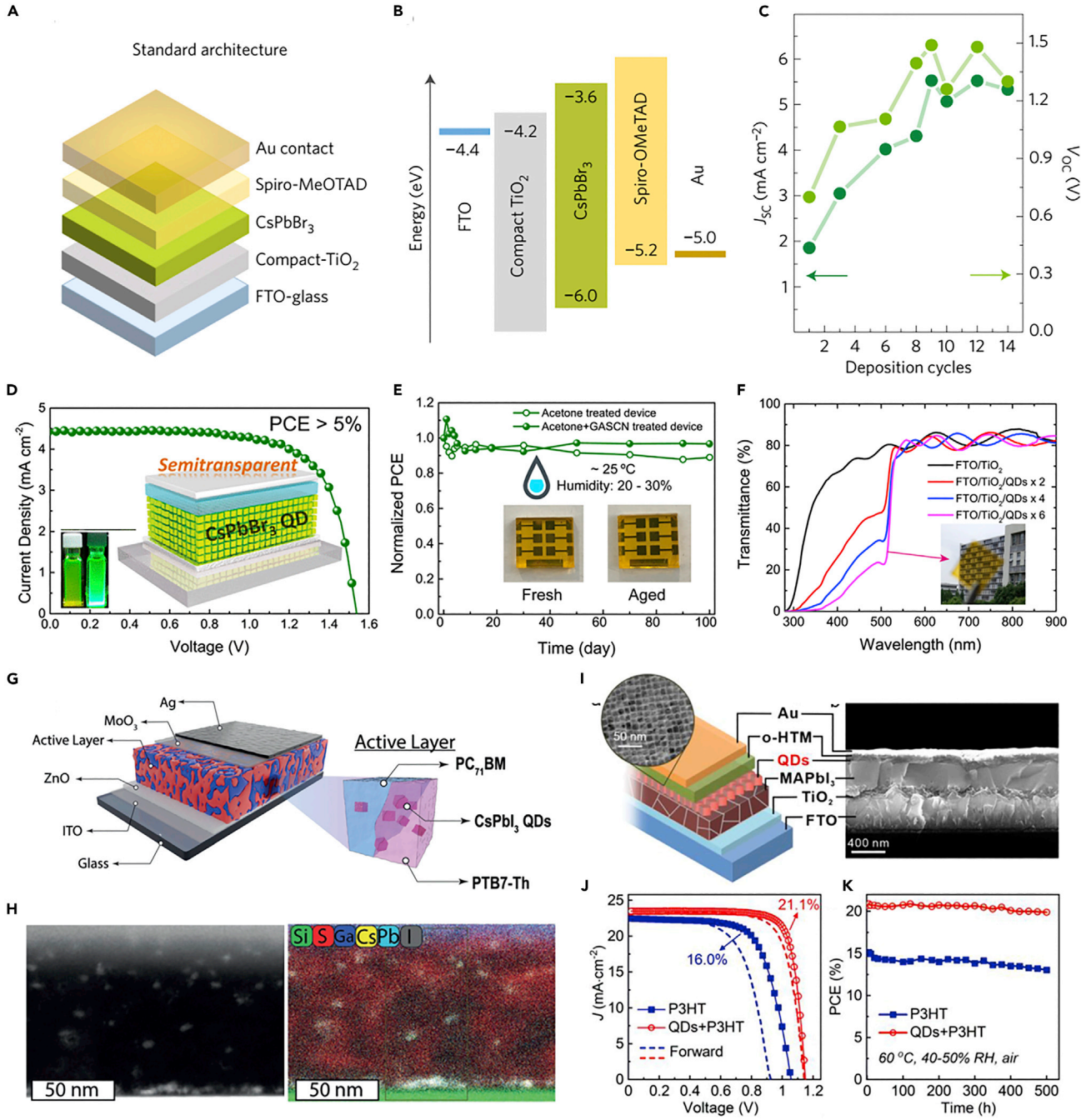


**Figure 18. High-voltage solar cells and bulk heterojunction solar cells based on perovskite NCs**

(A and B) Scheme of the architecture and energy-level diagram of $CsPbBr_3$-NC solar cell. Reprinted from.

(C) Evolution of the $J_{sc}$ and $V_{oc}$ for solar cells measured under AM 1.5G illumination, depending on the number of NC deposition cycles. Figures A–C reprinted from (Akkerman et al., 2016). Copyright © 2016, Springer Nature.

(D) J-V curve of a semitransparent solar cell based on $CsPbBr_3$ NCs with a high $V_{oc}$ approaching 1.6 eV.

(E) Long-term stability characterization of an optimal $CsPbBr_3$-NC solar cell compared with the acetone-treated device. Inset images show the photograph of the corresponding optimal device after storage in the air.

(F) Transmittance spectra of the $CsPbBr_3$-NC films with different thickness on a glass/FTO/$TiO_2$ substrate. The inset photograph shows the semitransparent NC film with six layers. Figures D–F reprinted from (Zhang et al., 2020b). Copyright © 2020, American Chemical Society.

(G) The device architecture includes the BHJ active layer showing $CsPbI_3$ NCs within the blend.

**Figure 18. *Continued***

(H) HAADF-STEM cross-sectional images and the corresponding EDX elemental mapping of the active layer with 20 wt % $CsPbI_3$ NCs loading. Figures G and H reprinted from (Guijarro et al., 2019). Copyright © 2019, Wiley.

(I) Schematic of perovskite solar cell structure using perovskite-NC interlayer, cross-section SEM image, and TEM image of $CsPbI_{1.85}Br_{1.15}$ NCs.

(J) Best PCE and (K) corresponding storage stability of undoped P3HT-based perovskite solar cells without or with NC interlayers. Figures I–K reprinted from (Cheng et al., 2021). Copyright © 2021, American Chemical Society.

Thin films cast from colloidal NCs possess higher mechanical endurance when compared with bulk thin film. Thus they can be readily integrated into a flexible device. Hu et al. demonstrated high-efficiency flexible solar cells based on $CsPbI_3$ NCs (Hu et al., 2021). By introducing phenyl-C61-butyric acid methyl ester into the $CsPbI_3$ NC layer, a thin hybrid interfacial architecture (HIA) was obtained. Using the ester, the undercoordinated $Pb^{2+}$ ions were bonded to the NC surface through functional carboxyl groups and an exciton cascade was formed between the $CsPbI_3$ NC layer and the electron transport layer (ETL) $SnO_2$. This enables efficient charge transfer and promotes exciton dissociation at the device interfaces, resulting in a champion PCE of 15.1%. Using the HIA strategy, they demonstrated flexible perovskite-NC solar cells with an impressive PCE of 12.3% and much improved mechanical flexibility compared to similar thin-film perovskite solar cells, signifying the potential of perovskite NCs on high performance and flexible optoelectronic devices.

High operation voltages have also been a critical criterion for perovskite solar cells. Akkerman et al. fabricated perovskite-NC solar cells by using $CsPbBr_3$ NCs with a larger bandgap (~2.4 eV) (Akkerman et al., 2016). The strongly emissive $CsPbBr_3$ NCs were synthesized in environmentally friendly solvents and surface terminated by short and low-boiling-point ligands (Figures 18A and 18B). The thin film casted from the high-quality NC inks exhibited PLQYs higher than 30% and an amplified spontaneous emission threshold as low as 1.5 $\mu J\ cm^{-2}$. Consequently, the solar cells processed in air delivered a PCE exceeding 5% with an extraordinary $V_{oc}$ higher than 1.5 V (Figure 18C).

However, $CsPbBr_3$ NCs that are surface-terminated with bulky organic ligands post-treatments should be performed before they are incorporated into a solar cell device. Via a solvent miscibility-induced ligand exchange method Kim et al. demonstrated the $V_{oc}$ of $CsPbBr_3$-NC solar cells could be further improved to above 1.6 V (Cho et al., 2020a). Recently, Zhang et al. reported using guanidinium thiocyanate (GASCN) to exchange the native capping ligands of $CsPbBr_3$ NCs (Zhang et al., 2020b). Both the morphology and carrier transport properties of NC films were clearly improved. Consequently, the $V_{oc}$, short-circuit current density ($J_{sc}$), and fill factor (FF) of solar cells were all boosted (Figures 18D–18F). With an optimal hole-transporting layer (HTL) a high efficiency exceeding 5% together with an ultra-high $V_{oc}$ of 1.65 V was obtained, representing the most efficient $CsPbBr_3$-NC solar cells to date.

### *Perovskite nanocrystals/organic hybrid solar cells*

Inorganic perovskite NCs/organic hybrid solar cells can be readily realized due to their capacities with a facile solution process. In 2018 Soltani et al. constructed bulk heterojunction hybrid solar cells based on blends of DPP:$PC_{61}$BM:$FAPbI_3$ perovskite NCs (Soltani et al., 2018). They found that the PCE of the hybrid solar cell comprising 5 wt % (weight ratio) $FAPbI_3$ NCs was nearly 10% enhanced compared to the organic reference, mainly due to the enlarged light harvesting and increased $J_{sc}$. However, increasing the content of perovskite NCs can induce bimolecular and trap-assisted recombination in the ternary devices. In the following, Guijarro's group reported hybrid organic solar cells containing $CsPbI_3$ NCs as a ternary component (Guijarro et al., 2019). They also demonstrated the incorporation of small amount (3 wt %) of $CsPbI_3$ NCs into the active layer of an inverted PTB7-Th:$PC_{71}$BM organic solar cell, increasing the PCE from 7.94% to 10.8%. The presence of $CsPbI_3$ NCs was evidenced in the HAADF-STEM cross-sectional images with the visualization of individual NCs about 7-8 nm in size within the blend, and further established with the corresponding EDX mapping (Figures 18G and 18H). Using a combination of intensity-modulated photovoltage spectroscopy and absorption spectra, it was revealed that the improved performance on one side originated from a promoted PTB7-Th:$PC_{71}$BM exciton dissociation mediated by the $CsPbI_3$ NCs. On another side, the $CsPbI_3$ NCs as a high dielectric-constant constituent suppressed exciton recombination by screening the coulomb interactions within the active layer.

Taking advantage of the intense absorption and high dielectric constant of $CsPbI_3$ NCs, Wang et al. reported the first example of efficient hybrid $CsPbI_3$ NCs/non-fullerene organic solar cells (Wang

et al., 2020b). The PCEs were boosted from 11.6% to 13.2% for PTB7-Th:FOIC blend and from 15.4% to 16.6% for PM6:Y6 blend due to simultaneously enhanced $V_{OC}$, $J_{SC}$, and FF. The increased $V_{OC}$ of the solar cell with perovskite NCs was attributed to the increased energy of the charge transfer state. The near-zero driving force in such a device configuration leads to efficient charge generation which is separated by the formation of a cascade band structure and an increased molecular ordering. Therefore, $J_{SC}$ was enhanced. The high dielectric constant of the $CsPbI_3$ NCs screens the Coulombic interactions and reduces charge recombination, which is beneficial for an increased FF. Lu and coworkers demonstrated that by heterovalent $Bi^{3+}$ doping of $CsPbI_3$ NCs the charge transfer properties between NCs and organic donor/acceptor interfaces could be finely tuned, inducing a higher $V_{oc}$ (Li et al., 2020b). In addition, they found that the incorporation of perovskite NCs with different sizes could effectively modify the nanoscale bulk heterojunction morphology toward more efficient charge collection and thus a higher FF. However, a clear drop in stability for unencapsulated devices was observed after the addition of $CsPbI_3$ NCs.

In a recent study, Miao et al. found the use of $CsPbBr_3$ NCs instead could enhance the device efficiency without scarifying the device stability (Miao et al., 2021). With the presence of 1 wt % $CsPbBr_3$ NCs doping, the highest PCE of the corresponding PM6:Y6-BO solar cell was improved from 16.4% to 17.1%, where the device stability was not affected due to the better phase stability of $CsPbBr_3$ NCs than $CsPbI_3$ NCs. The inclusion of $CsPbBr_3$ NCs shows no obvious impact on the molecular packing and phase separation of organic components, but enhances light absorption due to the Rayleigh scattering effect. This promotes exciton dissociation in the Y6-BO phase, and forms an efficient hole transfer pathway from Y6-BO to NCs and then to PM6 to improve hole transport. Together, they contribute to increased $J_{SC}$ and FF in the solar cell with a constant $V_{OC}$.

### *Perovskite nanocrystals/perovskite solar cells*

Halide perovskite NCs can also be used as interlayers between the active layers and carrier transporting layers to boost the performance of bulk perovskite solar cells. The inclusion of a perovskite-NC interlayer can be accomplished during the dropping of antisolvents containing perovskite NCs, or by directly spin-coating the NC colloids onto the perovskite active layer (Cha et al., 2016; Zai et al., 2017).

Cheng et al. systematically studied the role of perovskite-NC interlayers between perovskite bulk films and organic HTLs (Cheng et al., 2021). Specifically, the addition of a $CsPbI_xBr_{1-x}$-NC interlayer greatly enhances the performance of $MAPbI_3$ solar cells with dopant-free P3HT as the HTL (Figure 18I). The dopant-free P3HT-based devices with the NC interlayer show a negligible hysteresis of <5%. An improved PCE of 21.1% was obtained, with a $V_{OC}$ of 1.15 V, a $J_{SC}$ of 23.49 mA $cm^{-2}$, and an FF of 78.3%, ranking among the most efficient dopant-free-P3HT-based perovskite solar cells (Figures 18J and 18K). In addition, the stability of unencapsulated devices with NC interlayers in ambient air (60°C, 40-50% humidity) was also enhanced. Importantly, for the perovskite module with NC interlayer and dopant-free P3HT, a champion efficiency of 17.6% was achieved, compared to the 11.6% efficiency of the control. It is striking that the output at the maximum power point was stable for the encapsulated modules in ambient air (25°C, 65% humidity) for more than 10,000 h, superior to the one without an NC interlayer. After a careful examination of the mechanism, they found the NC interlayers played multifunctional roles. First, passivation of the perovskite surface with NC interlayers reduced the trap states. Second, the formation of cascade energy levels promoted hole extraction from perovskite to dopant-free HTLs. Third, the hole mobility of dopant-free HTLs was improved via regulating their polymer/molecule orientation.

Bakr et al. also reported a facile strategy for improving $MAPbI_3$ solar cells using a trace amount of ligand-capped $CsPbBrCl_2$ NCs (Zheng et al., 2019b). These doped $MAPbI_3$ devices showed reduced band-tail states, lower trap density, and longer carrier lifetime. These enhanced the $V_{OC}$ and consequently increased PCE to 21.5%. The device stability was also enhanced due to the self-assembly of ligands on the surface of $MAPbI_3$. By contrast, Xie et al. proposed a different ionic defect passivation strategy employing multi-cation hybrid halide perovskite NCs (Xie et al., 2020). Through prudent control over the composition of NCs, ionic defects at both the surface and grain boundaries of perovskite films can be effectively managed via a process termed ionic solid-state inter-diffusion. In particular, the NCs containing $Cs^+$ ($Cs_{0.05}(MA_{0.17}FA_{0.83})_{0.95}PbBr_3$) more seriously influence the effect of ionic defect passivation with significant enhancement to all photovoltaic characteristics. This enables PCE exceeding 21% with more than 90% of its initial PCE retained upon exposure to continuous illumination for more than 550 h.

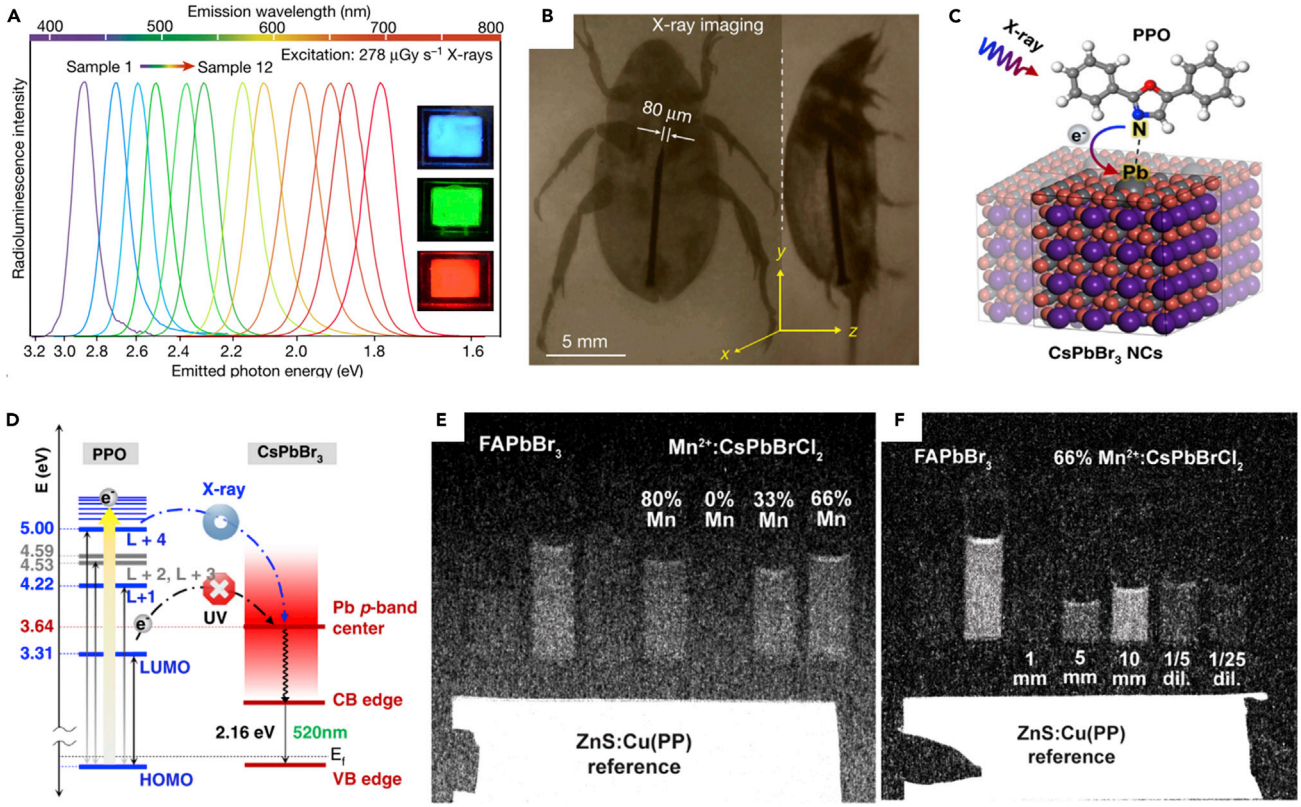


**Figure 19. Perovskite-NC scintillators and X-ray imaging**

(A) Tunable luminescence spectra of perovskite NCs under X-ray illumination.

(B) X-ray images of the sample, recorded with a digital camera. The X-ray images were recorded at a voltage of 50 kV. Figures A and B reprinted from (Chen et al., 2018b). Copyright © 2018, Springer Nature.

(C) Schematic diagram describing the hybridization of a $CsPbBr_3$ NC with PPO. The negatively charged N in the PPO binds to the positively charged Pb sites on the (001) surface of the $CsPbBr_3$ NC.

(D) DFT calculations of the energy level alignment for the proposed mechanism of enhanced RL in the hybrid $CsPbBr_3$ NCs/PPO scintillator. Under X-ray irradiation, a high-energy electron ($e^-$ in the solid circle) generated in the PPO moves to a neighboring p-type $CsPbBr_3$ NC, leading to green emission at 520 nm via an interband recombination. Figures C and D reprinted from (Cho et al., 2020b). Copyright © 2020, Springer Nature.

(E) Radiograph of $Mn^{2+}$:$CsPbBrCl_2$ NC scintillators under fast neutron irradiation as compared with reported $FAPbBr_3$ NCs and a commercial ZnS:Cu(PP) screen.

(F) Fast neutron radiograph of 66% $Mn^{2+}$:$CsPbBrCl_2$ thickness and concentration dependence. Figures E and F reprinted from (Montanarella et al., 2021). Copyright © 2021, American Chemical Society.

In a recent study, Zhang et al. reported the modification of $MAPbI_3$ perovskite solar cells by utilizing lead-free $Cs_2AgBi_{0.1}In_{0.9}Cl_6$ NCs as an interfacial layer to improve the stability of the devices (Zhang et al., 2022b). They demonstrated that the inclusion of the perovskite-NC interfacial layer could effectively suppress nonradiative recombination caused by interfacial defects without sacrificing the light absorption of the active layer. Consequently, a stable PCE of 19.9% in the $MAPbI_3$ devices was achieved, 11.2% higher than that of the control devices. This method can also be applied to $FAPbI_3$ solar cells, signifying a universe strategy for stable and efficient perovskite solar cells.

## Scintillators and X-Ray imaging

The growing demand for radiation detection materials in a variety of applications has led to extensive research on scintillators that are capable of converting small doses of high energy radiations (*e.g.*, X-ray) into multicolor visible light (Zhou et al., 2021b). For conventional semiconductor-based scintillators, however, the radioluminescence (RL) is rather difficult to be widely tuned across the visible spectrum.

In 2018, Liu et al. prepared all-inorganic $CsPbX_3$ perovskite-NC scintillators exhibiting both strong X-ray absorption and intense RL tuned across the whole visible spectrum (Figure 19A) (Chen et al., 2018b).

They further showed that these color-tunable perovskite-NC scintillators can provide a convenient visualization tool for X-ray radiography, as the associated image can be directly recorded by using standard digital cameras (Figure 19B). The researchers also demonstrated direct integration of these perovskite-NC scintillators with commercial flat-panel imagers equipped with α-Si photodiode arrays. The integrated functional device can be utilized for examining electronic circuit boards under low-dose X-ray radiation (15 μGy). Compared with commercial flat-panel X-ray detectors based on CsI:Tl, the X-ray detectors using perovskite NCs showed much higher spatial resolution due to the lower degree of light scattering, with a modulation transfer function of 0.72 at a spatial resolution of 2.0 line pairs per millimeter. In addition, a very fast response (44.6 ns) to X-ray was demonstrated, outperforming the commercial CsI:Tl scintillators. These merits made perovskite NCs excellent candidates for dynamic real-time X-ray imaging.

For most X-ray applications a thick and uniform solid film is necessary to enable high detecting functionalities. Hence, highly concentrated NC colloids are particularly desired when they are applied to solution-processed scintillator. Zhang et al. synthesized colloids of $CsPbBr_3$ NCs with concentration up to 150 mg/mL at room temperature (Zhang et al., 2019c). The $CsPbBr_3$ colloids can be readily casted into a uniform crack-free large-area film (8.5 × 8.5 $cm^2$ in area) with the requisite thickness for high-resolution X-ray imaging applications, showing a light yield (~21,000 photons/MeV) higher than that of the commercially available Ce:LuAG single-crystal scintillator (~18,000 photons/MeV). The synthesis method could be further extended for gram-scale production of high-quality $CsPbBr_3$ NCs with long-term stability that is suitable for industrial scintillator application (Wang et al., 2019c). After optimizing the film thickness for the X-ray imager, they achieved a high sensitivity down to 27 nGy/s, and an unprecedented spatial resolution of 26 μm which is one order of magnitude higher than reported perovskite scintillators (Wang et al., 2021b).

Perovskite NCs also hold considerable potential for flexible and printable X-ray detectors. Flexible and printable X-ray detectors with remarkable detecting functionalities have been developed by Bao et al. using high-quality colloidal $CsPbBr_3$ perovskite NCs (Liu et al., 2019a). A parallel structure comprising Au/$CsPbBr_3$ NCs/Au was adopted. Engineering the surface of $CsPbBr_3$ NCs using a mixture of ODE and IPA (volume ratio of ODE: IPA = 1:3) effectively reduced the density of defects. High sensitivities of up to 1450 μC $Gy_{air}^{-1}cm^{-2}$ were achieved under an X-ray dose rate of 0.0172 $mGy_{air}s^{-1}$ under a small applied bias voltage of 0.1 V. These parameters are about 70-fold more sensitive than those of conventional α-Se devices. Owing to the capacity of an ink-jet printing process, they succeeded in achieving the fabrication of arrays of multichannel detectors on the flexible PET substrates, demonstrating excellent mechanical flexibility that is suitable for advanced X-ray sensing and imaging.

Recently, Im et al. reported a new generation of highly efficient and low-cost liquid scintillators constructed by surface hybridization of colloidal $CsPbX_3$ NCs with organic molecules (2,5-diphenyloxazole, PPO) (Figure 19C) (Cho et al., 2020b). The hybrid liquid scintillators demonstrated markedly high RL QYs under X-ray irradiation typically employed in diagnosis and treatment. The enhanced QYs were found to be associated with the X-ray photon-induced charge transfer from the organic molecules to the NCs (Figure 19D). Finally, high-resolution X-ray imaging is demonstrated using a hybrid $CsPbBr_3$ NC-based liquid scintillator. The novel X-ray scintillation mechanism in the hybrid scintillators could be extended to enhance the QY of various types of scintillators, enabling low-dose radiation detection in many fields including fundamental science and imaging. Therefore, the hybrid liquid scintillators have the potential to compete with state-of-the-art CsI and $Gd_2O_2S$ scintillators.

In addition to X-ray imaging, the use of perovskite NCs for fast neutron imaging is also attracting increasing interest. The option of efficient fast neutron scintillators with high spatial resolution is critical for the imaging of thick and large-scale objects containing high-Z elements. Conventional phosphors such as microcrystalline ZnS:Cu suffer from intrinsic drawbacks including light scattering, γ-ray sensitivity, and afterglow, which could be greatly lessened in colloidal NCs. Kovalenko et al. demonstrated proof of concept scintillators by using colloidal $FAPbBr_3$ NCs as recoil proton detectors that are free of scattering or afterglow. Scintillators constructed from the $FAPbBr_3$ NCs with a near-unity PLQY demonstrated very high brightness. But the low Stokes shift led to bad spatial resolution. Subsequently, they reported a bright scintillator for fast neutron imaging that features simultaneously high QYs, high concentrations, and a large Stokes shift by using $CsPb(BrCl)_3$ NCs (Montanarella et al., 2021). The surface of $CsPb(BrCl)_3$ NCs was capped with long-chain zwitterionic ligands, allowing for attaining very high concentrations of NC colloids. In addition, the

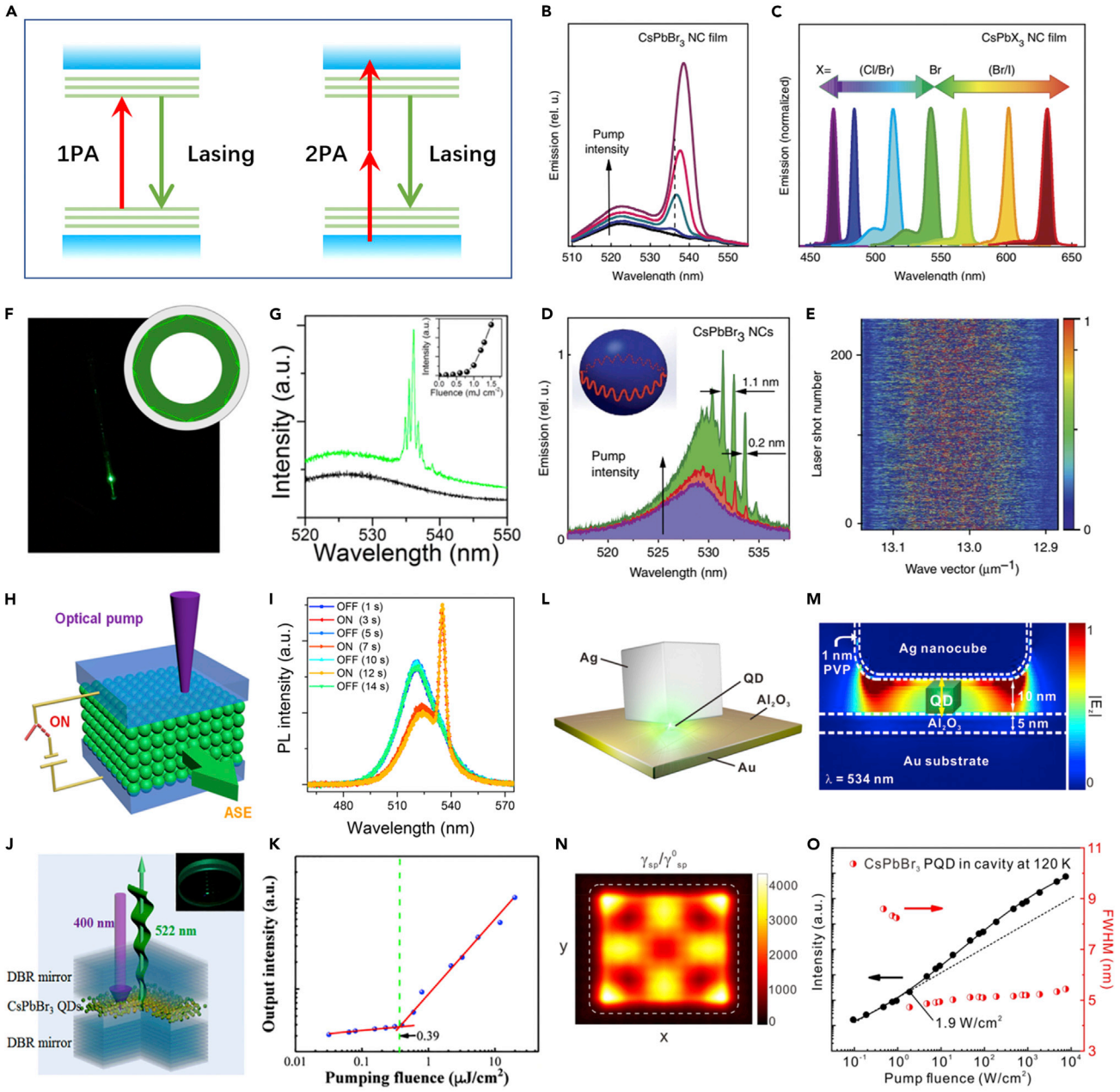


**Figure 20. Perovskite-NC lasers**

(A) Schematic of the mechanism of optical gain with one-photon and two-photon excitation. Adapted from (Xu et al., 2016). Copyright © 2016, American Chemical Society.

(B and C) ASE spectra from thin films of $CsPbX_3$ NCs.

(D) Evolution from PL to WGM lasing with increasing pump intensity in a microsphere resonator, covered by a $CsPbBr_3$-NC film.

(E) Stochastic mode distribution in a series of 256 pump laser shots. Figures B–E reprinted from (Yakunin et al., 2015). Copyright © 2015, American Chemical Society.

(F) Fluorescence image and (G) PL spectra of two-photon-pumped microring lasing from $CsPbBr_3$ NCs. Figures F and G reprinted from (Xu et al., 2016). Copyright © 2016, American Chemical Society.

(H) Electrical switching of optical gain in $CsPbBr_3$ NCs. The device consists of the NC film sandwiched by two ITO electrodes.

(I) Typical emission spectra recorded at different times for the ON and OFF states. Figures H and I reprinted from (Qin et al., 2021). Copyright © 2021, American Chemical Society.

(J) Schematic of the hybrid VCSEL consisting of a $CsPbBr_3$-NC thin film and two highly reflective DBRs.

**Figure 20. *Continued***

(K) The output intensity vs input pump fluence demonstrates lasing with a threshold of 0.39 μJ/cm$^2$. Figures J and K reprinted from (Huang et al., 2017a). Copyright © 2017, American Chemical Society.

(L) Plasmonic nanolaser based on a gap plasmon cavity.

(M) Calculated electric field distribution showing the cross-section of a film-coupled silver nanocube along with the simulated plasmonic gap mode at a wavelength of 534 nm.

(N) Simulated mapping of the spontaneous emission rate as a function of the dipole source position in the gap region.

(O) Light-in-light-out plots of the gap plasmonic nanolaser measured at 120 K showing a line width-narrowing behavior, with a lasing threshold of 1.9 W/cm$^2$. Figures L–O reprinted from (Hsieh et al., 2020). Copyright © 2020, American Chemical Society.

$Mn^{2+}$ doping gave rise to the $Mn^{2+}$-dominated emission band which is detrimental to minimal self-absorption. Because of a combination of advantages comprising high NC concentrations above 100 mg/mL, high QYs (>50%), and minimal self-absorption for good spatial resolution, the reported $Mn^{2+}$ doped $CsPb(BrCl)_3$ NCs were regarded to have the potential to replace the currently prevalent scintillator ZnS:Cu for fast neutron imaging (Figures 19E and 19F).

## Lasers

Inspired by the highly efficient PL of halide perovskite NCs, the utilization of perovskite NCs as an inexpensive optical gain medium has been intensively investigated. Due to the large absorption cross-sections of halide perovskite NCs, both one-photon and two-photon excitation could lead to optical gain and pumping (Figure 20A). An amplified spontaneous emission (ASE) and lasing from halide perovskite NCs with a low threshold was firstly demonstrated under one-photon pumping.

For thin films of $CsPbX_3$ NCs (9-10 nm) capped with OA and OAm as surface ligands, Yakunin et al. reported observation of ASE, tunable over the visible range (440-700 nm) with low thresholds down to 5 $\pm$ 1 μJ cm$^{-2}$ and high values of modal net gain above 450 cm$^{-1}$ (Figures 20B and 20C) (Yakunin et al., 2015). Such low-threshold pump fluencies have only been demonstrated for limited semiconductor nanostructures such as CdSe/CdS (Xing et al., 2012). Importantly, two different lasing regimes dependent on the resonator configuration have been realized, including the whispering-gallery-mode (WGM) lasing using single silica microsphere resonators coated with $CsPbX_3$ NCs, and the random lasing using $CsPbX_3$-NC films (Figures 20D and 20E). Later Yan et al. found that the ASE performance of $CsPbBr_3$ NCs could be improved when the surface ligands were replaced by the 2-hexyldecanoic acid (DA) with two short branched chains (Yan et al., 2019). The ASE threshold of $CsPbBr_3$-DA NC films was found to be reduced by more than 50% in comparison to films of $CsPbBr_3$-OA NCs.

A two-photon-pumped laser requires both efficient two-photon absorption and ease of achieving population inversion. A previous study on CdSe NCs indicated that efficient two-photon-pumped optical gain can only be achieved when the pumping power exceeds a relatively high threshold value (Xing et al., 2012). Xiao et al. demonstrated large optical gain (>500 cm$^{-1}$) and lasing under two-photon excitation in $CsPbBr_3$ NCs (Xu et al., 2016). The two-photon-pumped lasing arises from the highly efficient PL emission and large cross-section of two-photon absorption (~2.7 × 10$^6$ GM). By coupling the $CsPbBr_3$ NCs with microcapillary resonators, they successfully achieved WGM lasing under two-photon pumping at a remarkable low threshold of 0.8 mJ/cm$^2$, one-order of magnitude lower than that for CdSe NCs (Figures 20F and 20G). In a recent study, they. demonstrated a novel method for modulating the optical gain in perovskite NCs by electrical switching (Qin et al., 2021). It was shown that ASE in films of $CsPbBr_3$ NCs sandwiched by two ITO electrodes could be tuned by applying an external dc voltage of 20 V (Figures 20H and 20I). An over 50% threshold reduction was observed due to charged excitons induced by the external electric field.

The potential of perovskite NCs has also been exploited for practical laser devices. Sun and Zeng et al. realized for the first time high-performance vertical cavity surface emitting laser (VCSEL) by using solution-processed $CsPbX_3$ NCs (Wang et al., 2017c). A clear evolution from spontaneous emission to lasing in the device upon optical pumping was manifested by the spectral narrowing, nonlinear increase of the PL intensity, drastic reduction of PL lifetime, and remarkable decrease of output beam divergence. The laser device features a low threshold (9 μJ cm$^{-2}$), directional output (beam divergence of ≈3.6), and favorable stability. The lasing wavelength can be tuned across the visible spectrum maintaining low thresholds, which is promising in developing single-source-pumped full-color visible lasers. Lin et al. reported an ultralow lasing threshold (0.39 μJ/cm$^2$) from a hybrid VCSEL consisting of a $CsPbBr_3$ NC thin film and two highly reflective distributed Bragg reflectors (DBRs) (Figures 20J and 20K) (Huang et al., 2017a). In addition to the ultralow threshold, the

utilization of $CsPbBr_3$ NCs resulted in high device stability, and the laser maintained its performance over hours of operation under both fs and quasi-CW ns pulse pumping at ambient conditions. The ultralow threshold lasing performance demonstrates that $CsPbBr_3$ NCs integrated with a high-quality cavity provide a significant step forward toward the next-generation perovskite lasers. Itskos et al. demonstrated the monolithic fabrication of all-solution-processed microcavities based on perovskite NCs and polymer-based DBRs from spin-casted layers of cellulose acetate (CA) and polyvinylcarbazole (PVK) polymers (Athanasiou et al., 2021). In particular, $CsPbBr_3$ NCs capped with a dimethyldioctadecylammonium bromide (DDAB) ligand was used as the optical gain medium, which maintained a high PLQY of ~90% in the form of spin-casted films. The onset of ASE upon excitation with a continuous wave laser is evidenced by a clear threshold-type behavior and spectral narrowing on the excitation-variable PL.

In order to enhance the coupling between the optical gain medium and cavity Lu et al. demonstrated a continuous-wave nanolasing from a single perovskite NC by using a plasmonic gap-mode nanocavity (Hsieh et al., 2020). The localized gap plasmon nanocavity has an ultrasmall mode volume of ~0.002 $\lambda^3$, in which a silver nanocube is situated on a gold film, separated by a 15 nm bilayer spacer containing 5 nm $Al_2O_3$ and a single $CsPbBr_3$ NC with a mean size of 10 nm (Figure 20L). An intense localized electromagnetic field was formed between the gold film and the silver nanocube (Figure 20M). This greatly enhanced light-matter interactions in the nanocavity, facilitating lasing from the $CsPbBr_3$ NC with an ultralow threshold of 1.9 $Wcm^{-2}$ under 120 K (Figures 20N and 20O).

More recently, halide perovskite NCs have also been explored as a spin laser gain medium. Spin lasers emit circularly polarized photons that carry angular momentum information, offering new functionalities and reduced lasing thresholds in terms of the lifting of spin degeneracy. For the case of $CsPbBr_3$ NCs, it was found that the optical gain threshold could be depressed by polarizing the charge using circularly polarized photoexcitation. Nevertheless, the spin relaxation time was too short to realize a spin laser (Tang et al., 2022). If the spin relaxation time could be prolonged, the threshold reduction would be more remarkable under quasi-continuous wave photoexcitations.

### Thin-film transistors

Transistors are one of the most critical components of modern electronics. Constructing transistors based on thin films of perovskite NCs is rather challenging, mainly because of the limited conductivity and charge-carrier mobility. Chen et al. reported that the current in films of $CsPbBr_3$ NCs produced from hot-injection is ~6 nA at the voltage of ~60 V (Chen et al., 2018b). In another work reported by Lamberti et al., the current of $MAPbBr_3$ NCs produced from laser ablation is ~45 pA at the electric field of 2.5 V/μm (or the voltage of ~30 V) (Lamberti et al., 2017). These studies reveal the low charge transport properties in undoped perovskite NCs, which is possibly related to the surface bulky ligands and low carrier concentration.

Surface bulky ligands should be firstly replaced to improve the NC coupling and charge transport properties. Zhou et al. synthesized $CsPbBr_3$ NCs using a room temperature method that allows the incorporation of relatively short ligands with low boiling point. Consequently, as-synthesized $CsPbBr_3$ NCs were readily fabricated into TFTs (Figure 21A) (Zhou et al., 2019b). The transistor showed a *p*-type transport with a hole mobility of ~$7 \times 10^{-7}$ $cm^2V^{-1}s^{-1}$, which is orders of magnitude lower than the mobility measured in a single $CsPbBr_3$ thin platelet. This indicates that the charge transport in a $CsPbBr_3$-NC film is mainly limited by tunneling of carriers between the $CsPbBr_3$ NCs. But it is in the same order as that observed in $CsPbBr_3$ polycrystalline films, confirming that the employment of short ligands doesn't impede the charge transport between NCs.

To further promote the charge transport properties of perovskite NCs, surface treatments such as purification to remove the surface short ligands have also been tried. Nevertheless, these treatments do not contribute to the improvement of the charge transport in $CsPbBr_3$ NCs. The hole mobility is in the same order as untreated undoped $CsPbBr_3$ NCs. However, the extrinsic doping of $Ag^+$ significantly increases the electrical performance of $CsPbBr_3$ NCs. A typical *p*-type transport character could be gradually tuned up with doping concentration increasing. An exponential shape of curves was observed in the output characteristics of FETs, indicating the formation of a good-quality Schottky junction between the NCs and electrodes. At higher doping concentration, the *p*-type character was more prominent. $Ag^+$ doping led to about 3 orders of magnitude higher hole mobility, $8 \times 10^{-4}$ $cm^2V^{-1}s^{-1}$, when the $Ag^+$ concentration was increased to 0.48%. Furthermore, the researchers performed low-temperature TFT studies to prevent

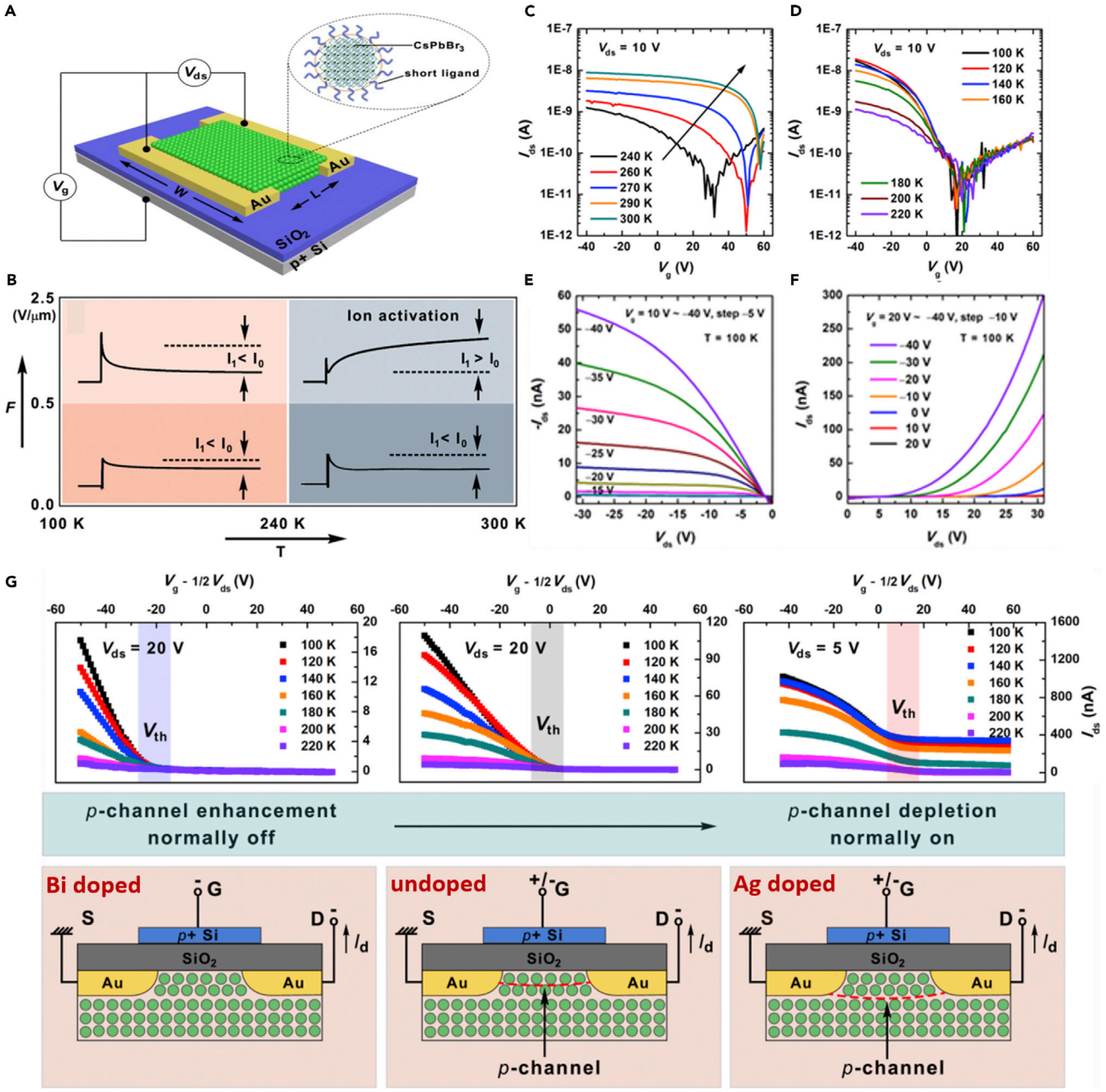


**Figure 21. Thin-film transistors based on perovskite NCs**

(A) Schematic to show the bottom-gate bottom-contact FET device structure based on $CsPbBr_3$ NCs terminated with short organic ligands.

(B) Electric-field (*F*)- and temperature (T)-dependent transient response of $I_{ds}$ of the undoped $CsPbBr_3$-NC film. Transfer characteristics of the undoped $CsPbBr_3$-NC TFT measured from (C) 240 to 300 K and (D) 100 to 220 K. Output characteristics of the undoped $CsPbBr_3$-NC TFT measured at 100 K under (E) negative and (F) positive $V_{ds}$. The channel length L is 20 μm, and the $V_{ds}$ is 10 V.

(G) Three types of transistors fabricated by using trivalent $Bi^{3+}$-doped (normally off *p*-channel device), undoped, and monovalent $Ag^{+}$-doped (normally on *p*-channel device) $CsPbBr_3$ NCs. Figures A–G adapted from (Zhou et al., 2020). Copyright © 2020, American Chemical Society.

the photon scattering and ion migration effects (Zhou et al., 2020). It can be seen that the mobility progressively increased as temperature decreased and saturated at ~100 K when phonon scattering and ion migration effect was surpassed. The hole mobility of $Ag^{+}$-doped $CsPbBr_3$ NCs was about two orders-of-magnitude higher than undoped NCs, confirming that $Ag^{+}$-doping should dominantly contribute to the conductivity and hole mobility improvement at room temperature. In addition, $Ag^{+}$-doped NCs-based

TFTs demonstrated negligible hysteresis, which could be ascribed to the effectively reduction in the density of hole traps in the perovskite NCs.

Subsequently, the same group carried out a systematic study on the ionic and electronic transport mechanism in films of $CsPbBr_3$ NCs by using a combination of transient response characterizations and field-effect transistor measurements (Figure 21B) (Zhou et al., 2020). In the transient response characterizations, they found that the channel current ($I_{ds}$) spiked quickly when the external bias was switched on. The $I_{ds}$ then dropped to $I_0$ within a second. After that, the $I_{ds}$ gradually increased toward a saturation value $I_1$ in a few tens of seconds. When the external bias was removed the $I_{ds}$ returned to zero immediately. Together, it is concluded that the device made of $CsPbBr_3$-NC film experiences a dominant electronic current rather than the ionic current. From the electric-field- and temperature-dependent transient response of $I_{ds}$ of the $CsPbBr_3$-NC film, the critical electric field, and temperature for ion activation were determined to be 0.5 V/μm and 240 K (Figures 21C and 21D).

An ion-induced doping model for the ionic–electronic transport in perovskite-NC films was proposed on the basis of the above results. Specifically, electronic transport was the dominant current source under dark conditions. It was interpreted that the long-range ionic transport that led to interfacial ion accumulation was not prominent. However, under external bias, a couple of Br ions ($I_{Br}^-$) and vacancies ($V_{Br}^+$) (bromine Frenkel pairs) could be formed. Therefore, $V_{Br}^+$ defects moving to the NC surface and the $I_{Br}^-$ defects remaining in the interior of $CsPbBr_3$ NCs induced a p-type self-doping and increased the conductivity. This implies a dominant role of ionic transport in modifying electronic properties. The corresponding FET transfer characteristics recorded at different temperatures also provided direct evidence of an enhanced *p*-type character of the $CsPbBr_3$ NC films by ion migration. A well-defined linear and saturation transport regime was observed in perovskite-NC-based FET devices at low temperature, suggesting the $I_{ds}$ was smoothly modulated by the gate (Figures 21E and 21F). However, the enhanced *p*-doping prevails over the gating effect at room temperature, resulting in no gate modulation of the channel current. When ionic transport was effectively suppressed at < 240 K, the electrical gating effect became dominant. In this situation, the $CsPbBr_3$-NC transistors exhibited a clean unipolar transport characteristic in a *p*-type mode featuring well-defined linear and saturation regimes. More significantly, the device could be readily switched from normally off (*p*-type enhancement) to normally on (*p*-type depletion) by electronic doping of $CsPbBr_3$ NCs with monovalent $Ag^+$ and trivalent $Bi^{3+}$, respectively (Figure 21G). Impressive hole mobility approaching $10^{-3}$ $cm^2$ $V^{-1}$ $s^{-1}$, on–off ratio of $\sim 10^4$, and turn-on voltage in a wide range of −30 to 20 V was finally demonstrated from the $CsPbBr_3$-NC-based TFTs.

## Synaptic devices

Neuromorphic computing has shown great potential in artificial intelligence and other frontiers of science and technology. Developing new materials and device structures to construct artificial synapses is critically important for the advance of neuromorphic computing. Halide perovskite NCs possess unique ionic-electronic ambipolar transport characteristics and outstanding optoelectronic properties that are particularly desired for high-performance synaptic devices.

Recently, applications of perovskite NCs in the field of resistive switching memories, memristors, and artificial synapses for neuromorphic computing are specially spotlighting (Kwak et al., 2021). It is well-known that the computing and memory units are physically separated in conventional computers. In such an architecture data must be transferred back and forth during computing. However, memory access typically consumes 100 to 1000 times more energy than a central processing unit, which greatly limits the performance and scalability of the structure, known as the von Neumann bottleneck. To overcome the bottleneck, it is critical to design new in-memory devices such as artificial synapses for efficient computing.

A synaptic device can be constructed in the framework of a two-terminal memristor or a three-terminal memtransistor (Periyal et al., 2020). A two-terminal memristor has a simple structure consisting of a top electrode, a layer of semiconductor, and a bottom electrode. It could be a limitation for the two-terminal memristor that the readout and programming occur through the same set of terminals. By contrast, a three-terminal memtransistor provides another handle with the gate electrode used for programming and the source-drain terminals used for readout (Wang et al., 2018b; Wen et al., 2021). Figure 22A illustrates the working principle of a biological synapse. In biological nervous systems, there are numerous neurons composed of the soma, dendrite, and axon. Numerous neurons are linked via the synaptic junction

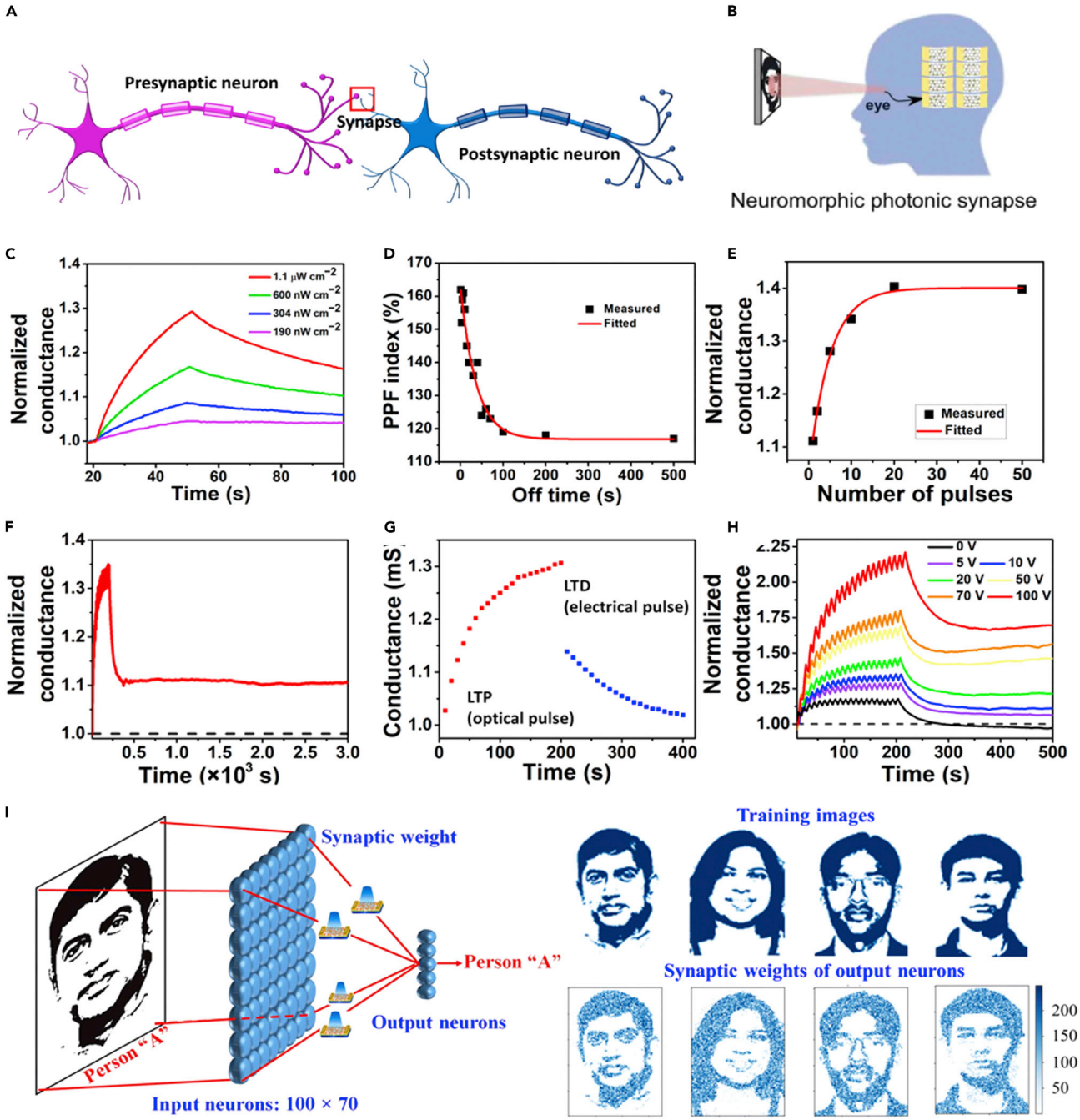


**Figure 22. Perovskite-NC synapse**

(A) Schematic illustration of a biological synapse.

(B) The application of photonic synapses in face recognition.

(C) Transient characteristic of the device ($V_D$ = 0.5 V and $V_G$ = 10 V) showing the change in conductance.

(D) PPF index of the device ($V_D$ = 0.5 V and $V_G$ = 10 V).

(E) Transient characteristic of the device ($V_D$ = 0.5 V and $V_G$ = 10 V) showing the change in conductance.

(F) Retention of the long-term potentiated device ($V_D$ = 0.5 V and $V_G$ = 10 V).

(G) Nonvolatile synaptic plasticity of the device ($V_G$ = 10 V) showing LTP by the train of optical pulses.

(H) Gate-dependent transient characteristic of the device ($V_D$ = 0.5 V) after application of 20 optical pulses.

(I) Neuron network structure for face recognition (left), images for training, and the synaptic weights of certain corresponding output neurons (right).

Figures A–I reprinted from (Pradhan et al., 2020). Copyright © 2020, American Association for the Advancement of Science.

synapses. A synapse involves a small gap where an electrical or chemical signal is transmitted from a signal-passing neuron (a presynaptic neuron) to another (a postsynaptic neuron). Figure 22B typically illustrates a photonic synapse for a high-order face recognition function.

Currently, few reports on electric-stimulated synaptic memristors and memtransistors based on perovskite-NC thin films largely due to the limited long-distance charge transport. In contrast, light-stimulated synapses using composite structures of perovskite NCs and organic or 2D materials, have been investigated. In these devices, perovskite NCs are mainly used as a light absorption layer. The interaction between perovskite NCs and organic or 2D materials can significantly enhance the charge separation of the photoexcited charges, thereby improving the photoresponsivity. In addition, blending perovskite NCs with organic or 2D materials will cause delayed decay of photocurrent, which is essential for achieving efficient photonic synapses.

In 2018, Yang et al. proposed the use of strongly emissive $CsPbBr_3$ perovskite NCs to construct a photonic flash memory with the structure of $Si/SiO_2/CsPbBr_3$ NCs/polymethyl methacrylate (PMMA)/pentacene/Au source-drain electrodes (Wang et al., 2018b). The obtained devices show light-induced charge trapping and electrical-mediated charge release characteristics, allowing programming operation in the optical mode and erasing operation in the electrical mode. Using the photonic flash memory, they emulated a variety of important synaptic functions including short-term plasticity (STP), long-term plasticity (LTP), paired-pulse facilitation (PPF), paired-pulse depression (PPD), and spike-rate-dependent plasticity (SRDP) at a device level.

Huang et al. showed that the blended film of $CsPbBr_3$ NCs and poly(3,3-didodecylquarter-thiophene) (PQT-12) could be used as the light-absorbing and charge transport layer, respectively, to fabricate photonic synaptic transistors (Wang et al., 2019b). A number of neuron-/synapse-like functions could be realized, including excitatory postsynaptic current (EPSC), PPF, high-pass dynamic filter, memory, and learning behaviors. In another work, poly[2,5-(2-octyldodecyl)-3,6-diketopyrrolopyrrole-alt-5,5-(2,5-di(thien-2-yl) thieno [3,2-b]thiophene)] (DPPDTT) was blended with $CsPbBr_3$ NCs to construct photonic synaptic transistors (Hao et al., 2020a). The synaptic behaviors were enhanced because a large energy barrier was formed between the VB of $CsPbBr_3$ NCs and the HOMO of DPPDTT. Abundant charge traps in the channel or at the interface resulted in the low combination rate of photogenerated charge carriers. When the operating voltage was reduced down to −0.0005 V, the device still showed an obvious synaptic response. Chen et al. reported the use of $CsPbBr_3$ NCs/poly(3-hexylthiophene) (P3HT) blend to improve the charge dissociation and photonic synaptic performance (Ercan et al., 2021). Upon solvent evaporation, the hybrid blend self-assembled into a one-dimensional nanostructure. Due to the homogeneous axial distribution of the NCs and the formation of P3HT nanofibrils and co-aggregates, the interfacial charge transfer was greatly enhanced. The photonic transistors showed fundamental synaptic functions with an ultralow energy consumption of 0.18 fJ and zero-gate operation.

Pradhan and coworkers reported photonic synapses using a graphene-perovskite-NC superstructure prepared by growing perovskite NCs directly from a graphene lattice (Pradhan et al., 2020). They found the superstructure acted as an artificial photonic synapse, where the presynaptic signal was the external light stimuli in the form of optical pulses and the postsynaptic signal was the current obtained across the channel keeping both drain source and gate voltage fixed. They recorded the change in conductance for light with different intensities (Figure 22C), which is helpful to understand the synaptic dynamics of the device under different conditions of the presynaptic signal spikes. The PPF index exponentially decreased with increasing off time between two pulses (Figure 22D), indicating that reduction in off time between two pulses ($\leq$10 s) would amplify the postsynaptic response. Figure 22E showed normalized conductance of the device increased for the incremental number of pulses at a fixed wavelength and intensity. Other memory effects including variation in normalized conductance triggered by 20 presynaptic light spikes under a gate bias of 10 V, LTP and long-term depression (LTD) were emulated in Figures 22F–22H. Furthermore, they constructed a spiking neural network to perform unsupervised machine learning and face recognition (Figure 22I). When the presynaptic neuron sensed pixels of the input images, it transformed them into presynaptic spikes, then at the postsynaptic neuron the postsynaptic signals were summed and make a spike. The real images used for training and the synaptic weights of some corresponding output neurons were shown in Figure 22I (right). The study highlighted the potential of perovskite NCs in novel synaptic devices for artificial intelligence and future neuromorphic computing.

### Light communication

The use of visible light emitted from a LED or a laser for simultaneous illumination and communication is an emerging technology regarded as a major part of the solution to the current bottlenecks in wireless data communication. Conventional lighting phosphors that are typically integrated with LEDs have limited modulation bandwidth. To provide the bandwidth required for visible light communication (VLS), a light converter to shape the light emission is usually employed. Dursun et al. presented a promising light converter for VLC by using green-emitting $CsPbBr_3$ NCs combined with a conventional red phosphor for the first time (Figure 23A) (Dursun et al., 2016). The novel $CsPbBr_3$-NC/phosphor light converter exhibits a relatively high bandwidth of 491.4 MHz (Figure 23B), which is much greater than those of conventional nitride-based phosphors (~12.4 MHz), organic materials (40-200 MHz) commercial YAG-based phosphors (3-12 MHz) and blue LEDs. The clear open eye as observed in the eye diagram suggests that the $CsPbBr_3$-NC phosphor-converted LD VLC is capable of transmitting a high data rate of up to 2 Gbit/s (Figure 23C). The perovskite-NC enhanced white light source combines ultrafast response characteristics with a high color rendering index of 89 and a correlated color temperature of 3236 K, thereby enabling dual VLC and solid-state lighting functionalities. In another work, Singh et al. proposed a flexible white-light system for high-speed VLC applications. The white-light system consists of a semipolar blue InGaN/GaN single-quantum-well micro-LED (μ-LED) on a flexible substrate for pumping a green $CsPbBr_3$-NC paper and a red CdSe NC paper (Singh et al., 2021). A high bandwidth of 229 MHz and a high data transmission rate of 400 Mbps were achieved for the $CsPbBr_3$-NC paper with a blue μ-LED pumping source (Figures 23D and 23E).

Perovskite NCs/polymethyl methacrylate (PMMA) composite films with multicolor light emission have also been prepared for VLC (Wang et al., 2021c). Due to the fast optical response and air stability, the composite films could be used to make broadband color converters for VLC based on a high-bandwidth 75 μm blue micro-LED (μ-LED). The composite films with yellow-emitting $CsPb(Br/I)_3$ NCs have a high bandwidth of 347 MHz, while the red-emitting composite films with $CsPbI_3$ NCs exhibit a higher modulation bandwidth of 822 MHz, which is ~65 times larger than that of conventional phosphors. In particular, by using the two composite films combined with the blue emission from the μ-LED, a warm white light was obtained with a correlated color temperature of 5670 K, a color rendering index of 75.7, and a de L'Eclairage (CIE) coordinate at (0.33, 0.35). The color conversion using the μ-LED sacrifices part of received power and slightly decreases the overall bandwidth from 1.130 to 1.005 GHz. However, a maximum real-time data rate of 1.7 Gbps could still be realized by using a non-return-to-zero on−off keying (NRZ-OOK) modulation scheme.

Kang et al. demonstrated perovskite NCs/polymer composites-based scintillating fibers as a near-omnidirectional detection platform for several tens-to-hundreds of Mbit/s optical communication in both free space and underwater links (Kang et al., 2022). As shown in Figures 23F–23I, the scintillating fibers offer good flexibility in terms of shape and near-omnidirectional detection features. Such fiber properties also introduce a scalable detection area that can resolve the resistance-capacitance and angle-of-acceptance limits in planar-based detectors, which conventionally impose a trade-off between the modulation bandwidth, detection area, and angle of view (Figures 23J and 23K). A high bit rate of 23 Mbit/s and 152.5 Mbit/s was achieved using an intensity-modulated laser for NRZ-OOK modulation scheme in free-space and quadrature amplitude modulation orthogonal frequency-division multiplexing (QAM-OFDM) modulation scheme in an underwater environment, respectively (Figures 23L–23N).

Perovskite NCs with a short emission lifetime and high luminous efficiency is strongly demanded underwater wireless optical communication (UWOC). However, the instability of perovskite NCs in water must be confronted first. Tang et al. synthesized extremely stable $CsPbBr_3$ NCs embedded in all-inorganic amorphous glass by all-solid reaction without any organic ligand (Xia et al., 2021). The amorphous glass protected the $CsPbBr_3$ NCs, showing high PLQY of 70%, excellent stability against water, thermal treatment (200°C in the air) and intensive laser irradiation (3.6 $kWcm^{-2}$). The application of perovskite NCs for UWOC was then realized for the first time, reaching a bandwidth as high as 180 MHz and data rates of 185 Mbps. Xu et al. proposed a quasi-omnidirectional transmitter for UWOC by taking advantages of the strong PL of $CsPbBr_3$ NCs (Li et al., 2022). The system was tested in a 50-m swimming pool and the water attenuation coefficient is 0.38 dB/m. It was found that the maximum data rates of OOK signals over 10-m and 20-m transmission distances can reach 60 Mbps and 40 Mbps, respectively. When four clients are adopted in a code division multiple access (CDMA) based UWOC network, the maximum data rates of each client can reach 10 Mbps and 7.5 Mbps over 10-m and 20-m underwater channels, respectively. These

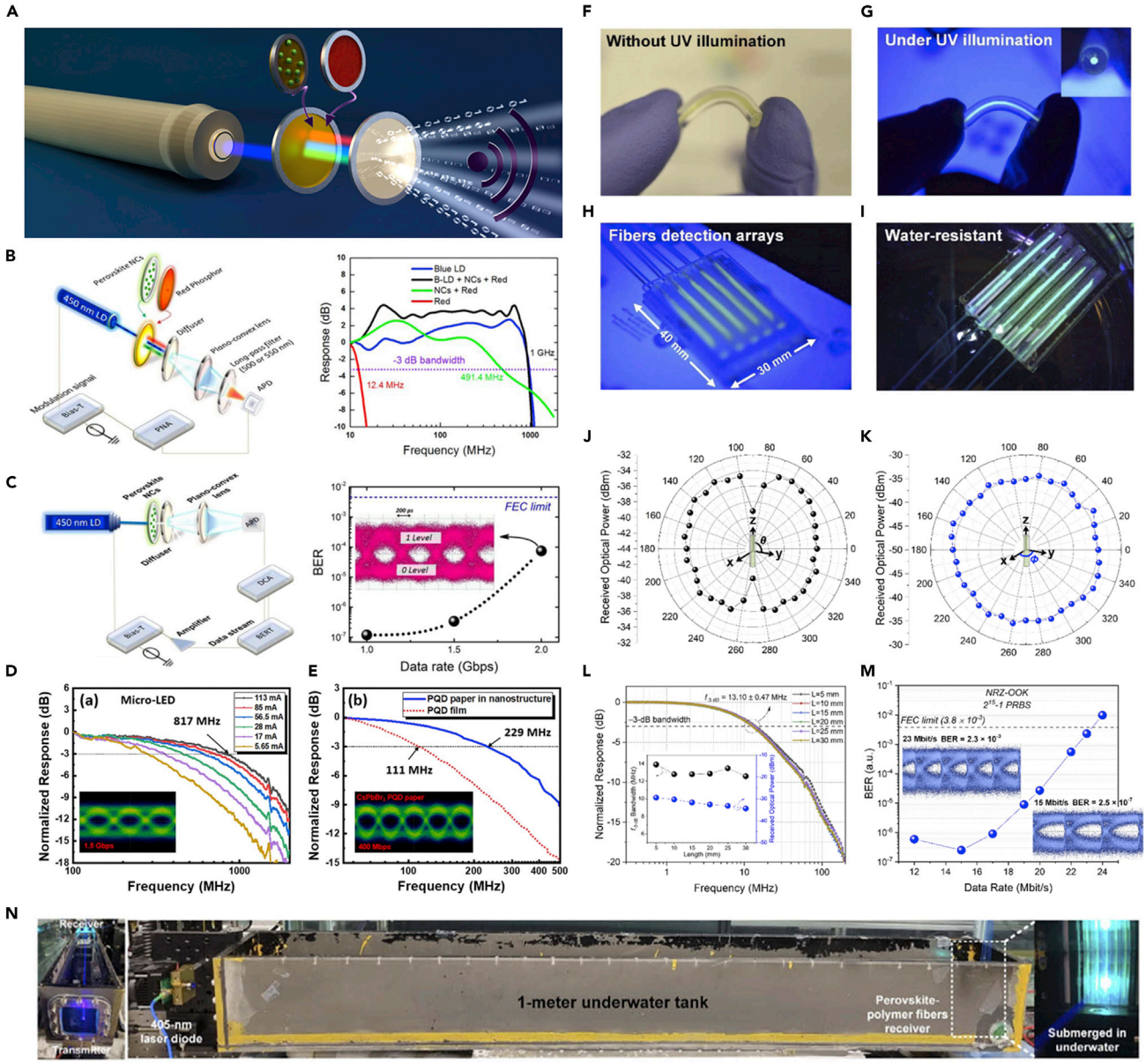


**Figure 23. Perovskite NCs for light communication**

(A) Schematic showing perovskite NCs as a color converter for visible light communication.

(B) Schematic of the small-signal frequency-response measurement setup and measured frequency responses for various devices.

(C) Schematic of the data transmission measurement using an OOK scheme and bit-error rates (BERs) measured at different data rates, with the forward error correction (FEC) limit labeled. Figures A–C reprinted from (Dursun et al., 2016). Copyright © 2016, American Chemical Society.

(D) Frequency responses for a semipolar blue micro-LED.

(E) Comparison of bandwidth of perovskite-NC paper with that of perovskite-NC film. Inset shows the eye diagram for the perovskite-NC paper. Figures D and E reprinted from (Singh et al., 2021). Copyright © 2021, Chinese Laser Press.

(F and G) Images of the $CsPbBr_3$ NCs/polymer fiber under ambient light and UV illumination.

(H and I) Images of the fiber detector array formed by a single $CsPbBr_3$ NCs/polymer fiber and that submerged in a water bath.

(J and K) The received optical power from the $CsPbBr_3$ NC-polymer fiber with respect to its polar (θ) and azimuthal (φ.) angles.

(L) Normalized frequency response of the $CsPbBr_3$ NCs/polymer fiber when measured at different lengths, *i.e.*, 5 to 30 mm, from the edge of the sample. The inset shows the corresponding –3-dB frequency bandwidth ($f_{-3dB}$) and the received optical power at different sections of the fiber.

(M) BER of data transmission based on the NRZ-OOK modulation scheme at different data rates.

(N) Photograph of the experimental setup with the transmitter (405-nm laser diode) and receiver (perovskite-polymer fibers) placed across a 1-m-long water tank. Figures F–N reprinted from (Kang et al., 2022). Copyright © 2022, Optical Society of America.

high-performance transmitters using perovskite NCs can meet the requirements of the last meter end-user access in the Internet of underwater things (IoUT) and underwater optical cellular network systems.

## INDUSTRIAL COMPATIBILITY

Owing to outstanding optical and electronic properties, halide perovskites have the potential to compete with state-of-the-art silicon technology. (Chen et al., 2016b; Saki et al., 2021; Wang et al., 2016a). In terms of the cost analysis in the established silicon photovoltaic industry, for a thin-film optoelectronic technology to be market-compatible, the cost of the active layer should be controlled <5 $/m$^2$, or a $/W value of <0.20 if we consider 20% PCE of modules. For the case of perovskite NCs, the active layer cost is dominated by materials required for NC synthesis, and the majority of this part comes from the solvents, *i.e.*, MeOAc, ODE, hexane, and so forth. Besides, labor cost, capital expenditure (capex), operating expenditure (opex), together with the loss of synthesis yield form another major contributor (Jean et al., 2018).

In a recent study by Kirmani et al. $CsPbI_3$ NCs were selected as a model to evaluate the cost benefits of perovskite NCs (Kirmani et al., 2022). $PbI_2$ is the major component of the reaction and most of it is wasted during the synthesis process. Hence, the synthesis yield (Y) is defined as the ratio of the final optoelectronic-grade NCs' mass to the $PbI_2$ mass as

$$Y(\%) = \frac{\text{mass of optoelectronic grade NCs}}{\text{mass of } PbI_2} \times 100\%. \quad \text{(Equation 6)}$$

The analysis suggests Y has a dramatic effect on the synthesis cost. $/m$^2$ reaches >50 at Y = 12% according to experimental data. This implies that the current synthesis protocol is highly cost-inefficient and actually incompatible with industrial scale-up. However, $/m$^2$ quickly drops to 10 when Y is increased to 50%. Using a technoeconomic model based on the price data from prominent materials suppliers in the United States, they highlighted that an improved synthesis yield, a recycling of solvents, and synthesis automation are critical to the market adoption of perovskite-NC technology. Specifically, this three-pronged approach can make the costs of NC film fabrication down from > $50/m$^2$ to ~ $2-3/m$^2$.

High-throughput and economical deposition of high-quality films from perovskite-NC inks represents another important part of industrial compatibility. Currently, spin-coating is the most frequently used in the lab for fabricating perovskite-NC-based optoelectronic devices, which is actually not a scalable method suitable for industry because of their high material wasting. Recently, scaling-up methods such as ink-jet printing, slot-die coating, spray-coating, and blade-coating have been applied to versatile optoelectronic devices, leading to exciting performance (Park and Zhu, 2020; Saki et al., 2021; Sukharevska et al., 2021). For instance, the EQE of doctor-bladed $MAPbI_3$ perovskite LEDs (54 cm$^2$) reached 16.1% and the cost of the active layer could be as low as 0.02 cents per cm$^2$, demonstrating its huge potential in practical applications of flat panel lighting and display (Chu et al., 2021). $FAPbBr_3$-NC LEDs by a modified bar-coating method reported an EQE of 23.26% for a pixel size of 4 mm$^2$ and an EQE of 22.5% for a large pixel area of 102 mm$^2$ with high reproducibility (Kim et al., 2022). A fully automated spray-coated technology could be used for the construction of $CsPbI_3$-NC-based solar cells (Yuan et al., 2019). Homogeneous $CsPbBr_3$ NCs film on various substrates for X-ray detectors by the inexpensive inkjet printing method, which could realize the formation of a desirable pattern with a smooth surface morphology (Liu et al., 2019a). Beyond perovskite NCs blade-coating has been employed for scalable production of PbS-NC solar cells with PCE over 10% at industrially viable speeds, presenting its commercial prospect for NC photovoltaics (Kirmani et al., 2018). Despite recent advances in scalable deposition methods, challenges still remain in the commercial relevance of perovskite NCs. Industry-compatible advanced techniques including large-scale, high-speed, and cost-effective device fabrication and synthetic methods should be developed in order to promote the niche market application of perovskite-NC-based optoelectronic technologies.

### Conclusions and remarks

In summary, we have made a comprehensive review of recent progress on the synthesis, properties, and applications of versatile perovskite NCs. The advance in both synthesis and post-synthesis of perovskite NCs enables active tuning of their size, surface, and component for outstanding optical and electronic properties that are demanded a variety of technical applications. In particular, visible PL with near-unity QYs and wide optical response ranging from NIR to UV regime have been achieved. Novel optical phenomena including a size-dependent Stocks Shift, multi-photon absorption, and multiple exciton generation have been revealed. Effective methods to improve the charge-carrier mobility as well as understanding

of the unique mixed ionic-electronic ambipolar transport mechanism in perovskite-NC films have been introduced. The continuous improvement of optical and electronic properties has made perovskite NCs a promising novel class of semiconductor nanomaterials for optoelectronics and beyond.

Despite recent significant progress made on perovskite-NC-based LEDs, serious concerns should be addressed before their commercial applications. Firstly, the performance of blue perovskite-NC LEDs is still lower than green and red LEDs. Exploring efficient and bright blue LEDs remains to be the most challenging task to date. Furthermore, attention should be turned to the lifetime and stability issues of devices to meet commercial demands when the EQEs are already high. Moreover, more efforts should be spared to address lead toxicity, as what has been suggested for perovskite solar cells. Development of stable and high-performance LEDs based on lead-free perovskite NCs and their derivatives should also be encouraged.

Solar cells based on perovskite NCs have achieved an impressive PCE of 16.6%. The most important task for perovskite-NC solar cells is to continue to push forward to higher efficiencies of over 20%, on a par with state-of-the-art organic solar cells and other thin-film photovoltaic technologies. It has been recognized that defects such as undercoordinated ions on the NC surface are typical roadblocks to the further improvement of perovskite-NC solar cells. Pursue of defect-free perovskite NCs should be the next big thing for photovoltaics and other optoelectronic devices. In addition, perovskite NCs offer precisely tunable optical absorption, holding the promise for the fabrication of optimized tandem devices to make full use of sunlight and enhance the overall stability.

At present, efficient methods for detecting high-energy radiations are limited and in great demand. Halide perovskite NCs feature high absorption efficiency and optical sensitivity to X-rays. The thermal and environmental instability issues that are often associated with solar cells and LEDs could also be largely avoided for X-ray scintillation. But perovskite-NC scintillators still require further improvements in terms of light yields and scalable production. Besides, investigations on perovskite-NC scintillators for advancing sensing and imaging based on gamma rays and neurons (>1 MeV) with higher energy are also worth exploring.

The applications of halide perovskite NCs for light communication in the visible region have been demonstrated and attracting a lot of attention. However, their applications in the infrared region remain much less explored due to their relatively large bandgap (>1.6 eV). In addition, efficient light absorption and emission in the short-wavelength infrared (>1000 nm) region has not been realized in spite of a few impressive attempts such as hybrid perovskite/semiconductor structures (Mei et al., 2022; Protesescu et al., 2017). Circumvention of the ''infrared-wall'' stands before perovskite NCs remains to be challenging, but promising for IR wireless data communication as well as a number of technological applications.

Compared to perovskite bulk films, perovskite NCs appear to be better positioned for synaptic memristors with very low power consumption approaching or even surpassing bio-synapses. On one hand, the increase of specific surface area is usually accompanied by the exposure of more surface and edge sites, which is easy to form ion vacancy defects. On the other hand, the increase of surface and interface can provide more transport channels for ion migration, which is beneficial to reduce the energy barrier of ion migration. Furthermore, the ion-electron transport in perovskite NCs is very sensitive to light irradiation. This helps to achieve a variety of unique photoelectric coupling, offering added possibilities for the development of artificial synapses.

However, improving devices based on perovskite NCs requires a better understanding of the charge transport mechanism, which has been much less explored to date compared with bulk perovskites. Given the fact that the charge-carrier behavior in an NC film is very different from bulk film, systematic studies on the ionic-electronic transport of perovskite-NC films are thus desirable. For instance, the influence of heterovalent doping and surface ligands on the carrier transport has been explored, but their impact on mobile ions such as diffusion energy barrier remains unclear (Eames et al., 2015; Zhou et al., 2021a). The charge transport properties of perovskite NCs are greatly dependent on the concentration of dopants that are incorporated into perovskite NCs. However, direct observation of the distribution and exact location of dopants in perovskite NCs is still lacking. Hence, it is of great importance to image the location of dopants directly to signify controlled doping of perovskite NCs.

Currently, the charge-carrier mobility in perovskite-NCs films remains much lower than that of bulk perovskite in transistor studies. It appears that the low carrier mobility associated with perovskite NCs may not hinder the fabrication of perovskite-NC-based optoelectronic devices with good performance because the light emitting/absorbing perovskite-NC layer in a LED or a solar cell with a vertical structure is quite thin (~20 and 300 nm). The carriers that are injected into the NC layers actually do not need to travel a long distance. In contrast, the channel length for a horizontal transistor is usually larger than several tens of micrometers, signifying the challenge in fabricating high-performance perovskite-NC-based TFT devices. Further efforts to promote the electronic coupling in arrays of perovskite NCs should contribute to the significant improvement of carrier mobility.

Beyond optoelectronics, the applications of halide perovskite NCs including gas sensors and photocatalysts have been attracting increasing attention in recent years. For instance, the utilization of a composite of $CsPbBr_3$ NC/graphene oxide for $CO_2$ reduction opens up the possibility for the deployment of perovskite NCs for versatile photochemical conversion applications (Xu et al., 2017). Wu et al. demonstrated that the *p*-type $CsPbBr_3$ NCs feature high gas-sensing selectivity to detect $NO_2$ with a detection limit down to 0.4 ppm (Kim et al., 2020). As research on perovskite NCs moves forward, there will be exciting opportunities to further improve perovskite-NC-based optoelectronic devices and explore the use of perovskite NCs for novel applications in the future.

## ACKNOWLEDGMENTS

This work is mainly supported by the National Natural Science Foundation of China (Grant Nos. 62004230, 91964107 and U20A20209) and the Science and Technology Innovation Commission of Shenzhen (Grant No. GXWD20200830152356001).

## AUTHOR CONTRIBUTIONS

S. Zhou conceived the idea. S. Zhou and Y. Mu wrote the manuscript. All authors discussed and commented on the article.

## DECLARATION OF INTERESTS

The authors declare no competing financial interests.

## REFERENCES

Ahmed, G.H., Yin, J., Bakr, O.M., and Mohammed, O.F. (2021). Successes and challenges of core/shell lead halide perovskite nanocrystals. ACS Energy Lett. *6*, 1340–1357. https://doi.org/10.1021/acsenergylett.1c00076.

Akkerman, Q.A., Abdelhady, A.L., and Manna, L. (2018a). Zero-dimensional cesium lead halides: history, properties, and challenges. J. Phys. Chem. Lett. *9*, 2326–2337. https://doi.org/10.1021/acs.jpclett.8b00572.

Akkerman, Q.A., D'Innocenzo, V., Accornero, S., Scarpellini, A., Petrozza, A., Prato, M., and Manna, L. (2015). Tuning the optical properties of cesium lead halide perovskite nanocrystals by anion exchange reactions. J. Am. Chem. Soc. *137*, 10276–10281. https://doi.org/10.1021/jacs.5b05602.

Akkerman, Q.A., Gandini, M., Di Stasio, F., Rastogi, P., Palazon, F., Bertoni, G., Ball, J.M., Prato, M., Petrozza, A., and Manna, L. (2016). Strongly emissive perovskite nanocrystal inks for high-voltage solar cells. Nat. Energy *2*, 16194. https://doi.org/10.1038/nenergy.2016.194.

Akkerman, Q.A., and Manna, L. (2020). What defines a halide perovskite? ACS Energy Lett. *5*, 604–610. https://doi.org/10.1021/acsenergylett.0c00039.

Akkerman, Q.A., Meggiolaro, D., Dang, Z., De Angelis, F., and Manna, L. (2017a). Fluorescent alloy CsPb x Mn1-x I3 perovskite nanocrystals with high structural and optical stability. ACS Energy Lett. *2*, 2183–2186. https://doi.org/10.1021/acsenergylett.7b00707.

Akkerman, Q.A., Park, S., Radicchi, E., Nunzi, F., Mosconi, E., De Angelis, F., Brescia, R., Rastogi, P., Prato, M., and Manna, L. (2017b). Nearly monodisperse insulator Cs4PbX6 (X = Cl, Br, I) nanocrystals, their mixed halide compositions, and their transformation into CsPbX3 nanocrystals. Nano Lett. *17*, 1924–1930. https://doi.org/10.1021/acs.nanolett.6b05262.

Akkerman, Q.A., Rainò, G., Kovalenko, M.V., and Manna, L. (2018b). Genesis, challenges and opportunities for colloidal lead halide perovskite nanocrystals. Nat. Mater. *17*, 394–405. https://doi.org/10.1038/s41563-018-0018-4.

Ali, R.F., Andreu, I., and Gates, B.D. (2019). Green solvent assisted synthesis of cesium bismuth halide perovskite nanocrystals and the influences of slow and fast anion exchange rates. Nanoscale Adv. *1*, 4442–4449. https://doi.org/10.1039/c9na00586b.

Almeida, G., Infante, I., and Manna, L. (2019). Resurfacing halide perovskite nanocrystals. Science *364*, 833–834. https://doi.org/10.1126/science.aax5825.

Amgar, D., Binyamin, T., Uvarov, V., and Etgar, L. (2018). Near ultra-violet to mid-visible band gap tuning of mixed cation RbxCs1-xPbX3 (X = Cl or Br) perovskite nanoparticles. Nanoscale *10*, 6060–6068. https://doi.org/10.1039/C7NR09607K.

Arfin, H., Kshirsagar, A.S., Kaur, J., Mondal, B., Xia, Z., Chakraborty, S., and Nag, A. (2020). ns2 electron (Bi3+ and Sb3+) doping in lead-free metal halide perovskite derivatives. Chem. Mater. *32*, 10255–10267. https://doi.org/10.1021/acs.chemmater.0c03394.

Ashley, M.J., O'Brien, M.N., Hedderick, K.R., Mason, J.A., Ross, M.B., and Mirkin, C.A. (2016). Templated synthesis of uniform perovskite nanowire arrays. J. Am. Chem. Soc. *138*, 10096–10099. https://doi.org/10.1021/jacs.6b05901.

Athanasiou, M., Papagiorgis, P., Manoli, A., Bernasconi, C., Bodnarchuk, M.I., Kovalenko, M.V., and Itskos, G. (2021). Efficient amplified spontaneous emission from solution-processed CsPbBr3 nanocrystal microcavities under continuous wave excitation. ACS Photonics *8*, 2120–2129. https://doi.org/10.1021/acsphotonics.1c00565.

Baranowski, M., and Plochocka, P. (2020). Excitons in metal-halide perovskites. Adv. Energy Mater. *10*, 1903659. https://doi.org/10.1002/aenm.201903659.

Bartel, C.J., Sutton, C., Goldsmith, B.R., Ouyang, R., Musgrave, C.B., Ghiringhelli, L.M., and Scheffler, M. (2019). New tolerance factor to predict the stability of perovskite oxides and halides. Sci. Adv. *5*, eaav0693. https://doi.org/10.1126/sciadv.aav0693.

Begum, R., Parida, M.R., Abdelhady, A.L., Murali, B., Alyami, N.M., Ahmed, G.H., Hedhili, M.N., Bakr, O.M., and Mohammed, O.F. (2017). Engineering interfacial charge transfer in CsPbBr3 perovskite nanocrystals by heterovalent doping. J. Am. Chem. Soc. *139*, 731–737. https://doi.org/10.1021/jacs.6b09575.

Bekenstein, Y., Dahl, J.C., Huang, J., Osowiecki, W.T., Swabeck, J.K., Chan, E.M., Yang, P., and Alivisatos, A.P. (2018). The making and breaking of lead-free double perovskite nanocrystals of cesium silver-bismuth halide compositions. Nano Lett. *18*, 3502–3508. https://doi.org/10.1021/acs.nanolett.8b00560.

Bekenstein, Y., Koscher, B.A., Eaton, S.W., Yang, P., and Alivisatos, A.P. (2015). Highly luminescent colloidal nanoplates of perovskite cesium lead halide and their oriented assemblies. J. Am. Chem. Soc. *137*, 16008–16011. https://doi.org/10.1021/jacs.5b11199.

Bi, C., Yao, Z., Sun, X., Wei, X., Wang, J., and Tian, J. (2021). Perovskite quantum dots with ultralow trap density by acid etching-driven ligand exchange for high luminance and stable pure-blue light-emitting diodes. Adv. Mater. *33*, e2006722. https://doi.org/10.1002/adma.202006722.

Bi, C., Wang, S., Wen, W., Yuan, J., Cao, G., and Tian, J. (2018). Room-temperature construction of mixed-halide perovskite quantum dots with high photoluminescence quantum yield. J. Phys. Chem. C *122*, 5151–5160. https://doi.org/10.1021/acs.jpcc.7b12607.

Biondi, M., Choi, M.-J., Lee, S., Bertens, K., Wei, M., Kirmani, A.R., Lee, G., Kung, H.T., Richter, L.J., Hoogland, S., et al. (2021). Control over ligand exchange reactivity in hole transport layer enables high-efficiency colloidal quantum dot solar cells. ACS Energy Lett. *6*, 468–476. https://doi.org/10.1021/acsenergylett.0c02500.

Brennan, M.C., Herr, J.E., Nguyen-Beck, T.S., Zinna, J., Draguta, S., Rouvimov, S., Parkhill, J., and Kuno, M. (2017a). Origin of the size-dependent Stokes shift in CsPbBr3 perovskite nanocrystals. J. Am. Chem. Soc. *139*, 12201–12208. https://doi.org/10.1021/jacs.7b05683.

Brennan, M.C., Zinna, J., and Kuno, M. (2017b). Existence of a size-dependent Stokes shift in CsPbBr3 perovskite nanocrystals. ACS Energy Lett. *2*, 1487–1488. https://doi.org/10.1021/acsenergylett.7b00383.

Butkus, J., Vashishtha, P., Chen, K., Gallaher, J.K., Prasad, S.K.K., Metin, D.Z., Laufersky, G., Gaston, N., Halpert, J.E., and Hodgkiss, J.M. (2017). The evolution of quantum confinement in CsPbBr3 perovskite nanocrystals. Chem. Mater. *29*, 3644–3652. https://doi.org/10.1021/acs.chemmater.7b00478.

Campbell, Z.S., Bateni, F., Volk, A.A., Abdel-Latif, K., and Abolhasani, M. (2020). Microfluidic synthesis of semiconductor materials: toward accelerated materials development in flow. Part. Part. Syst. Charact. *37*, 2000256. https://doi.org/10.1002/ppsc.202000256.

Cao, L., Liu, X., Li, Y., Li, X., Du, L., Chen, S., Zhao, S., and Wang, C. (2020). Recent progress in all-inorganic metal halide nanostructured perovskites: materials design, optical properties, and application. Front. Phys. *16*, 33201. https://doi.org/10.1007/s11467-020-1026-9.

Cao, Y., Wang, N., Tian, H., Guo, J., Wei, Y., Chen, H., Miao, Y., Zou, W., Pan, K., He, Y., et al. (2018). Perovskite light-emitting diodes based on spontaneously formed submicrometre-scale structures. Nature *562*, 249–253. https://doi.org/10.1038/s41586-018-0576-2.

Cha, M., Da, P., Wang, J., Wang, W., Chen, Z., Xiu, F., Zheng, G., and Wang, Z.S. (2016). Enhancing perovskite solar cell performance by interface engineering using CH3NH3PbBr0.9I2.1 quantum dots. J. Am. Chem. Soc. *138*, 8581–8587. https://doi.org/10.1021/jacs.6b04519.

Chen, D., Wan, Z., Chen, X., Yuan, Y., and Zhong, J. (2016a). Large-scale room-temperature synthesis and optical properties of perovskite-related Cs4PbBr6fluorophores. J. Mater. Chem. C *4*, 10646–10653. https://doi.org/10.1039/c6tc04036e.

Chen, D., Fang, G., Chen, X., Lei, L., Zhong, J., Mao, Q., Zhou, S., and Li, J. (2018a). Mn-Doped CsPbCl3 perovskite nanocrystals: solvothermal synthesis, dual-color luminescence and improved stability. J. Mater. Chem. C *6*, 8990–8998. https://doi.org/10.1039/c8tc03139h.

Chen, H., Li, R., Guo, A., and Xia, Y. (2021). Highly fluorescent CsPbBr3/TiO2 core/shell perovskite nanocrystals with excellent stability. SN Appl. Sci. *3*, 654. https://doi.org/10.1007/s42452-021-04648-8.

Chen, M., Zou, Y., Wu, L., Pan, Q., Yang, D., Hu, H., Tan, Y., Zhong, Q., Xu, Y., Liu, H., et al. (2017a). Solvothermal synthesis of high-quality all-inorganic cesium lead halide perovskite nanocrystals: from nanocube to ultrathin nanowire. Adv. Funct. Mater. *27*, 1701121. https://doi.org/10.1002/adfm.201701121.

Chen, Q., Wu, J., Ou, X., Huang, B., Almutlaq, J., Zhumekenov, A.A., Guan, X., Han, S., Liang, L., Yi, Z., et al. (2018b). All-inorganic perovskite nanocrystal scintillators. Nature *561*, 88–93. https://doi.org/10.1038/s41586-018-0451-1.

Chen, W., Bhaumik, S., Veldhuis, S.A., Xing, G., Xu, Q., Grätzel, M., Mhaisalkar, S., Mathews, N., and Sum, T.C. (2017b). Giant five-photon absorption from multidimensional core-shell halide perovskite colloidal nanocrystals. Nat. Commun. *8*, 15198. https://doi.org/10.1038/ncomms15198.

Chen, W., Tang, X., Wangyang, P., Yao, Z., Zhou, D., Chen, F., Li, S., Lin, H., Zeng, F., Wu, D., et al. (2018c). Surface-passivated cesium lead halide perovskite quantum dots: toward efficient light-emitting diodes with an inverted sandwich structure. Adv. Opt. Mater. *6*, 1800007. https://doi.org/10.1002/adom.201800007.

Chen, X., Peng, L., Huang, K., Shi, Z., Xie, R., and Yang, W. (2016b). Non-injection gram-scale synthesis of cesium lead halide perovskite quantum dots with controllable size and composition. Nano Res. *9*, 1994–2006. https://doi.org/10.1007/s12274-016-1090-1.

Chen, Y., Smock, S.R., Flintgruber, A.H., Perras, F.A., Brutchey, R.L., and Rossini, A.J. (2020). Surface termination of CsPbBr3 perovskite quantum dots determined by solid-state NMR spectroscopy. J. Am. Chem. Soc. *142*, 6117–6127. https://doi.org/10.1021/jacs.9b13396.

Chen, Y., Yin, J., Wei, Q., Wang, C., Wang, X., Ren, H., Yu, S.F., Bakr, O.M., Mohammed, O.F., and Li, M. (2022). Multiple exciton generation in tin–lead halide perovskite nanocrystals for photocurrent quantum efficiency enhancement. Nat. Photonics *16*, 1–6. https://doi.org/10.1038/s41566-022-01006-x.

Cheng, F., He, R., Nie, S., Zhang, C., Yin, J., Li, J., Zheng, N., and Wu, B. (2021). Perovskite quantum dots as multifunctional interlayers in perovskite solar cells with dopant-free organic hole transporting layers. J. Am. Chem. Soc. *143*, 5855–5866. https://doi.org/10.1021/jacs.1c00852.

Cho, S., Kim, J., Jeong, S.M., Ko, M.J., Lee, J.S., and Kim, Y. (2020a). High-voltage and green-emitting perovskite quantum dot solar cells via solvent miscibility-induced solid-state ligand exchange. Chem. Mater. *32*, 8808–8818. https://doi.org/10.1021/acs.chemmater.0c02102.

Cho, S., Kim, S., Kim, J., Jo, Y., Ryu, I., Hong, S., Lee, J.J., Cha, S., Nam, E.B., Lee, S.U., et al. (2020b). Hybridisation of perovskite nanocrystals with organic molecules for highly efficient liquid scintillators. Light Sci. Appl. *9*, 156. https://doi.org/10.1038/s41377-020-00391-8.

Chu, S., Chen, W., Fang, Z., Xiao, X., Liu, Y., Chen, J., Huang, J., and Xiao, Z. (2021). Large-area and efficient perovskite light-emitting diodes via low-temperature blade-coating. Nat. Commun. *12*, 147. https://doi.org/10.1038/s41467-020-20433-4.

Correa-Baena, J.P., Saliba, M., Buonassisi, T., Grätzel, M., Abate, A., Tress, W., and Hagfeldt, A. (2017). Promises and challenges of perovskite solar cells. Science *358*, 739–744. https://doi.org/10.1126/science.aam6323.

Creutz, S.E., Crites, E.N., De Siena, M.C., and Gamelin, D.R. (2018). Colloidal nanocrystals of lead-free double-perovskite (elpasolite) semiconductors: synthesis and anion exchange to access new materials. Nano Lett. *18*, 1118–1123. https://doi.org/10.1021/acs.nanolett.7b04659.

De Roo, J., Ibáñez, M., Geiregat, P., Nedelcu, G., Walravens, W., Maes, J., Martins, J.C., Van Driessche, I., Kovalenko, M.V., and Hens, Z. (2016). Highly dynamic ligand binding and light absorption coefficient of cesium lead bromide perovskite nanocrystals. ACS Nano *10*, 2071–2081. https://doi.org/10.1021/acsnano.5b06295.

Deng, W., Huang, L., Xu, X., Zhang, X., Jin, X., Lee, S.T., and Jie, J. (2017). Ultrahigh-responsivity photodetectors from perovskite nanowire arrays for sequentially tunable spectral measurement. Nano Lett. *17*, 2482–2489. https://doi.org/10.1021/acs.nanolett.7b00166.

Dey, A., Ye, J., De, A., Debroye, E., Ha, S.K., Bladt, E., Kshirsagar, A.S., Wang, Z., Yin, J., Wang, Y., et al. (2021). State of the art and prospects for halide perovskite nanocrystals. ACS Nano *15*, 10775–10981. https://doi.org/10.1021/acsnano.0c08903.

Di, D., Musselman, K.P., Li, G., Sadhanala, A., Ievskaya, Y., Song, Q., Tan, Z.K., Lai, M.L., MacManus-Driscoll, J.L., Greenham, N.C., and Friend, R.H. (2015). Size-dependent photon emission from organometal halide perovskite nanocrystals embedded in an organic matrix. J. Phys. Chem. Lett. *6*, 446–450. https://doi.org/10.1021/jz502615e.

Di Stasio, F., Christodoulou, S., Huo, N., and Konstantatos, G. (2017). Near-unity photoluminescence quantum yield in CsPbBr3 nanocrystal solid-state films via postsynthesis treatment with lead bromide. Chem. Mater. *29*, 7663–7667. https://doi.org/10.1021/acs.chemmater.7b02834.

Dirin, D.N., Protesescu, L., Trummer, D., Kochetygov, I.V., Yakunin, S., Krumeich, F., Stadie, N.P., and Kovalenko, M.V. (2016). Harnessing defect-tolerance at the nanoscale: highly luminescent lead halide perovskite nanocrystals in mesoporous silica matrixes. Nano Lett. *16*, 5866–5874. https://doi.org/10.1021/acs.nanolett.6b02688.

Dong, Y., Qiao, T., Kim, D., Parobek, D., Rossi, D., and Son, D.H. (2018). Precise control of quantum confinement in cesium lead halide perovskite quantum dots via thermodynamic equilibrium. Nano Lett. *18*, 3716–3722. https://doi.org/10.1021/acs.nanolett.8b00861.

Dong, Y., Wang, Y.K., Yuan, F., Johnston, A., Liu, Y., Ma, D., Choi, M.J., Chen, B., Chekini, M., Baek, S.W., et al. (2020). Bipolar-shell resurfacing for blue LEDs based on strongly confined perovskite quantum dots. Nat. Nanotechnol. *15*, 668–674. https://doi.org/10.1038/s41565-020-0714-5.

Dou, L., Lai, M., Kley, C.S., Yang, Y., Bischak, C.G., Zhang, D., Eaton, S.W., Ginsberg, N.S., and Yang, P. (2017). Spatially resolved multicolor CsPbX3 nanowire heterojunctions via anion exchange. Proc. Natl. Acad. Sci. USA *114*, 7216–7221. https://doi.org/10.1073/pnas.1703860114.

Dou, L., Wong, A.B., Yu, Y., Lai, M., Kornienko, N., Eaton, S.W., Fu, A., Bischak, C.G., Ma, J., Ding, T., et al. (2015). Atomically thin two-dimensional organic-inorganic hybrid perovskites. Science *349*, 1518–1521. https://doi.org/10.1126/science.aac7660.

Droseros, N., Longo, G., Brauer, J.C., Sessolo, M., Bolink, H.J., and Banerji, N. (2018). Origin of the enhanced photoluminescence quantum yield in MAPbBr3 perovskite with reduced crystal size. ACS Energy Lett. *3*, 1458–1466. https://doi.org/10.1021/acsenergylett.8b00475.

Dursun, I., Shen, C., Parida, M.R., Pan, J., Sarmah, S.P., Priante, D., Alyami, N., Liu, J., Saidaminov, M.I., Alias, M.S., et al. (2016). Perovskite nanocrystals as a color converter for visible light communication. ACS Photonics *3*, 1150–1156. https://doi.org/10.1021/acsphotonics.6b00187.

Eames, C., Frost, J.M., Barnes, P.R.F., O'Regan, B.C., Walsh, A., and Islam, M.S. (2015). Ionic transport in hybrid lead iodide perovskite solar cells. Nat. Commun. *6*, 7497. https://doi.org/10.1038/ncomms8497.

Efros, A.L., Rosen, M., Kuno, M., Nirmal, M., Norris, D.J., and Bawendi, M. (1996). Band-edge exciton in quantum dots of semiconductors with a degenerate valence band: dark and bright exciton states. Phys. Rev. B Condens. Matter *54*, 4843–4856. https://doi.org/10.1103/physrevb.54.4843.

Ercan, E., Lin, Y., Yang, W., and Chen, W. (2021). Self-assembled nanostructures of quantum dot/conjugated polymer hybrids for photonic synaptic transistors with ultralow energy consumption and zero-gate bias. Adv. Funct. Mater. *32*, 2107925. https://doi.org/10.1002/adfm.202107925.

Fang, C., Wang, H., and Li, D. (2021a). Recent progress in two-dimensional Ruddlesden-Popper perovskite based heterostructures. 2D Mater. *8*, 022006. https://doi.org/10.1088/2053-1583/abdbca.

Fang, T., Wang, T., Li, X., Dong, Y., Bai, S., and Song, J. (2021b). Perovskite QLED with an external quantum efficiency of over 21% by modulating electronic transport. Sci. Bull. *66*, 36–43. https://doi.org/10.1016/j.scib.2020.08.025.

Fedorovskiy, A.E., Queloz, V.I.E., and Nazeeruddin, M.K. (2021). Beyond tolerance factor: using deep learning for prediction formability of ABX3 perovskite structures. Adv. Theory Simul. *4*, 2100021. https://doi.org/10.1002/adts.202100021.

Filip, M.R., and Giustino, F. (2018). The geometric blueprint of perovskites. Proc. Natl. Acad. Sci. USA *115*, 5397–5402. https://doi.org/10.1073/pnas.1719179115.

Fu, Y., Zhu, H., Chen, J., Hautzinger, M.P., Zhu, X.Y., and Jin, S. (2019). Metal halide perovskite nanostructures for optoelectronic applications and the study of physical properties. Nat. Rev. Mater. *4*, 169–188. https://doi.org/10.1038/s41578-019-0080-9.

Gan, Z., Chen, W., Yuan, L., Cao, G., Zhou, C., Huang, S., Wen, X., and Jia, B. (2019). External stokes shift of perovskite nanocrystals enlarged by photon recycling. Appl. Phys. Lett. *114*, 011906. https://doi.org/10.1063/1.5081805.

Gandini, M., Villa, I., Beretta, M., Gotti, C., Imran, M., Carulli, F., Fantuzzi, E., Sassi, M., Zaffalon, M., Brofferio, C., et al. (2020). Efficient, fast and reabsorption-free perovskite nanocrystal-based sensitized plastic scintillators. Nat. Nanotechnol. *15*, 462–468. https://doi.org/10.1038/s41565-020-0683-8.

Gao, Y., Zhao, L., Shang, Q., Zhong, Y., Liu, Z., Chen, J., Zhang, Z., Shi, J., Du, W., Zhang, Y., et al. (2018). Ultrathin CsPbX3 nanowire arrays with strong emission anisotropy. Adv. Mater. *30*, e1801805. https://doi.org/10.1002/adma.201801805.

Gaulding, E.A., Hao, J., Kang, H.S., Miller, E.M., Habisreutinger, S.N., Zhao, Q., Hazarika, A., Sercel, P.C., Luther, J.M., and Blackburn, J.L. (2019). Conductivity tuning via doping with electron donating and withdrawing molecules in perovskite CsPbI3 nanocrystal films. Adv. Mater. *31*, e1902250. https://doi.org/10.1002/adma.201902250.

Ghosh, J., Ghosh, R., and Giri, P.K. (2018). Mesoporous Si nanowire templated controlled fabrication of organometal halide perovskite nanoparticles with high photoluminescence quantum yield for light-emitting applications. ACS Appl. Nano Mater. *1*, 1551–1562. https://doi.org/10.1021/acsanm.8b00047.

Green, M.A., Ho-Baillie, A., and Snaith, H.J. (2014). The emergence of perovskite solar cells. Nat. Photonics *8*, 506–514. https://doi.org/10.1038/nphoton.2014.134.

Guijarro, N., Yao, L., Le Formal, F., Wells, R.A., Liu, Y., Darwich, B.P., Navratilova, L., Cho, H.H., Yum, J.H., and Sivula, K. (2019). Lead halide perovskite quantum dots to enhance the power conversion efficiency of organic solar cells. Angew. Chem. Int. Ed. Engl. *58*, 12696–12704. https://doi.org/10.1002/anie.201906803.

Ha, S.T., Liu, X., Zhang, Q., Giovanni, D., Sum, T.C., and Xiong, Q. (2014). Synthesis of organic-inorganic lead halide perovskite nanoplatelets: towards high-performance perovskite solar cells and optoelectronic devices. Adv. Opt. Mater. *2*, 838–844. https://doi.org/10.1002/adom.201400106.

Ha, S.T., Su, R., Xing, J., Zhang, Q., and Xiong, Q. (2017). Metal halide perovskite nanomaterials: synthesis and applications. Chem. Sci. *8*, 2522–2536. https://doi.org/10.1039/c6sc04474c.

Han, B., Yuan, S., Cai, B., Song, J., Liu, W., Zhang, F., Fang, T., Wei, C., and Zeng, H. (2021a). Green perovskite light-emitting diodes with 200 hours stability and 16% efficiency: cross-linking strategy and mechanism. Adv. Funct. Mater. *31*, 2011003. https://doi.org/10.1002/adfm.202011003.

Han, X., Wu, W., Chen, H., Peng, D., Qiu, L., Yan, P., and Pan, C. (2021b). Metal halide perovskite arrays: from construction to optoelectronic applications. Adv. Funct. Mater. *31*, 2005230. https://doi.org/10.1002/adfm.202005230.

Han, Y., Wu, M., Gui, C., Zhu, C., Sun, Z., Zhao, M.H., Savina, A.A., Abakumov, A.M., Wang, B., Huang, F., et al. (2020). Data-driven computational prediction and experimental realization of exotic perovskite-related polar magnets. npj Quantum Mater. *5*, 92. https://doi.org/10.1038/s41535-020-00294-2.

Hao, D., Zhang, J., Dai, S., Zhang, J., and Huang, J. (2020a). Perovskite/organic semiconductor-based photonic synaptic transistor for artificial visual system. ACS Appl. Mater. Interfaces *12*, 39487–39495. https://doi.org/10.1021/acsami.0c10851.

Hao, M., Bai, Y., Zeiske, S., Ren, L., Liu, J., Yuan, Y., Zarrabi, N., Cheng, N., Ghasemi, M., Chen, P., et al. (2020b). Ligand-assisted cation-exchange engineering for high-efficiency colloidal Cs1−xFAxPbI3 quantum dot solar cells with reduced phase segregation. Nat. Energy *5*, 79–88. https://doi.org/10.1038/s41560-019-0535-7.

Hassan, Y., Park, J.H., Crawford, M.L., Sadhanala, A., Lee, J., Sadighian, J.C., Mosconi, E., Shivanna, R., Radicchi, E., Jeong, M., et al. (2021). Ligand-engineered bandgap stability in mixed-halide

perovskite LEDs. Nature *591*, 72–77. https://doi.org/10.1038/s41586-021-03217-8.

Haydous, F., Gardner, J.M., and Cappel, U.B. (2021). The impact of ligands on the synthesis and application of metal halide perovskite nanocrystals. J. Mater. Chem. *9*, 23419–23443. https://doi.org/10.1039/d1ta05242j.

Hens, Z., and Moreels, I. (2012). Light absorption by colloidal semiconductor quantum dots. J. Mater. Chem. *22*, 10406–10415. https://doi.org/10.1039/c2jm30760j.

Hintermayr, V.A., Lampe, C., Löw, M., Roemer, J., Vanderlinden, W., Gramlich, M., Böhm, A.X., Sattler, C., Nickel, B., Lohmüller, T., and Urban, A.S. (2019). Polymer nanoreactors shield perovskite nanocrystals from degradation. Nano Lett. *19*, 4928–4933. https://doi.org/10.1021/acs.nanolett.9b00982.

Hou, S., Guo, Y., Tang, Y., and Quan, Q. (2017). Synthesis and stabilization of colloidal perovskite nanocrystals by multidentate polymer micelles. ACS Appl. Mater. Interfaces *9*, 18417–18422. https://doi.org/10.1021/acsami.7b03445.

Hsieh, Y.H., Hsu, B.W., Peng, K.N., Lee, K.W., Chu, C.W., Chang, S.W., Lin, H.W., Yen, T.J., and Lu, Y.J. (2020). Perovskite quantum dot lasing in a gap-plasmon nanocavity with ultralow threshold. ACS Nano *14*, 11670–11676. https://doi.org/10.1021/acsnano.0c04224.

Hu, L., Zhao, Q., Huang, S., Zheng, J., Guan, X., Patterson, R., Kim, J., Shi, L., Lin, C.H., Lei, Q., et al. (2021). Flexible and efficient perovskite quantum dot solar cells via hybrid interfacial architecture. Nat. Commun. *12*, 466. https://doi.org/10.1038/s41467-020-20749-1.

Huang, C.-Y., Zou, C., Mao, C., Corp, K.L., Yao, Y.-C., Lee, Y.-J., Schlenker, C.W., Jen, A.K.Y., and Lin, L.Y. (2017a). CsPbBr3 perovskite quantum dot vertical cavity lasers with low threshold and high stability. ACS Photonics *4*, 2281–2289. https://doi.org/10.1021/acsphotonics.7b00520.

Huang, H., Bodnarchuk, M.I., Kershaw, S.V., Kovalenko, M.V., and Rogach, A.L. (2017b). Lead halide perovskite nanocrystals in the research spotlight: stability and defect tolerance. ACS Energy Lett. *2*, 2071–2083. https://doi.org/10.1021/acsenergylett.7b00547.

Huang, H., Polavarapu, L., Sichert, J.A., Susha, A.S., Urban, A.S., and Rogach, A.L. (2016). Colloidal lead halide perovskite nanocrystals: synthesis, optical properties and applications. NPG Asia Mater. *8*, e328. https://doi.org/10.1038/am.2016.167.

Huang, H., Xue, Q., Chen, B., Xiong, Y., Schneider, J., Zhi, C., Zhong, H., and Rogach, A.L. (2017c). Top-down fabrication of stable methylammonium lead halide perovskite nanocrystals by employing a mixture of ligands as coordinating solvents. Angew. Chem. Int. Ed. Engl. *56*, 9571–9576. https://doi.org/10.1002/anie.201705595.

Huang, H., Zhao, F., Liu, L., Zhang, F., Wu, X.G., Shi, L., Zou, B., Pei, Q., and Zhong, H. (2015). Emulsion synthesis of size-tunable CH3NH3PbBr3 quantum dots: an alternative route toward efficient light-emitting diodes. ACS Appl. Mater. Interfaces *7*, 28128–28133. https://doi.org/10.1021/acsami.5b10373.

Huang, J., Lei, T., Siron, M., Zhang, Y., Yu, S., Seeler, F., Dehestani, A., Quan, L.N., Schierle-Arndt, K., and Yang, P. (2020). Lead-free cesium Europium halide perovskite nanocrystals. Nano Lett. *20*, 3734–3739. https://doi.org/10.1021/acs.nanolett.0c00692.

Huang, S., Wang, B., Zhang, Q., Li, Z., Shan, A., and Li, L. (2018). Postsynthesis potassium-modification method to improve stability of CsPbBr3 perovskite nanocrystals. Adv. Opt. Mater. *6*, 1701106. https://doi.org/10.1002/adom.201701106.

Huang, X., Guo, Q., Yang, D., Xiao, X., Liu, X., Xia, Z., Fan, F., Qiu, J., and Dong, G. (2019). Reversible 3D laser printing of perovskite quantum dots inside a transparent medium. Nat. Photonics *14*, 82–88. https://doi.org/10.1038/s41566-019-0538-8.

Igbari, F., Wang, Z., and Liao, L. (2019). Progress of lead-free halide double perovskites. Adv. Energy Mater. *9*, 1803150. https://doi.org/10.1002/aenm.201803150.

Imran, M., Caligiuri, V., Wang, M., Goldoni, L., Prato, M., Krahne, R., De Trizio, L., and Manna, L. (2018). Benzoyl halides as alternative precursors for the colloidal synthesis of lead-based halide perovskite nanocrystals. J. Am. Chem. Soc. *140*, 2656–2664. https://doi.org/10.1021/jacs.7b13477.

Imran, M., Ijaz, P., Goldoni, L., Maggioni, D., Petralanda, U., Prato, M., Almeida, G., Infante, I., and Manna, L. (2019). Simultaneous cationic and anionic ligand exchange for colloidally stable CsPbBr3 nanocrystals. ACS Energy Lett. *4*, 819–824. https://doi.org/10.1021/acsenergylett.9b00140.

Iyikanat, F., Sari, E., and Sahin, H. (2017). Thinning CsPb2Br5 perovskite down to monolayers: Cs-dependent stability. Phys. Rev. B *96*, 155442. https://doi.org/10.1103/PhysRevB.96.155442.

Jang, D.M., Park, K., Kim, D.H., Park, J., Shojaei, F., Kang, H.S., Ahn, J.P., Lee, J.W., and Song, J.K. (2015). Reversible halide exchange reaction of organometal trihalide perovskite colloidal nanocrystals for full-range band gap tuning. Nano Lett. *15*, 5191–5199. https://doi.org/10.1021/acs.nanolett.5b01430.

Jasieniak, J., Califano, M., and Watkins, S.E. (2011). Size-dependent valence and conduction band-edge energies of semiconductor nanocrystals. ACS Nano *5*, 5888–5902. https://doi.org/10.1021/nn201681s.

Jean, J., Xiao, J., Nick, R., Moody, N., Nasilowski, M., Bawendi, M., and Bulović, V. (2018). Synthesis cost dictates the commercial viability of lead sulfide and perovskite quantum dot photovoltaics. Energy Environ. Sci. *11*, 2295–2305. https://doi.org/10.1039/c8ee01348a.

Jena, A.K., Kulkarni, A., and Miyasaka, T. (2019). Halide perovskite photovoltaics: background, status, and future prospects. Chem. Rev. *119*, 3036–3103. https://doi.org/10.1021/acs.chemrev.8b00539.

Jeong, J., Kim, M., Seo, J., Lu, H., Ahlawat, P., Mishra, A., Yang, Y., Hope, M.A., Eickemeyer, F.T., Kim, M., et al. (2021). Pseudo-halide anion engineering for alpha-FAPbI3 perovskite solar cells. Nature *592*, 381–385. https://doi.org/10.1038/s41586-021-03406-5.

Jia, C., Li, H., Meng, X., and Li, H. (2018). CsPbX3/Cs4PbX6 core/shell perovskite nanocrystals. Chem. Commun. *54*, 6300–6303. https://doi.org/10.1039/c8cc02802h.

Jia, D., Chen, J., Mei, X., Fan, W., Luo, S., Yu, M., Liu, J., and Zhang, X. (2021). Surface matrix curing of inorganic CsPbI3 perovskite quantum dots for solar cells with efficiency over 16. Energy Environ. Sci. *14*, 4599–4609. https://doi.org/10.1039/d1ee01463c.

Jia, D., Chen, J., Qiu, J., Ma, H., Yu, M., Liu, J., and Zhang, X. (2022). Tailoring solvent-mediated ligand exchange for CsPbI3 perovskite quantum dot solar cells with efficiency exceeding 16.5. Joule *6*, 1632–1653. https://doi.org/10.1016/j.joule.2022.05.007.

Jin, F., Zhao, B., Chu, B., Zhao, H., Su, Z., Li, W., and Zhu, F. (2018). Morphology control towards bright and stable inorganic halide perovskite light-emitting diodes. J. Mater. Chem. C *6*, 1573–1578. https://doi.org/10.1039/c7tc04631f.

Kang, C.H., Alkhazragi, O., Sinatra, L., Alshaibani, S., Wang, Y., Li, K.H., Kong, M., Lutfullin, M., Bakr, O.M., Ng, T.K., and Ooi, B.S. (2022). All-inorganic halide-perovskite polymer-fiber-photodetector for high-speed optical wireless communication. Opt Express *30*, 9823–9840. https://doi.org/10.1364/OE.452370.

Karlsson, M., Yi, Z., Reichert, S., Luo, X., Lin, W., Zhang, Z., Bao, C., Zhang, R., Bai, S., Zheng, G., et al. (2021). Mixed halide perovskites for spectrally stable and high-efficiency blue light-emitting diodes. Nat. Commun. *12*, 361. https://doi.org/10.1038/s41467-020-20582-6.

Kazes, M., Udayabhaskararao, T., Dey, S., and Oron, D. (2021). Effect of surface ligands in perovskite nanocrystals: extending in and reaching out. Acc. Chem. Res. *54*, 1409–1418. https://doi.org/10.1021/acs.accounts.0c00712.

Khan, J., Zhang, X., Yuan, J., Wang, Y., Shi, G., Patterson, R., Shi, J., Ling, X., Hu, L., Wu, T., et al. (2020). Tuning the surface-passivating ligand anchoring position enables phase robustness in CsPbI3 perovskite quantum dot solar cells. ACS Energy Lett. *5*, 3322–3329. https://doi.org/10.1021/acsenergylett.0c01849.

Kim, H., Bae, S., Lee, T.H., Lee, H., Kang, H., Park, S., Jang, H.W., and Kim, S.Y. (2021a). Enhanced optical properties and stability of CsPbBr3 nanocrystals through nickel doping. Adv. Funct. Mater. *31*, 2102770. https://doi.org/10.1002/adfm.202102770.

Kim, J., Hu, L., Chen, H., Guan, X., Anandan, P.R., Li, F., Tang, J., Lin, C.H., Kalantar-Zadeh, K., Tricoli, A., and Wu, T. (2020). P-Type charge transport and selective gas sensing of all-inorganic perovskite nanocrystals. ACS Mater. Lett. *2*, 1368–1374. https://doi.org/10.1021/acsmaterialslett.0c00346.

Kim, Y.-H., Kim, S., Kakekhani, A., Park, J., Park, J., Lee, Y.-H., Xu, H., Nagane, S., Wexler, R.B., Kim, D.-H., et al. (2021b). Comprehensive defect suppression in perovskite nanocrystals for high-efficiency light-emitting diodes. Nat. Photonics *15*, 148–155. https://doi.org/10.1038/s41566-020-00732-4.

Kim, Y.H., Park, J., Kim, S., Kim, J.S., Xu, H., Jeong, S.H., Hu, B., and Lee, T.W. (2022). Exploiting the full advantages of colloidal perovskite nanocrystals for large-area efficient light-emitting diodes. Nat. Nanotechnol. *17*, 590–597. https://doi.org/10.1038/s41565-022-01113-4.

Kirmani, A.R., Kiani, A., Said, M.M., Voznyy, O., Wehbe, N., Walters, G., Barlow, S., Sargent, E.H., Marder, S.R., and Amassian, A. (2016). Remote molecular doping of colloidal quantum dot photovoltaics. ACS Energy Lett. *1*, 922–930. https://doi.org/10.1021/acsenergylett.6b00429.

Kirmani, A.R., Sheikh, A.D., Niazi, M.R., Haque, M.A., Liu, M., de Arquer, F.P.G., Xu, J., Sun, B., Voznyy, O., Gasparini, N., et al. (2018). Overcoming the ambient manufacturability-scalability-performance bottleneck in colloidal quantum dot photovoltaics. Adv. Mater. *30*, e1801661. https://doi.org/10.1002/adma.201801661.

Kirmani, A.R., Woodhouse, M., and Luther, J.M. (2022). Technoeconomic model suggests scaling-up perovskite quantum dots for optoelectronics warrants improved synthesis yield, solvent recycling, and automation. ACS Energy Lett. *7*, 1255–1259. https://doi.org/10.1021/acsenergylett.2c00250.

Kojima, A., Ikegami, M., Teshima, K., and Miyasaka, T. (2012). Highly luminescent lead bromide perovskite nanoparticles synthesized with porous alumina media. Chem. Lett. *41*, 397–399. https://doi.org/10.1246/cl.2012.397.

Koscher, B.A., Swabeck, J.K., Bronstein, N.D., and Alivisatos, A.P. (2017). Essentially trap-free CsPbBr3 colloidal nanocrystals by postsynthetic thiocyanate surface treatment. J. Am. Chem. Soc. *139*, 6566–6569. https://doi.org/10.1021/jacs.7b02817.

Kostopoulou, A., Brintakis, K., Nasikas, N.K., and Stratakis, E. (2019). Perovskite nanocrystals for energy conversion and storage. Nanophotonics *8*, 1607–1640. https://doi.org/10.1515/nanoph-2019-0119.

Kovalenko, M.V., Protesescu, L., and Bodnarchuk, M.I. (2017). Properties and potential optoelectronic applications of lead halide perovskite nanocrystals. Science *358*, 745–750. https://doi.org/10.1126/science.aam7093.

Krieg, F., Ochsenbein, S.T., Yakunin, S., Ten Brinck, S., Aellen, P., Süess, A., Clerc, B., Guggisberg, D., Nazarenko, O., Shynkarenko, Y., et al. (2018). Colloidal CsPbX3 (X = Cl, Br, I) nanocrystals 2.0: zwitterionic capping ligands for improved durability and stability. ACS Energy Lett. *3*, 641–646. https://doi.org/10.1021/acsenergylett.8b00035.

Kubicki, D.J., Prochowicz, D., Salager, E., Rakhmatullin, A., Grey, C.P., Emsley, L., and Stranks, S.D. (2020). Local structure and dynamics in methylammonium, formamidinium, and cesium tin(II) mixed-halide perovskites from (119) Sn solid-state NMR. J. Am. Chem. Soc. *142*, 7813–7826. https://doi.org/10.1021/jacs.0c00647.

Kuno, M., Lee, J.K., Dabbousi, B.O., Mikulec, F.V., and Bawendi, M.G. (1997). The band edge luminescence of surface modified CdSe nanocrystallites: probing the luminescing state. J. Chem. Phys. *106*, 9869–9882. https://doi.org/10.1063/1.473875.

Kwak, K.J., Lee, D.E., Kim, S.J., and Jang, H.W. (2021). Halide perovskites for memristive data storage and artificial synapses. J. Phys. Chem. Lett. *12*, 8999–9010. https://doi.org/10.1021/acs.jpclett.1c02332.

Lamberti, F., Litti, L., De Bastiani, M., Sorrentino, R., Gandini, M., Meneghetti, M., and Petrozza, A. (2017). High-quality, ligands-free, mixed-halide perovskite nanocrystals inks for optoelectronic applications. Adv. Energy Mater. *7*, 1601703. https://doi.org/10.1002/aenm.201601703.

Lan, X., Voznyy, O., García de Arquer, F.P., Liu, M., Xu, J., Proppe, A.H., Walters, G., Fan, F., Tan, H., Liu, M., et al. (2016). 10.6% certified colloidal quantum dot solar cells via solvent-polarity-engineered halide passivation. Nano Lett. *16*, 4630–4634. https://doi.org/10.1021/acs.nanolett.6b01957.

Lan, Y.F., Yao, J.S., Yang, J.N., Song, Y.H., Ru, X.C., Zhang, Q., Feng, L.Z., Chen, T., Song, K.H., and Yao, H.B. (2021). Spectrally stable and efficient pure red CsPbI3 quantum dot light-emitting diodes enabled by sequential ligand post-treatment strategy. Nano Lett. *21*, 8756–8763. https://doi.org/10.1021/acs.nanolett.1c03011.

Law, M., Luther, J.M., Song, Q., Hughes, B.K., Perkins, C.L., and Nozik, A.J. (2008). Structural, optical, and electrical properties of PbSe nanocrystal solids treated thermally or with simple amines. J. Am. Chem. Soc. *130*, 5974–5985. https://doi.org/10.1021/ja800040c.

Lee, D., Kim, M., Woo, H.Y., Chae, J., Lee, D., Jeon, S., Oh, S.J., and Paik, T. (2020a). Heating-up synthesis of cesium bismuth bromide perovskite nanocrystals with tailored composition, morphology, and optical properties. RSC Adv. *10*, 7126–7133. https://doi.org/10.1039/c9ra10106c.

Lee, H.J., Cho, K.T., Paek, S., Lee, Y., Huckaba, A.J., Queloz, V.I.E., Zimmermann, I., Grancini, G., Oveisi, E., Yoo, S.M., et al. (2018). A facile preparative route of nanoscale perovskites over mesoporous metal oxide films and their applications to photosensitizers and light emitters. Adv. Funct. Mater. *28*, 1803801. https://doi.org/10.1002/adfm.201803801.

Lee, J.W., Tan, S., Seok, S.I., Yang, Y., and Park, N.G. (2022a). Rethinking the A cation in halide perovskites. Science *375*, eabj1186. https://doi.org/10.1126/science.abj1186.

Lee, M., Yoo, B., Im, J., Hyeon, T., and Chung, I. (2020b). Electronic band engineering via MI3 (M = Sb, Bi) doping remarkably enhances the air stability of perovskite CsSnI3. ACS Appl. Energy Mater. *3*, 10477–10484. https://doi.org/10.1021/acsaem.0c01484.

Lee, T., Kim, B.J., Lee, H., Hahm, D., Bae, W.K., Lim, J., and Kwak, J. (2022b). Bright and stable quantum dot light-emitting diodes. Adv. Mater. *34*, e2106276. https://doi.org/10.1002/adma.202106276.

Leng, M., Chen, Z., Yang, Y., Li, Z., Zeng, K., Li, K., Niu, G., He, Y., Zhou, Q., and Tang, J. (2016). Lead-free, blue emitting bismuth halide perovskite quantum dots. Angew. Chem. Int. Ed. Engl. *55*, 15012–15016. https://doi.org/10.1002/anie.201608160.

Li, C., Lu, X., Ding, W., Feng, L., Gao, Y., and Guo, Z. (2008). Formability of ABX3 (X = F, Cl, Br, I) halide perovskites. Acta Crystallogr. B *64*, 702–707. https://doi.org/10.1107/S0108768108032734.

Li, F., Lin, F., Huang, Y., Cai, Z., Qiu, L., Zhu, Y., Jiang, Y., Wang, Y., and Chen, X. (2019a). Bromobenzene aliphatic nucleophilic substitution guided controllable and reproducible synthesis of high quality cesium lead bromide perovskite nanocrystals. Inorg. Chem. Front. *6*, 3577–3582. https://doi.org/10.1039/c9qi01095e.

Li, F., Zhou, S., Yuan, J., Qin, C., Yang, Y., Shi, J., Ling, X., Li, Y., and Ma, W. (2019b). Perovskite quantum dot solar cells with 15.6% efficiency and improved stability enabled by an α-CsPbI3/FAPbI3 bilayer structure. ACS Energy Lett. *4*, 2571–2578. https://doi.org/10.1021/acsenergylett.9b01920.

Li, H., Lin, H., Ouyang, D., Yao, C., Li, C., Sun, J., Song, Y., Wang, Y., Yan, Y., Wang, Y., et al. (2021). Efficient and stable red perovskite light-emitting diodes with operational stability >300 h. Adv. Mater. *33*, e2008820. https://doi.org/10.1002/adma.202008820.

Li, J., Xu, L., Wang, T., Song, J., Chen, J., Xue, J., Dong, Y., Cai, B., Shan, Q., Han, B., and Zeng, H. (2017a). 50-Fold EQE improvement up to 6.27% of solution-processed all-inorganic perovskite CsPbBr3 QLEDs via surface ligand density control. Adv. Mater. *29*, 1603885. https://doi.org/10.1002/adma.201603885.

Li, M., Begum, R., Fu, J., Xu, Q., Koh, T.M., Veldhuis, S.A., Grätzel, M., Mathews, N., Mhaisalkar, S., and Sum, T.C. (2018a). Low threshold and efficient multiple exciton generation in halide perovskite nanocrystals. Nat. Commun. *9*, 4197. https://doi.org/10.1038/s41467-018-06596-1.

Li, M., Zhang, X., Matras-Postolek, K., Chen, H.S., and Yang, P. (2018b). An anion-driven Sn2+ exchange reaction in CsPbBr3 nanocrystals towards tunable and high photoluminescence. J. Mater. Chem. C *6*, 5506–5513. https://doi.org/10.1039/c8tc00990b.

Li, X., Tong, Z., Lyu, W., Chen, X., Yang, X., Zhang, Y., Liu, S., Dai, Y., Zhang, Z., Guo, C., and Xu, J. (2022). Underwater quasi-omnidirectional wireless optical communication based on perovskite quantum dots. Opt. Express *30*, 1709–1722. https://doi.org/10.1364/OE.448213.

Li, X., Zhang, K., Li, J., Chen, J., Wu, Y., Liu, K., Song, J., and Zeng, H. (2018c). Heterogeneous nucleation toward polar-solvent-free, fast, and one-pot synthesis of highly uniform perovskite quantum dots for wider color gamut display. Adv. Mater. Interfaces *5*, 1800010. https://doi.org/10.1002/admi.201800010.

Li, X., Ji, M., Li, H., Wang, H., Xu, M., Rong, H., Wei, J., Liu, J., Liu, J., Chen, W., et al. (2020a). Cation/anion exchange reactions toward the syntheses of upgraded nanostructures: principles and applications. Matter *2*, 554–586. https://doi.org/10.1016/j.matt.2019.12.024.

Li, Y., Huang, H., Xiong, Y., Kershaw, S.V., and Rogach, A.L. (2018d). Revealing the formation mechanism of CsPbBr3 perovskite nanocrystals produced via a slowed-down microwave-assisted synthesis. Angew. Chem. Int. Ed. Engl. *57*, 5833–5837. https://doi.org/10.1002/anie.201713332.

Li, Y., Zhou, S., Xiong, Z., Qin, M., Liu, K., Cai, G., Wang, H., Zhao, S., Li, G., Hsu, Y.J., et al. (2020b). Size modulation and heterovalent doping facilitated hybrid organic and perovskite quantum dot bulk heterojunction solar cells. ACS Appl. Energy Mater. *3*, 11359–11367. https://doi.org/10.1021/acsaem.0c02292.

Li, Z., Hofman, E., Li, J., Davis, A.H., Tung, C., Wu, L., and Zheng, W. (2017b). Photoelectrochemically active and environmentally stable CsPbBr3/TiO2 core/shell nanocrystals. Adv. Funct. Mater. *28*, 1704288. https://doi.org/10.1002/adfm.201704288.

Lignos, I., Stavrakis, S., Nedelcu, G., Protesescu, L., deMello, A.J., and Kovalenko, M.V. (2016). Synthesis of cesium lead halide perovskite nanocrystals in a droplet-based microfluidic platform: fast parametric space mapping. Nano Lett. *16*, 1869–1877. https://doi.org/10.1021/acs.nanolett.5b04981.

Lin, K., Xing, J., Quan, L.N., de Arquer, F.P.G., Gong, X., Lu, J., Xie, L., Zhao, W., Zhang, D., Yan, C., et al. (2018). Perovskite light-emitting diodes with external quantum efficiency exceeding 20 per cent. Nature *562*, 245–248. https://doi.org/10.1038/s41586-018-0575-3.

Liu, D., Yao, G., Jin, S., Chen, J., Lou, B., Li, Q., and Sa, R. (2021a). The effects of cation and halide anion on the electronic and optical properties of Ti-based double perovskite: a first-principles calculations. J. Phys. Chem. Solids *150*, 109852. https://doi.org/10.1016/j.jpcs.2020.109852.

Liu, F., Ding, C., Zhang, Y., Ripolles, T.S., Kamisaka, T., Toyoda, T., Hayase, S., Minemoto, T., Yoshino, K., Dai, S., et al. (2017a). Colloidal synthesis of air-stable Alloyed CsSn1-xPbxI3 perovskite nanocrystals for use in solar cells. J. Am. Chem. Soc. *139*, 16708–16719. https://doi.org/10.1021/jacs.7b08628.

Liu, F., Zhang, Y., Ding, C., Kobayashi, S., Izuishi, T., Nakazawa, N., Toyoda, T., Ohta, T., Hayase, S., Minemoto, T., et al. (2017b). Highly luminescent phase-stable CsPbI3 perovskite quantum dots achieving near 100% absolute photoluminescence quantum yield. ACS Nano *11*, 10373–10383. https://doi.org/10.1021/acsnano.7b05442.

Liu, J., Shabbir, B., Wang, C., Wan, T., Ou, Q., Yu, P., Tadich, A., Jiao, X., Chu, D., Qi, D., et al. (2019a). Flexible, printable soft-X-ray detectors based on all-inorganic perovskite quantum dots. Adv. Mater. *31*, e1901644. https://doi.org/10.1002/adma.201901644.

Liu, M., Zhong, G., Yin, Y., Miao, J., Li, K., Wang, C., Xu, X., Shen, C., and Meng, H. (2017c). Aluminum-doped cesium lead bromide perovskite nanocrystals with stable blue photoluminescence used for display backlight. Adv. Sci. *4*, 1700335. https://doi.org/10.1002/advs.201700335.

Liu, N., Sun, R., Wang, L., Ji, Y., Li, N., Cao, B., and Zhang, Y. (2020). Unexpected red emission from Cs4PbI6 nanocrystals. J. Mater. Chem. *8*, 5952–5958. https://doi.org/10.1039/d0ta00211a.

Liu, W., Lin, Q., Li, H., Wu, K., Robel, I., Pietryga, J.M., and Klimov, V.I. (2016). Mn(2+)-Doped lead halide perovskite nanocrystals with dual-color emission controlled by halide content. J. Am. Chem. Soc. *138*, 14954–14961. https://doi.org/10.1021/jacs.6b08085.

Liu, X., Zhang, X., Li, L., Xu, J., Yu, S., Gong, X., Zhang, J., and Yin, H. (2019b). Stable luminescence of CsPbBr3/nCdS core/shell perovskite quantum dots with Al self-passivation layer modification. ACS Appl. Mater. Interfaces *11*, 40923–40931. https://doi.org/10.1021/acsami.9b14967.

Liu, X.K., Xu, W., Bai, S., Jin, Y., Wang, J., Friend, R.H., and Gao, F. (2021b). Metal halide perovskites for light-emitting diodes. Nat. Mater. *20*, 10–21. https://doi.org/10.1038/s41563-020-0784-7.

Liu, Y., Cui, J., Du, K., Tian, H., He, Z., Zhou, Q., Yang, Z., Deng, Y., Chen, D., Zuo, X., et al. (2019c). Efficient blue light-emitting diodes based on quantum-confined bromide perovskite nanostructures. Nat. Photonics *13*, 760–764. https://doi.org/10.1038/s41566-019-0505-4.

Liu, Y., Dong, Y., Zhu, T., Ma, D., Proppe, A., Chen, B., Zheng, C., Hou, Y., Lee, S., Sun, B., et al. (2021c). Bright and stable light-emitting diodes based on perovskite quantum dots in perovskite matrix. J. Am. Chem. Soc. *143*, 15606–15615. https://doi.org/10.1021/jacs.1c02148.

Liu, Y., Li, Z., Xu, J., Dong, Y., Chen, B., Park, S.M., Ma, D., Lee, S., Huang, J.E., Teale, S., et al. (2022). Wide-bandgap perovskite quantum dots in perovskite matrix for sky-blue light-emitting diodes. J. Am. Chem. Soc. *144*, 4009–4016. https://doi.org/10.1021/jacs.1c12556.

Liu, Y., Nag, A., Manna, L., and Xia, Z. (2021d). Lead-free double perovskite Cs2 AgInCl6. Angew. Chem. Int. Ed. Engl. *60*, 11592–11603. https://doi.org/10.1002/anie.202011833.

Locardi, F., Cirignano, M., Baranov, D., Dang, Z., Prato, M., Drago, F., Ferretti, M., Pinchetti, V., Fanciulli, M., Brovelli, S., et al. (2018). Colloidal synthesis of double perovskite Cs2AgInCl6 and Mn-doped Cs2AgInCl6 nanocrystals. J. Am. Chem. Soc. *140*, 12989–12995. https://doi.org/10.1021/jacs.8b07983.

Lou, Y., Niu, Y., Yang, D., Xu, Q., Hu, Y., Shen, Y., Ming, J., Chen, J., Zhang, L., and Zhao, Y. (2018). Rod-shaped thiocyanate-induced abnormal band gap broadening in SCN− doped CsPbBr3 perovskite nanocrystals. Nano Res. *11*, 2715–2723. https://doi.org/10.1007/s12274-017-1901-z.

Lu, C.H., Biesold-McGee, G.V., Liu, Y., Kang, Z., and Lin, Z. (2020a). Doping and ion substitution in colloidal metal halide perovskite nanocrystals. Chem. Soc. Rev. *49*, 4953–5007. https://doi.org/10.1039/c9cs00790c.

Lu, L., Pan, X., Luo, J., and Sun, Z. (2020b). Recent advances and optoelectronic applications of lead-free halide double perovskites. Chemistry *26*, 16975–16984. https://doi.org/10.1002/chem.202000788.

Lu, P., Lu, M., Wang, H., Sui, N., Shi, Z., Yu, W.W., and Zhang, Y. (2019). Metal halide perovskite nanocrystals and their applications in optoelectronic devices. Infomat *1*, 430–459. https://doi.org/10.1002/inf2.12031.

Luo, B., Li, F., Xu, K., Guo, Y., Liu, Y., Xia, Z., and Zhang, J.Z. (2019). B-Site doped lead halide perovskites: synthesis, band engineering, photophysics, and light emission applications. J. Mater. Chem. C *7*, 2781–2808. https://doi.org/10.1039/c8tc05741a.

Luo, J., Wang, X., Li, S., Liu, J., Guo, Y., Niu, G., Yao, L., Fu, Y., Gao, L., Dong, Q., et al. (2018). Efficient and stable emission of warm-white light from lead-free halide double perovskites. Nature *563*, 541–545. https://doi.org/10.1038/s41586-018-0691-0.

Lv, W., Xu, M., Ge, L., Zhu, X., Hong, J., Huang, W., and Chen, R. (2020). Two-phase anion exchange synthesis: multiple passivation for highly efficient and stable CsPbCl3 nanocrystals. J. Mater. Chem. C *8*, 16083–16091. https://doi.org/10.1039/d0tc03602a.

Lyons, J.L. (2021). Effective donor dopants for lead halide perovskites. Chem. Mater. *33*, 6200–6205. https://doi.org/10.1021/acs.chemmater.1c01898.

Maceiczyk, R.M., Dümbgen, K., Lignos, I., Protesescu, L., Kovalenko, M.V., and deMello, A.J. (2017). Microfluidic reactors provide preparative and mechanistic insights into the synthesis of formamidinium lead halide perovskite nanocrystals. Chem. Mater. *29*, 8433–8439. https://doi.org/10.1021/acs.chemmater.7b02998.

Maes, J., Balcaen, L., Drijvers, E., Zhao, Q., De Roo, J., Vantomme, A., Vanhaecke, F., Geiregat, P., and Hens, Z. (2018). Light absorption coefficient of CsPbBr3 perovskite nanocrystals. J. Phys. Chem. Lett. *9*, 3093–3097. https://doi.org/10.1021/acs.jpclett.8b01065.

Malgras, V., Tominaka, S., Ryan, J.W., Henzie, J., Takei, T., Ohara, K., and Yamauchi, Y. (2016). Observation of quantum confinement in monodisperse methylammonium lead halide perovskite nanocrystals embedded in mesoporous silica. J. Am. Chem. Soc. *138*, 13874–13881. https://doi.org/10.1021/jacs.6b05608.

Manzi, A., Tong, Y., Feucht, J., Yao, E.P., Polavarapu, L., Urban, A.S., and Feldmann, J. (2018). Resonantly enhanced multiple exciton generation through below-band-gap multi-photon absorption in perovskite nanocrystals. Nat. Commun. *9*, 1518. https://doi.org/10.1038/s41467-018-03965-8.

Mao, L., Stoumpos, C.C., and Kanatzidis, M.G. (2019). Two-dimensional hybrid halide perovskites: principles and promises. J. Am. Chem. Soc. *141*, 1171–1190. https://doi.org/10.1021/jacs.8b10851.

Marin, R., and Jaque, D. (2021). Doping lanthanide ions in colloidal semiconductor nanocrystals for brighter photoluminescence. Chem. Rev. *121*, 1425–1462. https://doi.org/10.1021/acs.chemrev.0c00692.

Mary Vijila, C.V., Rajeev Kumar, K., and Jayaraj, M.K. (2019). Stokes shift engineered, stable core-shell perovskite nanoparticle – poly(methyl

methacrylate) composites with high photoluminescence quantum yield. Opt. Mater. *94*, 241–248. https://doi.org/10.1016/j.optmat.2019.05.046.

Mei, L., Huang, R., Shen, C., Hu, J., Wang, P., Xu, Z., Huang, Z., and Zhu, L. (2022). Hybrid halide perovskite-based near-infrared photodetectors and imaging arrays. Adv. Opt. Mater. *10*, 2102656. https://doi.org/10.1002/adom.202102656.

Meng, J.M., Yang, Z.X., Patil, S.B., Lin, J.C., Yeh, C.H., Chen, Y.C., Pao, C.W., Chen, J.L., Chen, W.Y., Lu, C.W., et al. (2021). Facile fabrication of highly stable and wavelength-tunable tin based perovskite materials with enhanced quantum yield via the cation transformation reaction. J. Phys. Chem. Lett. *12*, 8763–8769. https://doi.org/10.1021/acs.jpclett.1c02542.

Miao, W., Guo, C., Li, D., Li, T., Wang, P., Yang, Y., Liu, D., and Wang, T. (2021). Efficient hole transfer via CsPbBr3 quantum dots doping toward high-performance organic solar cells. Sol. RRL *5*, 2100499. https://doi.org/10.1002/solr.202100499.

Milstein, T.J., Kroupa, D.M., and Gamelin, D.R. (2018). Picosecond quantum cutting generates photoluminescence quantum yields over 100% in ytterbium-doped CsPbCl3 nanocrystals. Nano Lett. *18*, 3792–3799. https://doi.org/10.1021/acs.nanolett.8b01066.

Mittal, M., Jana, A., Sarkar, S., Mahadevan, P., and Sapra, S. (2016). Size of the organic cation tunes the band gap of colloidal organolead bromide perovskite nanocrystals. J. Phys. Chem. Lett. *7*, 3270–3277. https://doi.org/10.1021/acs.jpclett.6b01406.

Mokhlisse, R., Couzi, M., Chanh, N.B., Haget, Y., Hauw, C., and Meresse, A. (1985). Raman scattering and X-ray diffraction study of structural phase transitions in the perovskite-type layer compound (C3H7NH3)2CdCl4. J. Phys. Chem. Solids *46*, 187–195. https://doi.org/10.1016/0022-3697(85)90033-2.

Mondal, N., De, A., and Samanta, A. (2018). Achieving near-unity photoluminescence efficiency for blue-violet-emitting perovskite nanocrystals. ACS Energy Lett. *4*, 32–39. https://doi.org/10.1021/acsenergylett.8b01909.

Montanarella, F., McCall, K.M., Sakhatskyi, K., Yakunin, S., Trtik, P., Bernasconi, C., Cherniukh, I., Mannes, D., Bodnarchuk, M.I., Strobl, M., et al. (2021). Highly concentrated, zwitterionic ligand-capped Mn(2+):CsPb(Br x Cl1-x )3 nanocrystals as bright scintillators for fast neutron imaging. ACS Energy Lett. *6*, 4365–4373. https://doi.org/10.1021/acsenergylett.1c01923.

Moreels, I., Lambert, K., Smeets, D., De Muynck, D., Nollet, T., Martins, J.C., Vanhaecke, F., Vantomme, A., Delerue, C., Allan, G., and Hens, Z. (2009). Size-dependent optical properties of colloidal PbS quantum dots. ACS Nano *3*, 3023–3030. https://doi.org/10.1021/nn900863a.

Najman, S., Chen, H.A., Chen, H.Y.T., and Pao, C.W. (2021). Surface structures and equilibrium shapes of layered 2D Ruddlesden-Popper perovskite crystals from density functional theory calculations. Mater. Today Commun. *26*, 101745. https://doi.org/10.1016/j.mtcomm.2020.101745.

Ni, Z., Pi, X., Zhou, S., Nozaki, T., Grandidier, B., and Yang, D. (2016). Size-dependent structures and optical absorption of boron-hyperdoped silicon nanocrystals. Adv. Opt. Mater. *4*, 700–707. https://doi.org/10.1002/adom.201500706.

Ni, Z., Zhou, S., Zhao, S., Peng, W., Yang, D., and Pi, X. (2019). Silicon nanocrystals: unfading silicon materials for optoelectronics. Mater. Sci. Eng. R Rep. *138*, 85–117. https://doi.org/10.1016/j.mser.2019.06.001.

Pan, A., He, B., Fan, X., Liu, Z., Urban, J.J., Alivisatos, A.P., He, L., and Liu, Y. (2016a). Insight into the ligand-mediated synthesis of colloidal CsPbBr3 perovskite nanocrystals: the role of organic acid, base, and cesium precursors. ACS Nano *10*, 7943–7954. https://doi.org/10.1021/acsnano.6b03863.

Pan, G., Bai, X., Xu, W., Chen, X., Zhou, D., Zhu, J., Shao, H., Zhai, Y., Dong, B., Xu, L., and Song, H. (2018a). Impurity ions codoped cesium lead halide perovskite nanocrystals with bright white light emission toward ultraviolet-white light-emitting diode. ACS Appl. Mater. Interfaces *10*, 39040–39048. https://doi.org/10.1021/acsami.8b14275.

Pan, G., Bai, X., Yang, D., Chen, X., Jing, P., Qu, S., Zhang, L., Zhou, D., Zhu, J., Xu, W., et al. (2017a). Doping lanthanide into perovskite nanocrystals: highly improved and expanded optical properties. Nano Lett. *17*, 8005–8011. https://doi.org/10.1021/acs.nanolett.7b04575.

Pan, J., Quan, L.N., Zhao, Y., Peng, W., Murali, B., Sarmah, S.P., Yuan, M., Sinatra, L., Alyami, N.M., Liu, J., et al. (2016b). Highly efficient perovskite-quantum-dot light-emitting diodes by surface engineering. Adv. Mater. *28*, 8718–8725. https://doi.org/10.1002/adma.201600784.

Pan, J., Shang, Y., Yin, J., De Bastiani, M., Peng, W., Dursun, I., Sinatra, L., El-Zohry, A.M., Hedhili, M.N., Emwas, A.H., et al. (2018b). Bidentate ligand-passivated CsPbI3 perovskite nanocrystals for stable near-unity photoluminescence quantum yield and efficient red light-emitting diodes. J. Am. Chem. Soc. *140*, 562–565. https://doi.org/10.1021/jacs.7b10647.

Pan, Q., Hu, H., Zou, Y., Chen, M., Wu, L., Yang, D., Yuan, X., Fan, J., Sun, B., and Zhang, Q. (2017b). Microwave-assisted synthesis of high-quality "all-inorganic" CsPbX3 (X = Cl, Br, I) perovskite nanocrystals and their application in light emitting diodes. J. Mater. Chem. C *5*, 10947–10954. https://doi.org/10.1039/c7tc03774k.

Park, N.-G., and Zhu, K. (2020). Scalable fabrication and coating methods for perovskite solar cells and solar modules. Nat. Rev. Mater. *5*, 333–350. https://doi.org/10.1038/s41578-019-0176-2.

Parobek, D., Dong, Y., Qiao, T., Rossi, D., and Son, D.H. (2017). Photoinduced anion exchange in cesium lead halide perovskite nanocrystals. J. Am. Chem. Soc. *139*, 4358–4361. https://doi.org/10.1021/jacs.7b01480.

Parobek, D., Roman, B.J., Dong, Y., Jin, H., Lee, E., Sheldon, M., and Son, D.H. (2016). Exciton-to-Dopant energy transfer in Mn-doped cesium lead halide perovskite nanocrystals. Nano Lett. *16*, 7376–7380. https://doi.org/10.1021/acs.nanolett.6b02772.

Periyal, S.S., Jagadeeswararao, M., Ng, S.E., John, R.A., and Mathews, N. (2020). Halide perovskite quantum dots photosensitized-amorphous oxide transistors for multimodal synapses. Adv. Mater. Technol. *5*, 2000514. https://doi.org/10.1002/admt.202000514.

Pi, X.D., Liptak, R.W., Deneen Nowak, J., Wells, N.P., Carter, C.B., Campbell, S.A., and Kortshagen, U. (2008). Air-stable full-visible-spectrum emission from silicon nanocrystals synthesized by an all-gas-phase plasma approach. Nanotechnology *19*, 245603. https://doi.org/10.1088/0957-4484/19/24/245603.

Pradhan, B., Das, S., Li, J., Chowdhury, F., Cherusseri, J., Pandey, D., Dev, D., Krishnaprasad, A., Barrios, E., Towers, A., et al. (2020). Ultrasensitive and ultrathin phototransistors and photonic synapses using perovskite quantum dots grown from graphene lattice. Sci. Adv. *6*, eaay5225. https://doi.org/10.1126/sciadv.aay5225.

Prochowicz, D., Franckevičius, M., Cieślak, A.M., Zakeeruddin, S.M., Grätzel, M., and Lewiński, J. (2015). Mechanosynthesis of the hybrid perovskite CH3NH3PbI3: characterization and the corresponding solar cell efficiency. J. Mater. Chem. *3*, 20772–20777. https://doi.org/10.1039/c5ta04904k.

Prochowicz, D., Saski, M., Yadav, P., Grätzel, M., and Lewiński, J. (2019). Mechanoperovskites for photovoltaic applications: preparation, characterization, and device fabrication. Acc. Chem. Res. *52*, 3233–3243. https://doi.org/10.1021/acs.accounts.9b00454.

Protesescu, L., Yakunin, S., Bodnarchuk, M.I., Bertolotti, F., Masciocchi, N., Guagliardi, A., and Kovalenko, M.V. (2016). Monodisperse formamidinium lead bromide nanocrystals with bright and stable green photoluminescence. J. Am. Chem. Soc. *138*, 14202–14205. https://doi.org/10.1021/jacs.6b08900.

Protesescu, L., Yakunin, S., Bodnarchuk, M.I., Krieg, F., Caputo, R., Hendon, C.H., Yang, R.X., Walsh, A., and Kovalenko, M.V. (2015). Nanocrystals of cesium lead halide perovskites (CsPbX(3), X = Cl, Br, and I): novel optoelectronic materials showing bright emission with wide color gamut. Nano Lett. *15*, 3692–3696. https://doi.org/10.1021/nl5048779.

Protesescu, L., Yakunin, S., Kumar, S., Bär, J., Bertolotti, F., Masciocchi, N., Guagliardi, A., Grotevent, M., Shorubalko, I., Bodnarchuk, M.I., et al. (2017). Dismantling the "red wall" of colloidal perovskites: highly luminescent formamidinium and formamidinium-cesium lead iodide nanocrystals. ACS Nano *11*, 3119–3134. https://doi.org/10.1021/acsnano.7b00116.

Protesescu, L., Yakunin, S., Nazarenko, O., Dirin, D.N., and Kovalenko, M.V. (2018). Low-cost synthesis of highly luminescent colloidal lead halide perovskite nanocrystals by wet ball milling. ACS Appl. Nano Mater. *1*, 1300–1308. https://doi.org/10.1021/acsanm.8b00038.

Puthenpurayil, J., Cheng, O.H.C., Qiao, T., Rossi, D., and Son, D.H. (2019). On the determination of absorption cross section of colloidal lead halide perovskite quantum dots. J. Chem. Phys. *151*, 154706. https://doi.org/10.1063/1.5126039.

Qiao, G.Y., Guan, D., Yuan, S., Rao, H., Chen, X., Wang, J.A., Qin, J.S., Xu, J.J., and Yu, J. (2021). Perovskite quantum dots encapsulated in a mesoporous metal-organic framework as synergistic photocathode materials. J. Am. Chem. Soc. *143*, 14253–14260. https://doi.org/10.1021/jacs.1c05907.

Qin, Z., Zhang, C., Chen, L., Yu, T., Wang, X., and Xiao, M. (2021). Electrical switching of optical gain in perovskite semiconductor nanocrystals. Nano Lett. *21*, 7831–7838. https://doi.org/10.1021/acs.nanolett.1c02880.

Qiu, T., Hu, Y., Xu, F., Yan, Z., Bai, F., Jia, G., and Zhang, S. (2018). Recent advances in one-dimensional halide perovskites for optoelectronic applications. Nanoscale *10*, 20963–20989. https://doi.org/10.1039/c8nr05862h.

Qu, L., and Peng, X. (2002). Control of photoluminescence properties of CdSe nanocrystals in growth. J. Am. Chem. Soc. *124*, 2049–2055. https://doi.org/10.1021/ja017002j.

Quan, L.N., Yuan, M., Comin, R., Voznyy, O., Beauregard, E.M., Hoogland, S., Buin, A., Kirmani, A.R., Zhao, K., Amassian, A., et al. (2016). Ligand-stabilized reduced-dimensionality perovskites. J. Am. Chem. Soc. *138*, 2649–2655. https://doi.org/10.1021/jacs.5b11740.

Raino, G., Becker, M.A., Bodnarchuk, M.I., Mahrt, R.F., Kovalenko, M.V., and Stöferle, T. (2018). Superfluorescence from lead halide perovskite quantum dot superlattices. Nature *563*, 671–675. https://doi.org/10.1038/s41586-018-0683-0.

Ranke, D., Perini, C.A.R., and Correa-Baena, J.P. (2021). In data science we trust: machine learning for stable halide perovskites. Matter *4*, 1092–1094. https://doi.org/10.1016/j.matt.2021.03.007.

Rao, L., Tang, Y., Song, C., Xu, K., Vickers, E.T., Bonabi Naghadeh, S., Ding, X., Li, Z., and Zhang, J.Z. (2018). Polar-solvent-free synthesis of highly photoluminescent and stable CsPbBr3 nanocrystals with controlled shape and size by ultrasonication. Chem. Mater. *31*, 365–375. https://doi.org/10.1021/acs.chemmater.8b03298.

Rastogi, P., Chu, A., Gréboval, C., Qu, J., Noumbé, U.N., Chee, S.S., Goyal, M., Khalili, A., Xu, X.Z., Cruguel, H., et al. (2020). Pushing absorption of perovskite nanocrystals into the infrared. Nano Lett. *20*, 3999–4006. https://doi.org/10.1021/acs.nanolett.0c01302.

Ren, J., Li, T., Zhou, X., Dong, X., Shorokhov, A.V., Semenov, M.B., Krevchik, V.D., and Wang, Y. (2019). Encapsulating all-inorganic perovskite quantum dots into mesoporous metal organic frameworks with significantly enhanced stability for optoelectronic applications. Chem. Eng. J. *358*, 30–39. https://doi.org/10.1016/j.cej.2018.09.149.

Ricciarelli, D., Meggiolaro, D., Belanzoni, P., Alothman, A.A., Mosconi, E., and De Angelis, F. (2021). Energy vs charge transfer in manganese-doped lead halide perovskites. ACS Energy Lett. *6*, 1869–1878. https://doi.org/10.1021/acsenergylett.1c00553.

Rubino, A., Caliò, L., García-Bennett, A., Calvo, M.E., and Míguez, H. (2020). Mesoporous matrices as hosts for metal halide perovskite nanocrystals. Adv. Opt. Mater. *8*, 1901868. https://doi.org/10.1002/adom.201901868.

Saidaminov, M.I., Mohammed, O.F., and Bakr, O.M. (2017). Low-dimensional-networked metal halide perovskites: the next big thing. ACS Energy Lett. *2*, 889–896. https://doi.org/10.1021/acsenergylett.6b00705.

Saki, Z., Byranvand, M.M., Taghavinia, N., Kedia, M., and Saliba, M. (2021). Solution-processed perovskite thin-films: the journey from lab- to large-scale solar cells. Energy Environ. Sci. *14*, 5690–5722. https://doi.org/10.1039/d1ee02018h.

Sanehira, E.M., Marshall, A.R., Christians, J.A., Harvey, S.P., Ciesielski, P.N., Wheeler, L.M., Schulz, P., Lin, L.Y., Beard, M.C., and Luther, J.M. (2017). Enhanced mobility CsPbI3 quantum dot arrays for record-efficiency, high-voltage photovoltaic cells. Sci. Adv. *3*, eaao4204. https://doi.org/10.1126/sciadv.aao4204.

Sargent, E.H. (2012). Colloidal quantum dot solar cells. Nat. Photonics *6*, 133–135. https://doi.org/10.1038/nphoton.2012.33.

Saruyama, M., Sato, R., and Teranishi, T. (2021). Transformations of ionic nanocrystals via full and partial ion exchange reactions. Acc. Chem. Res. *54*, 765–775. https://doi.org/10.1021/acs.accounts.0c00701.

Schmidt, L.C., Pertegás, A., González-Carrero, S., Malinkiewicz, O., Agouram, S., Mínguez Espallargas, G., Bolink, H.J., Galian, R.E., and Pérez-Prieto, J. (2014). Nontemplate synthesis of CH3NH3PbBr3 perovskite nanoparticles. J. Am. Chem. Soc. *136*, 850–853. https://doi.org/10.1021/ja4109209.

Shamsi, J., Rainò, G., Kovalenko, M.V., and Stranks, S.D. (2021). To nano or not to nano for bright halide perovskite emitters. Nat. Nanotechnol. *16*, 1164–1168. https://doi.org/10.1038/s41565-021-01005-z.

Shamsi, J., Urban, A.S., Imran, M., De Trizio, L., and Manna, L. (2019). Metal halide perovskite nanocrystals: synthesis, post-synthesis modifications, and their optical properties. Chem. Rev. *119*, 3296–3348. https://doi.org/10.1021/acs.chemrev.8b00644.

Shangguan, Z., Zheng, X., Zhang, J., Lin, W., Guo, W., Li, C., Wu, T., Lin, Y., and Chen, Z. (2020). The stability of metal halide perovskite nanocrystals-A key issue for the application on quantum-dot-based micro light-emitting diodes display. Nanomaterials *10*, 1375. https://doi.org/10.3390/nano10071375.

Shen, W., Zhang, J., Dong, R., Chen, Y., Yang, L., Chen, S., Su, Z., Dai, Y., Cao, K., Liu, L., et al. (2021). Stable and efficient red perovskite light-emitting diodes based on Ca(2+)-doped CsPbI3 nanocrystals. Research *2021*, 9829374. https://doi.org/10.34133/2021/9829374.

Shen, X., Sun, C., Bai, X., Zhang, X., Wang, Y., Wang, Y., Song, H., and Yu, W.W. (2018). Efficient and stable CsPb(Br/I)3@Anthracene composites for white light-emitting devices. ACS Appl. Mater. Interfaces *10*, 16768–16775. https://doi.org/10.1021/acsami.8b03158.

Sheng, Y., Zhao, A., Yuan, S., Liu, C., Zhang, X., Di, Y., and Gan, Z. (2020). Dynamics of anion exchange in cesium lead halide (CsPbX3) perovskite nanocrystals. New J. Chem. *44*, 20592–20599. https://doi.org/10.1039/d0nj04987e.

Sikorski, C., and Merkt, U. (1989). Spectroscopy of electronic states in InSb quantum dots. Phys. Rev. Lett. *62*, 2164–2167. https://doi.org/10.1103/PhysRevLett.62.2164.

Singh, K.J., Fan, X., Sadhu, A.S., Lin, C.H., Liou, F.J., Wu, T., Lu, Y.J., He, J.H., Chen, Z., Wu, T., and Kuo, H.C. (2021). CsPbBr3 perovskite quantum-dot paper exhibiting a highest 3 dB bandwidth and realizing a flexible white-light system for visible-light communication. Photon. Res. *9*, 2341–2350. https://doi.org/10.1364/Prj.434270.

Soltani, R., Puscher, B.M.D., Katbab, A.A., Levchuk, I., Kazerouni, N., Gasparini, N., Camaioni, N., Osvet, A., Batentschuk, M., Fink, R.H., et al. (2018). Improved charge carrier dynamics in polymer/perovskite nanocrystal based hybrid ternary solar cells. Phys. Chem. Chem. Phys. *20*, 23674–23683. https://doi.org/10.1039/c8cp03743d.

Song, J., Li, J., Li, X., Xu, L., Dong, Y., and Zeng, H. (2015). Quantum dot light-emitting diodes based on inorganic perovskite cesium lead halides (CsPbX3). Adv. Mater. *27*, 7162–7167. https://doi.org/10.1002/adma.201502567.

Song, J., Li, J., Xu, L., Li, J., Zhang, F., Han, B., Shan, Q., and Zeng, H. (2018). Room-temperature triple-ligand surface engineering synergistically boosts ink stability, recombination dynamics, and charge injection toward EQE-11.6% perovskite QLEDs. Adv. Mater. *30*, e1800764. https://doi.org/10.1002/adma.201800764.

Stoumpos, C.C., Cao, D.H., Clark, D.J., Young, J., Rondinelli, J.M., Jang, J.I., Hupp, J.T., and Kanatzidis, M.G. (2016). Ruddlesden–popper hybrid lead iodide perovskite 2D homologous semiconductors. Chem. Mater. *28*, 2852–2867. https://doi.org/10.1021/acs.chemmater.6b00847.

Sukharevska, N., Bederak, D., Goossens, V.M., Momand, J., Duim, H., Dirin, D.N., Kovalenko, M.V., Kooi, B.J., and Loi, M.A. (2021). Scalable PbS quantum dot solar cell production by blade coating from stable inks. ACS Appl. Mater. Interfaces *13*, 5195–5207. https://doi.org/10.1021/acsami.0c18204.

Sun, S., Yuan, D., Xu, Y., Wang, A., and Deng, Z. (2016). Ligand-mediated synthesis of shape-controlled cesium lead halide perovskite nanocrystals via reprecipitation process at room temperature. ACS Nano *10*, 3648–3657. https://doi.org/10.1021/acsnano.5b08193.

Sun, S., Tiihonen, A., Oviedo, F., Liu, Z., Thapa, J., Zhao, Y., Hartono, N.T.P., Goyal, A., Heumueller, T., Batali, C., et al. (2021). A data fusion approach to optimize compositional stability of halide perovskites. Matter *4*, 1305–1322. https://doi.org/10.1016/j.matt.2021.01.008.

Sutherland, B.R., and Sargent, E.H. (2016). Perovskite photonic sources. Nat. Photonics *10*, 295–302. https://doi.org/10.1038/Nphoton.2016.62.

Swarnkar, A., Marshall, A.R., Sanehira, E.M., Chernomordik, B.D., Moore, D.T., Christians, J.A., Chakrabarti, T., and Luther, J.M. (2016). Quantum dot-induced phase stabilization of

alpha-CsPbI3 perovskite for high-efficiency photovoltaics. Science *354*, 92–95. https://doi.org/10.1126/science.aag2700.

Tablero Crespo, C. (2019). The effect of the halide anion on the optical properties of lead halide perovskites. Sol. Energy Mater. Sol. Cells *195*, 269–273. https://doi.org/10.1016/j.solmat.2019.03.023.

Tan, Z.K., Moghaddam, R.S., Lai, M.L., Docampo, P., Higler, R., Deschler, F., Price, M., Sadhanala, A., Pazos, L.M., Credgington, D., et al. (2014). Bright light-emitting diodes based on organometal halide perovskite. Nat. Nanotechnol. *9*, 687–692. https://doi.org/10.1038/nnano.2014.149.

Tang, B., Li, G., Ru, X., Gao, Y., Li, Z., Shen, H., Yao, H.B., Fan, F., and Du, J. (2022). Evaluating lead halide perovskite nanocrystals as a spin laser gain medium. Nano Lett. *22*, 658–664. https://doi.org/10.1021/acs.nanolett.1c03671.

ten Brinck, S., and Infante, I. (2016). Surface termination, morphology, and bright photoluminescence of cesium lead halide perovskite nanocrystals. ACS Energy Lett. *1*, 1266–1272. https://doi.org/10.1021/acsenergylett.6b00595.

ten Brinck, S., Zaccaria, F., and Infante, I. (2019). Defects in lead halide perovskite nanocrystals: analogies and (many) differences with the bulk. ACS Energy Lett. *4*, 2739–2747. https://doi.org/10.1021/acsenergylett.9b01945.

Tong, Y., Bladt, E., Aygüler, M.F., Manzi, A., Milowska, K.Z., Hintermayr, V.A., Docampo, P., Bals, S., Urban, A.S., Polavarapu, L., and Feldmann, J. (2016). Highly luminescent cesium lead halide perovskite nanocrystals with tunable composition and thickness by ultrasonication. Angew. Chem. Int. Ed. Engl. *55*, 13887–13892. https://doi.org/10.1002/anie.201605909.

Travis, W., Glover, E.N.K., Bronstein, H., Scanlon, D.O., and Palgrave, R.G. (2016). On the application of the tolerance factor to inorganic and hybrid halide perovskites: a revised system. Chem. Sci. *7*, 4548–4556. https://doi.org/10.1039/c5sc04845a.

Tsai, H., Nie, W., Blancon, J.C., Stoumpos, C.C., Asadpour, R., Harutyunyan, B., Neukirch, A.J., Verduzco, R., Crochet, J.J., Tretiak, S., et al. (2016). High-efficiency two-dimensional Ruddlesden-Popper perovskite solar cells. Nature *536*, 312–316. https://doi.org/10.1038/nature18306.

Tsai, H., Shrestha, S., Vilá, R.A., Huang, W., Liu, C., Hou, C.-H., Huang, H.-H., Wen, X., Li, M., Wiederrecht, G., et al. (2021). Bright and stable light-emitting diodes made with perovskite nanocrystals stabilized in metal–organic frameworks. Nat. Photonics *15*, 843–849. https://doi.org/10.1038/s41566-021-00857-0.

Umemoto, K., Ebe, H., Sato, R., Enomoto, J., Oshita, N., Kimura, T., Inose, T., Nakamura, T., Chiba, T., Asakura, S., et al. (2020). Simple production of highly luminescent organometal halide perovskite nanocrystals using ultrasound-assisted bead milling. ACS Sustain. Chem. Eng. *8*, 16469–16476. https://doi.org/10.1021/acssuschemeng.0c05171.

van der Stam, W., Geuchies, J.J., Altantzis, T., van den Bos, K.H.W., Meeldijk, J.D., Van Aert, S., Bals, S., Vanmaekelbergh, D., and de Mello Donega, C. (2017). Highly emissive divalent-ion-doped colloidal CsPb1-xMxBr3 perovskite nanocrystals through cation exchange. J. Am. Chem. Soc. *139*, 4087–4097. https://doi.org/10.1021/jacs.6b13079.

van Embden, J., Chesman, A.S.R., and Jasieniak, J.J. (2015). The heat-up synthesis of colloidal nanocrystals. Chem. Mater. *27*, 2246–2285. https://doi.org/10.1021/cm5028964.

Vashishtha, P., and Halpert, J.E. (2017). Field-driven ion migration and color instability in red-emitting mixed halide perovskite nanocrystal light-emitting diodes. Chem. Mater. *29*, 5965–5973. https://doi.org/10.1021/acs.chemmater.7b01609.

Volonakis, G., Filip, M.R., Haghighirad, A.A., Sakai, N., Wenger, B., Snaith, H.J., and Giustino, F. (2016). Lead-free halide double perovskites via heterovalent substitution of noble metals. J. Phys. Chem. Lett. *7*, 1254–1259. https://doi.org/10.1021/acs.jpclett.6b00376.

Volonakis, G., Haghighirad, A.A., Milot, R.L., Sio, W.H., Filip, M.R., Wenger, B., Johnston, M.B., Herz, L.M., Snaith, H.J., and Giustino, F. (2017). Cs2InAgCl6: a new lead-free halide double perovskite with direct band gap. J. Phys. Chem. Lett. *8*, 772–778. https://doi.org/10.1021/acs.jpclett.6b02682.

Voznyy, O., Levina, L., Fan, F., Walters, G., Fan, J.Z., Kiani, A., Ip, A.H., Thon, S.M., Proppe, A.H., Liu, M., and Sargent, E.H. (2017). Origins of Stokes shift in PbS nanocrystals. Nano Lett. *17*, 7191–7195. https://doi.org/10.1021/acs.nanolett.7b01843.

Wang, D., Zhang, D., and Sadtler, B. (2020a). Irreversibility in anion exchange between cesium lead bromide and iodide nanocrystals imaged by single-particle fluorescence. J. Phys. Chem. C *124*, 27158–27168. https://doi.org/10.1021/acs.jpcc.0c08323.

Wang, H., Sui, N., Bai, X., Zhang, Y., Rice, Q., Seo, F.J., Zhang, Q., Colvin, V.L., and Yu, W.W. (2018a). Emission recovery and stability enhancement of inorganic perovskite quantum dots. J. Phys. Chem. Lett. *9*, 4166–4173. https://doi.org/10.1021/acs.jpclett.8b01752.

Wang, J., Dong, J., Lu, F., Sun, C., Zhang, Q., and Wang, N. (2019a). Two-dimensional lead-free halide perovskite materials and devices. J. Mater. Chem. *7*, 23563–23576. https://doi.org/10.1039/c9ta06455a.

Wang, K., Dai, S., Zhao, Y., Wang, Y., Liu, C., and Huang, J. (2019b). Light-stimulated synaptic transistors fabricated by a facile solution process based on inorganic perovskite quantum dots and organic semiconductors. Small *15*, e1900010. https://doi.org/10.1002/smll.201900010.

Wang, K.H., Wu, L., Li, L., Yao, H.B., Qian, H.S., and Yu, S.H. (2016a). Large-scale synthesis of highly luminescent perovskite-related CsPb2 Br5 nanoplatelets and their fast anion exchange. Angew. Chem. Int. Ed. Engl. *55*, 8328–8332. https://doi.org/10.1002/anie.201602787.

Wang, L., Fu, K., Sun, R., Lian, H., Hu, X., and Zhang, Y. (2019c). Ultra-stable CsPbBr3 perovskite nanosheets for X-ray imaging screen. Nano-Micro Lett. *11*, 52. https://doi.org/10.1007/s40820-019-0283-z.

Wang, L., Williams, N.E., Malachosky, E.W., Otto, J.P., Hayes, D., Wood, R.E., Guyot-Sionnest, P., and Engel, G.S. (2017a). Scalable ligand-mediated transport synthesis of organic-inorganic hybrid perovskite nanocrystals with resolved electronic structure and ultrafast dynamics. ACS Nano *11*, 2689–2696. https://doi.org/10.1021/acsnano.6b07574.

Wang, N., Cheng, L., Ge, R., Zhang, S., Miao, Y., Zou, W., Yi, C., Sun, Y., Cao, Y., Yang, R., et al. (2016b). Perovskite light-emitting diodes based on solution-processed self-organized multiple quantum wells. Nat. Photonics *10*, 699–704. https://doi.org/10.1038/nphoton.2016.185.

Wang, S., Bi, C., Yuan, J., Zhang, L., and Tian, J. (2017b). Original core–shell structure of cubic CsPbBr3@Amorphous CsPbBrx perovskite quantum dots with a high blue photoluminescence quantum yield of over 80. ACS Energy Lett. *3*, 245–251. https://doi.org/10.1021/acsenergylett.7b01243.

Wang, X., Li, W., Liao, J., and Kuang, D. (2019d). Recent advances in halide perovskite single-crystal thin films: fabrication methods and optoelectronic applications. Sol. RRL *3*, 1800294. https://doi.org/10.1002/solr.201800294.

Wang, Y., Jia, B., Wang, J., Xue, P., Xiao, Y., Li, T., Wang, J., Lu, H., Tang, Z., Lu, X., et al. (2020b). High-efficiency perovskite quantum dot hybrid nonfullerene organic solar cells with near-zero driving force. Adv. Mater. *32*, e2002066. https://doi.org/10.1002/adma.202002066.

Wang, Y., Li, X., Nalla, V., Zeng, H., and Sun, H. (2017c). Solution-processed low threshold vertical cavity surface emitting lasers from all-inorganic perovskite nanocrystals. Adv. Funct. Mater. *27*, 1605088. https://doi.org/10.1002/adfm.201605088.

Wang, Y., Lv, Z., Chen, J., Wang, Z., Zhou, Y., Zhou, L., Chen, X., and Han, S.T. (2018b). Photonic synapses based on inorganic perovskite quantum dots for neuromorphic computing. Adv. Mater. *30*, e1802883. https://doi.org/10.1002/adma.201802883.

Wang, Y., Zhi, M., Chang, Y.Q., Zhang, J.P., and Chan, Y. (2018c). Stable, ultralow threshold amplified spontaneous emission from CsPbBr3 nanoparticles exhibiting trion gain. Nano Lett. *18*, 4976–4984. https://doi.org/10.1021/acs.nanolett.8b01817.

Wang, Y.K., Singh, K., Li, J.Y., Dong, Y., Wang, X.Q., Pina, J.M., Yu, Y.J., Sabatini, R., Liu, Y., Ma, D., et al. (2022). In situ inorganic ligand replenishment enables bandgap stability in mixed-halide perovskite quantum dot solids. Adv. Mater. *34*, e2200854. https://doi.org/10.1002/adma.202200854.

Wang, Y.K., Yuan, F., Dong, Y., Li, J.Y., Johnston, A., Chen, B., Saidaminov, M.I., Zhou, C., Zheng, X., Hou, Y., et al. (2021a). All-inorganic quantum-dot LEDs based on a phase-stabilized alpha-CsPbI3 perovskite. Angew. Chem. Int. Ed. Engl. *60*, 16164–16170. https://doi.org/10.1002/anie.202104812.

Wang, Z., Sun, R., Liu, N., Fan, H., Hu, X., Shen, D., Zhang, Y., and Liu, H. (2021b). X-Ray imager of 26-μm resolution achieved by perovskite assembly. Nano Res. *15*, 2399–2404. https://doi.org/10.1007/s12274-021-3808-y.

Wang, Z., Wei, Z., Cai, Y., Wang, L., Li, M., Liu, P., Xie, R., Wang, L., Wei, G., and Fu, H.Y. (2021c). Encapsulation-enabled perovskite-PMMA films combining a micro-LED for high-speed white-light communication. ACS Appl. Mater. Interfaces *13*, 54143–54151. https://doi.org/10.1021/acsami.1c15873.

Wei, C., Su, W., Li, J., Xu, B., Shan, Q., Wu, Y., Zhang, F., Luo, M., Xiang, H., Cui, Z., and Zeng, H. (2022). A universal ternary-solvent-ink strategy toward efficient inkjet-printed perovskite quantum dot light-emitting diodes. Adv. Mater. *34*, e2107798. https://doi.org/10.1002/adma.202107798.

Wei, Y., Cheng, Z., and Lin, J. (2019). An overview on enhancing the stability of lead halide perovskite quantum dots and their applications in phosphor-converted LEDs. Chem. Soc. Rev. *48*, 310–350. https://doi.org/10.1039/c8cs00740c.

Wen, J., Hu, H., Wen, G., Wang, S., Sun, Z., and Ye, S. (2021). Thin film transistors integrating CsPbBr3 quantum dots for optoelectronic memory application. J. Phys. D Appl. Phys. *54*, 114002. https://doi.org/10.1088/1361-6463/abcbc0.

Wheeler, L.M., Sanehira, E.M., Marshall, A.R., Schulz, P., Suri, M., Anderson, N.C., Christians, J.A., Nordlund, D., Sokaras, D., Kroll, T., et al. (2018). Targeted ligand-exchange chemistry on cesium lead halide perovskite quantum dots for high-efficiency photovoltaics. J. Am. Chem. Soc. *140*, 10504–10513. https://doi.org/10.1021/jacs.8b04984.

Wolf, N.R., Connor, B.A., Slavney, A.H., and Karunadasa, H.I. (2021). Doubling the stakes: the promise of halide double perovskites. Angew. Chem. Int. Ed. Engl. *60*, 16264–16278. https://doi.org/10.1002/anie.202016185.

Wu, H., Wang, S., Cao, F., Zhou, J., Wu, Q., Wang, H., Li, X., Yin, L., and Yang, X. (2019). Ultrastable inorganic perovskite nanocrystals coated with a thick long-chain polymer for efficient white light-emitting diodes. Chem. Mater. *31*, 1936–1940. https://doi.org/10.1021/acs.chemmater.8b04634.

Wu, M., Shi, J.-j., Zhang, M., Cen, Y.-l., Guo, W.-h., and Zhu, Y.-h. (2018a). Promising photovoltaic and solid-state-lighting materials: two-dimensional Ruddlesden–Popper type lead-free halide double perovskites Csn+1Inn/2Sbn/2I3n+1 (n = 3) and Csn+1Inn/2Sbn/2Cl3n+1/Csm+1Cum/2Bim/2Cl3m+1 (n = 3, m = 1). J. Mater. Chem. C *6*, 11575–11586. https://doi.org/10.1039/c8tc03926g.

Wu, S., Li, Z., Li, M.Q., Diao, Y., Lin, F., Liu, T., Zhang, J., Tieu, P., Gao, W., Qi, F., et al. (2020). 2D metal-organic framework for stable perovskite solar cells with minimized lead leakage. Nat. Nanotechnol. *15*, 934–940. https://doi.org/10.1038/s41565-020-0765-7.

Wu, W.Q., Wang, Q., Fang, Y., Shao, Y., Tang, S., Deng, Y., Lu, H., Liu, Y., Li, T., Yang, Z., et al. (2018b). Molecular doping enabled scalable blading of efficient hole-transport-layer-free perovskite solar cells. Nat. Commun. *9*, 1625. https://doi.org/10.1038/s41467-018-04028-8.

Xia, M., Zhu, S., Luo, J., Xu, Y., Tian, P., Niu, G., and Tang, J. (2021). Ultrastable perovskite nanocrystals in all-inorganic transparent matrix for high-speed underwater wireless optical communication. Adv. Opt. Mater. *9*, 2002239. https://doi.org/10.1002/adom.202002239.

Xiao, Z., Kerner, R.A., Tran, N., Zhao, L., Scholes, G.D., and Rand, B.P. (2019). Engineering perovskite nanocrystal surface termination for light-emitting diodes with external quantum efficiency exceeding 15%. Adv. Funct. Mater. *29*, 1807284. https://doi.org/10.1002/adfm.201807284.

Xie, J.L., Huang, Z.Q., Wang, B., Chen, W.J., Lu, W.X., Liu, X., and Song, J.L. (2019). New lead-free perovskite Rb7Bi3Cl16 nanocrystals with blue luminescence and excellent moisture-stability. Nanoscale *11*, 6719–6726. https://doi.org/10.1039/c9nr00600a.

Xie, L., Vashishtha, P., Koh, T.M., Harikesh, P.C., Jamaludin, N.F., Bruno, A., Hooper, T.J.N., Li, J., Ng, Y.F., Mhaisalkar, S.G., and Mathews, N. (2020). Realizing reduced imperfections via quantum dots interdiffusion in high efficiency perovskite solar cells. Adv. Mater. *32*, e2003296. https://doi.org/10.1002/adma.202003296.

Xing, G., Liao, Y., Wu, X., Chakrabortty, S., Liu, X., Yeow, E.K.L., Chan, Y., and Sum, T.C. (2012). Ultralow-threshold two-photon pumped amplified spontaneous emission and lasing from seeded CdSe/CdS nanorod heterostructures. ACS Nano *6*, 10835–10844. https://doi.org/10.1021/nn304200a.

Xu, L., Li, J., Cai, B., Song, J., Zhang, F., Fang, T., and Zeng, H. (2020). A bilateral interfacial passivation strategy promoting efficiency and stability of perovskite quantum dot light-emitting diodes. Nat. Commun. *11*, 3902. https://doi.org/10.1038/s41467-020-17633-3.

Xu, Y., Chen, Q., Zhang, C., Wang, R., Wu, H., Zhang, X., Xing, G., Yu, W.W., Wang, X., Zhang, Y., and Xiao, M. (2016). Two-photon-pumped perovskite semiconductor nanocrystal lasers. J. Am. Chem. Soc. *138*, 3761–3768. https://doi.org/10.1021/jacs.5b12662.

Xu, Y.F., Yang, M.Z., Chen, B.X., Wang, X.D., Chen, H.Y., Kuang, D.B., and Su, C.Y. (2017). A CsPbBr3 perovskite quantum dot/graphene oxide composite for photocatalytic CO2 reduction. J. Am. Chem. Soc. *139*, 5660–5663. https://doi.org/10.1021/jacs.7b00489.

Xuan, T., Guo, S., Bai, W., Zhou, T., Wang, L., and Xie, R.-J. (2022). Ultrastable and highly efficient green-emitting perovskite quantum dot composites for Mini-LED displays or backlights. Nano Energy *95*, 107003. https://doi.org/10.1016/j.nanoen.2022.107003.

Yakunin, S., Protesescu, L., Krieg, F., Bodnarchuk, M.I., Nedelcu, G., Humer, M., De Luca, G., Fiebig, M., Heiss, W., and Kovalenko, M.V. (2015). Low-threshold amplified spontaneous emission and lasing from colloidal nanocrystals of caesium lead halide perovskites. Nat. Commun. *6*, 8056. https://doi.org/10.1038/ncomms9056.

Yan, D., Shi, T., Zang, Z., Zhou, T., Liu, Z., Zhang, Z., Du, J., Leng, Y., and Tang, X. (2019). Ultrastable CsPbBr3 perovskite quantum dot and their enhanced amplified spontaneous emission by surface ligand modification. Small *15*, e1901173. https://doi.org/10.1002/smll.201901173.

Yang, D., Li, X., Zhou, W., Zhang, S., Meng, C., Wu, Y., Wang, Y., and Zeng, H. (2019). CsPbBr3 quantum dots 2.0: benzenesulfonic acid equivalent ligand awakens complete purification. Adv. Mater. *31*, e1900767. https://doi.org/10.1002/adma.201900767.

Yang, J.N., Chen, T., Ge, J., Wang, J.J., Yin, Y.C., Lan, Y.F., Ru, X.C., Ma, Z.Y., Zhang, Q., and Yao, H.B. (2021). High color purity and efficient green light-emitting diode using perovskite nanocrystals with the size overly exceeding Bohr exciton diameter. J. Am. Chem. Soc. *143*, 19928–19937. https://doi.org/10.1021/jacs.1c09948.

Yao, J.S., Ge, J., Han, B.N., Wang, K.H., Yao, H.B., Yu, H.L., Li, J.H., Zhu, B.S., Song, J.Z., Chen, C., et al. (2018). Ce(3+)-Doping to modulate photoluminescence kinetics for efficient CsPbBr3 nanocrystals based light-emitting diodes. J. Am. Chem. Soc. *140*, 3626–3634. https://doi.org/10.1021/jacs.7b11955.

Yin, H., Kong, Q., Zhang, R., Zheng, D., Yang, B., and Han, K. (2021). Lead-free rare-earth double perovskite Cs2AgIn1−γ−xBixLaγCl6 nanocrystals with highly efficient warm-white emission. Sci. China Mater. *64*, 2667–2674. https://doi.org/10.1007/s40843-021-1681-7.

Yong, Z.J., Guo, S.Q., Ma, J.P., Zhang, J.Y., Li, Z.Y., Chen, Y.M., Zhang, B.B., Zhou, Y., Shu, J., Gu, J.L., et al. (2018). Doping-enhanced short-range order of perovskite nanocrystals for near-unity violet luminescence quantum yield. J. Am. Chem. Soc. *140*, 9942–9951. https://doi.org/10.1021/jacs.8b04763.

Yuan, J., Bi, C., Wang, S., Guo, R., Shen, T., Zhang, L., and Tian, J. (2019). Spray-coated colloidal perovskite quantum dot films for highly efficient solar cells. Adv. Funct. Mater. *29*, 1906615. https://doi.org/10.1002/adfm.201906615.

Yuan, J., Hazarika, A., Zhao, Q., Ling, X., Moot, T., Ma, W., and Luther, J.M. (2020). Metal halide perovskites in quantum dot solar cells: progress and prospects. Joule *4*, 1160–1185. https://doi.org/10.1016/j.joule.2020.04.006.

Yuan, M., Quan, L.N., Comin, R., Walters, G., Sabatini, R., Voznyy, O., Hoogland, S., Zhao, Y., Beauregard, E.M., Kanjanaboos, P., et al. (2016). Perovskite energy funnels for efficient light-emitting diodes. Nat. Nanotechnol. *11*, 872–877. https://doi.org/10.1038/nnano.2016.110.

Zai, H., Zhu, C., Xie, H., Zhao, Y., Shi, C., Chen, Z., Ke, X., Sui, M., Chen, C., Hu, J., et al. (2017). Congeneric incorporation of CsPbBr3 nanocrystals in a hybrid perovskite heterojunction for photovoltaic efficiency enhancement. ACS Energy Lett. *3*, 30–38. https://doi.org/10.1021/acsenergylett.7b00925.

Zhan, W., Meng, L., Shao, C., Wu, X.G., Shi, K., and Zhong, H. (2021). In situ patterning perovskite quantum dots by direct laser writing fabrication. ACS Photonics *8*, 765–770. https://doi.org/10.1021/acsphotonics.1c00118.

Zhang, C., Wang, B., Li, W., Huang, S., Kong, L., Li, Z., and Li, L. (2017a). Conversion of invisible

metal-organic frameworks to luminescent perovskite nanocrystals for confidential information encryption and decryption. Nat. Commun. *8*, 1138. https://doi.org/10.1038/s41467-017-01248-2.

Zhang, C., Wang, S., Li, X., Yuan, M., Turyanska, L., and Yang, X. (2020a). Core/shell perovskite nanocrystals: synthesis of highly efficient and environmentally stable FAPbBr3/CsPbBr3 for LED applications. Adv. Funct. Mater. *30*, 1910582. https://doi.org/10.1002/adfm.201910582.

Zhang, C., Chen, J., Kong, L., Wang, L., Wang, S., Chen, W., Mao, R., Turyanska, L., Jia, G., and Yang, X. (2021a). Core/shell metal halide perovskite nanocrystals for optoelectronic applications. Adv. Funct. Mater. *31*, 2100438. https://doi.org/10.1002/adfm.202100438.

Zhang, F., Huang, S., Wang, P., Chen, X., Zhao, S., Dong, Y., and Zhong, H. (2017b). Colloidal synthesis of air-stable CH3NH3PbI3 quantum dots by gaining chemical insight into the solvent effects. Chem. Mater. *29*, 3793–3799. https://doi.org/10.1021/acs.chemmater.7b01100.

Zhang, F., Shi, Z., Li, S., Ma, Z., Li, Y., Wang, L., Wu, D., Tian, Y., Du, G., Li, X., and Shan, C. (2019a). Synergetic effect of the surfactant and silica coating on the enhanced emission and stability of perovskite quantum dots for anticounterfeiting. ACS Appl. Mater. Interfaces *11*, 28013–28022. https://doi.org/10.1021/acsami.9b07518.

Zhang, F., Zhong, H., Chen, C., Wu, X.G., Hu, X., Huang, H., Han, J., Zou, B., and Dong, Y. (2015). Brightly luminescent and color-tunable colloidal CH3NH3PbX3 (X = Br, I, Cl) quantum dots: potential alternatives for display technology. ACS Nano *9*, 4533–4542. https://doi.org/10.1021/acsnano.5b01154.

Zhang, H., Qin, M., Chen, Z., Yu, W., Ren, Z., Liu, K., Huang, J., Zhang, Y., Liang, Q., Chandran, H.T., et al. (2021b). Bottom-up quasi-epitaxial growth of hybrid perovskite from solution process-achieving high-efficiency solar cells via template-guided crystallization. Adv. Mater. *33*, e2100009. https://doi.org/10.1002/adma.202100009.

Zhang, J., Yang, Y., Deng, H., Farooq, U., Yang, X., Khan, J., Tang, J., and Song, H. (2017c). High quantum yield blue emission from lead-free inorganic antimony halide perovskite colloidal quantum dots. ACS Nano *11*, 9294–9302. https://doi.org/10.1021/acsnano.7b04683.

Zhang, X., Guo, Z., Li, R., Yu, J., Yuan, B., Chen, B., He, T., and Chen, R. (2021c). Quasi-type II core-shell perovskite nanocrystals for improved structural stability and optical gain. ACS Appl. Mater. Interfaces *13*, 58170–58178. https://doi.org/10.1021/acsami.1c18025.

Zhang, X., Huang, H., Ling, X., Sun, J., Jiang, X., Wang, Y., Xue, D., Huang, L., Chi, L., Yuan, J., and Ma, W. (2022a). Homojunction perovskite quantum dot solar cells with over 1 microm-thick photoactive layer. Adv. Mater. *34*, e2105977. https://doi.org/10.1002/adma.202105977.

Zhang, X., Qian, Y., Ling, X., Wang, Y., Zhang, Y., Shi, J., Shi, Y., Yuan, J., and Ma, W. (2020b). alpha-CsPbBr3 perovskite quantum dots for application in semitransparent photovoltaics. ACS Appl. Mater. Interfaces *12*, 27307–27315. https://doi.org/10.1021/acsami.0c07667.

Zhang, X., Chen, S., Wang, X., and Pan, A. (2019b). Controlled synthesis and photonics applications of metal halide perovskite nanowires. Small Methods *3*, 1800294. https://doi.org/10.1002/smtd.201800294.

Zhang, Y., Saidaminov, M.I., Dursun, I., Yang, H., Murali, B., Alarousu, E., Yengel, E., Alshankiti, B.A., Bakr, O.M., and Mohammed, O.F. (2017d). Zero-dimensional Cs4PbBr6 perovskite nanocrystals. J. Phys. Chem. Lett. *8*, 961–965. https://doi.org/10.1021/acs.jpclett.7b00105.

Zhang, Y., Sun, R., Ou, X., Fu, K., Chen, Q., Ding, Y., Xu, L.J., Liu, L., Han, Y., Malko, A.V., et al. (2019c). Metal halide perovskite nanosheet for X-ray high-resolution scintillation imaging screens. ACS Nano *13*, 2520–2525. https://doi.org/10.1021/acsnano.8b09484.

Zhang, Y., Wang, C., and Deng, Z. (2018). Colloidal synthesis of monolayer-thick formamidinium lead bromide perovskite nanosheets with a lateral size of micrometers. Chem. Commun. *54*, 4021–4024. https://doi.org/10.1039/c8cc01466c.

Zhang, Z., Zhang, Y., Guo, X., Wang, D., Lao, Y., Qu, B., Xiao, L., and Chen, Z. (2022b). Realizing high-efficiency and stable perovskite solar cells via double-perovskite nanocrystal passivation. ACS Appl. Energy Mater. *5*, 1169–1174. https://doi.org/10.1021/acsaem.1c03544.

Zhao, Q., Hazarika, A., Chen, X., Harvey, S.P., Larson, B.W., Teeter, G.R., Liu, J., Song, T., Xiao, C., Shaw, L., et al. (2019a). High efficiency perovskite quantum dot solar cells with charge separating heterostructure. Nat. Commun. *10*, 2842. https://doi.org/10.1038/s41467-019-10856-z.

Zhao, Q., Hazarika, A., Schelhas, L.T., Liu, J., Gaulding, E.A., Li, G., Zhang, M., Toney, M.F., Sercel, P.C., and Luther, J.M. (2019b). Size-dependent lattice structure and confinement properties in CsPbI3 perovskite nanocrystals: negative surface energy for stabilization. ACS Energy Lett. *5*, 238–247. https://doi.org/10.1021/acsenergylett.9b02395.

Zheng, C., Bi, C., Huang, F., Binks, D., and Tian, J. (2019a). Stable and strong emission CsPbBr3 quantum dots by surface engineering for high-performance optoelectronic films. ACS Appl. Mater. Interfaces *11*, 25410–25416. https://doi.org/10.1021/acsami.9b07818.

Zheng, W., Sun, R., Liu, Y., Wang, X., Liu, N., Ji, Y., Wang, L., Liu, H., and Zhang, Y. (2021). Excitation management of lead-free perovskite nanocrystals through doping. ACS Appl. Mater. Interfaces *13*, 6404–6410. https://doi.org/10.1021/acsami.0c20230.

Zheng, X., Troughton, J., Gasparini, N., Lin, Y., Wei, M., Hou, Y., Liu, J., Song, K., Chen, Z., Yang, C., et al. (2019b). Quantum dots supply bulk- and surface-passivation agents for efficient and stable perovskite solar cells. Joule *3*, 1963–1976. https://doi.org/10.1016/j.joule.2019.05.005.

Zheng, X., Yuan, S., Liu, J., Yin, J., Yuan, F., Shen, W.-S., Yao, K., Wei, M., Zhou, C., Song, K., et al. (2020). Chlorine vacancy passivation in mixed halide perovskite quantum dots by organic pseudohalides enables efficient Rec. 2020 blue light-emitting diodes. ACS Energy Lett *5*, 793–798. https://doi.org/10.1021/acsenergylett.0c00057.

Zhong, H., and Wang, Y. (2020). Quantum dots on demand. Nat. Photonics *14*, 65–66. https://doi.org/10.1038/s41566-019-0579-z.

Zhong, Q., Cao, M., Hu, H., Yang, D., Chen, M., Li, P., Wu, L., and Zhang, Q. (2018). One-pot synthesis of highly stable CsPbBr3@SiO2 core-shell nanoparticles. ACS Nano *12*, 8579–8587. https://doi.org/10.1021/acsnano.8b04209.

Zhong, Q., Cao, M., Xu, Y., Li, P., Zhang, Y., Hu, H., Yang, D., Xu, Y., Wang, L., Li, Y., et al. (2019). L-type ligand-assisted acid-free synthesis of CsPbBr3 nanocrystals with near-unity photoluminescence quantum yield and high stability. Nano Lett. *19*, 4151–4157. https://doi.org/10.1021/acs.nanolett.9b01666.

Zhou, C., Lin, H., He, Q., Xu, L., Worku, M., Chaaban, M., Lee, S., Shi, X., Du, M.H., and Ma, B. (2019a). Low dimensional metal halide perovskites and hybrids. Mater. Sci. Eng. R Rep. *137*, 38–65. https://doi.org/10.1016/j.mser.2018.12.001.

Zhou, D., Liu, D., Pan, G., Chen, X., Li, D., Xu, W., Bai, X., and Song, H. (2017a). Cerium and ytterbium codoped halide perovskite quantum dots: a novel and efficient downconverter for improving the performance of silicon solar cells. Adv. Mater. *29*, 1704149. https://doi.org/10.1002/adma.201704149.

Zhou, H., Yuan, S., Wang, X., Xu, T., Wang, X., Li, H., Zheng, W., Fan, P., Li, Y., Sun, L., and Pan, A. (2017b). Vapor growth and tunable lasing of band gap engineered cesium lead halide perovskite micro/nanorods with triangular cross section. ACS Nano *11*, 1189–1195. https://doi.org/10.1021/acsnano.6b07374.

Zhou, S. (2021). Rapid separation and purification of lead halide perovskite quantum dots through differential centrifugation in nonpolar solvent. RSC Adv. *11*, 28410–28419. https://doi.org/10.1039/d1ra04578d.

Zhou, S., Ding, Y., Pi, X., and Nozaki, T. (2014). Doped silicon nanocrystals from organic dopant precursor by a SiCl4-based high frequency nonthermal plasma. Appl. Phys. Lett. *105*, 183110. https://doi.org/10.1063/1.4901278.

Zhou, S., Ma, Y., Zhou, G., Xu, X., Qin, M., Li, Y., Hsu, Y.J., Hu, H., Li, G., Zhao, N., et al. (2019b). Ag-doped halide perovskite nanocrystals for tunable band structure and efficient charge transport. ACS Energy Lett. *4*, 534–541. https://doi.org/10.1021/acsenergylett.8b02478.

Zhou, S., Ni, Z., Ding, Y., Sugaya, M., Pi, X., and Nozaki, T. (2016). Ligand-free, colloidal, and plasmonic silicon nanocrystals heavily doped with boron. ACS Photonics *3*, 415–422. https://doi.org/10.1021/acsphotonics.5b00568.

Zhou, S., Nozaki, T., and Pi, X. (2018). Boron nanocrystals as high-energy-density fuels. J. Phys. D Appl. Phys. *51*, 025305. https://doi.org/10.1088/1361-6463/aa9df6.

Zhou, S., Pi, X., Ni, Z., Ding, Y., Jiang, Y., Jin, C., Delerue, C., Yang, D., and Nozaki, T. (2015a). Comparative study on the localized surface plasmon resonance of boron- and phosphorus-doped silicon nanocrystals. ACS Nano *9*, 378–386. https://doi.org/10.1021/nn505416r.

Zhou, S., Pi, X., Ni, Z., Luan, Q., Jiang, Y., Jin, C., Nozaki, T., and Yang, D. (2015b). Boron- and phosphorus-hyperdoped silicon nanocrystals. Part. Part. Syst. Charact. *32*, 213–221. https://doi.org/10.1002/ppsc.201400103.

Zhou, S., Zhou, G., Li, Y., Xu, X., Hsu, Y.J., Xu, J., Zhao, N., and Lu, X. (2020). Understanding charge transport in all-inorganic halide perovskite nanocrystal thin-film field effect transistors. ACS Energy Lett. *5*, 2614–2623. https://doi.org/10.1021/acsenergylett.0c01295.

Zhou, S., Zhu, S., Guan, J., Wang, R., Zheng, W., Gao, P., and Lu, X. (2021a). Confronting the air instability of cesium tin halide perovskites by metal ion incorporation. J. Phys. Chem. Lett. *12*, 10996–11004. https://doi.org/10.1021/acs.jpclett.1c03170.

Zhou, Y., Chen, J., Bakr, O.M., and Mohammed, O.F. (2021b). Metal halide perovskites for X-ray imaging scintillators and detectors. ACS Energy Lett. *6*, 739–768. https://doi.org/10.1021/acsenergylett.0c02430.

Zhu, D., Zito, J., Pinchetti, V., Dang, Z., Olivati, A., Pasquale, L., Tang, A., Zaffalon, M.L., Meinardi, F., Infante, I., et al. (2020). Compositional tuning of carrier dynamics in Cs2Na1-x Ag x BiCl6 double-perovskite nanocrystals. ACS Energy Lett. *5*, 1840–1847. https://doi.org/10.1021/acsenergylett.0c00914.

Zhu, P., and Zhu, J. (2020). Low-dimensional metal halide perovskites and related optoelectronic applications. Infomat *2*, 341–378. https://doi.org/10.1002/inf2.12086.